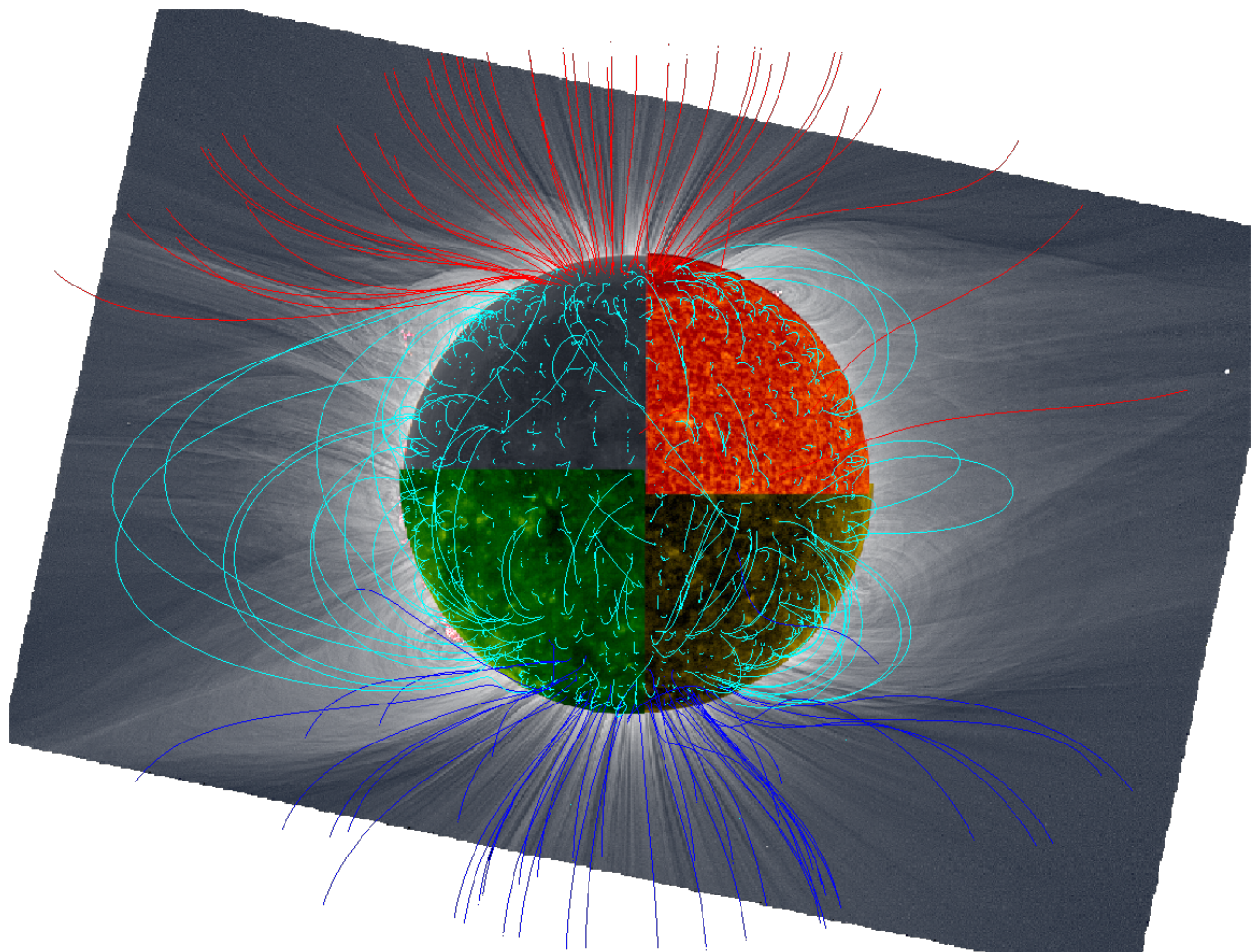


# EXPANDING THE POTENTIAL FIELD SOURCE SURFACE MODEL WITH AN ELLIPSOIDAL SOURCE SURFACE



Dissertation  
zur Erlangung des Doktorgrades  
der Mathematisch-Naturwissenschaftlichen Fakultät  
der Christian-Albrechts-Universität zu Kiel  
vorgelegt von

MARTIN ALEXANDER KRUSE

– Kiel, November 2020 –

Martin Alexander Kruse:

*Expanding the Potential Field Source Surface Model  
With an Ellipsoidal Source Surface,*

© November 2020

Cover: Rendering of a PFSS model with oblate source surface ( $R_{ss} = 2.0 \cdot R_{\odot}$ ,  $A = 1.5$ ). The coronal overlay is a composite image of the 2008 solar eclipse captured from Mongolia, reproduced with permission from Prof. Dr. Druckmüller. Visible in the upper left corner of the solar disk is the moon. SOHO/EIT images cover the other three quadrants. From top-right clockwise, the wavelengths are 304 Å, 284 Å, and 195 Å.

**ERSTER GUTACHTER (SUPERVISOR):**  
Prof. Dr. R. F. Wimmer-Schweingruber

**ZWEITER GUTACHTER (ADVISOR):**  
Prof. Dr. W. J. Duschl

**TAG DER MÜNDLICHEN PRÜFUNG:**  
05.02.2021

**ZUM DRUCK GENEHMIGT:**  
05.02.2021



## ABSTRACT

---

Phenomena such as solar wind acceleration and propagation are tightly linked with the magnetic field configuration close to the solar surface. Heliospheric studies of the solar corona and interplanetary space require a knowledge of the large-scale magnetic field orientation. Particles and electromagnetic fields can be measured at select points in the heliosphere via in-situ instrumentation aboard spacecraft. The magnetic configuration in the solar photosphere can be quantified using remote sensing instruments exploiting the Zeeman effect. However, for the region directly above the photosphere (i.e., the corona), no accurate measurement method exists. The magnetic field can neither be measured in-situ due to the harsh environment for spacecraft travel, nor can it be remotely sensed due to the coronal medium's optical transparency and resulting projection effects. Therefore, computational models that extrapolate the little information available on the solar magnetic field to the heliosphere's vast extent are required for a more thorough picture of the heliospheric physics.

One such model is the Potential Field Source Surface ([PFSS](#)) model that extrapolates the photospheric magnetic line-of-sight configuration up to a virtual spherical outer boundary referred to as the source surface. As part of this work, the well-established theoretical framework of the [PFSS](#) model is extended to incorporate specifically oriented ellipsoidal source surfaces. Thereby, it is lifting the source surface's restriction of being spherical, as the spherical shape has no strong physical motivation besides being the most straightforward boundary that can be implemented. An efficient computational implementation has been developed that permits the rapid computation of the predicted coronal magnetic field [[Kruse et al., 2020b](#)]. Moreover, the prediction accuracy of both the enhanced and the original [PFSS](#) models have been evaluated employing in-situ spacecraft measurements in the ecliptic near Earth's orbit, finding that the [PFSS](#) model performs slightly better with oblate ellipsoidal source surfaces than with a spherical source surface [[Kruse et al., 2020a](#)]. Both models perform considerably better during the solar activity cycle minimum than during solar activity maximum.

Furthermore, the [PFSS](#) implementation developed as part of this work has been employed to identify photospheric source regions of solar wind plasma, aiding the effort to establish a meaningful solar wind classification scheme [[Heidrich-Meisner et al., 2016, 2017](#)]. This implementation has been used to predict the most probable solar wind source regions, facilitating an improved orientation algorithm for the remote-sensing Spectral Imaging of the Coronal Environment ([SPICE](#)) instrument aboard the Solar Orbiter spacecraft [[Peleikis et al., 2017](#)]. This work is part of a collaborative effort combining remote-sensing with in-situ measurements to better understand the solar wind phenomenon.

## ZUSAMMENFASSUNG

---

Phänomene wie die Beschleunigung und Ausbreitung des Sonnenwindes sind eng mit der Magnetfeldkonfiguration nahe der Sonnenoberfläche verbunden. Studien der Sonnenkorona und des interplanetaren Raums erfordern die Kenntnis des großräumigen Magnetfelds. Partikel und elektromagnetische Felder können an ausgewählten Punkten in der Heliosphäre mit in-situ Instrumenten an Bord von Sonden gemessen werden. Die magnetische Konfiguration in der solaren Photosphäre kann per Fernerkundung unter Ausnutzung des Zeeman-Effekts ermittelt werden. Für die Korona gibt es jedoch keine genauen Messmethoden. Das Magnetfeld kann aufgrund der für Weltraumfahrzeuge schädlichen Umgebung weder in-situ gemessen werden, noch kann es aufgrund der optischen Transparenz des koronalen Mediums und der daraus resultierenden Projektionseffekte aus der Ferne korrekt erfasst werden. Daher sind Computermodelle erforderlich, welche die wenigen Informationen, die über das solare Magnetfeld verfügbar sind, auf das große Ausmaß der Heliosphäre extrapoliieren, um ein genaueres Bild der heliosphärischen Physik zu erhalten.

Ein solches Modell ist das Potential Field Source Surface ([PFSS](#))-Modell, welches die photosphärische Magnetfeldkonfiguration bis zu einer virtuellen sphärischen Außengrenze, der Source Surface, extrapoliert. Als Teil dieser Arbeit wird der theoretische Rahmen des [PFSS](#)-Modells erweitert, um ellipsoide Source Surfaces einzubeziehen. Dadurch wird die Beschränkung der Source Surface auf die Kugelform aufgehoben, da diese keine starke physikalische Motivation hat, dafür aber leicht implementierbar ist. Es wurde eine effiziente Implementierung entwickelt, welche eine schnelle Berechnung des vorhergesagten koronalen Magnetfeldes erlaubt [[Kruse et al., 2020b](#)]. Darüber hinaus wurde die Genauigkeit sowohl des erweiterten als auch des ursprünglichen [PFSS](#)-Modells unter Verwendung von in-situ Raumsondenmessungen in der Ekliptik evaluiert, wobei festgestellt wurde, dass das [PFSS](#)-Modell mit abgeflachten ellipsoiden Source Surfaces etwas besser abschneidet als mit einer sphärischen Source Surface [[Kruse et al., 2020a](#)]. Beide Modelle schneiden während des Sonnenaktivitäts-Minimums erheblich besser ab als während des Sonnenaktivitäts-Maximums.

Darüber hinaus wurde die im Rahmen dieser Arbeit entwickelte Implementierung verwendet, um photosphärische Quellregionen des Sonnenwindplasmas zu identifizieren, was die Erstellung eines aussagekräftigen Sonnenwind-Klassifikationsschemas unterstützt [[Heidrich-Meisner et al., 2016, 2017](#)]. Diese Implementierung wurde zur Vorhersage der wahrscheinlichsten Sonnenwindquellenregionen verwendet, wodurch ein Algorithmus zur Orientierung des Spectral Imaging of the Coronal Environment ([SPICE](#)) Instruments an Bord der Sonde Solar Orbiter entwickelt wurde [[Peleikis et al., 2017](#)]. Dieses Arbeit ist Teil eines gemeinschaftlichen Projekts zur Kombination von Fernerkundungsinstrumenten und in-situ Messungen, um das Phänomen des Sonnenwinds besser zu verstehen.



## PUBLICATIONS

---

### Publication 1:

#### AN ELLIPTIC EXPANSION OF THE POTENTIAL FIELD SOURCE SURFACE MODEL

M. Kruse, V. Heidrich-Meisner, R. F. Wimmer-Schweingruber and M. Hauptmann,  
A&A, A109, 638, 2020  
DOI: [10.1051/0004-6361/202037734](https://doi.org/10.1051/0004-6361/202037734)

Own contribution: 90%

### Publication 2:

#### EVALUATION OF A POTENTIAL FIELD SOURCE SURFACE MODEL WITH ELLIPTICAL SOURCE SURFACES VIA BALLISTIC BACKMAPPING OF IN-SITU SPACECRAFT DATA

M. Kruse, V. Heidrich-Meisner and R. F. Wimmer-Schweingruber, A&A, accepted,  
in production, 2020  
DOI: [10.1051/0004-6361/202039120](https://doi.org/10.1051/0004-6361/202039120)

Own contribution: 90%

### Publication 3:

#### ORIGIN OF THE SOLAR WIND: A NOVEL APPROACH TO LINK IN SITU AND REMOTE OBSERVATIONS

T. Peleikis, M. Kruse, L. Berger and R. F. Wimmer-Schweingruber, A&A, A24, 602,  
2017  
DOI: [10.1051/0004-6361/201629727](https://doi.org/10.1051/0004-6361/201629727)

Own contribution: 25%

### Publication 4:

#### OBSERVATIONS OF HIGH AND LOW Fe CHARGE STATES IN INDIVIDUAL SOLAR WIND STREAMS WITH CORONAL-HOLE ORIGIN

V. Heidrich-Meisner, T. Peleikis, M. Kruse, L. Berger and R. F. Wimmer-Schweingruber, A&A, A70, 593, 2016  
DOI: [10.1051/0004-6361/201527998](https://doi.org/10.1051/0004-6361/201527998)

Own contribution: 25%

### Publication 5:

#### EVOLUTION OF AN EQUATORIAL CORONAL HOLE STRUCTURE AND THE RELEASED CORONAL HOLE WIND STREAM: CARRINGTON ROTATIONS 2039 TO 2050

V. Heidrich-Meisner, T. Peleikis, M. Kruse, L. Berger and R. F. Wimmer-Schweingruber, A&A, A84, 603, 2017  
DOI: [10.1051/0004-6361/201730574](https://doi.org/10.1051/0004-6361/201730574)

Own contribution: 15%

## CONTENTS

---

<b>1</b>	<b>INTRODUCTION</b>	<b>1</b>
1.1	Solar wind . . . . .	1
1.2	Solar wind classification . . . . .	2
1.3	Coronal magnetic field . . . . .	4
1.4	Potential Field Source Surface model . . . . .	5
1.5	Improving the PFSS model . . . . .	6
1.6	Structural overview of the thesis . . . . .	7
<b>2</b>	<b>BASICS OF THE POTENTIAL FIELD SOURCE SURFACE MODEL</b>	<b>9</b>
2.1	The Potential Field Source Surface model . . . . .	9
2.2	The WSO approach . . . . .	10
2.2.1	Coronal magnetic field representation . . . . .	12
2.2.2	Coordinates of pixels in the magnetograms . . . . .	15
2.3	PFSS reference implementation . . . . .	16
<b>3</b>	<b>SPHERICAL GRID IMPLEMENTATION</b>	<b>19</b>
3.1	Grid topology and notation . . . . .	20
3.2	Finite-difference expressions of the differential operators . . . . .	20
3.2.1	First derivative . . . . .	21
3.2.2	Second derivative . . . . .	22
3.2.3	Mixed derivatives . . . . .	22
3.3	Computational boundaries . . . . .	23
3.4	Finite-difference representation of the Laplace operator . . . . .	25
3.5	Solution method . . . . .	25
3.6	Numerical considerations . . . . .	26
<b>4</b>	<b>ELLIPSOIDAL GRID IMPLEMENTATION</b>	<b>27</b>
4.1	General notation, computational and physical domain . . . . .	28
4.2	The ellipsoid stretching function . . . . .	31
4.3	Covariant and contravariant basis vectors . . . . .	32
4.4	Laplace operator in general curvilinear coordinates . . . . .	37
<b>5</b>	<b>GRID PARAMETERS AND PROCESSING OF INPUT / OUTPUT DATA</b>	<b>41</b>
5.1	Grid point distribution and density . . . . .	41
5.1.1	Numerical considerations . . . . .	42
5.1.2	Comparison metrics . . . . .	44
5.1.3	Determination of grid parameters . . . . .	46
5.2	Preprocessing of input data . . . . .	48
5.2.1	Overview of solar magnetographs . . . . .	48
5.2.2	Scaling of magnetograms . . . . .	49
5.3	Postprocessing of model output data . . . . .	52
5.3.1	Magnetic field line tracking . . . . .	52
5.3.2	Interpolation accuracy . . . . .	54
5.3.3	Polarity maps . . . . .	55

5.3.4	Expansion factor maps . . . . .	55
5.3.5	Visualization of model predictions . . . . .	56
5.4	Comparing implementations . . . . .	56
5.5	Publication 1 . . . . .	58
5.5.1	Introduction . . . . .	61
5.5.2	Methods . . . . .	62
5.5.3	Results . . . . .	64
5.5.4	Discussion and conclusions . . . . .	66
5.5.5	Appendix A: Mathematical framework of the elliptical grid solver . . . . .	70
6	<b>EVALUATING THE NEW SOLVER</b>	71
6.1	Ballistic back mapping . . . . .	72
6.2	Spacecraft data used . . . . .	72
6.2.1	Advanced Composition Explorer . . . . .	72
6.2.2	Solar Terrestrial Relations Observatories . . . . .	73
6.3	Selection of time periods and magnetogram data . . . . .	73
6.4	Back mapping polarity measure . . . . .	74
6.5	Publication 2 . . . . .	77
6.5.1	Introduction . . . . .	79
6.5.2	Methods . . . . .	80
6.5.3	Results: Magnetic field polarity prediction accuracy . . . . .	84
6.5.4	Conclusions . . . . .	85
7	<b>APPLICATIONS</b>	89
7.1	Solar wind origin . . . . .	89
7.2	Solar wind tracers . . . . .	90
7.3	Publication 3 . . . . .	91
7.3.1	Introduction . . . . .	93
7.3.2	Methods and analysis . . . . .	94
7.3.3	Solar orbiter forward mapping . . . . .	97
7.3.4	Comparison with the CSSS model . . . . .	101
7.3.5	Summary and conclusion . . . . .	101
7.4	Publication 4 . . . . .	103
7.4.1	Introduction . . . . .	104
7.4.2	Data analysis and event selection . . . . .	105
7.4.3	Fe charge states of individual coronal-hole-wind streams . . . . .	106
7.4.4	Conclusions . . . . .	112
7.5	Publication 5 . . . . .	113
7.5.1	Introduction . . . . .	115
7.5.2	Data selection solar wind characterisation and methods . . . . .	116
7.5.3	A recurring coronal structure . . . . .	118
7.5.4	Implications for temperature profiles . . . . .	123
7.5.5	Discussion and conclusions . . . . .	130
8	<b>SUMMARY &amp; OUTLOOK</b>	133
A	<b>IMPLEMENTATION DETAILS AND RUN TIME MEASUREMENTS</b>	137
	<b>BIBLIOGRAPHY</b>	143

## ACRONYMS

---

ACE	Advanced Composition Explorer
ASCII	American Standard Code for Information Interchange
AU	Astronomical Unit
CIR	Co-rotating Interaction Region
CME	Coronal Mass Ejection
CPU	Central Processing Unit
CSSS	Current Sheet Source Surface
EUV	Extreme Ultra-Violet
FIP	First Ionization Potential
GONG	Global Oscillation Network Group
GPU	Graphics Processing Unit
HCCS	Horizontal Current Current Sheet
HCS	Heliospheric Current Sheet
HMI	Helioseismic and Magnetic Imager
ICME	Interplanetary Coronal Mass Ejection
IMP	Interplanetary Monitoring Platform
IMPACT	In situ Measurements of Particles and CME Transients
KPVT	Kitt Peak Vacuum Tower Telescope
L <sub>1</sub>	Lagrangian point 1
MHD	Magnetohydrodynamics
MDI	Michelson Doppler Imager
MWO	Mount Wilson Observatory
NSO	National Solar Observatory
PFCS	Potential Field Current Sheet
PFSS	Potential Field Source Surface
PLASTIC	Plasma and Supra-Thermal Ion and Composition instrument
PSP	Parker Solar Probe
SWEPAM	Solar Wind Electron, Proton and Alpha Monitor
SDO	Solar Dynamics Observatory
SHC	Spherical Harmonic Coefficient
SIR	Stream Interaction Region
SLERP	Spherical Linear Interpolation
SOHO	Solar and Heliospheric Observatory
SPICE	Spectral Imaging of the Coronal Environment
STEREO	Solar Terrestrial Relations Observatory
SWA	Solar Wind Analyser
SWICS	Solar Wind Ion Composition Spectrometer
WSO	Wilcox Solar Observatory

## INTRODUCTION

---

The Sun plays a vital role in all our lives. It generates heat, which makes life on Earth as we know it possible in the first place. Understanding the nature of the Sun has been a matter of human interest for millennia. While the ramifications of its gravity and heat could be felt and (more or less) understood for most of history, the knowledge of charged particle streams emanating from it is a comparatively recent scientific achievement. With the advent of human interplanetary space flight, understanding and predicting these particle streams become ever more pressing for the safety of astronauts and spacecraft.

The *photosphere* is regarded as the Sun's surface, where the particle density experiences a steep decline of several orders of magnitude in a very narrow region [e.g., [Cranmer et al., 2007](#)]. High temperatures, strong magnetic fields, and massive convection processes generate an environment that hosts many physical processes that shape the solar vicinity. The *corona* is a region near the Sun that dynamically extends a few solar radii above the photosphere. This region's exact size is not clearly defined and varies in time and location above the solar body. It is mostly associated with the region of visible light emission in solar eclipse imagery, in which the solar body is occluded either by a natural (the moon) or an artificial body (in so-called coronagraph instruments). It is also the domain of a sharp temperature increase, also known as the transition region, where the temperature grows from approximately 5800 Kelvin on the solar surface to more than a million Kelvin in the lower corona. The nature of this region's heating process is still under debate. Strong magnetic fields, combined with low particle densities (low  $\beta$ ) in this region, constitute an environment dominated by the structure of the magnetic field that charged particles adhere to. Knowledge of the magnetic configuration in this domain is of particular interest in understanding how the Sun emits mass in the form of charged particles into the *heliosphere* and interplanetary space. The coronal magnetic field and plasma streams originating from it are the focus of the study at hand.

### 1.1 SOLAR WIND

The interplanetary space is filled with particles and electromagnetic fields from various sources, but the most dominant contributor is arguably the Sun, emanating a constant stream of charged particles, also known as the *solar wind*. It mainly consists of protons, electrons, and helium ions, the latter contributing a few percent of the overall number of particles. Traces of heavier ions can be found as well; however, these elements do not contribute considerably to the propagation and acceleration processes of the solar wind and are neglected in most solar wind models. They carry information about the physical properties of different sections of the

recently traveled path along which the plasma parcel has propagated. Measuring minor ions and their characteristics in-situ at spacecraft in interplanetary space allow probing conditions at lower positions in the heliosphere where in-situ measurements cannot be conducted. Publications 4 (Sect. 7.4) and 5 (Sect. 7.5) make use of this remote sensing mechanism.

The existence of "corpuscular radiation" emanating from the Sun has been theorized since the beginning of the 20th century [Birkeland, 1914; Chapman, 1917]. While Carrington [1859] observed the onset of a Coronal Mass Ejection (CME) and suggested, it ejects matter out into interplanetary space half a century before, the first implicit mention of a steady solar stream wind is generally attributed to Eddington [1910], who observed the solar wind deforming the tail of comet Morehouse. Parker showed in the middle of the 20th century that a static heliosphere cannot maintain hydrostatic equilibrium and that a constant particle stream was necessary to explain the observations of our central star [Parker, 1958]. Shortly thereafter, Soviet and American experiments showed the existence of ionized particle streams in near-Earth space [Neugebauer and Snyder, 1962]. Since the 1970s, the solar wind has continuously been observed and analyzed by a growing number of space-based instruments.

Because the solar corona is a hostile environment for in-situ instrumentation, probing this regime via spacecraft travel is not (yet) feasible. The solar wind carries particles and information from the lower corona out into interplanetary space. For research, this provides a significant opportunity to probe the near solar surface regime by measuring the solar wind's in-situ characteristics further out in the heliosphere. These remote probing measurements can then be combined with remote sensing observations of the expected source region (given that a solar magnetic field model is available) to form a more comprehensive picture of the physical processes involved. The Solar Orbiter mission combines remote sensing and in-situ instrumentation on a single platform to investigate the link between the photosphere and the solar wind plasma. An application that utilizes this observation platform is discussed in Publication 3 (Sect. 7.3).

Solar wind streams can have vastly different characteristics depending on the processes accelerating them into the heliosphere and transport effects they are subjected to during their journey through the heliosphere. Several classification schemes have been developed to distinguish measurements of the interplanetary plasma.

## 1.2 SOLAR WIND CLASSIFICATION

Historically, the solar wind has been partitioned into three classes: the *fast solar wind* with proton velocities above 500 km/s, the *slow solar wind* with velocities below 500 km/s, and *transient streams* with an origin in disruptive events like CMEs [Zhao et al., 2009; Verscharen et al., 2019; Lepri et al., 2013]. Some of the acceleration processes are well-understood, for example, fast streams originating from coronal holes [McComas et al., 1998c; Hackenberg et al., 2000; Tu et al., 2005; Verscharen et al., 2019; Krieger et al., 1973], while others remain elusive even af-

ter decades of scientific effort. Especially the source regions of slow solar wind streams are under debate. While some type of slow solar wind is widely believed to originate near the streamer belt [McComas et al. \[1998b\]](#); [Woo and Martin \[1997\]](#); [Strachan et al. \[2002\]](#); [Zhao et al. \[2009\]](#), other sources such as active regions [[Hick et al., 1995](#); [Neugebauer et al., 2002](#); [Liewer et al., 2004](#); [Liu and Su, 2014](#); [Marsch et al., 2008](#)], coronal hole boundaries [[Neugebauer et al., 1998](#); [Wang and Sheeley, 1990](#); [Tian et al., 2011](#)] or a structure called the S-Web [[Antiochos et al., 2012](#)] are valid candidates as well.

Studies have shown that the bulk velocity is not the most characteristic feature of these wind types and that there are many dimensions along which solar wind plasma streams can be distinguished [[von Steiger et al., 2000](#); [Stakhiv et al., 2015](#)]. More intricate models have been developed in the past decades to classify solar plasma streams according to characteristics like chemical composition, proton-specific entropy, proton Alfvén speed, temperature, density, or a combination thereof. For example, the electron temperature allows separating hot and cold solar wind streams by measuring ionic charge state ratios of  $O^{7+}/C^{6+}$  [[Zhao et al., 2014](#)] or  $C^{6+}/C^{4+}$  [[Landi et al., 2012](#)]. [Heidrich-Meisner and Wimmer-Schweingruber \[2018\]](#) utilized a machine learning algorithm working on several sets of in-situ plasma data and a varying number of classes to obtain insight from the automatic clustering of samples. In contrast to solar wind classification via evaluation of spacecraft in-situ instrument data, [Zhao et al. \[2017\]](#) developed a back mapping algorithm that traces solar wind packages to their most probable source regions on the photosphere via a classical Potential Field Source Surface ([PFSS](#)) implementation. The solar wind parcel is then classified as one of six types according to the ascertained footpoint's brightness in a synoptic Extreme Ultra-Violet ([EUV](#)) photospheric map.

Another fairly recent categorization scheme is the four-type classification developed by [Xu and Borovsky \[2015\]](#). It draws distinction hyperplanes in the four-dimensional parameter room of proton temperature  $T_p$ , bulk flow speed  $v_p$ , magnetic field strength  $B$ , and proton number density  $n_p$ . The four classes distinguished by this model are coronal hole plasma (fast wind), helmet-streamer plasma (normal slow wind), sector-reversal plasma (slow wind emanating near the current sheet crossings), and the ejecta type plasma (emitted from violent eruptions such as [CMEs](#)). This classification scheme has been developed for data from the Advanced Composition Explorer ([ACE](#)), which is positioned at the Lagrangian point 1 ([L1](#)) of the Sun-Earth system near one Astronomical Unit ([AU](#)) heliocentric distance. Thus, the scheme is only valid for instrumentation near Earth's orbit. In Sect. 6.4 and Publication 2 (Sect. 6.5), the [Xu and Borovsky \[2015\]](#) categorization scheme is employed to help evaluate the prediction accuracy of the newly developed [PFSS](#) implementation.

Several phenomena complicate the solar wind classification process. Eruptions such as flares or Interplanetary Coronal Mass Ejections (ICMEs) eject large amounts of plasma into the heliosphere, disrupting the magnetic field and quasi-static particle stream in its wake. When a fast solar wind stream flows into a slower wind stream, a Co-rotating Interaction Region ([CIR](#)) forms where the plasma of the fast stream accumulates, creating a compression region. The opposite happens when a

slow solar wind stream follows a fast stream. In this case, an instrument measuring the fast stream will recognize a rarefaction region of very low plasma density following the fast stream before measuring the subsequent slow stream. These phenomena are typically excluded from the classification schemes (or sorted into a separate class) because their origin and characteristics are different from those of quasi-steady streams.

A critical factor for the expansion of all (steady) solar wind types is the magnetic configuration of their coronal origin and the subsequent path traversed by the particle streams. In the corona, charged particles are forced to travel along the solar magnetic field. Therefore, understanding the acceleration mechanisms relies heavily on comprehending the solar surface's magnetic configuration, coronal environment, and interplanetary space. Based on the particles' charged state making up the solar wind, their expansion into interplanetary space and the background magnetic field is tightly coupled. The magnetic field can be thought of as the canvas on which heliospheric particle phenomena are painted [Wiegmann and Sakurai, 2012].

### 1.3 CORONAL MAGNETIC FIELD

Without modern-day spacecraft exploration of the heliosphere, experimental evidence from the heliosphere's physical properties was scarce in the first half of the 20th century. While there were hypotheses and observations about particle flows emanating from the Sun as far back as the beginning of the 20th century, the first models of what would become the modern view of the solar wind were developed in the 1950s. Building on top of the observational work of Biermann [1951, 1957] and the theoretical considerations of Chapman [1954], Parker [1958] proposed a model of the large-scale quasi-static structure of the solar wind and magnetic field that still shapes the current understanding of the heliospheric medium. As the Space Race gathered pace in the 1960s, so did the instrumental observation of the heliosphere. Several missions measured the magnetic field and the interplanetary plasma (e.g., the Pioneer missions [Lasher, 1997; Dunbar, 2017], the Interplanetary Monitoring Platform (IMP) [King, 1982; Paularena and King, 1999; Smith, 2006], the twin Voyager spacecraft [Kohlhase and Penzo, 1977; Heacock, 1980], Ulysses [Marsden et al., 1992], the twin Helios mission Porsche [1981]; Schwenn and Marsch [1990]), confirming the models presented in the preceding years.

The magnetic field in the Sun's vicinity up to a few solar radii is of particular interest because the magnetic field configuration dictates the solar wind's behavior in this regime. In contrast, in the outer regions above the Alfvén critical point, which is well above ten solar radii heliocentric distance [Marsch and Richter, 1984], the situation is reversed: The solar wind carries the magnetic field and drags it out in the Archimedean spiral that is now known as the *Parker spiral*. While the magnetic field in a narrow region near the photosphere has been continuously measured since the early 1950s [Babcock, 1953], the coronal magnetic field has eluded direct accurate observation ever since. Due to the corona's low plasma density, direct remote measurement is not reliably possible besides in some denser

coronal structures. Nevertheless, the coronal magnetic configuration is essential for linking the photosphere and solar wind sources to the interplanetary medium's large-scale structure.

Measurements and models of the coronal magnetic field in the 1960s were mostly limited to local phenomena near the photosphere or specific coronal structures. [Rust \[1970\]](#), for example, measured the line-of-sight component of solar prominences above the solar limb. [Newkirk \[1967\]](#) described the coronal magnetic field above specific structures, particularly active regions and helmet streamers, and inferred that a potential dipole model could explain the magnetic structure of these phenomena. The magnetic field configuration near and above helmeted coronal structures has been qualitatively analyzed by [Pneuman \[1968\]](#).

Measuring the magnetic field via in-situ instrumentation aboard spacecraft close to the Sun with high spatial resolution is not feasible because of the heliosphere's vast extent. Remote measurements are possible only for small volumes of high particle density and additionally suffer from projection effects. Therefore, heliospheric magnetic field models are necessary to bridge the gap between spacecraft instrumentation and the solar surface. The development of the [PFSS](#) model allowed modelers finally to predict the coronal magnetic field in its entirety and lifted the restriction of models to apply to local coronal phenomena only. It links the interplanetary magnetic field and plasma to the lower regions of the corona and the photosphere.

#### 1.4 POTENTIAL FIELD SOURCE SURFACE MODEL

Because in-situ measurements cannot accurately determine the large-scale heliospheric magnetic field structure due to this domain's sheer size, magnetic models need to be based on remote sensing instruments. One of these models is the [PFSS](#) model [[Altschuler and Newkirk, 1969](#); [Schatten et al., 1969](#)], which is the main focus of this work. This model is restricted to a static view of the heliosphere. It can only predict the magnetic configuration for an entire Carrington rotation (synodic period), which equals about 27 days. However, to achieve this, it only requires the line-of-sight configuration of the solar photosphere as input and few assumptions of the modeled domain, which makes it a powerful tool and a first choice for the scientific community if the large-scale magnetic field is of interest [e.g., [Szabo et al., 2020](#); [Panasenco and Velli, 2013](#); [Fujiki et al., 2005](#), or the publications in Chapter 7].

The [PFSS](#) model relies on an upper computational boundary called the source surface, which is assumed to be a sphere where magnetic field lines extend radially into interplanetary space. The height of the source surface  $R_{ss}$  is the only free parameter of the model, and several optimal values have been proposed. A typical value is  $R_{ss} = 2.5 \cdot R_\odot$  (solar radius) [[Altschuler and Newkirk, 1969](#); [Pinto and Rouillard, 2017](#); [Zhao and Fisk, 2010](#); [Zhao et al., 2017](#)], though lower [[Hoeksema, 1984](#); [Lee et al., 2011](#); [Badman et al., 2020](#); [Panasenco et al., 2020](#)] and higher values [[Riley et al., 2006](#); [Levine et al., 1982](#); [Hoeksema, b](#)] have been suggested as well. The model's lower computational boundary is the photosphere, where a synoptic

(i.e., stitched together for an entire Carrington rotation) magnetogram is required as model input. Between the boundaries at the photosphere and the source surface is the computational domain, for which the [PFSS](#) model generates magnetic field predictions.

The two main restrictions of the [PFSS](#) model are the assumption of a static magnetic configuration for an entire Carrington rotation and the assumption of the computational domain to be current-free. The latter assumption enables the magnetic field to be described by a scalar potential field, considerably reducing the mathematical complexity. The first assumption stems from the unavailability of magnetic photospheric data from the backside of the Sun. To obtain the magnetic configuration of the entire solar surface, the measuring instruments (on Earth or in near-Earth space, see Sect. 5.2.1) are required to wait for the Sun to rotate (synodically) below them. During quiet periods of the solar activity cycle, structures such as sunspots can persist for several Carrington rotations. Therefore, as a first approximation, this assumption is a reasonable starting point. However, during the active periods of the solar activity cycle, the solar surface and corona feature more dynamic processes, thereby diminishing the predictive power of the [PFSS](#) model.

## 1.5 IMPROVING THE PFSS MODEL

Because the [PFSS](#) model is simple, relies on few assumptions and input data, and can be computed quickly, it is widely used as a first estimate of the coronal magnetic field for many applications. Enhancing its predictive power can help to improve applications without employing full Magnetohydrodynamics ([MHD](#)) models to predict the heliospheric magnetic field. Several improvements to the [PFSS](#) model have been developed. [Schatten \[1971\]](#) included a second internal boundary, the cusp surface, above which current sheets are modeled to relinquish, in parts, the strong constraint of the entire computational domain to be current-free. The new model is now referred to as the Potential Field Current Sheet ([PFCS](#)) model, and it was improved upon by [Zhao and Hoeksema \[1994\]](#) by incorporating horizontal current sheets and considering plasma parameters (such as density and pressure), thereby creating the Horizontal Current Current Sheet ([HCCS](#)) model. Another advancement is the Current Sheet Source Surface ([CSSS](#)) model [[Zhao and Hoeksema, 1995; Poduval and Zhao, 2014](#)] that as the [PFCS](#) and [HCCS](#) models before, employs a cusp surface but demands all field lines above this inner boundary to be open. The outer source surface in this model typically lies higher than the  $R_{ss} = 2.5 \cdot R_\odot$  of the [PFSS](#) model, thereby bringing it closer to the actual Alfvénic surface the source surface is supposed to mimic.

In recent years models with full [MHD](#) treatment of the plasma and electromagnetic fields have been developed. A very early implementation utilizing an iterative process to model the plasma parameters was developed by [Pneuman and Kopp \[1971\]](#) and is frequently used as a comparison for other models such as the [PFSS](#) model. While full [MHD](#) models offer a potentially more accurate description of the magnetic field and the possibility to model dynamic processes, more input parameters and considerably more computing power is required [[Lionello et al., 2009; Linker et al., 1999; Riley et al., 2006; Feng et al., 2012](#)]. Between these two computational

extremes, several improvements to the [PFSS](#) model, on the one hand, and simplifications of the full [MHD](#) approach, on the other hand, have been developed. [Mackay and Yeates \[2012\]](#) give an overview of models predicting the large-scale coronal magnetic field.

A significant advantage of the [PFSS](#) and related models without treatment of plasma parameters such as density and pressure is the reliance on as few assumptions as possible. The [MHD](#) models require additional assumptions on the plasma state, including potential falsehoods into the modeling process. The only input data required for [PFSS](#)-like models is the magnetic configuration of the photosphere. Of course, this simplification can also be regarded as a weak point: The coronal environment is more complex than the simple model suggests. Also, the static model paradigm cannot capture dynamic processes like flares or CMEs.

Based on the simplification of the mathematical description and the computational algorithm, the spherical shape is the obvious choice that can be implemented in the absence of information on the magnetic configuration's exact nature. Several authors have suggested altering this shape to predict the heliospheric magnetic field more accurately [[Riley et al., 2006](#); [Schulz et al., 1978](#); [Schulz, 1997](#); [Levine et al., 1982](#)]. In this work, the classical [PFSS](#) model is enhanced by incorporating an ellipsoidal shape as the source surface. It does not include other plasma parameters (as, for example, the [HCCS](#) model does) but only deforms the outer virtual surface and thereby restricts the magnetic field's orientation. The ellipsoidal shape breaks up the equatorial-polar symmetry imposed by the spherical source surface. The new model was disclosed to the public in Publication 1 (Sect. 5.5). A rough estimate of the improved prediction accuracy is presented. In addition to evaluating the ellipsoidal [PFSS](#) implementation presented in this work, Publication 2 (Sect. 6.5) also assesses the classical spherical [PFSS](#) model throughout the solar cycle. As was expected, both the spherical and ellipsoidal [PFSS](#) models perform considerably better during the quiet phase of the solar activity cycle than during the active Sun when many of the underlying assumptions of the model break down.

## 1.6 STRUCTURAL OVERVIEW OF THE THESIS

The remainder of this work is structured as follows. In Chapter 2, the fundamental paradigm of the [PFSS](#) model is presented. The mathematical framework for obtaining the magnetic field configuration according to the model is summarized, and a detailed procedure list explains all steps involved. This chapter and the implementation described therein are reproductions of the well-established [PFSS](#) model that has been in use for decades and serve as a reference to the reader and other implementations presented in the later chapters. A second implementation of the classical [PFSS](#) model with a standard spherical source surface employing finite differences is described in Chapter 3 alongside the mathematical and computational foundation the solver requires. This implementation is then improved upon in Chapter 4 where the integration of ellipsoidal source surfaces into the model paradigm is discussed in detail. The resulting third implementation is the main focus of this work. It contributes a major extension to the widely utilized [PFSS](#) model. Chapter 5 addresses numerical considerations to improve prediction accuracy and

reduce the new solver's computational run time. It also discusses several observatories that produce photospheric magnetograms, which can be utilized as input data for the implementations presented here. Furthermore, it presents several data products that can be obtained from the implementations' output data, and that can be employed for subsequent studies. One of these studies is the *backmapping polarity measure* evaluating the merits of the new solver. It is utilized to compare in-situ spacecraft data to the model predictions and is described in Chapter 6. The PFSS model is frequently used for studies requiring the approximate large-scale configuration of the coronal magnetic field. Several examples for such applications are discussed in Chapter 7. The findings of this work are summarized and discussed in Chapter 8 and prospects for additional model advancements are described. Details for the implementations and run time measurements are assembled in Appendix A.

# 2

## BASICS OF THE POTENTIAL FIELD SOURCE SURFACE MODEL

---

In the late 1960s, Altschuler and Newkirk [1969] as well as Schatten et al. [1969] independently proposed a magnetostatic model for the structure of the solar corona. This model is today known as the *potential field source surface (PFSS) model*. In the following, the PFSS model is described, including its basic assumptions, the computational domain, the mathematical foundations, and the procedure to compute the magnetic field for a given input magnetogram.

### 2.1 THE POTENTIAL FIELD SOURCE SURFACE MODEL

The domain of interest is partitioned into three regions (see Fig. 1). Employing a variety of instruments, the magnetic field can be measured at the photosphere, which is the intersection between regions 1 and 2. Region 2 is the computational domain and scope of the PFSS model. The intersection between regions 2 and 3 is called the *source surface*. Above the source surface in region 3, the solar wind dominates the magnetic configuration. During quiet times of the solar activity cycle and aside from exceptions such as eruptions or flares, the Sun's photosphere displays features that persist over several Carrington rotations. Therefore, in a first approach the lower region of the solar corona (region 2) can be assumed to be electrostatic, that is,  $\frac{\partial \vec{E}}{\partial t} = \vec{0}$ , where  $\vec{E}$  is the electric field. Additionally, it is assumed that the electric current density  $\vec{j}$  can be neglected, at least up to some point (i.e.,  $\vec{j} = \vec{0}$ ). Ampère's law then states

$$\nabla \times \vec{B} = \mu_0 \left( \vec{j} + \epsilon_0 \frac{\partial \vec{E}}{\partial t} \right) = \vec{0}$$

where

- $\vec{B}$  is the magnetic flux density or simply magnetic field,
- $\mu_0$  is the permeability of free space, and
- $\epsilon_0$  is the permittivity of free space.

A curl-free vector field can be described as the gradient of a scalar potential ( $\nabla \times \nabla f = \vec{0}$  for twice continuously differentiable  $f$ , the curl of a gradient vanishes everywhere). Let  $\vec{B} = -\nabla \Psi$  with scalar potential field  $\Psi$ . Gauss's law then states

$$\nabla \cdot \vec{B} = -\nabla \cdot \nabla \Psi = -\Delta \Psi = 0 . \quad (1)$$

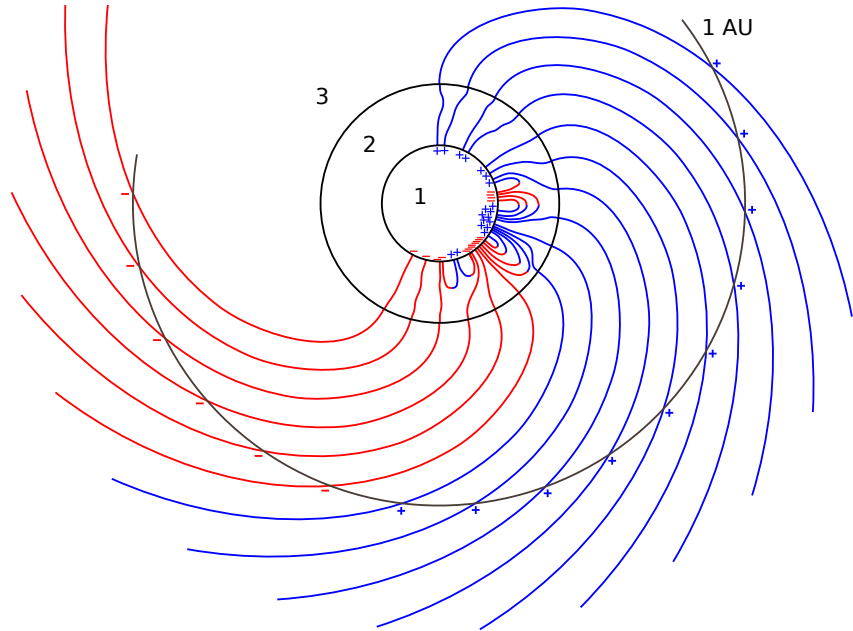


Figure 1: Depiction of the three regions underlying the PFSS model: Region 1 is the inside of the Sun, region 2 the computational domain between the photosphere and source surface and region 3 the interplanetary space where the solar wind flows radially outward and the magnetic field lines form Parker spirals. Figure modified based on Schatten et al. [1969].

The last equation of Expression 1 is called *Laplace's equation* and can be integrated within region 2, given two boundary conditions at the photosphere and the source surface. In the outer corona above the source surface, the solar wind carries the magnetic field outward; the magnetic field is frozen in. The ratio of plasma to magnetic pressure ( $\beta$ ) exceeds 1 in this region. As the solar wind flows radially away from the Sun, the magnetic field lines have to be radial as well at this point. Therefore, the upper boundary condition is given by the magnetic field lines' restriction to be perpendicular to the source surface (*Neumann boundary condition*). For the lower boundary, the photosphere, the magnetic configuration is known and supplied to the algorithms by synoptic line-of-sight magnetograms (*Dirichlet boundary condition*).

## 2.2 THE WSO APPROACH

To compute the PFSS model, the photosphere's magnetic field must be supplied to the implementation. While today there are instruments capable of measuring the vector magnetic field at the photosphere, older instruments could only measure the line-of-sight component along the viewing direction (see Sect. 5.2.1 and Table 1 for an overview of several instruments). Therefore, simplifying assumptions regarding the field configuration had to be made. The community uses two approaches, called the *radial* and the *non-radial* approach. Here and throughout this work, the standard *spherical coordinate system* with radial coordinate  $r \in [0, \infty)$ , polar angle or co-latitude  $\theta \in [0, \pi]$  and azimuth angle  $\phi \in [0, 2\pi)$  is utilized. The coordinates are

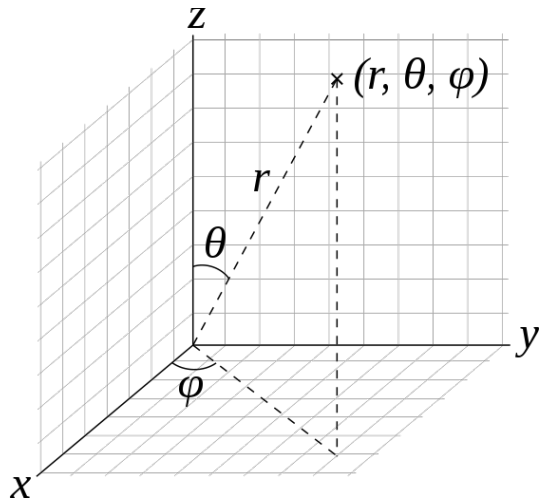


Figure 2: Spherical coordinates and symbols. The coordinates are radial distance  $r$ , polar angle  $\theta$  and azimuth angle  $\phi$ . Image obtained from [https://commons.wikimedia.org/wiki/File:3D\\_Spherical.svg](https://commons.wikimedia.org/wiki/File:3D_Spherical.svg).

illustrated in Fig. 2. The radial approach assumes the magnetic field to be purely radial at the photosphere with

$$B_{\text{los}}(R_{\odot}, \theta, \phi) = B_r(R_{\odot}, \theta, \phi) \cdot \sin \theta \quad (2)$$

while the non-radial approach allows for an additional meridional component of the magnetic field:

$$B_{\text{los}}(R_{\odot}, \theta, \phi) = B_r(R_{\odot}, \theta, \phi) \cdot \sin \theta + B_{\theta}(R_{\odot}, \theta, \phi) \cdot \cos \theta \quad (3)$$

where

- $R_{\odot}$  is the solar radius,
- $B_r$  is the radial component of the magnetic field,
- $B_{\theta}$  is the meridional component of the magnetic field, and
- $B_{\text{los}}$  is the line-of-sight component of the magnetic field.

Because the plane of the ecliptic is tilted with respect to the solar rotation axis by about  $7.25^{\circ}$  [Seidelmann, 1992], the polar photospheric magnetic fields are measured inaccurately by the instruments positioned at the Earth or at L<sub>1</sub>, where one pole might be invisible entirely depending on the orbital position of the Earth. The non-radial approach requires information on the polar fields so that additional measurements have to be conducted and supplied. The polar fields may be measured at another position in orbit and assumed to be nearly constant throughout the year. There are convincing arguments for both the radial and non-radial approach to be more accurate [Hoeksema and Scherrer, 1986]. For simplicity and a

more straightforward comparison with existing data services, the implementations presented here employ only the radial approach.

### 2.2.1 CORONAL MAGNETIC FIELD REPRESENTATION

In this section, the mathematical framework to obtain the coronal magnetic field according to the [PFSS](#) implementation from Wilcox Solar Observatory ([WSO](#)) is presented. It combines information found in [Chapman and Bartels \[1940\]](#), [Hoeksema and Scherrer \[1986\]](#), and [Sun \[2009\]](#); their work is briefly summed up here for convenience. The description of the magnetic configuration in the computational domain of the [PFSS](#) implementation relies on *spherical harmonics*, or more accurately, on the *associated Legendre polynomials* that can be utilized as follows.

The *Legendre polynomial* of degree  $n \in \mathbb{N}$  is defined as a solution to *Legendre's differential equation*

$$\frac{d}{dx} \left[ (1-x^2) \frac{d}{dx} P_n(x) \right] + n(n+1)P_n(x) = 0 . \quad (4)$$

An explicit representation of the Legendre polynomial is

$$P_n(x) = 2^n \cdot \sum_{k=0}^n x^k \cdot \binom{n}{k} \cdot \binom{\frac{n+k-1}{2}}{n} \quad (5)$$

with the binomial coefficient defined as

$$\binom{n}{k} = \prod_{i=1}^k \frac{n+1-i}{i} . \quad (6)$$

The associated Legendre polynomials of *order*  $l \in \mathbb{N}$  and *degree*  $m \in \mathbb{N}$  with Schmidt semi-normalization are defined as

$$P_l^m(x) = \sqrt{q \frac{(l-m)!}{(l+m)!}} \cdot (1-x^2)^{\frac{m}{2}} \cdot \frac{d^m}{dx^m} P_l(x) \quad (7)$$

with

$$\begin{aligned} q &= 1 && \text{if } m = 0 \text{ and} \\ && & \\ q &= 2 && \text{if } m > 0. \end{aligned}$$

There is a subtle difference between this definition  $P_l^m$  (Eq. 7) and the one given by Chapman and Bartels [1940, pp. 609], denoted here as  $\hat{P}_l^m$ : They define the

argument of their function as the cosine of the argument of the function presented here, or  $P_l^m(\cos x) = \hat{P}_l^m(x)$ .

With the orthogonal functions  $P_l^m$  the current-free potential field  $\Psi$  may be approximated by

$$\Psi(r, \theta, \phi) \approx R_\odot \cdot \sum_{l=0}^N \sum_{m=0}^l P_l^m(\cos \theta) \cdot \frac{\left(\frac{R_\odot}{r}\right)^{l+1} - \frac{R_{ss}}{R_\odot} \left(\frac{r}{R_{ss}}\right)^l \left(\frac{R_\odot}{R_{ss}}\right)^{l+2}}{l+1 + l \left(\frac{R_\odot}{R_{ss}}\right)^{2l+1}} \cdot \left( g_{lm} \cos(m\phi) + h_{lm} \sin(m\phi) \right) \quad (8)$$

where

- $N$  is the *maximum principal index*,
- $R_\odot$  is the solar radius,
- $R_{ss}$  is the source surface radius (usually  $R_{ss} = 2.5 \cdot R_\odot$ ), and
- $g_{lm}, h_{lm}$  are the *spherical harmonic coefficients*.

The maximum principal index determines the accuracy with which the magnetic field can be described. A higher index allows for a more fine-grained description utilizing more harmonic functions; however, there are other factors that limit the magnetic prediction quality, e.g., the resolution of the employed synoptic magnetograms (see Sect. 5.4). In the radial approach 2 the harmonic coefficients  $g_{lm}$  and  $h_{lm}$  are obtained by evaluating the following equations utilizing photospheric magnetograms:

$$g_{lm} = \frac{2l+1}{XY} \sum_{j=1}^X \sum_{i=1}^Y \frac{B_{los}(R_\odot, \theta_i, \phi_j)}{\sin(\theta_i)} \cdot P_l^m(\cos \theta_i) \cdot \cos(m\phi_j) \quad (9)$$

$$h_{lm} = \frac{2l+1}{XY} \sum_{j=1}^X \sum_{i=1}^Y \frac{B_{los}(R_\odot, \theta_i, \phi_j)}{\sin(\theta_i)} \cdot P_l^m(\cos \theta_i) \cdot \sin(m\phi_j) \quad (10)$$

where  $X$  and  $Y$  are the number of pixels in zonal and meridional direction, respectively. As can be seen from Eqs. 9 and 10, the coefficients are independent of the source surface height. The magnetic field can then be obtained via

$$\vec{B} = -\vec{\nabla}\Psi = -\frac{\partial \Psi}{\partial r} \cdot \vec{e}_r - \frac{1}{r} \frac{\partial \Psi}{\partial \theta} \cdot \vec{e}_\theta - \frac{1}{r \sin \theta} \frac{\partial \Psi}{\partial \phi} \cdot \vec{e}_\phi . \quad (11)$$

Expanding the single components of Eq. 11 and inserting Eq. 8 for  $\Psi$  gives the three expressions

$$B_r(r, \theta, \phi) = \sum_{l=0}^N \sum_{m=0}^l d_{r,l} \cdot P_l^m(\cos \theta) \cdot \left( g_{lm} \cos(m\phi) + h_{lm} \sin(m\phi) \right), \quad (12)$$

$$B_\theta(r, \theta, \phi) = \sum_{l=0}^N \sum_{m=0}^l e_{r,l} \cdot \frac{\partial P_l^m(\cos \theta)}{\partial \theta} \cdot \left( g_{lm} \cos(m\phi) + h_{lm} \sin(m\phi) \right), \text{ and} \quad (13)$$

$$B_\phi(r, \theta, \phi) = \sum_{l=0}^N \sum_{m=0}^l e_{r,l} \cdot P_l^m(\cos \theta) \cdot \left( g_{lm} \sin(m\phi) + h_{lm} \cos(m\phi) \right), \quad (14)$$

with terms

$$d_{r,l} = \left( \frac{R_\odot}{r} \right)^{l+1} \frac{l+1+l \left( \frac{r}{R_{ss}} \right)^{2l+1}}{l+1+l \left( \frac{R_\odot}{R_{ss}} \right)^{2l+1}} \quad e_{r,l} = \left( \frac{R_\odot}{r} \right)^{l+1} \frac{1 - \left( \frac{r}{R_{ss}} \right)^{2l+1}}{l+1+l \left( \frac{R_\odot}{R_{ss}} \right)^{2l+1}}$$

and partial derivatives of the associated Legendre polynomials

$$\begin{aligned} \frac{\partial P_l^m(\cos \theta)}{\partial \theta} &= -\sin \theta \cdot \frac{dP_l^m}{dx} \Big|_{x=\cos \theta} \\ &= -\sin \theta \cdot \frac{\partial}{\partial x} \cdot \left[ (1-x^2)^{m/2} \cdot \frac{d^m P_l}{dx^m} \right] \Big|_{x=\cos \theta} \\ &= -\sin \theta \cdot \left[ \frac{m}{2} (1-x^2)^{m/2-1} \cdot (-2x) \cdot \frac{d^m P_l}{dx^m} \right. \\ &\quad \left. + (1-x^2)^{m/2} \cdot \frac{d^{m+1} P_l}{dx^{m+1}} \right] \Big|_{x=\cos \theta} \\ &= \sin \theta \cdot \left[ m \cdot \cos \theta \cdot (1-\cos^2 \theta)^{m/2-1} \cdot \frac{d^m P_l}{dx^m} \Big|_{x=\cos \theta} \right. \\ &\quad \left. - (1-\cos^2 \theta)^{m/2} \cdot \frac{d^{m+1} P_l}{dx^{m+1}} \Big|_{x=\cos \theta} \right] \\ &= \sin \theta \cdot \left[ m \cdot \cos \theta \cdot \sin^{m-2} \theta \cdot \frac{d^m P_l}{dx^m} \Big|_{x=\cos \theta} \right. \\ &\quad \left. - \sin^m \theta \cdot \frac{d^{m+1} P_l}{dx^{m+1}} \Big|_{x=\cos \theta} \right] \\ &= m \cdot \cos \theta \cdot \sin^{m-1} \theta \cdot \frac{d^m P_l}{dx^m} \Big|_{x=\cos \theta} - \sin^{m+1} \theta \cdot \frac{d^{m+1} P_l}{dx^{m+1}} \Big|_{x=\cos \theta}. \end{aligned}$$

In the [WSO](#) approach the procedure to obtain an expression for the coronal magnetic field inside the computational boundary of the [PFSS](#) model is to obtain the harmonic coefficients  $g_{lm}$  and  $h_{lm}$  via Eqs. 9 and 10 and subsequently evaluating Eqs. 12, 13 and 14. A synopsis of all steps involved are described in Sect. 2.3.

### 2.2.2 COORDINATES OF PIXELS IN THE MAGNETOGRAMS

As input data, the PFSS implementations require synoptic magnetograms of the photosphere available from several sources. Synoptic magnetograms have the form of images that picture the (line-of-sight) magnetic field and are available in several resolutions (see Table 1). The reference implementations developed as part of this work utilize WSO magnetograms [Duvall et al., 1977; Hoeksema, a] for comparison purposes. All magnetogram pixels have a finite width and height, so the pixels' position is essential for the implementations to work correctly. Unfortunately, the exact positions in the WSO magnetograms are not documented well, so this section summarizes the pixels' coordinates (T. Hoeksema, personal communication, Oktober 20, 2017).

The data from the WSO website states that the meridional positions of pixels stretch in sine-latitude from  $\frac{14.5}{15.0}$  on the northern hemisphere to  $-\frac{14.5}{15.0}$  on the southern hemisphere. The explanatory line in the magnetograms' metadata [Hoeksema, a] reads as follows:

"30 data points in equal steps of sine-latitude from +14.5/15 to -14.5/15"

However, these are not the northern/southern borders of the first/last line of pixels in the magnetograms, but rather their central positions. For high-resolution magnetograms, this distinction does not matter as the error diminishes with increasing pixel density. The WSO data has only 30 pixels in this direction, so the difference between these two interpretations is considerable. To obtain the center positions of each pixel in the meridional direction, one can employ the following formalism. Let  $\lambda_{\max} = \frac{14.5}{15.0}$  and  $\lambda_{\min} = -\frac{14.5}{15.0}$  be the northernmost and southernmost sine-latitude pixel center positions in the magnetograms, respectively. The equal step size in sine-latitude is defined by

$$\delta\lambda = \frac{\lambda_{\max} - \lambda_{\min}}{N_\theta - 1}$$

where  $N_\theta$  is the number of pixels in the meridional direction. For WSO magnetograms,  $N_\theta = 30$ . The meridional coordinate of the center position of the  $j$ -th pixel in spherical coordinates measured from north to south is

$$\theta_j = \pi/2 - \arcsin(\lambda_{\max} - j \cdot \delta\lambda) .$$

The positions of the pixel borders are important when resizing magnetograms for higher/lower resolution analysis. The northern and southern boundaries of the  $j$ -th pixel are

$$\theta_{j-1/2} = \pi/2 - \arcsin(\lambda_{\max} - (j - 1/2) \cdot \delta\lambda) \text{ and}$$

$$\theta_{j+1/2} = \pi/2 - \arcsin(\lambda_{\max} - (j + 1/2) \cdot \delta\lambda) .$$

In contrast to the meridional coordinates, the coordinates given are those of the eastward (left) pixel boundary in the zonal direction. The [WSO](#) magnetograms are presented in American Standard Code for Information Interchange ([ASCII](#)) format. Each column of the magnetogram (each longitude value) is preceded by a marker of the form 'CT2206:360', where the four-digit number denotes the Carrington rotation number (here: 2206) of the magnetogram and the number following the colon is the zonal angle of that rotation (here: 360°).

The center positions in the zonal direction can be obtained as follows. Let  $d\phi = \frac{2\pi}{N_\phi}$  be the angular distance between two neighboring pixels and  $N_\phi$  the number of pixels in zonal direction. For [WSO](#) magnetograms  $N_\phi = 72$ . The zonal coordinate of the  $i$ -th pixels center position in spherical coordinates measured from east to west (decreasing Carrington angle, increasing longitude) is

$$\phi_i = \left(i + \frac{1}{2}\right) \cdot d\phi.$$

The eastward and westward pixel boundaries are  $\phi_i = i \cdot d\phi$  and  $\phi_i = (i + 1) \cdot d\phi$ , respectively.

The [WSO](#) files contain 73 zonal entries, where the last entry is the 360-degree entry of the following rotation. This allows for a smoother transition between rotations by computing the average of the first and last column of these files instead of just using the first entry. Alternatively, the last entry may be ignored, as has been done for the coefficients computed and released publicly on the [WSO](#) webpage [[Hoeksema](#), [b](#)].

### 2.3 PFSS REFERENCE IMPLEMENTATION

As part of this work, a reference implementation of the classical, radial (see Eq. 2) [PFSS](#) implementation has been developed. The goal was to obtain an implementation that resembles the one from [WSO](#) and can be employed to compare the performances of other more complex implementations. This reference version is called the *Spherical Harmonic Coefficient (SHC) implementation*.

The motivation to use the [PFSS](#) model is to obtain the lower solar corona's magnetic field configuration. The procedure to infer values for the vector-valued coronal magnetic field between the photosphere and the source surface via a classical [PFSS](#) implementation is straightforward and described as a protocol with brief explanations of each step. Here, [WSO](#) synoptic magnetograms will be referenced, but the procedure is valid for all similar magnetograms from other sources.

**Step 1: Obtain a line-of-sight synoptic magnetogram of the photosphere.**

Synoptic magnetograms are kindly made available online by the [WSO](#) [Hoeksema, a]. The magnetograms are [ASCII](#) tables with 30x72 entries each.

**Step 2: Correct the magnetogram for the magnetic monopole.**

Because synoptic magnetograms are composites of several measurements over a period of roughly 27 days and the magnetic field changes slightly during this period, there is usually an artificial magnetic monopole contained within this data. If  $\hat{B}_{\text{los},ij}$  denotes the line-of-sight magnetic field at pixel  $(i,j)$ , the monopole-free magnetic field  $B_{\text{los},ij}$  can easily be obtained by computing the weighted sum over all pixels and subtracting it from the input data:

$$B_{\text{los},ij} = \hat{B}_{\text{los},ij} - \delta \quad \delta = \frac{\sum_{j=1}^X \sum_{i=1}^Y \frac{\hat{B}_{\text{los},ij}}{\sin \theta_j}}{X \cdot \sum_{i=1}^Y \frac{1}{\sin \theta_i}}$$

While this method eliminates the magnetic monopole, it alters the input data and, therefore, the result of the [PFSS](#) model. This step is omitted in the computation process of the harmonic coefficients released on the [WSO](#) web page.

**Step 3: Compute coefficients  $g_{lm}$  and  $h_{lm}$ .**

A maximum principal index  $N$  for the spherical harmonic functions is set. For the data released on the [WSO](#) website, the maximum principal index is either  $N = 9$  or  $N = 20$ . The harmonic coefficients can be computed according to Eqs. 9 and 10.

**Step 4: Compute the magnetic field.**

Employing Eqs. 12, 13 and 14 the vector-valued magnetic field can be computed at arbitrary positions between photosphere and source surface.

The [SHC](#) implementation developed as part of this work produces the same spherical harmonic coefficients as the original implementation from [WSO](#) does within numerical floating-point accuracy. The source code of the original implementation employed by [WSO](#) has kindly been made available by Hoeksema (T. Hoeksema, personal communication, Oktober 20, 2017). Comparisons of the other implementations with the [SHC](#) version are elaborated in Chapter 5 and in Publication 1 (Sect. 5.5).



# 3

## SPHERICAL GRID IMPLEMENTATION

---

In the classical PFSS implementations, the photospheric magnetograms are extrapolated throughout the computational domain between photosphere and source surface employing the analytical expression in terms of spherical harmonic functions (see Sect. 2.2). While this has the advantage that, in principle, a value for the magnetic field can be obtained at arbitrary positions throughout the computational domain, its applicability is restricted to a spherical source surface model. Altering the source surface shape requires changing the underlying mathematical procedure to solve Laplace's equation 1.

A solver relying on fully numerical rather than analytical solution procedures would be free of the constraint for the source surface needing to be a specific shape. While this is a desirable characteristic, this type of solver requires a numerical grid generation algorithm that, as a byproduct introduces many problems in itself [Gilding, 1988; Thompson et al., 1985; Pletcher et al., 2012], for example, sharp edges in an arbitrary source surface. For this, a first remedy could be to increase grid point density at these positions, thereby increasing computation time. Another idea is to restrict the shape of the source surface to "well-behaved" geometries, but then a metric for "well-behaved" would be needed. How should the grid points be distributed to minimize numerical errors while increasing accuracy and keeping computation time low? Numerical grid generation is a fascinating topic on its own, and a fully numerical solver could produce magnetic configurations that are more accurate than the results of classical implementations. Using a fully numerical solver with its own grid generation technique in the first step of moving away from spherical source surfaces would be out of proportion concerning costs versus benefit.

To maximize efficiency, the solver presented here relies on a semi-numerical approach: While the solution process employs finite differences to obtain the magnetic field configuration, the utilized grid is regular, non-adaptive, and its grid points are distributed according to simple analytical functions. The computational grid is discussed in more detail in Sect. 3.1. This approach's drawback is that the source surface again is restricted to a specific analytically expressible shape, although this shape does not have to be spherical anymore.

This chapter is concerned with the necessary mathematical and computational tools for the semi-numerical spherical grid solver. All equations are derived so that the spherical upper boundary condition (i.e., the source surface) can be easily modified in Chapter 4 to accommodate ellipsoidal shapes.

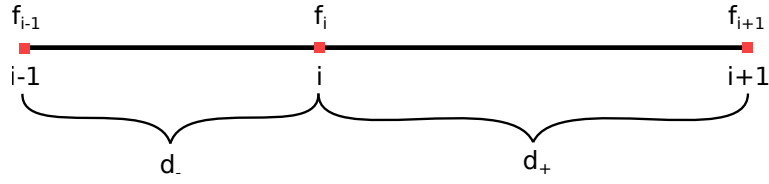


Figure 3: Schematic grid for demonstrating the finite-difference scheme used in this work

### 3.1 GRID TOPOLOGY AND NOTATION

The three-dimensional computational grid stretches from the photosphere (at  $r = R_\odot$ ) to the source surface in the radial direction, from the northern boundary supplied by the magnetogram to the southern boundary in the meridional direction and around the sphere in zonal direction with cyclic boundaries. It has a spherical symmetry with equidistant spacing in zonal directions and equidistant spacing in sine-latitude for the meridional direction. The spacing in radial direction increases geometrically from the lower to the upper boundary to ensure the distances between grid points in radial and meridional/zonal directions stay almost identical throughout the grid. The geometric progression function was chosen so that the space between neighboring grid points in radial direction increases by a constant factor. In the following, this will be called the *geometric factor*, or *q-factor*. A q-factor of, e.g., 1.03 means that the spacing between subsequent grid points increases by 3%.

Grid positions and computational values at grid points are denoted with the subscripts  $i$ ,  $j$ , and  $k$  for the radial, meridional, and zonal directions. For example, the position of a single grid point is denoted by  $\vec{r}_{ijk}$ , the magnetic potential at that point  $\Psi_{ijk}$  and the magnetic field  $\vec{B}_{ijk}$ . The indices are chosen according to  $i \in \{0, \dots, N_r - 1\}$ ,  $j \in \{0, \dots, N_\theta - 1\}$ , and  $k \in \{0, \dots, N_\phi - 1\}$ .  $N_r$  is the number of grid points in  $r$ -direction or the number of radial grid shells.  $N_\theta$  and  $N_\phi$  are the number of grid points in meridional and zonal directions, respectively. The finite differences presented in the following section are developed to be employed on grids with non-equidistant spacing between grid points.

### 3.2 FINITE-DIFFERENCE EXPRESSIONS OF THE DIFFERENTIAL OPERATORS

Pure derivatives along one axis for each of the three dimensions may be treated separately, so for ease of notation, they are given for the one-dimensional case and combined later on. Let  $f_i$ ,  $f'_i$ , and  $f''_i$  denote the value of an arbitrary computational quantity and its first two derivatives at grid point  $i$ ,  $d_+$  the distance between grid points  $i$  and  $i + 1$ , and  $d_-$  the distance between grid points  $i - 1$  and  $i$  (see Fig. 3). The index  $i$  varies from 0 at one computational boundary to  $N - 1$  at the other boundary, where  $N$  is the number of all grid points along this one-dimensional grid. A *Taylor expansion* around point  $i$  in both directions gives the expressions

$$f_{i+1} = f_i + d_+ f'_i + \frac{d_+^2}{2} f''_i + O(d_+^3) \text{ and} \quad (15)$$

$$f_{i-1} = f_i - d_- f'_i + \frac{d_-^2}{2} f''_i + O(d_-^3) . \quad (16)$$

### 3.2.1 FIRST DERIVATIVE

To obtain an expression for the first derivative of the computational quantity  $f$  inside the grid (i.e., deferring the boundaries for now), the expression

$$(Eq. 15) \cdot \frac{1}{d_+^2} - (Eq. 16) \cdot \frac{1}{d_-^2}$$

is calculated ignoring the terms of third and higher orders:

$$\begin{aligned} & f_{i+1} \cdot \frac{1}{d_+^2} - f_{i-1} \cdot \frac{1}{d_-^2} = f_i \left( \frac{1}{d_+^2} - \frac{1}{d_-^2} \right) + f'_i \left( \frac{1}{d_+} + \frac{1}{d_-} \right) \\ \Leftrightarrow & f_{i+1} \cdot \frac{d_-^2}{d_+^2 d_-^2} - f_{i-1} \cdot \frac{d_+^2}{d_+^2 d_-^2} \\ = & f_i \left( \frac{d_-^2}{d_+^2 d_-^2} - \frac{d_+^2}{d_+^2 d_-^2} \right) + f'_i \left( \frac{d_+ d_-^2}{d_+^2 d_-^2} + \frac{d_+^2 d_-}{d_+^2 d_-^2} \right) \\ \Leftrightarrow & f'_i = \frac{1}{d_+ d_-^2 + d_+^2 d_-} (f_{i-1}(-d_+^2) - f_i(d_-^2 - d_+^2) + f_{i+1} d_-^2) \\ \Leftrightarrow & f'_i = C \cdot (f_{i-1}(-d_+^2) - f_i(d_-^2 - d_+^2) + f_{i+1} d_-^2) \end{aligned} \quad (17)$$

with scaling factor  $C = \frac{1}{d_+ d_-^2 + d_+^2 d_-}$ .

Expression 17 is known as a *central difference* of second-order accuracy. It allows to numerically compute the first derivative of quantity  $f$  at grid point  $i$  with the knowledge of the values for its two neighboring grid points,  $f_{i+1}$  and  $f_{i-1}$ , and the distances to the adjacent grid points,  $d_+$  and  $d_-$ . It is also possible to obtain one-sided expressions for the derivatives. Rearranging Eq. 15 and ignoring terms of order two and higher results in

$$f'_i = \frac{f_{i+1} - f_i}{d_+} . \quad (18)$$

This is called a *forward difference* of first order accuracy and allows to compute the derivative of  $f$  with the knowledge of only the value at the next grid point and the distance to it. Similarly, the derivative of  $f$  can be obtained from Eq. 16 to achieve a *backward difference* of first order,

$$f'_i = \frac{f_i - f_{i-1}}{d_-} , \quad (19)$$

which requires knowledge of the value at the previous grid point and its distance. The forward and backward difference expressions can be utilized, for example, at computational boundaries (see Sect. 3.3).

### 3.2.2 SECOND DERIVATIVE

The second derivative of a computational grid quantity of  $f$  can be obtained similarly to the first derivative. Calculating  $(\text{Eq. 15}) \cdot \frac{1}{d_+} + (\text{Eq. 16}) \cdot \frac{1}{d_-}$  and rearranging yields the second order central difference expression

$$\begin{aligned} f_{i+1} \cdot \frac{1}{d_+} + f_{i-1} \cdot \frac{1}{d_-} &= f_i \left( \frac{1}{d_+} + \frac{1}{d_-} \right) + f''_i \left( \frac{d_+}{2} + \frac{d_-}{2} \right) \\ \Leftrightarrow f_{i+1} \cdot \frac{d_-}{d_+ d_-} + f_{i-1} \cdot \frac{d_+}{d_+ d_-} &= f_i \left( \frac{d_-}{d_+ d_-} + \frac{d_+}{d_+ d_-} \right) + f''_i \left( \frac{d_+^2 d_-}{2d_+ d_-} + \frac{d_+ d_-^2}{2d_+ d_-} \right) \\ \Leftrightarrow f''_i &= \frac{2}{d_+ d_-^2 + d_+^2 d_-} \left( f_{i-1} d_+ - f_i (d_+ + d_-) + f_{i+1} d_- \right) \\ \Leftrightarrow f''_i &= 2C \cdot \left( f_{i-1} d_+ - f_i (d_+ + d_-) + f_{i+1} d_- \right). \end{aligned} \quad (20)$$

The procedure to obtain one-sided finite-difference expressions for the second derivative, if required, would be analogous to the one described in Sect. 3.2.1.

### 3.2.3 MIXED DERIVATIVES

In addition to the first and second derivatives along one dimension of the computational grid, the solver requires expressions for mixed partial derivatives along two different dimensions. The one-dimensional function  $f$  from the previous two finite-difference expressions is in the following substituted for the three-dimensional function  $\Psi$ . Per the spherical coordinate system to be employed, these three dimensions are denoted by  $r$ ,  $\theta$ , and  $\phi$ . The distances between grid points are denoted in a similar manner as in the one-dimensional case by  $d_{r-}$ ,  $d_{r+}$ ,  $d_{\theta-}$ ,  $d_{\theta+}$ ,  $d_{\phi-}$ ,  $d_{\phi+}$  for distances in the negative/positive direction of the respective coordinate axes. The three scaling factors are

$$\begin{aligned} C_r &= \frac{1}{d_{r+} d_{r-}^2 + d_{r-}^2 d_{r+}} , & C_\theta &= \frac{1}{d_{\theta+} d_{\theta-}^2 + d_{\theta-}^2 d_{\theta+}} , \text{ and} \\ C_\phi &= \frac{1}{d_{\phi+} d_{\phi-}^2 + d_{\phi-}^2 d_{\phi+}} . \end{aligned}$$

The finite-difference scheme needs to be applied twice to obtain an expression for the mixed derivatives in two directions. The order in which the differencing scheme is applied does not matter, as all computational quantities are modeled to be continuous functions. Therefore,  $\frac{\partial^2}{\partial q^1 \partial q^2} = \frac{\partial^2}{\partial q^2 \partial q^1}$  holds true everywhere

for  $q^1, q^2 \in \{r, \theta, \phi\}$ . Here, as an example and without loss of generality, the two directions along which the differencing scheme is applied are  $r$  first and  $\theta$  second.

$$\begin{aligned} \frac{\partial^2 \Psi}{\partial r \partial \theta} &= \frac{\partial}{\partial r} \left( \frac{\partial \Psi}{\partial \theta} \right) \quad (21) \\ &= C_r \left\{ \left( \frac{\partial \Psi}{\partial \theta} \right)_{i-1,j,k} (-d_{r+}^2) - \left( \frac{\partial \Psi}{\partial \theta} \right)_{i,j,k} (d_{r-}^2 - d_{r+}^2) + \left( \frac{\partial \Psi}{\partial \theta} \right)_{i+1,j,k} d_{r-}^2 \right\} \\ &= -C_r C_\theta d_{r+}^2 \cdot \left( -d_{\theta+}^2 \Psi_{i-1,j-1,k} - (d_{\theta-}^2 - d_{\theta+}^2) \Psi_{i-1,j,k} + d_{\theta-}^2 \Psi_{i-1,j+1,k} \right) \\ &\quad -C_r C_\theta (d_{r-}^2 - d_{r+}^2) \cdot \left( -d_{\theta+}^2 \Psi_{i,j-1,k} - (d_{\theta-}^2 - d_{\theta+}^2) \Psi_{i,j,k} + d_{\theta-}^2 \Psi_{i,j+1,k} \right) \\ &\quad +C_r C_\theta d_{r-}^2 \cdot \left( -d_{\theta+}^2 \Psi_{i+1,j-1,k} - (d_{\theta-}^2 - d_{\theta+}^2) \Psi_{i+1,j,k} + d_{\theta-}^2 \Psi_{i+1,j+1,k} \right). \end{aligned}$$

This is a second-order accuracy central difference representation of the mixed differential operator  $\frac{\partial^2}{\partial r \partial \theta}$  along the coordinate axes  $r$  and  $\theta$ . As can be seen from this expression, to compute a value for the mixed derivative at a grid point with indices  $i, j, k$ , only neighboring grid points along these coordinate axes need to be considered, and only the next neighbor is required. In expression 21, the index  $k$  does not vary. The other finite-difference expressions of the mixed partial differential operators are obtained accordingly. Increasing (decreasing) the accuracy of these mixed derivatives works the same way as it does for the pure derivatives described above: The Taylor expansion is truncated at a higher (lower) order, increasing (decreasing) the number of neighboring grid points to be considered.

### 3.3 COMPUTATIONAL BOUNDARIES

Central differences, such as Eq. 17, cannot be employed at the computational grid's boundaries because one side is missing. Therefore, boundaries need to be treated separately from the interior of the grid. In the case of the grid solver presented here, only the lower boundary requires special treatment in the radial direction. The upper radial boundary is kept constant. Thus, no derivatives need to be computed there. The lower boundary condition is implemented by converting the supplied line-of-sight magnetogram to the radial magnetic field component according to the radial approach (Eq. 2). Equation 1 for the relation of the scalar potential  $\Psi$  with the magnetic field  $\vec{B}$  states

$$\vec{B}_{0,j,k} = -(\vec{\nabla} \Psi)_{0,j,k} .$$

At the lower boundary, only the radial component  $B_{r,0jk}$  is of interest because the other components of the magnetic field  $\vec{B}_{0,j,k}$  are assumed to vanish. Substituting the generic quantities  $f$  and  $f'$  for the physically relevant quantities  $\Psi_{i,j,k}$  and  $\vec{B}_{i,j,k}$  on the three-dimensional grid, the first order finite-difference Eq. 18 at the lower boundary translates to

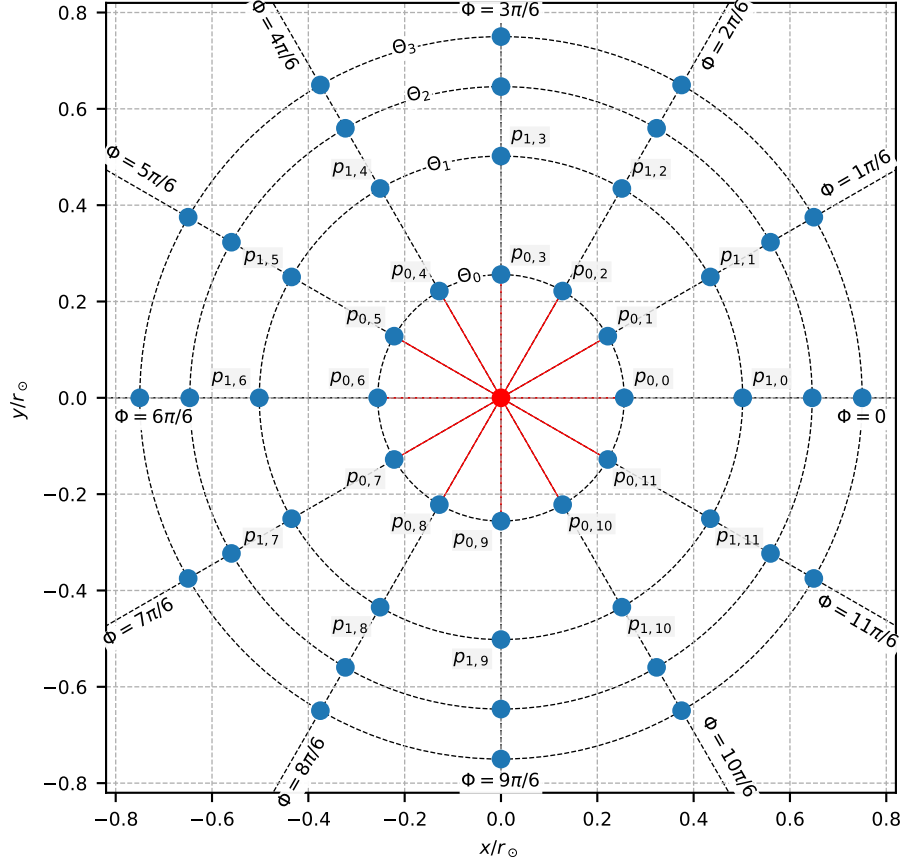


Figure 4: Projection of grid points in the inner shell (i.e., at the photosphere) on the x/y-plane. Grid points are depicted as blue dots and labeled  $p_{j,k}$  where  $j$  and  $k$  are the indices in meridional ( $\theta$ ) and zonal ( $\phi$ ) direction, respectively. Only the first four grid lines in the meridional direction are shown, and only the first two lines are labeled. The virtual polar boundary grid point (red) is defined as the average of the northernmost grid points, connected to the pole by red lines.

$$\begin{aligned} B_{r,0jk} &= -\left. \frac{\partial \Psi}{\partial r} \right|_{0jk} = -\frac{\Psi_{1jk} - \Psi_{0jk}}{r_{1jk} - r_{0jk}} \\ \Leftrightarrow \Psi_{0jk} &= B_{r,0jk}(r_{1jk} - r_{0jk}) + \Psi_{1jk} . \end{aligned} \quad (22)$$

Equation 22 permits to implement the lower boundary condition by combining pixel values of the line-of-sight magnetograms ( $B_{r,0jk}$ ) with computational values for the magnetic potential at the two lower grid shells ( $\Psi_{0jk}$  and  $\Psi_{1jk}$ ).

Along the meridional ( $\theta$ ) direction, there is no clear northern (southern) neighbor for any grid point  $i, 0(N_\theta - 1), k$  for  $i \in \{0, \dots, N_r - 1\}$  and  $k \in \{0, \dots, N_\phi - 1\}$ . While it is possible to define the northern neighbor of a northernmost grid point as a grid point on the other side of the pole, the distance to that point is usually considerably larger than the distance to the next grid point in the southern direction, which reinforces numerical instabilities. Therefore, a virtual boundary point at the poles is defined in each radial grid shell by the average of the grid points

closest to the pole. Figure 4 illustrates the neighborhood relations in the photospheric grid shell. To evaluate the finite-difference expressions, the pole's virtual point is considered the neighbor for all grid points at the polar edge of the grid shell. With this approach, the central difference expressions can be utilized at the grid's northern and southern edges.

No special treatment needs to be applied for the zonal ( $\phi$ ) direction. The neighbor of grid point  $i, j, 0$  in the negative zonal direction is grid point  $i, j, N_\phi - 1$  and vice versa, for all grid points with indices  $i \in \{0, \dots, N_r - 1\}$  and  $j \in \{0, \dots, N_\theta - 1\}$ . The central difference expressions in Sect. 3.2 can be applied for all derivatives along the zonal direction.

### 3.4 FINITE-DIFFERENCE REPRESENTATION OF THE LAPLACE OPERATOR

For completeness, the finite-difference version of Laplace's Eq. 1 is rearranged to obtain a numerical expression at a specific grid point  $i, j, k$ , and is presented in the following. The procedure transforming the analytical equation using finite differences and rearranging its terms to obtain a calculation rule for the numerical solver is discussed in detail for the more interesting case of the ellipsoidal PFSS implementation in Sect. 4.4.

The computation rule for the scalar magnetic potential at grid point  $i, j, k$  is

$$\begin{aligned} \Psi_{i,j,k} = -1/S_{i,j,k} \left[ \right. & \Psi_{i-1,j,k} \cdot \left( 2 \cdot C_r \cdot d_{r+} \cdot \left( 1 - \frac{d_{r+}}{r} \right) \right) + \Psi_{i+1,j,k} \cdot \left( 2 \cdot C_r \cdot d_{r-} \cdot \left( 1 + \frac{d_{r-}}{r} \right) \right) \\ & + \Psi_{i,j-1,k} \cdot \left( \frac{C_\theta}{r^2} \cdot d_{\theta+} \cdot \left( 2 - \frac{\cos(\theta) \cdot d_{\theta+}}{\sin(\theta)} \right) + \Psi_{i,j+1,k} \cdot \left( \frac{C_\theta}{r^2} \cdot d_{\theta-} \cdot \left( 2 + \frac{\cos(\theta) \cdot d_{\theta-}}{\sin(\theta)} \right) \right) \right. \\ & \left. \left. + \Psi_{i,j,k-1} \cdot \left( \frac{2 \cdot C_\phi}{r^2 \sin^2(\theta)} \cdot d_{\phi+} \right) + \Psi_{i,j,k+1} \cdot \left( \frac{2 \cdot C_\phi}{r^2 \sin^2(\theta)} \cdot d_{\phi-} \right) \right] \right]$$

with scaling factor

$$S_{i,j,k} = \left[ \begin{array}{l} 2 \cdot C_r \cdot \frac{d_{r+}^2 - d_{r-}^2}{r} - 2 \cdot C_r \cdot (d_{r+} + d_{r-}) + \cos(\theta) \cdot C_\theta \cdot \frac{d_{\theta+}^2 - d_{\theta-}^2}{\sin(\theta) \cdot r^2} \\ - 2 \cdot C_\theta \cdot \frac{d_{\theta+} + d_{\theta-}}{r^2} - 2 \cdot C_\phi \cdot \frac{d_{\phi+} + d_{\phi-}}{\sin^2(\theta) \cdot r^2} \end{array} \right].$$

### 3.5 SOLUTION METHOD

The solution method is an explicit time-stepping algorithm that solves Laplace's equation at each grid point for the potential field  $\Psi$  from an initial state until changes from one time-step to the next drop below a specified threshold. These time-steps are just implementing an iterative process and have no connection to physical time. The result is a static, time-independent solution valid for an entire Carrington rotation. In the initial state, the potential field is set to zero at each

grid point except the lowest grid shell (see Eq. 22). The potential at the uppermost grid shell (at  $r = R_{ss}$ ) is kept constant (zero) throughout the iteration process, thus implementing the radial boundary condition at the source surface. Every time-step  $t$ , the potential at each grid point is stored and compared to that obtained in the previous time-step  $t - 1$ . Let  $\Psi_{ijk}^t$  denote the magnetic potential at position  $i, j, k$  in time-step  $t$ , and  $\Psi_{ijk}^{t-1}$  the potential computed in the previous time-step. The algorithm terminates if

$$\max_{ijk} \left( \frac{|\Psi_{ijk}^t - \Psi_{ijk}^{t-1}|}{|\Psi_{ijk}^t|} \right) < p . \quad (23)$$

The *termination threshold*  $p$  is chosen to be  $p = 0.01$ , meaning the algorithm terminates if the maximum difference from one time-step to the next at all grid points is less than 1%.

### 3.6 NUMERICAL CONSIDERATIONS

The finite-difference expression at the lower boundary has a lower order of accuracy (one) compared to the expressions inside the grid (two). It is possible to obtain higher-order expressions by considering higher orders in the Taylor expansion (Eqs. 15 and 16), increasing the number of grid points considered. Such higher-order finite differences have been calculated and tested with the solver. The convergence of the solution process (see Sect. 3.5) is faster (i.e., the number of time-steps was lower), though the computation time per time-step increases, resulting in longer overall run times. The final result for the solver's magnetic field after the termination of the solution process is the same. Therefore, the first-order forward difference Eq. 22 suffices and is indeed preferred over a higher-order finite-difference.

As demonstrated in Sect. 3.2, expressions of finite differences can be either one-sided (forward/backward differences) or two-sided (central differences). In principle, these one-sided finite differences could be used inside the grid instead of only at its boundaries. However, central differences are preferred, as they utilize information from both directions at a specific grid point. While it is true that higher-order accuracy differences can be accomplished one-sided, information from the other side has no impact on the computations at a specific grid point. In extreme cases, as with the solver presented here, no solution can be computed by simply employing one-sided finite differences throughout the grid, no matter the accuracy order. If all radial derivatives are solely computed as forward-differences, information from the lower boundary (compare Eq. 22) cannot leave the lowest radial grid shell, immediately triggering the termination criterion (Eq. 23) in the initial setup.

# 4

## ELLIPSOIDAL GRID IMPLEMENTATION

---

The previous chapter describes the inner computational structure of the new, semi-numerical PFSS solver. So far, it is just another implementation that produces a prediction of the coronal magnetic configuration according to the well-established PFSS model with a spherical source surface that was presented more than 50 years ago [Altschuler and Newkirk, 1969; Schatten et al., 1969] and that has been employed in the heliospheric physics community ever since. In this chapter, key alterations to this implementation are presented, which permit the utilization of ellipsoidal source surfaces in the model paradigm. The resulting solver can be utilized with both spherical and ellipsoidal source surfaces, allowing for a broader range of model assumptions to be evaluated.

In general, three-dimensional ellipsoids are characterized by three principal perpendicular axes and can be oriented freely. To simplify the mathematical description and accommodate the Sun's special geometry, the ellipsoids are constrained as follows: One of the ellipsoids principal axes is aligned with the solar rotation axis. The other two principal axes lie in the solar equatorial plane, and because there is no preferential direction in the equatorial plane for this problem, both principal axes are restricted to be the same length. An ellipsoid with two principal axes connected in this way is called a *spheroid* and has rotation symmetry around the single axis that is not restricted by the other two. If the ellipsoids principal axis along the symmetry axis (in this case along the solar rotation axis) is longer than the two axes in the equatorial plane, it is called a *prolate spheroid*, otherwise an *oblate spheroid*. (Cuts through both oblate and prolate ellipsoids are also illustrated in Fig. 6.)

The idea is to establish a *boundary-fitted computational grid* where the lower boundary coincides with the solar surface, and the upper boundary is the prolate or oblate ellipsoidal source surface. Because the solar surface is nearly spherical, the physical grid features a spherical symmetry at the lower boundary and an ellipsoidal symmetry higher up in the corona. A continuous and monotonous stretching function establishes a smooth transition of the grid from spherical at the photosphere to maximum ellipticity at the source surface.

Two coordinate domains are presented in Fig. 5 to illustrate the employed computational approach of the grid solver. The first domain is denoted by dashes above the respective coordinate symbols (e.g.,  $\bar{x}, \bar{\theta}$ ). This is called the *computational domain* in which Laplace's equation is computationally solved, as is the tracing of magnetic field lines. The second domain without dashes above its coordinates (e.g.,  $x, \theta$ ) is called the *physical domain*, which depicts the magnetic configuration's actual geometry in the heliosphere. Because the problem has near-spherical symmetry, the following sections will mostly feature spherical coordinates, but for completeness

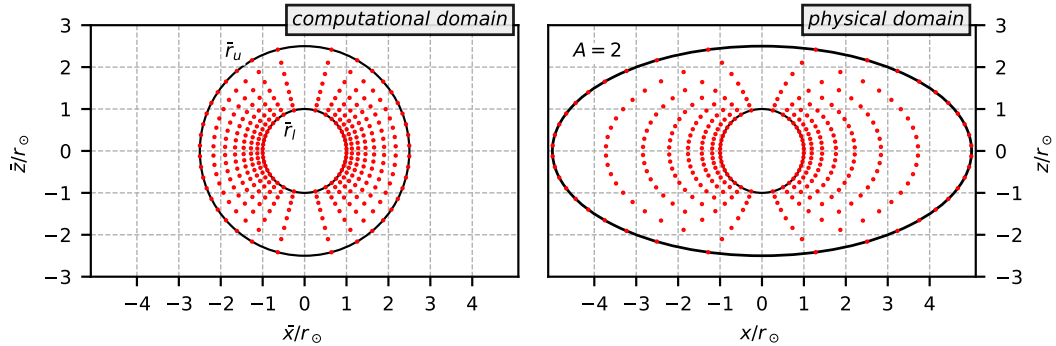


Figure 5: Computational (left) and physical (right) grid employed by the presented [PFSS](#) solver implementation. This is an example of an oblate ellipsoidal grid with a source surface ellipticity of  $A = 2$ . Distances measured in multiples of the solar radius  $R_\odot$ .

and simplicity of the differential operators, the cartesian representations are shown as well, where appropriate. Figure 5 shows the computational and physical grids representing the setup for a [PFSS](#) model implementation with an oblate source surface that is twice as high above the equator compared to above the poles.

The oblate and prolate [PFSS](#) models are implemented by a case differentiation of the employed coordinate system transformation in Sect. 4.1. No additional marker is employed to differentiate the two ellipsoidal cases of the [PFSS](#) solver to reduce the cluttering of sub- and superscripts and increase readability. The distinction is made clear by emphasizing the surrounding text in the few segments where the difference between **oblate** and **prolate** models is discussed.

#### 4.1 GENERAL NOTATION, COMPUTATIONAL AND PHYSICAL DOMAIN

Let  $\mathbb{R}^3$  be the well-known three-dimensional vector space of real-valued numbers with vector addition and scalar multiplication. Further let  $\bar{x}, \bar{y}, \bar{z}$  and  $x, y, z$  be the cartesian coordinates of the computational and physical domains, respectively, and  $\bar{r}, \bar{\theta}, \bar{\phi}$  and  $r, \theta, \phi$  the corresponding spherical coordinates. The transformation between cartesian and spherical coordinates is well known and repeated here for convenience:

computational domain	physical domain
$\bar{x} = \bar{r} \sin \bar{\theta} \cos \bar{\phi}$	$x = r \sin \theta \cos \phi$
$\bar{y} = \bar{r} \sin \bar{\theta} \sin \bar{\phi}$	$y = r \sin \theta \sin \phi$
$\bar{z} = \bar{r} \cos \bar{\theta}$	$z = r \cos \theta$
$\bar{r} = \sqrt{\bar{x}^2 + \bar{y}^2 + \bar{z}^2}$	$r = \sqrt{x^2 + y^2 + z^2}$
$\bar{\theta} = \arccos \left( \frac{\bar{z}}{\sqrt{\bar{x}^2 + \bar{y}^2 + \bar{z}^2}} \right)$	$\theta = \arccos \left( \frac{z}{\sqrt{x^2 + y^2 + z^2}} \right)$
$\bar{\phi} = \arctan \left( \frac{\bar{y}}{\bar{x}} \right)$	$\phi = \arctan \left( \frac{y}{x} \right)$

with  $\bar{\theta}, \theta \in [0, \pi]$ ;  $\bar{\phi}, \phi \in [0, 2\pi]$ ;  $\bar{r}, r \in [0, \infty)$ .

The coupling between the computational and physical systems is achieved via a single stretching parameter  $\bar{a} = \bar{a}(\bar{r})$  as follows. In the **oblate** case, the x- and y-axes are stretched

$$x = \bar{a}\bar{x} = \bar{a}(\bar{r})\bar{r} \sin \bar{\theta} \cos \bar{\phi} \quad (24)$$

$$y = \bar{a}\bar{y} = \bar{a}(\bar{r})\bar{r} \sin \bar{\theta} \sin \bar{\phi} \quad (25)$$

$$z = \bar{z} = \bar{r} \cos \bar{\theta} \quad (26)$$

while in the **prolate** case the z-axis is stretched

$$x = \bar{x} = \bar{r} \sin \bar{\theta} \cos \bar{\phi} \quad (27)$$

$$y = \bar{y} = \bar{r} \sin \bar{\theta} \sin \bar{\phi} \quad (28)$$

$$z = \bar{a}\bar{z} = \bar{a}(\bar{r})\bar{r} \cos \bar{\theta} \quad (29)$$

Grid points of constant  $\bar{r}$  in the computational domain form oblate or prolate spheroids in the physical domain, dependent on the parameter  $\bar{a}$ . The selection of the function  $\bar{a}(\bar{r})$  is discussed in Sect. 4.2.

Some relations between the coordinates are accumulated below to transform coordinates from the physical domain to the computational domain and vice versa. First, the radial coordinates  $r$  and  $\bar{r}$  may be expressed by the other through applying the well-known spherical-cartesian coordinate transformation and inserting the stretching transformations Eqs. 24 - 26 or Eqs. 27 - 29, which gives for the **oblate** case

$$\begin{aligned}
r &= \sqrt{x^2 + y^2 + z^2} \\
&= \sqrt{\bar{a}^2 \bar{r}^2 \sin^2 \bar{\theta} \cos^2 \bar{\phi} + \bar{a}^2 \bar{r}^2 \sin^2 \bar{\theta} \sin^2 \bar{\phi} + \bar{r}^2 \cos^2 \bar{\theta}} \\
&= \bar{r} \sqrt{\bar{a}^2 \sin^2 \bar{\theta} + \cos^2 \bar{\theta}} = \bar{r} \bar{k} ,
\end{aligned} \tag{30}$$

$$\begin{aligned}
\bar{r} &= \sqrt{\bar{x}^2 + \bar{y}^2 + \bar{z}^2} \\
&= \sqrt{r^2 \sin^2 \theta \cos^2 \phi / a^2 + r^2 \sin^2 \theta \sin^2 \phi / a^2 + r^2 \cos^2 \theta} \\
&= r \sqrt{\sin^2 \theta / a^2 + \cos^2 \theta} = rk ,
\end{aligned} \tag{31}$$

with

$$\begin{aligned}
\bar{k} &= \sqrt{\bar{a}^2 \sin^2 \bar{\theta} + \cos^2 \bar{\theta}} , \\
k &= \sqrt{\sin^2 \theta / a^2 + \cos^2 \theta} ,
\end{aligned}$$

and for the **prolate** case

$$\begin{aligned}
r &= \sqrt{x^2 + y^2 + z^2} \\
&= \sqrt{\bar{r}^2 \sin^2 \bar{\theta} \cos^2 \bar{\phi} + \bar{r}^2 \sin^2 \bar{\theta} \sin^2 \bar{\phi} + \bar{a}^2 \bar{r}^2 \cos^2 \bar{\theta}} \\
&= \bar{r} \sqrt{\sin^2 \bar{\theta} + \bar{a}^2 \cos^2 \bar{\theta}} = \bar{r} \bar{k} ,
\end{aligned} \tag{32}$$

$$\begin{aligned}
\bar{r} &= \sqrt{\bar{x}^2 + \bar{y}^2 + \bar{z}^2} \\
&= \sqrt{r^2 \sin^2 \theta \cos^2 \phi + r^2 \sin^2 \theta \sin^2 \phi + r^2 \cos^2 \theta / a^2} \\
&= r \sqrt{\sin^2 \theta + \cos^2 \theta / a^2} = rk ,
\end{aligned} \tag{33}$$

with

$$\begin{aligned}
\bar{k} &= \sqrt{\sin^2 \bar{\theta} + \bar{a}^2 \cos^2 \bar{\theta}} , \text{ and} \\
k &= \sqrt{\sin^2 \theta + \cos^2 \theta / a^2} .
\end{aligned}$$

Here  $a$  is the ellipticity function in physical space, which is discussed in Sect. 4.2. Second, the meridional coordinates of each domain can be expressed by the coordinates of the other domain: In the **oblate** case, the relations are

$$\sin \theta = \frac{\sqrt{x^2 + y^2}}{r} = \frac{\sqrt{\bar{a}^2 (\bar{x}^2 + \bar{y}^2)}}{\bar{r} \bar{k}} = \frac{\bar{a} \sin \bar{\theta}}{\bar{k}} \tag{34}$$

$$\cos \theta = \frac{z}{r} = \frac{\bar{z}}{\bar{r} \bar{k}} = \frac{\cos \bar{\theta}}{\bar{k}} \tag{35}$$

and

$$\sin \bar{\theta} = \frac{\sqrt{\bar{x}^2 + \bar{y}^2}}{\bar{r}} = \frac{\sqrt{(x^2 + y^2)/a^2}}{rk} = \frac{\sin \theta}{ak} \quad (36)$$

$$\cos \bar{\theta} = \frac{\bar{z}}{\bar{r}} = \frac{z}{rk} = \frac{\cos \theta}{k} \quad (37)$$

while in the **prolate** case, the relations take the following form:

$$\sin \theta = \frac{\sqrt{x^2 + y^2}}{r} = \frac{\sqrt{\bar{x}^2 + \bar{y}^2}}{\bar{r}\bar{k}} = \frac{\sin \bar{\theta}}{\bar{k}} \quad (38)$$

$$\cos \theta = \frac{z}{r} = \frac{\bar{a}\bar{z}}{\bar{r}\bar{k}} = \frac{\bar{a} \cos \bar{\theta}}{\bar{k}} \quad (39)$$

and

$$\sin \bar{\theta} = \frac{\sqrt{\bar{x}^2 + \bar{y}^2}}{\bar{r}} = \frac{\sqrt{(x^2 + y^2)}}{rk} = \frac{\sin \theta}{k} \quad (40)$$

$$\cos \bar{\theta} = \frac{\bar{z}}{\bar{r}} = \frac{z/a}{rk} = \frac{\cos \theta}{ak} \quad (41)$$

Third, the zonal coordinates  $\phi = \bar{\phi}$  are unaffected by the stretching parameter  $a$  in both the oblate and prolate models.

#### 4.2 THE ELLIPSOID STRETCHING FUNCTION

The stretching parameter  $\bar{a}$  is chosen to be dependent on the radial coordinate of the computational domain only (i.e.,  $\bar{a}(\bar{r})$ ). To accommodate higher computational gradients in the grids' lower part, a squared radial dependence is chosen, which results in a higher grid point density near the lower boundary (i.e., the photosphere). The exact dependence is not essential, as long as the function is continuous, monotonously growing, and the number of grid points is large enough to keep numerical inaccuracies low. The ellipticity function to be employed throughout this work is

$$\bar{a}(\bar{r}) = 1 + \frac{A - 1}{\bar{r}_u^2 - \bar{r}_l^2} (\bar{r}^2 - \bar{r}_l^2) = 2\alpha + a_s \bar{r}^2 \quad (42)$$

where  $A$  is the stretching parameter at the upper boundary,  $\bar{r}_u$  and  $\bar{r}_l$  are the radial positions of the upper and lower computational boundaries, respectively,  $\alpha = (1 - a_s \bar{r}_l^2)/2$  and  $a_s = (A - 1)/(\bar{r}_u^2 - \bar{r}_l^2)$ . With Eqs. 24 to 42, the positions in the physical domain can be computed from coordinates given in the computational domain.

Because the stretching function  $\bar{a}$  is non-constant, the resulting coordinate system is no longer orthogonal everywhere, which commands special treatment of the coordinate system basis vectors and differential operators discussed in Sects. 4.3 and 4.4. The coordinate transformations according to Eqs. 24 to 29 with the monotonous stretching function 42 are bijective transformations between the computational and physical coordinates; therefore, the function  $a$  in physical space can be defined which takes the physical coordinates  $r, \theta$  and  $\phi$  and gives the same result as the original function  $\bar{a}$  at the respective position  $\bar{r} = \bar{r}(r, \theta, \phi)$ . The function  $a$  in the physical domain is dependent on at least two parameters ( $r$  and  $\theta$ ) compared to the one-parameter function  $\bar{a}(\bar{r})$  in the computational domain because no single physical coordinate holds all the information to determine the ellipticity at that specific point. For a specific radial position  $\bar{r}$  in computational space, the "reverse" ellipticity function  $a$  must give the same value as  $\bar{a}$  because this function uniquely couples the two domains. Therefore, it holds

$$\bar{a}(\bar{r}) = \bar{a}(\bar{r}(r, \theta, \phi)) = a(r, \theta, \phi) = a(r, \theta) . \quad (43)$$

By inserting Eq. 31 (or Eq. 33) in Eq. 42, it can be seen that the physical coordinate  $\phi$  is not necessary to determine the stretching parameter. This also provides a blueprint to obtain the reverse ellipticity function  $a$ :

$$\bar{a}(\bar{r}) = 2\alpha + a_s \bar{r}^2 = 2\alpha + a_s r^2 \left( \frac{\sin^2 \theta}{a^2} + \cos^2 \theta \right) = a(r, \theta) \quad (44)$$

The second equation in 44 can be rearranged to be a cubic equation of  $a$ , which has exactly one real-valued solution for  $A \geq 1$ . The exact analytical expression is convoluted and not necessary for the new PFSS solver. A simple numerical algorithm can be employed to obtain the value of  $a$  at arbitrary positions in the physical domain.

With the relations presented in this section, physical and computational coordinates in both models with oblate and prolate source surfaces can be transformed into each other.

#### 4.3 COVARIANT AND CONTRAVARIANT BASIS VECTORS

The PFSS implementations solve Laplace's equation 1. To do so, a computational version of the *Laplace operator* is required. In a first step, the Laplace operator is derived for the ellipsoidal coordinate systems presented in Sects. 4.1 and 4.2. The Laplace operator in general, curvilinear coordinates is [Piercey, 2007]

$$\nabla^2 \Psi = \frac{1}{\sqrt{g}} \sum_i \sum_j \frac{\partial}{\partial q^i} \left( \sqrt{g} g^{ij} \frac{\partial \Psi}{\partial q^j} \right) \quad (45)$$

with *metric coefficients*  $g^{ij}$ , determinant of the metric coefficient matrix  $g$  and coordinates  $q^i, q^j$  (the latter are defined below, the former two are discussed in more detail in Sect. 4.4). In a second step, this analytical expression 45 is transformed via the finite difference approach (see Sect. 3.2) into a version that can be utilized by the computational PFSS implementation. This section is concerned with the derivation of the *coordinate basis vectors* that are essential for computing the metric coefficients in Eq. 45. The following Sect. 4.4 presents the analytical Laplace operator 45 in a more thorough form and its transformation into a finite difference representation.

For  $i \in \{1, 2, 3\}$  let  $\vec{g}_i = \frac{\partial \vec{R}}{\partial q^i}$  be the *covariant* basis vectors and  $\vec{g}^i = \vec{\nabla} q^i$  be the *contravariant* basis vectors, where  $q^i$  denote a set of three appropriate coordinates, e.g.  $q^1 = \bar{r}$ ,  $q^2 = \bar{\theta}$  and  $q^3 = \bar{\phi}$ . For the coordinate system presented in Sects. 4.1 and 4.2, this translates to the cartesian representation of the covariant and contravariant basis vectors:

$$\begin{aligned}\vec{g}_{\bar{r}} &= \begin{pmatrix} \frac{\partial x}{\partial \bar{r}} \\ \frac{\partial y}{\partial \bar{r}} \\ \frac{\partial z}{\partial \bar{r}} \end{pmatrix} & \vec{g}_{\bar{\theta}} &= \begin{pmatrix} \frac{\partial x}{\partial \bar{\theta}} \\ \frac{\partial y}{\partial \bar{\theta}} \\ \frac{\partial z}{\partial \bar{\theta}} \end{pmatrix} & \vec{g}_{\bar{\phi}} &= \begin{pmatrix} \frac{\partial x}{\partial \bar{\phi}} \\ \frac{\partial y}{\partial \bar{\phi}} \\ \frac{\partial z}{\partial \bar{\phi}} \end{pmatrix} \\ \vec{g}^{\bar{r}} &= \begin{pmatrix} \frac{\partial \bar{r}}{\partial x} \\ \frac{\partial \bar{r}}{\partial y} \\ \frac{\partial \bar{r}}{\partial z} \end{pmatrix} & \vec{g}^{\bar{\theta}} &= \begin{pmatrix} \frac{\partial \bar{\theta}}{\partial x} \\ \frac{\partial \bar{\theta}}{\partial y} \\ \frac{\partial \bar{\theta}}{\partial z} \end{pmatrix} & \vec{g}^{\bar{\phi}} &= \begin{pmatrix} \frac{\partial \bar{\phi}}{\partial x} \\ \frac{\partial \bar{\phi}}{\partial y} \\ \frac{\partial \bar{\phi}}{\partial z} \end{pmatrix}\end{aligned}$$

The two sets  $\{\vec{g}_1, \vec{g}_2, \vec{g}_3\}$  and  $\{\vec{g}^1, \vec{g}^2, \vec{g}^3\}$  each define three linearly independent vectors that span the vector space  $\mathbb{R}^3$ , therefore each set is a basis of  $\mathbb{R}^3$ , also called the covariant and contravariant bases. As can also easily be seen from the expressions above, it holds that  $\vec{g}_i \cdot \vec{g}^j = \delta_{ij}$  for  $i, j \in \{1, 2, 3\}$ , therefore both sets form reciprocal or dual bases of  $\mathbb{R}^3$ .

Evaluating the expressions for the covariant basis vectors  $\vec{g}_{\bar{r}}$ ,  $\vec{g}_{\bar{\theta}}$  and  $\vec{g}_{\bar{\phi}}$  is a straightforward exercise. Calculating the derivatives of Eqs. 24 - 26 results in the **oblate** covariant basis vectors

$$\vec{g}_1 = \vec{g}_{\bar{r}} = \begin{pmatrix} \frac{\partial x}{\partial \bar{r}} \\ \frac{\partial y}{\partial \bar{r}} \\ \frac{\partial z}{\partial \bar{r}} \end{pmatrix} = \begin{pmatrix} \left(\bar{a}(\bar{r}) + \bar{r} \frac{\partial \bar{a}}{\partial \bar{r}}\right) \sin \bar{\theta} \cos \bar{\phi} \\ \left(\bar{a}(\bar{r}) + \bar{r} \frac{\partial \bar{a}}{\partial \bar{r}}\right) \sin \bar{\theta} \sin \bar{\phi} \\ \cos \bar{\theta} \end{pmatrix}, \quad (46)$$

$$\vec{g}_2 = \vec{g}_{\bar{\theta}} = \begin{pmatrix} \frac{\partial x}{\partial \bar{\theta}} \\ \frac{\partial y}{\partial \bar{\theta}} \\ \frac{\partial z}{\partial \bar{\theta}} \end{pmatrix} = \bar{r} \begin{pmatrix} \bar{a}(\bar{r}) \cos \bar{\theta} \cos \bar{\phi} \\ \bar{a}(\bar{r}) \cos \bar{\theta} \sin \bar{\phi} \\ \cos \bar{\theta} \end{pmatrix}, \quad (47)$$

$$\vec{g}_3 = \vec{g}_{\bar{\phi}} = \begin{pmatrix} \frac{\partial x}{\partial \bar{\phi}} \\ \frac{\partial y}{\partial \bar{\phi}} \\ \frac{\partial z}{\partial \bar{\phi}} \end{pmatrix} = \bar{a}(\bar{r}) \bar{r} \sin \bar{\theta} \begin{pmatrix} -\sin \bar{\phi} \\ \cos \bar{\phi} \\ 0 \end{pmatrix}, \quad (48)$$

and employing Eqs. 27 - 29 gives the **prolate** covariant basis vectors

$$\vec{g}_1 = \vec{g}_{\bar{r}} = \begin{pmatrix} \frac{\partial x}{\partial \bar{r}} \\ \frac{\partial y}{\partial \bar{r}} \\ \frac{\partial z}{\partial \bar{r}} \end{pmatrix} = \begin{pmatrix} \sin \bar{\theta} \cos \bar{\phi} \\ \sin \bar{\theta} \sin \bar{\phi} \\ (\bar{a}(\bar{r}) + \bar{r} \frac{\partial \bar{a}}{\partial \bar{r}}) \cos \bar{\theta} \end{pmatrix}, \quad (49)$$

$$\vec{g}_2 = \vec{g}_{\bar{\theta}} = \begin{pmatrix} \frac{\partial x}{\partial \bar{\theta}} \\ \frac{\partial y}{\partial \bar{\theta}} \\ \frac{\partial z}{\partial \bar{\theta}} \end{pmatrix} = \bar{r} \begin{pmatrix} \cos \bar{\theta} \cos \bar{\phi} \\ \cos \bar{\theta} \sin \bar{\phi} \\ \bar{a}(\bar{r}) \cos \bar{\theta} \end{pmatrix}, \text{ and} \quad (50)$$

$$\vec{g}_3 = \vec{g}_{\bar{\phi}} = \begin{pmatrix} \frac{\partial x}{\partial \bar{\phi}} \\ \frac{\partial y}{\partial \bar{\phi}} \\ \frac{\partial z}{\partial \bar{\phi}} \end{pmatrix} = \bar{r} \sin \bar{\theta} \begin{pmatrix} -\sin \bar{\phi} \\ \cos \bar{\phi} \\ 0 \end{pmatrix}. \quad (51)$$

The three contravariant basis vectors can be obtained similarly. However, due to the complex connection between the stretching function  $\bar{a}$  and the physical grid coordinates  $r$  and  $\theta$ , this results in a very convoluted derivation process. It is more efficient to state the contravariant basis vectors and supply proof of their correctness and uniqueness:

In the case of **oblate** source surfaces (i.e. employing coordinate transformations 24 - 26), the three contravariant basis vectors are

$$\vec{g}^1 = \vec{g}^{\bar{r}} = \frac{1}{\bar{a} + r \sin^2 \bar{\theta} \frac{\partial \bar{a}}{\partial \bar{r}}} \begin{pmatrix} \sin \bar{\theta} \cos \bar{\phi} \\ \sin \bar{\theta} \sin \bar{\phi} \\ \bar{a} \cos \bar{\theta} \end{pmatrix}, \quad (52)$$

$$\vec{g}^2 = \vec{g}^{\bar{\theta}} = \frac{1}{r (\bar{a} + r \sin^2 \bar{\theta} \frac{\partial \bar{a}}{\partial \bar{r}})} \begin{pmatrix} \cos \bar{\theta} \cos \bar{\phi} \\ \cos \bar{\theta} \sin \bar{\phi} \\ -\sin \bar{\theta} (\bar{a} + \bar{r} \frac{\partial \bar{a}}{\partial \bar{r}}) \end{pmatrix}, \text{ and} \quad (53)$$

$$\vec{g}^3 = \vec{g}^{\bar{\phi}} = \frac{1}{\bar{a} \bar{r} \sin \bar{\theta}} \begin{pmatrix} -\sin \bar{\phi} \\ \cos \bar{\phi} \\ 0 \end{pmatrix}, \quad (54)$$

while in the **prolate** case (Eqs. 27 - 29) they are

$$\vec{g}^1 = \vec{g}^{\bar{r}} = \frac{1}{\bar{a} + \bar{r} \cos^2 \bar{\theta} \frac{\partial \bar{a}}{\partial \bar{r}}} \begin{pmatrix} \bar{a} \sin \bar{\theta} \cos \bar{\phi} \\ \bar{a} \sin \bar{\theta} \sin \bar{\phi} \\ \cos \theta \end{pmatrix}, \quad (55)$$

$$\vec{g}^2 = \vec{g}^{\bar{\theta}} = \frac{1}{\bar{r}(\bar{a} + \bar{r} \cos^2 \bar{\theta} \frac{\partial \bar{a}}{\partial \bar{r}})} \begin{pmatrix} \cos \bar{\theta} \cos \bar{\phi} (\bar{a} + \bar{r} \frac{\partial \bar{a}}{\partial \bar{r}}) \\ \cos \bar{\theta} \sin \bar{\phi} (\bar{a} + \bar{r} \frac{\partial \bar{a}}{\partial \bar{r}}) \\ -\sin \bar{\theta} \end{pmatrix}, \text{ and} \quad (56)$$

$$\vec{g}^3 = \vec{g}^{\bar{\phi}} = \frac{1}{\bar{r} \sin \bar{\theta}} \begin{pmatrix} -\sin \bar{\phi} \\ \cos \bar{\phi} \\ 0 \end{pmatrix}. \quad (57)$$

Define two matrices  $H$  and  $\hat{H}$  such that the covariant basis vector  $\vec{g}_i$  forms the  $i$ -th row of matrix  $H$  and the contravariant basis vector  $\vec{g}^i$  forms the  $i$ -th column of matrix  $\hat{H}$  for  $i \in \{1, 2, 3\}$ , or

$$H = \begin{pmatrix} \vec{g}_{11} & \vec{g}_{12} & \vec{g}_{13} \\ \vec{g}_{21} & \vec{g}_{22} & \vec{g}_{23} \\ \vec{g}_{31} & \vec{g}_{32} & \vec{g}_{33} \end{pmatrix} \quad \hat{H} = \begin{pmatrix} \vec{g}_1^1 & \vec{g}_1^2 & \vec{g}_1^3 \\ \vec{g}_2^1 & \vec{g}_2^2 & \vec{g}_2^3 \\ \vec{g}_3^1 & \vec{g}_3^2 & \vec{g}_3^3 \end{pmatrix}.$$

Calculating the matrix product  $H \cdot \hat{H}$  by inserting the expressions for the basis vectors 46 - 48 and 52 - 54 (oblate case) or vectors 49 - 51 and 55 - 57 (prolate case) yields in both cases

$$H \cdot \hat{H} = \begin{pmatrix} \vec{g}_1 \vec{g}^1 & \vec{g}_1 \vec{g}^2 & \vec{g}_1 \vec{g}^3 \\ \vec{g}_2 \vec{g}^1 & \vec{g}_2 \vec{g}^2 & \vec{g}_2 \vec{g}^3 \\ \vec{g}_3 \vec{g}^1 & \vec{g}_3 \vec{g}^2 & \vec{g}_3 \vec{g}^3 \end{pmatrix} = \begin{pmatrix} 1 & 0 & 0 \\ 0 & 1 & 0 \\ 0 & 0 & 1 \end{pmatrix}.$$

Therefore,  $H$  is invertible and its unique inverse is  $\hat{H}$  and vice versa. The vectors 52 to 57 are indeed the sought-for contravariant basis vectors which together with the covariant basis vectors 46 - 51 form the dual bases  $\{\vec{g}_1, \vec{g}_2, \vec{g}_3\}$  and  $\{\vec{g}^1, \vec{g}^2, \vec{g}^3\}$ .

The basis vectors are defined using the coordinates of the computational domain rather than the physical domain. In principle, the coordinates can be converted employing the relationships 24 - 37, though the resulting expressions are rather lengthy and unwieldy. It is instead preferred to transform physical positions into the computational domain and perform computations therein.

Figure 6 shows two basis vectors of each basis at different positions in the oblate and prolate models. Aside from particular positions like the photosphere and the poles or above the equator, the chosen coordinate system's basis vectors are non-orthogonal.

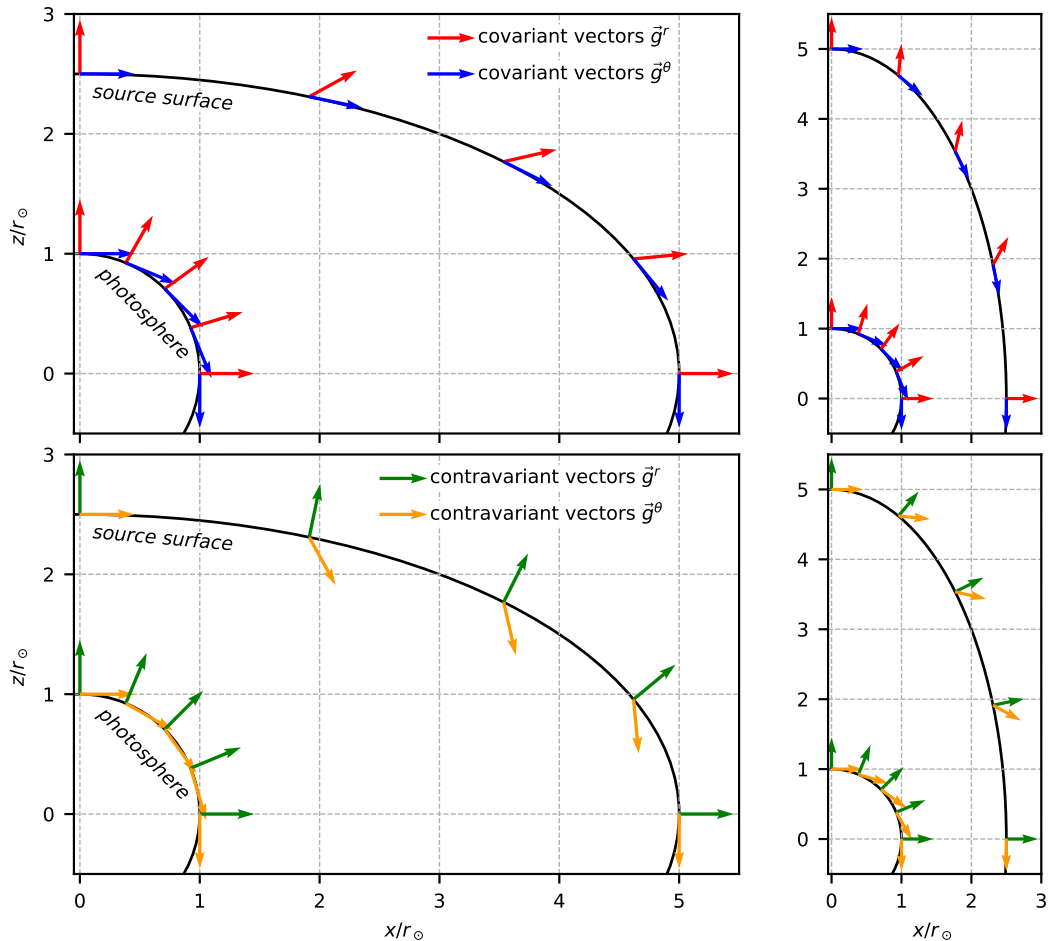


Figure 6: Covariant (first row) and contravariant (second row) basis vectors at different positions in the physical domain of the oblate (left column) and prolate (right column) PFSS models. The third basis vector in zonal direction is always perpendicular to the vectors drawn and points into the plane. As can be seen from this figure, in general, the bases defined by these vectors are non-orthogonal. The solar rotation axis is aligned with the z-axis.

## 4.4 LAPLACE OPERATOR IN GENERAL CURVILINEAR COORDINATES

This section presents the Laplace operator 45 in the special case of the ellipsoidal coordinate system discussed in Sects. 4.1 and 4.2, and its transformation into a finite difference form.

The metric coefficients are defined by  $g_{ij} = \vec{g}_i \vec{g}_j$  and the reciprocal metric coefficients by  $g^{ij} = \vec{g}^i \vec{g}^j$  for  $i, j \in \{1, 2, 3\}$ . Arranging the metric coefficients in a matrix

$$G = \begin{pmatrix} g_{11} & g_{12} & g_{13} \\ g_{21} & g_{22} & g_{23} \\ g_{31} & g_{32} & g_{33} \end{pmatrix} \quad (58)$$

and defining  $g = \det(G)$ , the Laplace operator in general, non-orthogonal, curvilinear coordinates (Eq. 45) takes the form

$$\begin{aligned} \nabla^2 \Psi &= \frac{1}{\sqrt{g}} \sum_i \sum_j \frac{\partial}{\partial q^i} \left( \sqrt{g} g^{ij} \frac{\partial \Psi}{\partial q^j} \right) \\ &= \frac{1}{\sqrt{g}} \sum_i \sum_j \left( \underbrace{\frac{\partial}{\partial q^i} \left( \sqrt{g} g^{ij} \right)}_{p^{ij}} \frac{\partial \Psi}{\partial q^j} + \sqrt{g} g^{ij} \frac{\partial^2 \Psi}{\partial q^i \partial q^j} \right) \\ &= \frac{1}{\sqrt{g}} \left( \frac{\partial p^{11}}{\partial r} \frac{\partial \Psi}{\partial r} + p^{11} \frac{\partial^2 \Psi}{\partial r^2} + \frac{\partial p^{12}}{\partial r} \frac{\partial \Psi}{\partial \theta} + p^{12} \frac{\partial^2 \Psi}{\partial r \partial \theta} + \frac{\partial p^{13}}{\partial r} \frac{\partial \Psi}{\partial \phi} + p^{13} \frac{\partial^2 \Psi}{\partial r \partial \phi} \right. \\ &\quad + \frac{\partial p^{21}}{\partial \theta} \frac{\partial \Psi}{\partial r} + p^{21} \frac{\partial^2 \Psi}{\partial r \partial \theta} + \frac{\partial p^{22}}{\partial \theta} \frac{\partial \Psi}{\partial \theta} + p^{22} \frac{\partial^2 \Psi}{\partial \theta^2} + \frac{\partial p^{23}}{\partial \theta} \frac{\partial \Psi}{\partial \phi} + p^{23} \frac{\partial^2 \Psi}{\partial \theta \partial \phi} \\ &\quad + \frac{\partial p^{31}}{\partial \phi} \frac{\partial \Psi}{\partial r} + p^{31} \frac{\partial^2 \Psi}{\partial r \partial \phi} + \frac{\partial p^{32}}{\partial \phi} \frac{\partial \Psi}{\partial \theta} + p^{32} \frac{\partial^2 \Psi}{\partial \theta \partial \phi} + \frac{\partial p^{33}}{\partial \phi} \frac{\partial \Psi}{\partial \phi} + p^{33} \frac{\partial^2 \Psi}{\partial \phi^2} \Big) \\ &= \frac{1}{\sqrt{g}} \left( \underbrace{\frac{\partial \Psi}{\partial r} \left( \frac{\partial p^{11}}{\partial r} + \frac{\partial p^{21}}{\partial \theta} + \frac{\partial p^{31}}{\partial \phi} \right)}_{t_r} + \underbrace{\frac{\partial \Psi}{\partial \theta} \left( \frac{\partial p^{12}}{\partial r} + \frac{\partial p^{22}}{\partial \theta} + \frac{\partial p^{32}}{\partial \phi} \right)}_{t_\theta} \right. \\ &\quad + \underbrace{\frac{\partial \Psi}{\partial \phi} \left( \frac{\partial p^{13}}{\partial r} + \frac{\partial p^{23}}{\partial \theta} + \frac{\partial p^{33}}{\partial \phi} \right)}_{t_\phi} \\ &\quad + \underbrace{\frac{\partial^2 \Psi}{\partial r \partial \theta} \left( p^{12} + p^{21} \right)}_{t_{r\theta}} + \underbrace{\frac{\partial^2 \Psi}{\partial r \partial \phi} \left( p^{13} + p^{31} \right)}_{t_{r\phi}} + \underbrace{\frac{\partial^2 \Psi}{\partial \theta \partial \phi} \left( p^{23} + p^{32} \right)}_{t_{\theta\phi}} \\ &\quad \left. + \frac{\partial^2 \Psi}{\partial r^2} p^{11} + \frac{\partial^2 \Psi}{\partial \theta^2} p^{22} + \frac{\partial^2 \Psi}{\partial \phi^2} p^{33} \right) \\ &= \frac{1}{\sqrt{g}} \left( \frac{\partial \Psi}{\partial r} t_r + \frac{\partial \Psi}{\partial \theta} t_\theta + \frac{\partial \Psi}{\partial \phi} t_\phi + \frac{\partial^2 \Psi}{\partial r \partial \theta} t_{r\theta} + \frac{\partial^2 \Psi}{\partial r \partial \phi} t_{r\phi} + \frac{\partial^2 \Psi}{\partial \theta \partial \phi} t_{\theta\phi} \right. \\ &\quad \left. + \frac{\partial^2 \Psi}{\partial r^2} p^{11} + \frac{\partial^2 \Psi}{\partial \theta^2} p^{22} + \frac{\partial^2 \Psi}{\partial \phi^2} p^{33} \right). \end{aligned} \quad (59)$$

The PFSS solver presented in this work requires a numerical representation of the Laplace operator. To translate the analytic expression of the Laplace operator into a version that can be utilized by the numerical solver, the partial derivatives in Eq. 59 need to be replaced by their finite difference versions established in Sect. 3.2. The process is straightforward and results in the following expression:

$$\nabla^2 \Psi = \frac{1}{\sqrt{g}} \left\{ \begin{array}{l} t_r C_r \left( -d_{r+}^2 \Psi_{i-1,j,k} - (d_{r-}^2 - d_{r+}^2) \Psi_{i,j,k} + d_{r-}^2 \Psi_{i+1,j,k} \right) \\ + t_\theta C_\theta \left( -d_{\theta+}^2 \Psi_{i,j-1,k} - (d_{\theta-}^2 - d_{\theta+}^2) \Psi_{i,j,k} + d_{\theta-}^2 \Psi_{i,j+1,k} \right) \\ + t_\phi C_\phi \left( -d_{\phi+}^2 \Psi_{i,j,k-1} - (d_{\phi-}^2 - d_{\phi+}^2) \Psi_{i,j,k} + d_{\phi-}^2 \Psi_{i,j,k+1} \right) \\ + t_{r\theta} C_r C_\theta \left[ \begin{array}{l} -d_{r+}^2 \left( -d_{\theta+}^2 \Psi_{i-1,j-1,k} - (d_{\theta-}^2 - d_{\theta+}^2) \Psi_{i-1,j,k} + d_{\theta-}^2 \Psi_{i-1,j+1,k} \right) \\ - (d_{r-}^2 - d_{r+}^2) \left( -d_{\theta+}^2 \Psi_{i,j-1,k} - (d_{\theta-}^2 - d_{\theta+}^2) \Psi_{i,j,k} + d_{\theta-}^2 \Psi_{i,j+1,k} \right) \\ + d_{r-}^2 \left( -d_{\theta+}^2 \Psi_{i+1,j-1,k} - (d_{\theta-}^2 - d_{\theta+}^2) \Psi_{i+1,j,k} + d_{\theta-}^2 \Psi_{i+1,j+1,k} \right) \end{array} \right] \\ + t_{r\phi} C_r C_\phi \left[ \begin{array}{l} -d_{r+}^2 \left( d_{\phi+}^2 \Psi_{i-1,j,k-1} - (d_{\phi-}^2 - d_{\phi+}^2) \Psi_{i-1,j,k} + d_{\phi-}^2 \Psi_{i-1,j,k+1} \right) \\ - (d_{r-}^2 - d_{r+}^2) \left( -d_{\phi+}^2 \Psi_{i,j,k-1} - (d_{\phi-}^2 - d_{\phi+}^2) \Psi_{i,j,k} + d_{\phi-}^2 \Psi_{i,j,k+1} \right) \\ + d_{r-}^2 \left( -d_{\phi+}^2 \Psi_{i+1,j,k-1} - (d_{\phi-}^2 - d_{\phi+}^2) \Psi_{i+1,j,k} + d_{\phi-}^2 \Psi_{i+1,j,k+1} \right) \end{array} \right] \\ + t_{\theta\phi} C_\theta C_\phi \left[ \begin{array}{l} -d_{\theta+}^2 \left( -d_{\phi+}^2 \Psi_{i,j-1,k-1} - (d_{\phi-}^2 - d_{\phi+}^2) \Psi_{i,j-1,k} + d_{\phi-}^2 \Psi_{i,j-1,k+1} \right) \\ - (d_{\theta-}^2 - d_{\theta+}^2) \left( -d_{\phi+}^2 \Psi_{i,j,k-1} - (d_{\phi-}^2 - d_{\phi+}^2) \Psi_{i,j,k} + d_{\phi-}^2 \Psi_{i,j,k+1} \right) \\ + d_{\theta-}^2 \left( -d_{\phi+}^2 \Psi_{i,j+1,k-1} - (d_{\phi-}^2 - d_{\phi+}^2) \Psi_{i,j+1,k} + d_{\phi-}^2 \Psi_{i,j+1,k+1} \right) \end{array} \right] \\ + 2p^{11} C_r \left( d_{r+} \Psi_{i-1,j,k} - (d_{r+} + d_{r-}) \Psi_{i,j,k} + d_{r-} \Psi_{i+1,j,k} \right) \\ + 2p^{22} C_\theta \left( d_{\theta+} \Psi_{i,j-1,k} - (d_{\theta+} + d_{\theta-}) \Psi_{i,j,k} + d_{\theta-} \Psi_{i,j+1,k} \right) \\ + 2p^{33} C_\phi \left( d_{\phi+} \Psi_{i,j,k-1} - (d_{\phi+} + d_{\phi-}) \Psi_{i,j,k} + d_{\phi-} \Psi_{i,j,k+1} \right) \end{array} \right\}.$$

Rearranging for the  $\Psi$  terms at the different grid points, multiplying by the square root of the determinant of the metric coefficient matrix  $\sqrt{g}$  and introducing  $k_m = t_m C_m$  and  $k_{mn} = t_{mn} C_m C_n$  for  $m, n \in \{r, \theta, \phi\}$  results in

$$\begin{aligned}
& \nabla^2 \Psi \sqrt{g} \\
&= \Psi_{i-1,j-1,k} \left( -k_{r\theta} d_{r+}^2 d_{\theta+}^2 \right) + \Psi_{i-1,j+1,k} \left( -k_{r\theta} d_{r+}^2 d_{\theta-}^2 \right) \\
&+ \Psi_{i+1,j-1,k} \left( -k_{r\theta} d_{r-}^2 d_{\theta+}^2 \right) + \Psi_{i+1,j+1,k} \left( k_{r\theta} d_{r-}^2 d_{\theta-}^2 \right) \\
&+ \Psi_{i-1,j,k-1} \left( k_{r\phi} d_{r+}^2 d_{\phi+}^2 \right) + \Psi_{i-1,j,k+1} \left( -k_{r\phi} d_{r+}^2 d_{\phi-}^2 \right) \\
&+ \Psi_{i+1,j,k-1} \left( -k_{r\phi} d_{r-}^2 d_{\phi+}^2 \right) + \Psi_{i+1,j,k+1} \left( k_{r\phi} d_{r-}^2 d_{\phi-}^2 \right) \\
&+ \Psi_{i,j-1,k-1} \left( k_{\theta\phi} d_{\theta+}^2 d_{\phi+}^2 \right) + \Psi_{i,j-1,k+1} \left( -k_{\theta\phi} d_{\theta+}^2 d_{\phi-}^2 \right) \\
&+ \Psi_{i,j+1,k-1} \left( -k_{\theta\phi} d_{\theta-}^2 d_{\phi+}^2 \right) + \Psi_{i,j+1,k+1} \left( k_{\theta\phi} d_{\theta-}^2 d_{\phi-}^2 \right) \\
&+ \Psi_{i-1,j,k} \left[ -k_r d_{r+}^2 + k_{r\theta} d_{r+}^2 (d_{\theta-}^2 - d_{\theta+}^2) + k_{r\phi} d_{r+}^2 (d_{\phi-}^2 - d_{\phi+}^2) + 2p^{11} C_r d_{r+} \right] \\
&+ \Psi_{i+1,j,k} \left[ k_r d_{r-}^2 - k_{r\theta} d_{r-}^2 (d_{\theta-}^2 - d_{\theta+}^2) - k_{r\phi} d_{r-}^2 (d_{\phi-}^2 - d_{\phi+}^2) + 2p^{11} C_r d_{r-} \right] \\
&+ \Psi_{i,j-1,k} \left[ -k_\theta d_{\theta+}^2 + k_{r\theta} (d_{r-}^2 - d_{r+}^2) d_{\theta+}^2 + k_{\theta\phi} d_{\theta+}^2 (d_{\phi-}^2 - d_{\phi+}^2) + 2p^{22} C_\theta d_{\theta+} \right] \\
&+ \Psi_{i,j+1,k} \left[ k_\theta d_{\theta-}^2 - k_{r\theta} (d_{r-}^2 - d_{r+}^2) d_{\theta-}^2 - k_{\theta\phi} d_{\theta-}^2 (d_{\phi-}^2 - d_{\phi+}^2) + 2p^{22} C_\theta d_{\theta-} \right] \\
&+ \Psi_{i,j,k-1} \left[ -k_\phi d_{\phi+}^2 + k_{r\phi} (d_{r-}^2 - d_{r+}^2) d_{\phi+}^2 + k_{\theta\phi} (d_{\theta-}^2 - d_{\theta+}^2) d_{\phi+}^2 + 2p^{33} C_\phi d_{\phi+} \right] \\
&+ \Psi_{i,j,k+1} \left[ k_\phi d_{\phi-}^2 - k_{r\phi} (d_{r-}^2 - d_{r+}^2) d_{\phi-}^2 - k_{\theta\phi} (d_{\theta-}^2 - d_{\theta+}^2) d_{\phi-}^2 + 2p^{33} C_\phi d_{\phi-} \right] \\
&+ \Psi_{i,j,k} \left[ -k_r (d_{r-}^2 - d_{r+}^2) - k_\theta (d_{\theta-}^2 - d_{\theta+}^2) - k_\phi (d_{\phi-}^2 - d_{\phi+}^2) \right. \\
&\quad \left. + k_{r\theta} (d_{r-}^2 - d_{r+}^2) (d_{\theta-}^2 - d_{\theta+}^2) \right. \\
&\quad \left. + k_{r\phi} (d_{r-}^2 - d_{r+}^2) (d_{\phi-}^2 - d_{\phi+}^2) \right. \\
&\quad \left. + k_{\theta\phi} (d_{\theta-}^2 - d_{\theta+}^2) (d_{\phi-}^2 - d_{\phi+}^2) \right. \\
&\quad \left. - 2p^{11} C_r (d_{r+} + d_{r-}) - 2p^{22} C_\theta (d_{\theta+} + d_{\theta-}) - 2p^{33} C_\phi (d_{\phi+} + d_{\phi-}) \right].
\end{aligned}$$

The PFSS model utilizes Laplace's equation  $\nabla^2 \Psi = 0$ . Inserting this statement into the equation above, introducing a scaling factor

$$\begin{aligned}
S_{i,j,k} = & \left[ -k_r (d_{r-}^2 - d_{r+}^2) - k_\theta (d_{\theta-}^2 - d_{\theta+}^2) - k_\phi (d_{\phi-}^2 - d_{\phi+}^2) \right. \\
& + k_{r\theta} (d_{r-}^2 - d_{r+}^2) (d_{\theta-}^2 - d_{\theta+}^2) \\
& + k_{r\phi} (d_{r-}^2 - d_{r+}^2) (d_{\phi-}^2 - d_{\phi+}^2) \\
& + k_{\theta\phi} (d_{\theta-}^2 - d_{\theta+}^2) (d_{\phi-}^2 - d_{\phi+}^2) \\
& \left. - 2p^{11} C_r (d_{r+} + d_{r-}) - 2p^{22} C_\theta (d_{\theta+} + d_{\theta-}) - 2p^{33} C_\phi (d_{\phi+} + d_{\phi-}) \right],
\end{aligned}$$

and solving for  $\Psi_{i,j,k}$  results in an expression for  $\Psi$  at the respective grid position  $i, j, k$

$$\begin{aligned}
\Psi_{i,j,k} = -1/S_{ijk} \left[ \right. & \Psi_{i-1,j-1,k} \left( -k_{r\theta} d_{r+}^2 d_{\theta+}^2 \right) + \Psi_{i-1,j+1,k} \left( -k_{r\theta} d_{r+}^2 d_{\theta-}^2 \right) \\
& + \Psi_{i+1,j-1,k} \left( -k_{r\theta} d_{r-}^2 d_{\theta+}^2 \right) + \Psi_{i+1,j+1,k} \left( -k_{r\theta} d_{r-}^2 d_{\theta-}^2 \right) \\
& + \Psi_{i-1,j,k-1} \left( -k_{r\phi} d_{r+}^2 d_{\phi+}^2 \right) + \Psi_{i-1,j,k+1} \left( -k_{r\phi} d_{r+}^2 d_{\phi-}^2 \right) \\
& + \Psi_{i+1,j,k-1} \left( -k_{r\phi} d_{r-}^2 d_{\phi+}^2 \right) + \Psi_{i+1,j,k+1} \left( -k_{r\phi} d_{r-}^2 d_{\phi-}^2 \right) \\
& + \Psi_{i,j-1,k-1} \left( -k_{\theta\phi} d_{\theta+}^2 d_{\phi+}^2 \right) + \Psi_{i,j-1,k+1} \left( -k_{\theta\phi} d_{\theta+}^2 d_{\phi-}^2 \right) \\
& + \Psi_{i,j+1,k-1} \left( -k_{\theta\phi} d_{\theta-}^2 d_{\phi+}^2 \right) + \Psi_{i,j+1,k+1} \left( -k_{\theta\phi} d_{\theta-}^2 d_{\phi-}^2 \right) \\
& + \Psi_{i-1,j,k} \left( -k_r d_{r+}^2 + k_{r\theta} d_{r+}^2 \left( d_{\theta-}^2 - d_{\theta+}^2 \right) + k_{r\phi} d_{r+}^2 \left( d_{\phi-}^2 - d_{\phi+}^2 \right) + 2p^{11} C_r d_{r+} \right) \\
& + \Psi_{i+1,j,k} \left( -k_r d_{r-}^2 - k_{r\theta} d_{r-}^2 \left( d_{\theta-}^2 - d_{\theta+}^2 \right) - k_{r\phi} d_{r-}^2 \left( d_{\phi-}^2 - d_{\phi+}^2 \right) + 2p^{11} C_r d_{r-} \right) \\
& + \Psi_{i,j-1,k} \left( -k_\theta d_{\theta+}^2 + k_{r\theta} \left( d_{r-}^2 - d_{r+}^2 \right) d_{\theta+}^2 + k_{\theta\phi} d_{\theta+}^2 \left( d_{\phi-}^2 - d_{\phi+}^2 \right) + 2p^{22} C_\theta d_{\theta+} \right) \\
& + \Psi_{i,j+1,k} \left( -k_\theta d_{\theta-}^2 - k_{r\theta} \left( d_{r-}^2 - d_{r+}^2 \right) d_{\theta-}^2 - k_{\theta\phi} d_{\theta-}^2 \left( d_{\phi-}^2 - d_{\phi+}^2 \right) + 2p^{22} C_\theta d_{\theta-} \right) \\
& + \Psi_{i,j,k-1} \left( -k_\phi d_{\phi+}^2 + k_{r\phi} \left( d_{r-}^2 - d_{r+}^2 \right) d_{\phi+}^2 + k_{\theta\phi} \left( d_{\theta-}^2 - d_{\theta+}^2 \right) d_{\phi+}^2 + 2p^{33} C_\phi d_{\phi+} \right) \\
& \left. + \Psi_{i,j,k+1} \left( -k_\phi d_{\phi-}^2 - k_{r\phi} \left( d_{r-}^2 - d_{r+}^2 \right) d_{\phi-}^2 - k_{\theta\phi} \left( d_{\theta-}^2 - d_{\theta+}^2 \right) d_{\phi-}^2 + 2p^{33} C_\phi d_{\phi-} \right) \right]. \tag{60}
\end{aligned}$$

Equation 60 is the centerpiece of the new ellipsoidal PFSS solver. Each time-step it is evaluated at every grid point  $i, j, k$  throughout the grid until the change from one time-step to the next falls below a certain threshold at all grid points (see Sect. 3.5). Computing a new value for  $\Psi$  requires knowledge of the neighboring 18 grid points. The corners of the neighbor cube (e.g., at position  $i+1, j+1, k+1$ ) are not required. Because Eq. 60 has the same format at every grid point, it can be parallelized, and the algorithm is sped up significantly.

## GRID PARAMETERS AND PROCESSING OF INPUT/OUTPUT DATA

---

Before the new model can be reasonably applied to analyzing experimental data sets, it has to be ensured that the results produced by the implementations yield the best predictions possible within the restricted framework of the PFSS paradigm. Two opposing computational factors, prediction accuracy and implementation run time, need to be conformed. Increasing the number of grid points improves the accuracy of the prediction. However, this will also increase the computation time. Due to the nature of the implementation, only directly neighboring grid points influence one another. Therefore, an increase in grid point density does not increase the computation time linearly because the information has to travel further to reach the other end of the grid. Each time step scales linearly with grid points to be computed, but on top of that, more time steps are required to let the solution process (Sect. 3.5) converge to the desired result.

The balance between these two opposing factors is achieved by carefully evaluating different computational parameters and assessing their fitness for the model. The model parameters ellipticity  $A$  and source surface height  $R_{ss}$  are model parameters opposed to computational (implementation) parameters and need to be evaluated separately and with respect to experimental heliospheric measurements, which is performed in Chapter 6. This chapter concentrates on finding the optimal computational parameters to be utilized with the new solver, a purely numerical study. The number of grid points and their distribution throughout the computational domain is analyzed in Sect. 5.1. In Sect. 5.2, preprocessing of magnetogram input data is discussed. The chapter closes by presenting computational data products that can be derived from the implementation output in Sect. 5.3. These data products can visualize the model predictions of the new PFSS solver and help evaluate its prediction quality.

### 5.1 GRID POINT DISTRIBUTION AND DENSITY

Increasing the new solver's grid point density also increases its accuracy due to smaller steps in the finite differences employed (see Sect. 3.2) and, therefore, its results. If the solver is internally consistent, at some point, increasing the number of grid points yields only small changes in the results. If there were no convergence and a small change in grid point density results in considerable output changes, subsequent scientific-analytical validity would be impaired. In the following, the solver's internal consistency is investigated, and values for grid point density and distribution are presented that exhibit an acceptable accuracy for model predictions in all relevant use cases of the new PFSS implementation.

### 5.1.1 NUMERICAL CONSIDERATIONS

The three-dimensional grid used by the new solver employs spherical geometry (see Sect. 3.1). Because it is also structured (i.e., the neighborhood relation between grid points form hexahedra, each grid point not at the grid's boundary has exactly six neighbors), the number of grid points on each radial grid shell is the same, leading to a higher grid point density at the lower compared to the upper boundary. The magnetic field has stronger gradients near the photosphere; therefore, this grid point distribution is desired. As a consequence, grid spacing increases from the lower to the upper boundary. In the radial direction, the geometric factor  $q$  introduced in Sect. 3.1 ensures increasing radial distances. A reasonable starting point is to keep distances between grid points equal in all three directions, that is,  $dr_{i,j,k} \approx d\theta_{i,j,k} \approx d\phi_{i,j,k}$  for all grid points  $i, j, k$  throughout the grid. This can only result in an approximation due to the sine-latitude spacing in the meridional direction, which incurs larger distances between grid points near the poles compared to grid points near the equator.

Let  $N_r$ ,  $N_\theta$ , and  $N_\phi$  be the number of grid points in radial, meridional and zonal directions, respectively. In the following analysis, the resolution in meridional and zonal directions are coupled by  $N_\phi = 2 \cdot N_\theta$ . This approach ensures the distances in both directions to be similar, although it neglects the small deviation due to the grid not reaching the poles and the non-equidistant sine-latitude spacing in the meridional direction.

First, the geometric expansion factor  $q$  (see Sect. 3.1) needs to be determined. Let  $r_i$  be the radial position of the  $i$ -th grid point,  $r_0 = R_\odot = 6.957 \cdot 10^8$  m be the solar radius and the lower boundary of the numerical grid.  $r_{N_r-1} = R_{ss}$  denotes the upper grid boundary and  $dr_i$  is the radial distance between grid points  $i$  and  $i + 1$ . The distance between the lower boundary and radial grid point  $n$  can then be expressed by the geometric sum

$$\sum_{i=0}^{n-2} dr_0 \cdot q^i = dr_0 \frac{1 - q^{n-1}}{1 - q} = r_n - R_\odot . \quad (61)$$

The distance at radial grid shell  $n$  between two neighboring grid points in meridional direction (again ignoring the deviation due to the sine-latitude spacing) is

$$d\theta_n \approx \frac{r_n \pi}{N_\theta - 1} . \quad (62)$$

Utilizing Eqs. 61 and 62 and restricting the ratio of meridional to radial grid spacing to be equal at the lower and upper boundary, one obtains

$$\begin{aligned}
& \frac{d\theta_{N_r-2}}{dr_{N_r-2}} = \frac{d\theta_0}{dr_0} \\
\Leftrightarrow & \frac{\frac{r_{N_r-1}\pi}{N_\theta-1}}{r_{N_r-1} - r_{N_r-2}} = \frac{\frac{r_0\pi}{N_\theta-1}}{r_1 - r_0} \\
\Leftrightarrow & \frac{r_{N_r-1}}{r_{N_r-1} - r_{N_r-2}} = \frac{r_0}{r_1 - r_0} \\
\stackrel{61}{\Leftrightarrow} & \frac{R_{ss}}{dr_0 \frac{1-q^{N_r-1}}{1-q} - dr_0 \frac{1-q^{N_r-2}}{1-q}} = \frac{R_\odot}{dr_0} \\
\Leftrightarrow & \frac{1-q}{q^{N_r-2} - q^{N_r-1}} = \frac{R_\odot}{R_{ss}} . \tag{63}
\end{aligned}$$

Equation 63 can be solved numerically for  $q$ . It is independent of the number of grid points in the meridional direction and only states that the ratio of meridional to radial spacing must be equal throughout the grid. In a second step, an expression for  $N_\theta$  is required. The radial and meridional spacing at the photosphere are supposed to be equal. Therefore, it holds that

$$\begin{aligned}
dr_0 = d\theta_0 &= \frac{R_\odot \pi}{N_\theta - 1} \\
\Leftrightarrow N_\theta &= \frac{R_\odot \pi}{dr_0} + 1 \\
\stackrel{61}{\Leftrightarrow} N_\theta &= \frac{1-q^{N_r-1}}{1-q} \frac{R_\odot \pi}{R_{ss} - R_\odot} + 1 \\
\Leftrightarrow N_\theta &= \frac{1-q^{N_r-1}}{1-q} \frac{\pi}{R_{ss}/R_\odot - 1} + 1 . \tag{64}
\end{aligned}$$

To obtain a grid with this constraint to have the same spacing in all directions, one

1. selects a number of radial grid shells ( $N_r$ ),
2. solves Eq. 63 for the geometric expansion factor ( $q$ ),
3. evaluates Eq. 64 to obtain the number of meridional grid points ( $N_\theta$ ), and
4. determines the number of grid points in zonal direction by  $N_\phi = 2N_\theta$ .

With this approach, a single parameter (i.e., the number of grid points in the radial direction,  $N_r$ ) determines the distribution of grid points, which allows for a simple evaluation procedure (Sect. 5.1.2). A grid obtained according to this procedure is called a *large grid* and denoted by "l" in the evaluation procedure (Sect. 5.1.3).

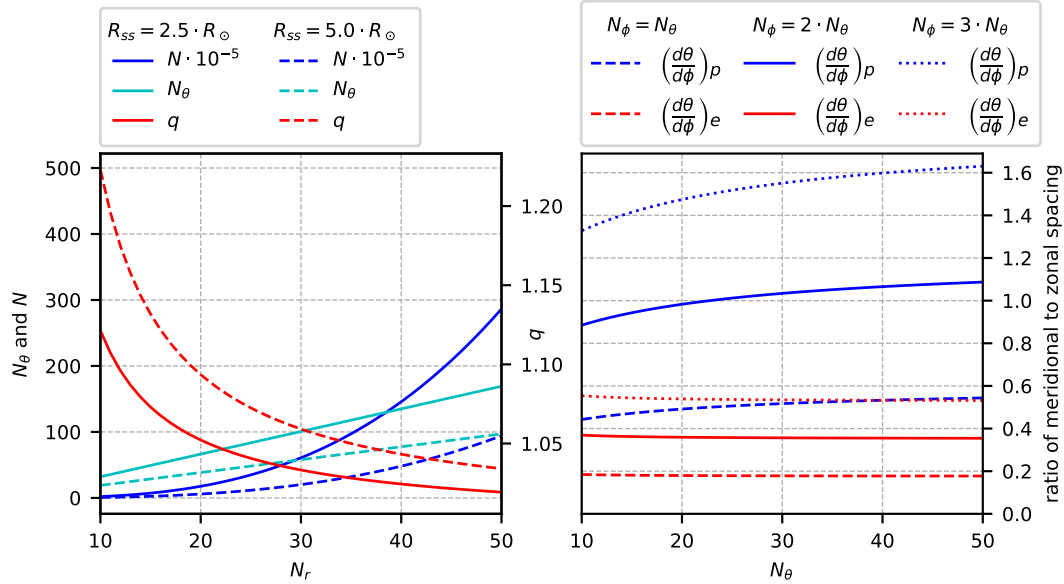


Figure 7: Left: Overall number of grid points ( $N = N_r \cdot N_\theta \cdot N_\phi$ ), number of grid points in meridional direction ( $N_\theta$ ), and geometric progression factor ( $q$ ) determined by the number of radial grid shells ( $N_r$ ) according to Eqs. 63 and 64. Dependencies for source surfaces at  $R_{ss} = 2.5 \cdot R_\odot$  and  $R_{ss} = 5 \cdot R_\odot$  are distinguished. Right: Ratio of grid spacing in meridional direction ( $d\theta$ ) to grid spacing in zonal direction ( $d\phi$ ) near the poles (subscript "p") and near the equator (subscript "e") for three relations between  $N_\phi$  and  $N_\theta$ . A maximum sine-latitude of 14.5/15 is assumed. The ratios are independent of the model's source surface radius.

The left panel in Fig. 7 illustrates the dependency of the geometric expansion factor  $q$ , the number of meridional grid points  $N_\theta$ , and the overall number of grid points in the entire grid  $N$  on the number of radial grid points  $N_r$ . Dependencies for two source surface heights are shown. The grid is much coarser for the source surface at height  $R_{ss} = 5 \cdot R_\odot$  because the computational domain is much larger. Also, the demand of almost equal spacing in all directions fans out the grid points in the meridional and zonal directions. This does not mean that a higher source surface requires fewer grid points for the same accuracy, but rather it requests fewer grid points for the same number of radial grid points compared to the grid with the lower source surface. In a sine-latitude grid, the spacing in meridional and zonal directions cannot be equal everywhere, as assumed for the derivations in this section. The right panel of Fig. 7 illustrates this deviation for select relations between  $N_\phi$  and  $N_\theta$ .

### 5.1.2 COMPARISON METRICS

As a proxy for the convergence of the solver, the PFSS prediction is computed for several three-dimensional computational resolutions of the underlying grid, magnetic field lines are obtained from the prediction and their positions and polarities compared. The procedure to obtain magnetic field lines from the PFSS output is described in Sect. 5.3.1.

Two "magnetic images" with  $200 \times 400$  pixels are computed for each grid resolution, one at the source surface and the other at the photosphere. The positions of these "magnetic pixels" are always the same, independent of the grid resolution to be analyzed. At each pixel, a magnetic field line is spawned and traced to the other side of the computational domain, that is, from the source surface down to the photosphere and vice versa. The polarity of the spawned magnetic field lines obtained from one grid resolution (denoted with subscript  $i$ ) is compared to the same field line's polarity obtained from the next highest resolution (denoted with subscript  $i + 1$ ). Of the 80000 ( $= 200 \times 400$ ) field lines for each of the two magnetic maps, the number of polarity changes are noted. When the solution converges, the number of changes approaches zero.

Additionally, the photospheric footpoint positions of magnetic field lines in the first magnetic image (traced from source surface to photosphere) for both grid resolutions are compared. This choice has two advantages compared to the polarity comparisons. First, as the magnetic field line is traced from the upper to the lower boundary of the computational domain, it contains information from the solver's entire radial structure. Second, these footpoint positions are used for subsequent scientific analyses, so evaluating this metric ensures that the new algorithm is optimized for the data product to be employed later on.

The summarized procedure is as follows:

1. Determine number of grid points  $N_{r_i} \times N_{\theta_i} \times N_{\phi_i}$  for computational grid resolution  $i \in \{1, 2, \dots\}$ .
2. Scale input magnetogram to resolution  $N_{\theta_i} \times N_{\phi_i}$  (lower boundary condition).
3. Compute PFSS solution.
4. Deploy two sine-latitude grids of  $200 \times 400$  elements at the source surface and at the photosphere, stretching from  $\sin(\text{latitude}_{\max}) = 14.5/15$  to  $\sin(\text{latitude}_{\min}) = -14.5/15$ .
5. Spawn and track magnetic field lines from each of these "pixels" down to the photosphere/up to the source surface.
6. Store the polarity of each of these field lines for both mappings.
7. For the downward mapping, note the photospheric footpoint positions of all field lines.
8. Repeat steps 1 to 7 for computational grid resolution  $i + 1$ .
9. Compare the polarities of magnetic field lines from step 6 between resolutions  $i$  and  $i + 1$ . Note the number of polarity changes.
10. Compute the distance for each of the  $200 \times 400$  field lines between resolutions  $i$  and  $i + 1$  from step 7 and determine their average.

For the grid solver to be used in further analyses and publications, an acceptable balance between computational accuracy and computation time is required. Of course, accuracy is essential, but because solutions for lots of Carrington rotations and parameter sets need to be analyzed, the solver is required to terminate quickly. In the first step, the best numerical accuracy for the grid implementation is searched for, and in the second step, the computation time is reduced while keeping results accurate.

### 5.1.3 DETERMINATION OF GRID PARAMETERS

One goal of this study is to keep computation time low to perform a high number of model evaluations. Therefore, the number of grid points should be reduced as much as possible while retaining high computational accuracy. Parameters derived in Sect. 5.1.1 are just a first idea of how a numerical grid might be generated to yield good results in the most general manner. When no information about the underlying problem is known, a more or less equidistant grid spacing is a reasonable starting point. The grid spacing in the upper region of the computational domain is already increased due to the geometric progression of grid point positions in Eq. 61, based on two reasons: First, gradients of the magnetic field decrease far away from the photosphere. Therefore, numeric accuracy can safely be reduced near the source surface. Second, a constant grid spacing in radial direction would increase the number of grid points ( $N \propto r^3$ ). The geometric progression ensures higher

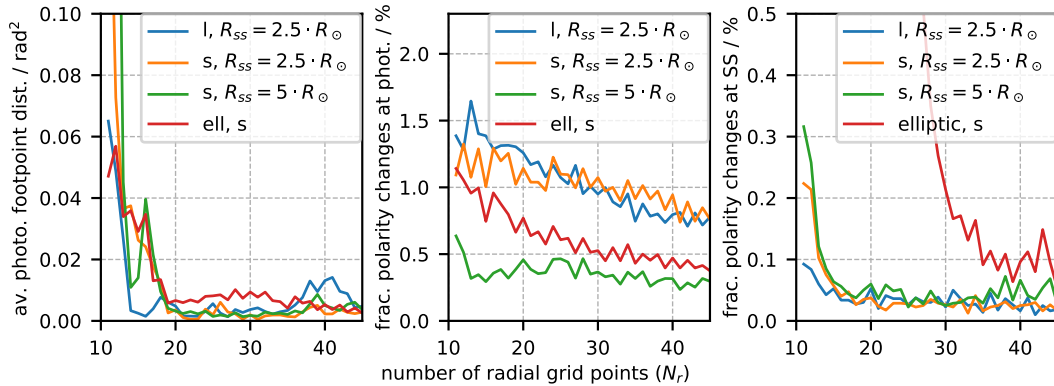


Figure 8: Left: Convergence of the average photospheric distance measure with increasing grid point density. Middle: Convergence of the photospheric polarity pixel measure with increasing grid point density. Right: Convergence of the source surface polarity pixel measure with increasing grid point density.

accuracy near the photosphere while simultaneously reducing the overall number of required grid points.

The computational parameters have been extensively evaluated utilizing several Carrington rotations, different relations between radial, meridional, and zonal grid point densities, other values for the geometric expansion factor  $q$ , and several ellipticities. In the following, four parameter sets are presented that illustrate the evaluation process. The first parameter set is the large grid derived in Sect. 5.1.1 and denoted by "l". A grid point distribution that achieves a good balance between computation time and convergence behavior for a wide range of ellipticities is defined by

$$N_r \times N_\theta \times N_\phi = N_r \times 2.5 \cdot N_r \times 5 \cdot N_r . \quad (65)$$

A grid adhering to this simple grid point distribution is called *small grid* and denoted by "s". This small grid is evaluated with source surface radii  $R_{ss} = 2.5 \cdot R_\odot$  and  $R_{ss} = 5 \cdot R_\odot$ . The last parameter set evaluates an oblate PFSS model on a small grid with an ellipticity of  $A = 2$  and with minimal source surface radius of  $R_{ss} = 2.5 \cdot R_\odot$ . The ellipticity parameter  $A$  is selected to be larger than a reasonable ellipsoidal PFSS model will likely require.

The evaluation procedure described in Sect. 5.1.2 was performed for the four parameter sets and an Michelson Doppler Imager (MDI) input magnetogram of Carrington rotation 2066 (during solar minimum in 2008). The results are illustrated in Fig. 8. Its left panel illustrates the average photospheric footpoint distance measure (step 10 from the list above), and its middle and right panel the polarity change measure at the photosphere and source surface, respectively (step 9 from the list above). As can be seen for most of the studied cases, an increase in grid point density above  $N_r = 20$  only results in minor deviations. Only for the ellipsoidal grid, there is an improvement of up to  $N_r = 35$  and only in the source surface polarity metric. For comparison, the sizes of solar granules and super-granules are about

1000 km and 30000 km [see, e.g., [Rast, 2003](#)] or an angular extent of 0.0014 rad and 0.043 rad, respectively.

Interestingly, the spherical [PFSS](#) model with the higher source surface radius converges faster than the other models. This is probably due to more space in the computational domain and lower gradients of the magnetic potential, thereby increasing numerical accuracy. That the ellipsoidal grid requires a higher grid point density is not surprising when analyzing the governing equations in Chapter 4, which have more terms and utilize information from more neighboring grid points.

To be able to use the same parameter set for both spherical and ellipsoidal implementations in subsequent studies, the grid point numbers selected as the optimal grid are  $N_r \times N_\theta \times N_\phi = 35 \times 87 \times 175$ , slightly more than half a million grid points. This ensures high numerical accuracy even for the ellipsoidal [PFSS](#) model with high ellipticities (see right panel of Fig. 7). The corresponding geometric expansion factor is  $q \approx 1.028$ .

## 5.2 PREPROCESSING OF INPUT DATA

The [PFSS](#) model requires line-of-sight magnetograms as input for the lower boundary at the photosphere. The number of grid points in the lowest grid shell ( $87 \times 175$ , see Sect.5.1.3) determines the required resolution of these magnetograms. The synoptic magnetograms have different resolutions depending on their origin. Therefore, an algorithm is required to match up the original magnetogram resolution with the resolution of the [PFSS](#) solver.

Due to the Sun's rotation axis' inclination with respect to the ecliptic, near-Earth instruments observe a slightly different portion of the solar surface changing with Earth's orbital position. This results in latitudinal coverage gaps near the poles in the magnetograms and near-polar pixels distorted by the inclined viewing angle.

This section describes the main preprocessing steps performed on the synoptic magnetograms to account for the necessity of rescaling the image data and the handling of unreliable data near the polar boundaries. The following is a brief overview of selected sources for photospheric synoptic magnetograms. The main characteristics are summarized in Table 1.

### 5.2.1 OVERVIEW OF SOLAR MAGNETOGRAPHS

One of the earliest magnetographs for long-term observations of the solar photospheric magnetic field was installed on the 150 ft tower of the Mount Wilson Observatory ([MWO](#)) in the early 1950s [[Babcock, 1953](#)]. The published synoptic magnetograms have a resolution of  $512 \times 971$  pixels and cover the entire solar disk, though data gaps are apparent near the poles in these images.

Another source is the [WSO](#) [[Duvall et al., 1977](#); [Scherrer et al., 1977](#)]. Their synoptic magnetograms have a low resolution of  $30 \times 72$  pixels, though data from this source is available since 1974. The coverage in polar direction goes to  $\sin(\text{latitude}_{\text{max}}) = 14.5/15.0 \approx 0.96667$  which converts to a maximum latitude of about  $75.2^\circ$ . The

low resolution allows for rapid computation of **PFSS** solutions and requires no pre-processing of the data (see Sect. 5.2.2). Data from the **WSO** was used in the initial tests for the new **PFSS** implementations presented in this work. Several other data products like the coefficients of the classical **PFSS** solver are kindly made available by the **WSO** staff, allowing the new solvers to be compared to established implementations. The coefficients produced by the newly implemented reference implementation (see Sect. 2.3) were compared with the coefficients published on the **WSO** webpage, and no relevant differences in the output data were found.

Another Earth-bound source of synoptic magnetogram data is the Global Oscillation Network Group (**GONG**) project group headed by the National Solar Observatory (**NSO**) [Harvey et al., 1996]. Six identical instruments were deployed all over the world to obtain continuous observation of the Sun. The project has been in operation since 1995, the resolution of produced synoptic magnetograms is  $180 \times 360$  and the maps cover a sine-latitude up to  $\sin(\text{latitude}_{\text{max}}) = 0.99999$ , or a latitude of approximately  $89^\circ$ .

Also operated by the **NSO** was the Kitt Peak Vacuum Tower Telescope (**KPVT**) [Livingston et al., 1976]. Magnetograms from this telescope have a resolution of  $180 \times 360$  and a latitudinal coverage up to the poles.

Due to the disturbances of the atmosphere, higher-resolution measurements need to be performed by spacecraft mounted observatories. The **MDI** instrument onboard Solar and Heliospheric Observatory (**SOHO**) was operated jointly by the W.W. Hansen Experimental Physics Laboratory and the Lockheed Palo Alto Research Laboratory [Scherrer et al., 1995]. It had a resolution of  $1080 \times 3600$  pixels, far more than the simple **PFSS** model requires. The meridional coverage reached  $\sin(\text{latitude}_{\text{max}}) = 539.5/540 = 0.99907$  which translates to a latitude of about  $87.5$  deg. The instrument was operated from 1996 to 2010.

Its successor, the Helioseismic and Magnetic Imager (**HMI**) onboard Solar Dynamics Observatory (**SDO**), operated by the same institutes [Scherrer et al., 2012] has an even higher resolution of  $1440 \times 3600$  pixels and a poleward coverage up to  $\sin(\text{latitude}_{\text{max}}) = 719.5/720 = 0.99931$  or a latitude of  $87.9$  deg. The instrument started operation in 2009 and is still in operation as of 2020. Because **MDI** and **HMI** are very similar instruments, and together they cover a period of over two solar cycles by now, most of the analyses presented in this work are based on these two instruments.

### 5.2.2 SCALING OF MAGNETOGRAMS

Magnetogram data serve as the boundary value at the lowest grid shell of the **PFSS** solver. Each grid point in that shell requires information from the magnetogram at its respective position. One approach is to define the grid point values by the pixels closest to them, also called nearest-neighbor scaling. This method discards information between the grid points. When shifting the grid slightly or changing the resolution, the values at the grid points might be altered substantially, thereby changing the algorithm's output. A robust magnetic peak, for example, might be missed by the first grid but recognized by a second, slightly shifted grid. Different

Instrument	Resolution (meridional x zonal)	Maximum latitude	Data available online
MWO (g)	512 × 971	90°	1981-2012
WSO (g)	30 × 72	75°	1974-
GONG (g)	180 × 360	89°	1995-
KPVT (g)	180 × 360	90°	1973-2004
MDI (s)	1080 × 3600	88°	1996-2010
HMI (s)	1440 × 3600	88°	2009-

Table 1: Comparision of different sources of synoptic magnetograms. The first column lists in parentheses next to the instrument acronym, if the measurement is performed on ground (g) or in space (s) outside the atmosphere. The operational column shows the time for which synoptic magnetograms are available online (as of November 2020), the instruments from which these are derived might have been operational for a longer duration.

model predictions for the same input data are not acceptable; therefore, a method must retain as much information as possible from the synoptic magnetogram.

Rescaling image data without losing information (or losing as little information as possible) is no trivial task, and there are many algorithms available, each with its advantages and shortcomings. One algorithm might be the right choice for one task while failing at another. This section focuses on the best choice for the scaling algorithm concerning the [PFSS](#) solvers described in this work.

The different scaling algorithms are not discussed in detail; for more information on their definitions and properties, several textbooks are concerned with image processing that explain these scaling methods and which algorithm to use for which purpose [see, e.g., [Burger and Burge, 2009](#); [Petrou and Petrou, 2010](#)]. The evaluation procedure is similar to the one presented in Sect. 5.1.2:

1. Compute the [PFSS](#) model with one resolution.
2. Note the footpoint positions of magnetic field lines.
3. Compute the [PFSS](#) model with the next highest resolution.
4. Note the new footpoint positions.
5. Calculate the average distance between the footpoint positions from steps 2 and 4.

Figure 9 shows this analysis' results for eight different scaling algorithms. The first two filters (*Down-Upsample* and *Supersampling*) were developed as part of this work, the other filters are frequently utilized by the image processing community. The first algorithm, *Down-Upsampling*, works as follows: Downscale to resolution 20x40, then upscale via bilinear interpolation to the desired resolution. This procedure ensures a smooth transition between resolutions, though it discards much information in that first downscale step.

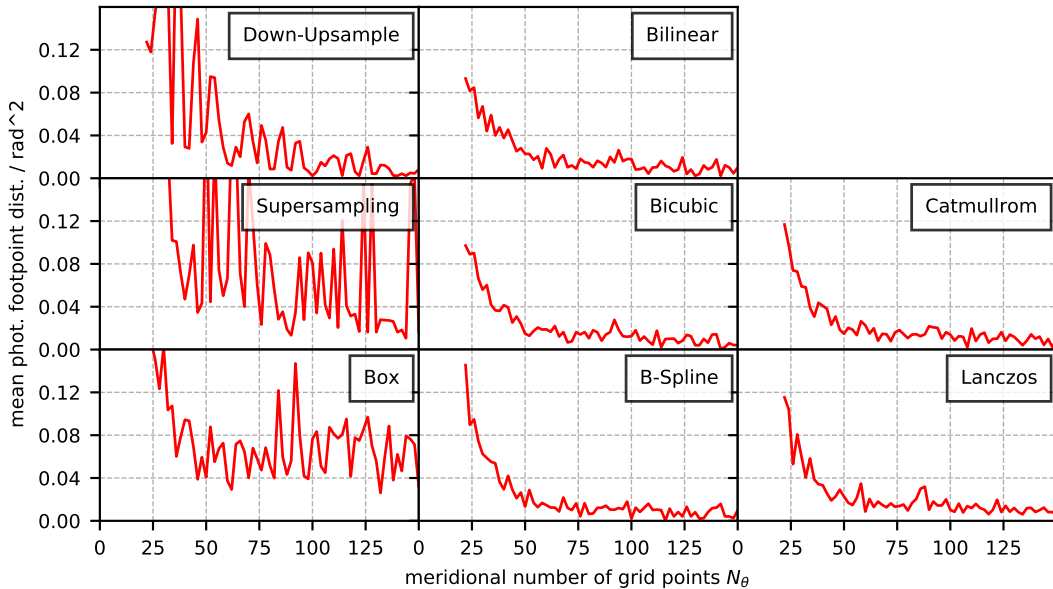


Figure 9: Impact of different scaling algorithms used on input magnetograms on the results of the [PFSS](#) solver. The solver worked on an [MDI](#) magnetogram for Carrington rotation 2048 (in 2006 during the declining solar activity phase near minimum).

The second algorithm, *Supersampling*, is a simple algorithm that determines the sizes and dimensions of the new pixels in the downsampled image and sums up the values of overlapping pixels in the original image weighted by the area they cover in the new pixel. The open-source library FreeImage (version 3.18, released July 31st, 2018) and its scaling methods have been utilized for all other algorithms. The algorithms can be found in FreeImage's documentation [[Drolon](#)] or in [Burger and Burge \[2009\]](#). All scaling algorithms in the FreeImage library have been invoked with their default parameters.

As can be seen from Fig. 9, all methods except the *Box* filter and the *Supersampling* filter result in a converging progression of photospheric footpoint distances with increasing magnetogram resolution. The *Lanczos* filter is selected as the default scaling algorithm for the new [PFSS](#) solver. Based on this analysis, its convergence is the fastest from all tested algorithms, though any algorithm except *Down-Upsample*, *Supersampling* and *Box* perform sufficiently.

Another problem with the input data aside from the scaling issue is posed by the pixels near the poles. Even though some synoptic magnetograms boast a coverage up to the solar poles (see Table 1), this information should be considered with caution. Due to the nature of solar observations (i.e., the observation point located in the ecliptic), photospheric positions near the poles have a large angle between the observation's line-of-sight and the radial orientation, which increases the uncertainty of the measurement (projection effect). Regions near the equator can be measured more reliably than regions near the poles. Therefore, the top-most and bottom-most pixel rows in the magnetograms contain the highest errors and data gaps due to the inclination of the solar rotation axis with respect to the ecliptic. Also, the ratio of grid point spacing in zonal direction to grid point spacing in meridional direction deviates further from 1 when incorporating high latitude

data (see Sect. 5.1.2), thereby potentially increasing numerical inaccuracies. To accommodate for all these shortcomings, only data points in the magnetograms up to a latitude of around  $80^\circ$  are used in the following analyses. This ensures that the utilized grid is centered around the solar equator and has the same configuration throughout the orbital cycle.

As Tóth et al. [2011] pointed out, using a sine-latitude grid comes with several disadvantages. However, rescaling the magnetograms would potentially introduce interpolation artifacts that might alter the produced results of the PFSS solvers (similar or even worse to the effect of scaling discussed in Sect. 5.3.1). This work focuses on depicting qualitative differences between several spherical/ellipsoidal solvers and not on the overall quality of the PFSS model itself; therefore, a rescaling of the magnetograms was not performed. In future studies, the difference between sine-latitude and latitude grids should be investigated further.

### 5.3 POSTPROCESSING OF MODEL OUTPUT DATA

The heliosphere's magnetic configuration is of particular interest for tracking solar wind packages to their photospheric origin. A straightforward approach is to perform a ballistic back mapping from an in-situ measurement on a spacecraft down to the source surface and then further down to the photosphere along magnetic field lines. More details on the ballistic back mapping method is presented in Chapter 6 and in Publications 2 (Sect. 6.5) and 3 (Sect. 7.3). This section discusses how to obtain magnetic field lines from the PFSS model output and describes a few data products derived from these.

#### 5.3.1 MAGNETIC FIELD LINE TRACKING

The new PFSS solver produces predictions of the magnetic field only at the grid point positions. To track the magnetic field lines in the computational domain (e.g., from the source surface down to the photosphere), the magnetic field's values at arbitrary positions between the grid points are required. Tri-linear interpolation on the numerical grid is applied to obtain these values, where the value is linearly interpolated along the three spatial directions consecutively. Two more involved methods are Spherical Linear Interpolation (SLERP) [Shoemake, 1985] and spline interpolation [Burger and Burge, 2009]. The grid employed for the PFSS implementations presented here has enough grid points, so the slightly increased interpolation accuracy does not warrant the increased computation time (see Sect. 5.3.2).

The tracking of field lines inside the numerical solver's computational grid is achieved by employing a 5th-order Runge-Kutta-Fehlberg method. Runge and Kutta developed the scheme today known as Runge-Kutta method for numerical analysis of ordinary differential equations [Runge, 1895]. The Runge-Kutta-Fehlberg method is an adaptive improvement over the Runge-Kutta methods [Fehlberg, 1969]. Because tracking magnetic field lines can be posed as an ordinary differential equation, this method has been chosen to compute magnetic field lines from the numerical grid solver.

If the distances between neighboring discrete positions on the magnetic field line were infinitesimally small, the magnetic field vector at one position would point to the next position. The goal is to employ an algorithm that best approximates this behavior. Starting from an arbitrary point  $\vec{r}_0$  in the computational domain, the magnetic field  $\vec{B}$  is followed to the next position  $\vec{r}_1$ . In this case the ordinary differential equation describes the parametric curve of the magnetic field line, where  $\vec{r}(s)$  is the cartesian position on the curve,  $s$  is the independent variable and  $\partial \vec{r} / \partial s = \vec{B}(\vec{r})$  is the tangential along the curve. Let  $\vec{r}_i$  be some position on the magnetic field line. The procedure to find the next position  $\vec{r}_{i+1}$  is as follows:

The *minimum step size*  $h_{\min}$  of the algorithm is defined as a tenth of the smallest distance in the numerical grid. Because of the tri-linear interpolation between the grid points, the algorithm does not need a small step size like this at most locations, but keeping it small allows for steep gradients to be computed accurately. Because the algorithm is adaptive, it will choose to use a larger step size almost everywhere. *Intermediate directions*  $\vec{k}_j$  ( $j \in \{1, 2, 3, 4, 5, 6\}$ ) are defined by

$$\begin{aligned}\vec{k}_1 &= h \vec{B}(\vec{r}_i), \\ \vec{k}_2 &= h \vec{B}\left(\vec{r}_i + \frac{1}{4} \vec{k}_1\right), \\ \vec{k}_3 &= h \vec{B}\left(\vec{r}_i + \frac{3}{32} \vec{k}_1 + \frac{9}{32} \vec{k}_2\right), \\ \vec{k}_4 &= h \vec{B}\left(\vec{r}_i + \frac{1932}{2197} \vec{k}_1 - \frac{7200}{2197} \vec{k}_2 + \frac{7296}{2197} \vec{k}_3\right), \\ \vec{k}_5 &= h \vec{B}\left(\vec{r}_i + \frac{439}{216} \vec{k}_1 - 8 \vec{k}_2 + \frac{3680}{513} \vec{k}_3 - \frac{845}{4104} \vec{k}_4\right), \text{ and} \\ \vec{k}_6 &= h \vec{B}\left(\vec{r}_i - \frac{8}{27} \vec{k}_1 + 2 \vec{k}_2 - \frac{3544}{2565} \vec{k}_3 + \frac{1859}{4104} \vec{k}_4 - \frac{11}{40} \vec{k}_5\right),\end{aligned}$$

where  $h$  is the current step size. The  $(i+1)$ st position along the magnetic field line is given by the 4th and 5th-order Runge-Kutta methods as

$$\begin{aligned}\vec{y}_{i+1} &= \vec{r}_i + \frac{25}{216} \vec{k}_1 + \frac{1408}{2565} \vec{k}_3 + \frac{2197}{4104} \vec{k}_4 - \frac{1}{5} \vec{k}_5 \text{ and} \\ \vec{z}_{i+1} &= \vec{r}_i + \frac{16}{135} \vec{k}_1 + \frac{6656}{12825} \vec{k}_3 + \frac{28561}{56430} \vec{k}_4 - \frac{9}{50} \vec{k}_5 + \frac{2}{55} \vec{k}_6,\end{aligned}$$

respectively. The *discretization error* is given by the difference between the predicted positions of the Runge-Kutta methods of order four and five as

$$e = |\vec{z}_{i+1} - \vec{y}_{i+1}|.$$

If  $e_{\min} \leq e \leq e_{\max}$ , the step size  $h$  is adequate depending on the chosen *error boundaries*  $e_{\min}$  and  $e_{\max}$ , and the next point along the magnetic field line is

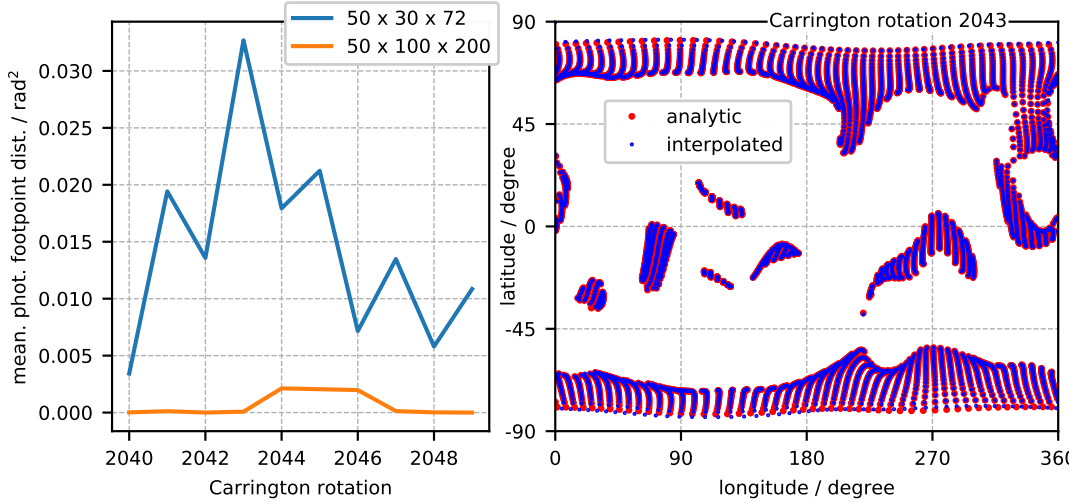


Figure 10: Left panel: Averaged photospheric footpoint distance between analytic and interpolated magnetic field line tracking for two numeric grid resolutions. MDI magnetograms were used for this analysis. Right panel: Photospheric magnetic field line footpoint positions tracked analytically (red) and via interpolation (blue). The depicted footpoints are obtained from the small grid with  $50 \times 30 \times 72$  grid points and during Carrington rotation 2043, the worst solution in the left panel.

chosen to be  $\vec{r}_{i+1} = \vec{z}_{i+1}$ . The values  $e_{\min} = 1$  m and  $e_{\max} = 100$  m are supplied to the algorithm, which are strict limits resulting in both methods to give roughly the same position. Because of the vast extent of the computational domain, this ensures the algorithm is performing near the maximum floating-point accuracy. If  $e < e_{\min}$ , the step size can be increased by  $h \rightarrow 2 \cdot h$ . If  $e > e_{\max}$ , the algorithm does not work accurately enough and the step size has to be reduced by  $h \rightarrow h/2$ , provided  $h > h_{\min}$ .

This adaptive step size allows fast computation of magnetic field lines without sacrificing accuracy, which would be necessary when using the Runge-Kutta method with a fixed step size. It also permits the algorithm to decrease step sizes in regions of steep magnetic gradients (mostly near the photosphere) while using huge steps near the source surface, where the magnetic field does not change very much. (Renderings of magnetic field lines obtained with this method can be found in the first row of Fig. 11.)

### 5.3.2 INTERPOLATION ACCURACY

The SHC approach (see Sect. 2.3) gives an elegant handle to test the tri-linear interpolation scheme's accuracy. When the Runge-Kutta-Fehlberg method requests the magnetic field orientation at some position, the SHC solver returns an analytically derived value at that position via Eqs. 12 to 14. Alternatively, the analytical expressions may be evaluated at the grid points, and magnetic field values requested at arbitrary positions can be obtained by employing the interpolation scheme between these grid points.

Fewer grid points produce more inaccurate interpolation values, therefore a more coarse grid than the one established in Sect. 5.1.2 was employed for evaluating interpolation accuracy. The grid for this investigation has  $50 \times 30 \times 72$  grid points with equidistant radial spacing. The left panel of Fig. 10 shows the averaged squared photospheric angular distance of all field lines between analytical and interpolated tracking for several Carrington rotations. The same analysis was performed with a much denser grid of  $50 \times 100 \times 200$  grid points. The right panel depicts the photospheric footpoint positions of tracked magnetic field lines for both analytical and tri-linear interpolation tracking for Carrington rotation 2043 and the low grid resolution  $50 \times 30 \times 72$ . As can be seen, the tri-linear interpolation scheme differs only slightly from the analytical scheme, even for the coarse grid. More advanced interpolation schemes are therefore not necessary.

### 5.3.3 POLARITY MAPS

A simple yet effective way of visualizing the magnetic configuration is to obtain two-dimensional cuts through the domain of interest and produce images that resemble the two-dimensional map's configuration. While, in principle, the three components of the magnetic field can be visualized separately in three individual images, the polarity of magnetic field lines holds much information on the magnetic configuration (e.g., the current sheet's position on the source surface). The procedure is as follows. A spherical or ellipsoidal surface is spanned in the PFSS solver's computational domain between the photosphere and the source surface. The map's pixels in the meridional direction are distributed in a sine-latitude format similar to the solver's grid point distribution. Distances between the pixels in zonal direction are equidistant. The maps presented here typically have a resolution of  $200 \times 400$  pixels. At each pixel position a magnetic field line is spawned and traced throughout the computational domain to its endpoints. Field lines can be either open (i.e., one endpoint is on the photosphere and the other on the source surface) or closed (i.e., both endpoints lie on the photosphere). The open field lines can be further categorized as positive or negative field lines, depending on the magnetic field's direction at their endpoints. The field lines' types are then color-coded in their respective pixels and presented as a two-dimensional map. Columns 2 and 3 of Fig. 11 illustrate the polarity maps at the photosphere and the source surface.

### 5.3.4 EXPANSION FACTOR MAPS

The *flux-tube expansion factor*  $f_s$  is a measure of how strong the magnetic expansion deviates from the square-cube law. A factor  $f_s = 1$  implies a *radial* expansion, magnetic configurations with  $f_s > 1$  are designated *super-radial*, and  $f_s < 1$  stands for a *sub-radial* expansion. The flux-tube expansion factor has been related to the

solar wind speed [Wang and Sheeley, 1990] and is easily computed from the output of the PFSS implementations presented here. It is defined as

$$f_s = \frac{B_\odot R_\odot^2}{B_{ss} R_{ss}^2} \quad (66)$$

where  $B_\odot$  and  $B_{ss}$  are the magnetic field strengths and  $R_\odot$  and  $R_{ss}$  are the heliocentric distances of the photosphere and the source surface, respectively. The flux-tube expansion factor can be computed and presented in the same way as the polarity maps discussed in Sect. 5.3.3: Every pixel in a two-dimensional map spawns a magnetic field line that can be traced throughout the computational domain. The endpoints of these magnetic field lines can then be used to compute the flux-tube expansion factor according to Eq. 66 and the pixel of the map colored accordingly. The expansion factor maps of the photosphere and the source surface are depicted in columns 4 and 5 of Fig. 11, respectively.

### 5.3.5 VISUALIZATION OF MODEL PREDICTIONS

The model output data products discussed in the sections above are visualized for four example model parameters in Fig. 11. All models depicted use a minimum source surface radius  $r_{ss} = 2.5 \cdot R_\odot$ . A synoptic magnetogram from MDI and Carrington rotation 2066 was employed to demonstrate the computed data products. The first and second row illustrate the output of the reference SHC solver with maximum principle orders 9 and 35, respectively. The third row depicts the output of the new semi-numerical PFSS solver with a spherical source surface and the last row shows the situation for an ellipsoidal source surface with ellipticity  $A = 2$ . The first column contains a rendering for all models using the method described in Sect. 5.3.1. The rendering in the ellipsoidal row is zoomed out to fit in the figure. Blue field lines are pointing anti-sunward, red field lines are pointing sunward, and cyan field lines are closed. In the second and third columns, polarity maps of the photosphere and source surface are depicted according to Sect. 5.3.3. The color scheme is the same as in the renderings in column one. The fourth and fifth columns illustrate the fluxtube expansion factor maps at the photosphere and the source surface discussed in Sect. 5.3.4. The expansion factor maps are colored according to the color bar at the figure's bottom.

## 5.4 COMPARING IMPLEMENTATIONS

As part of this work, three distinct implementations have been developed: The SHC solver (see Sect. 2.3), a semi-numerical purely spherical solver (see Chapter 3) and a semi-numerical solver with ellipsoidal source surfaces (see Chapter 4). The SHC solver output (i.e., the table of harmonic coefficients  $g_{lm}$  and  $h_{lm}$ ) has been compared to the coefficients published on the WSO website and found to be identical within machine accuracy. Similarly, the ellipsoidal solver output with a spherical source surface ( $A = 1$ ) has been compared with the purely spherical solver's output, and the results are also the same.

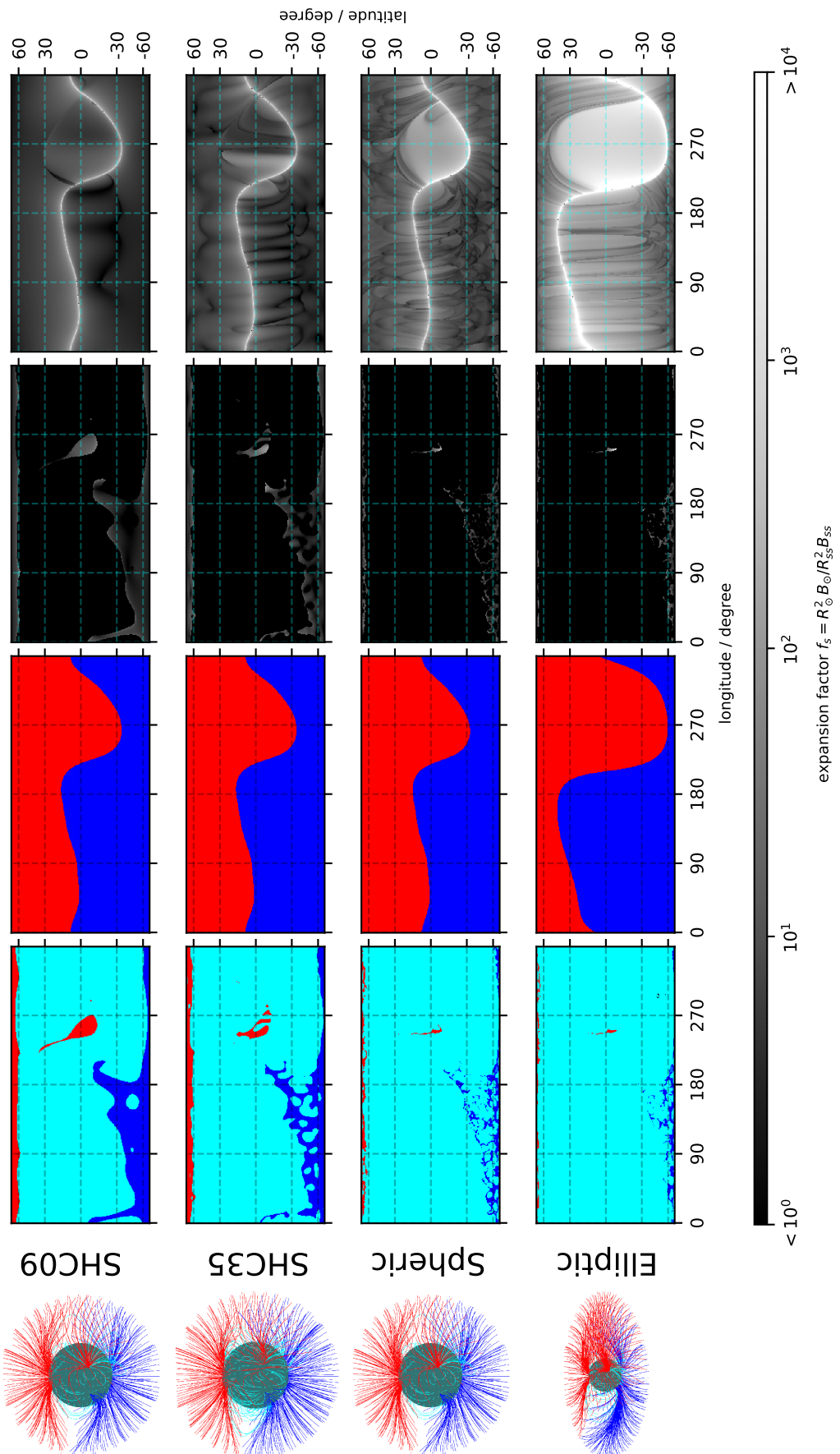


Figure 11: Explanation can be obtained from the main text.

Increasing the maximum principal order of the [SHC](#) solver allows for a better fit of the coronal magnetic field to the supplied photospheric magnetogram. Figure 12 illustrates how increasing the maximum order changes the magnetic polarity at the source surface and the photosphere. [SHC PFSS](#) solutions for both [WSO](#) and [MDI](#) show no polarity changes at the source surface beyond a maximum principle order of 12. At the photosphere, increasing the maximum principle order beyond 20 still improves prediction accuracy with the [WSO](#) magnetogram benefiting more than [MDI](#).

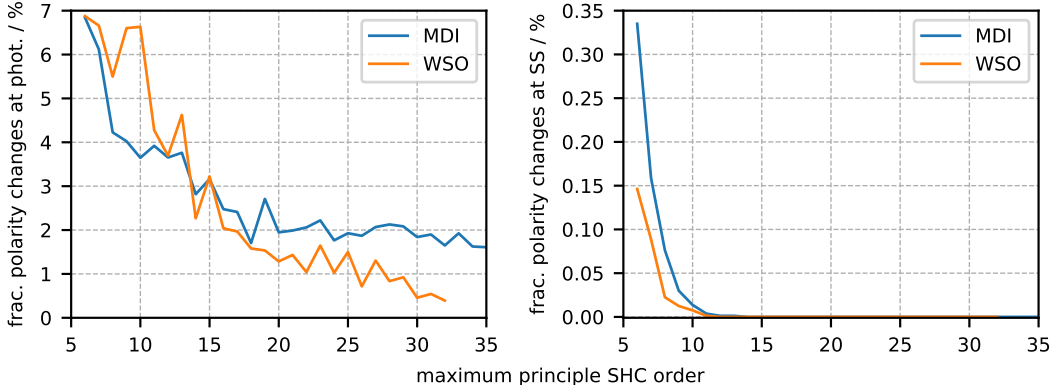


Figure 12: Convergence for the maximum principle order of the [SHC](#) solver. The computational grid for this analysis has  $35 \times 87 \times 175$  grid points. [WSO](#) and [MDI](#) magnetograms for Carrington rotation 2066 were analyzed. Left panel: Photospheric polarity change measure. Right panel: Source surface polarity change measure.

Four different [PFSS](#) models are compared in Fig. 11, two [SHC](#) models with principle orders 9 and 35, a spherical source surface model computed with the new semi-numerical implementation, and an ellipsoidal source surface model using the same solver. As can be seen in this figure, the source surface polarity map (column three) for the [SHC](#) implementations (rows one and two) and the semi-numerical implementation (row three) are very similar. Contrarily, the photospheric polarity map (column two) shows structural differences. As is expected, the [SHC](#) implementation is capable of resolving a finer structure if a higher maximum principle order is used. This is even more apparent in the source surface expansion map (column five). The [SHC](#) model with principle index 35 shows more features than with principle index 9, and the semi-numerical implementation shows more features than both the [SHC](#) models. An interpretation of the ellipsoidal source surface model output is more complex and has been performed in Publication 1 (Sect. 5.5). Details about the specific implementations running on Central Processing Units ([CPUs](#)) and Graphics Processing Units ([GPUs](#)) as well as run time measurements and speedup are discussed in Appendix A.

## 5.5 PUBLICATION 1

Despite the relative simplicity of both the [PFSS](#) model and the computational tool of finite differences, a specific implementation harbors several pitfalls. Besides the apparent error source of translating the lengthy mathematical expressions derived in Sect. 4.4 into machine-readable code, there are a lot of minor sources of ambiguities

and uncertainties, such as the interpolation scheme used for scaling magnetograms (Sect. 5.2.2) and the selection of a finite differencing scheme at the computational boundaries (Sect. 3.3). A comparison with other implementations that have been used and vetted by the scientific community is necessary to show that all these minor error sources have been accounted for during the development process.

A particular focus of this study was the careful implementation of the ellipsoidal PFSS solver because, as of the time of writing this thesis, there are no existing reference implementations to compare to as can be done with the spherical reference solver. The first sanity check compares the ellipsoidal solver results with a spherical surface, that is, the special case of the ellipticity parameter between oblate and prolate surfaces ( $A = 1$ ), to the reference implementation of the spherical PFSS model.

A comparison of the predicted magnetic fields at various heights of the grid solver presented here with the decade-old spherical harmonic function solver by [WSO](#) [Hoeksema, b] has been performed. The same comparison has been drawn between the predicted magnetic fields for different ellipsoidal parameters of the grid solver to illustrate the impact of using ellipsoidal source surfaces. The results have been published in:

**AN ELLIPTIC EXPANSION OF THE POTENTIAL FIELD SOURCE SURFACE MODEL**

M. Kruse, V. Heidrich-Meisner, R. F. Wimmer-Schweingruber and M. Hauptmann, *A&A*, A109, 638, 2020, reproduced with permission © ESO.

DOI: [10.1051/0004-6361/202037734](https://doi.org/10.1051/0004-6361/202037734)

Own contribution: 90%

### *Summary*

A brief overview of the classical PFSS model paradigm is followed by discussing some of its shortcomings, especially the constraint of the source surface to be spherical. It is described why ellipsoids have the potential to be a better choice for source surfaces. A short section explains the mathematical framework of the PFSS model and its most widely employed implementation utilizing an analytical approach by employing spherical harmonic functions. The following section briefly explains the grid solver approach developed here and the parameters used for the following illustration of characteristics. The results section illustrates the similarities between the spherical grid solver and the classical PFSS implementation by the [WSO](#) and differences between the oblate and prolate source surfaces. The comparison metrics are magnetic polarity images of different height levels in the computational domain (i.e., between photosphere and source surface) and depictions of the magnetic expansion factor at the same levels. The key findings can be summarized as follows:

- The presented spherical grid solver and the reference implementation by the [WSO](#) are in good agreement near the source surface.
- The grid solver allows for more details to be visible near the photosphere.

- Visualizations of the magnetic field configuration illustrate differences between the spherical, oblate ellipsoidal, and prolate ellipsoidal implementations.

# An elliptic expansion of the potential field source surface model

M. Kruse<sup>1</sup>, V. Heidrich-Meisner<sup>1</sup>, R. F. Wimmer-Schweingruber<sup>1</sup>, and M. Hauptmann<sup>2</sup>

<sup>1</sup> University of Kiel, Institute for Experimental and Applied Physics, Leibnizstr. 11, 24118 Kiel, Germany  
 e-mail: kruse@physik.uni-kiel.de

<sup>2</sup> University of Kiel, Department of Mathematics, Ludewig-Meyn-Str. 4, 24118 Kiel, Germany

Received 14 February 2020 / Accepted 19 March 2020

## ABSTRACT

**Context.** The potential field source surface model is frequently used as a basis for further scientific investigations where a comprehensive coronal magnetic field is of importance. Its parameters, especially the position and shape of the source surface, are crucial for the interpretation of the state of the interplanetary medium. Improvements have been suggested that introduce one or more additional free parameters to the model, for example, the current sheet source surface model.

**Aims.** Relaxing the spherical constraint of the source surface and allowing it to be elliptical gives modelers the option of deforming it to more accurately match the physical environment of the specific period or location to be analyzed.

**Methods.** A numerical solver is presented that solves Laplace's equation on a three-dimensional grid using finite differences. The solver is capable of working on structured spherical grids that can be deformed to create elliptical source surfaces.

**Results.** The configurations of the coronal magnetic field are presented using this new solver. Three-dimensional renderings are complemented by Carrington-like synoptic maps of the magnetic configuration at different heights in the solar corona. Differences in the magnetic configuration computed by the spherical and elliptical models are illustrated.

**Key words.** Sun: magnetic fields

## 1. Introduction

The Sun's coronal magnetic field configuration is an important component in understanding the physics of the heliosphere and the solar dynamo. Due to the vast extent of the heliosphere, a direct measurement of its global structure is not possible. Therefore, computational modeling tools are employed to approximate its structure. Modern high-accuracy algorithms, like full magnetohydrodynamic (MHD) solvers, compute a vast set of physical phenomena and require significant computing power. These models rely on additional modeling assumptions that are difficult to verify and on boundary conditions that have to be modeled because they cannot be observed directly.

Simpler models exist that produce less precise results, but that can be computed orders of magnitude more quickly. For some scientific efforts like long-running data evaluation tasks, for example characterizing solar wind streams, rapid computation of the heliospheric magnetic field over long periods is crucial, while the overall accuracy can be lower without affecting the large-scale results of these studies.

One of the earliest models that was used to model the solar coronal magnetic field is the potential field source surface (PFSS) model (Altschuler & Newkirk 1969; Schatten et al. 1969). A brief description of this model is presented in Sect. 2.2. The PFSS model returns an analytic expression that allows us to predict the magnetic field configuration of the Sun between the photosphere and a virtual spherical surface, called the source surface, at a height of a few solar radii in the corona. The boundary condition for the PFSS model is that all magnetic field lines have to be oriented radially at the source surface, which is in accordance with observations farther out in the heliosphere.

An improved version of this model is the current sheet source surface (CSSS) model (Zhao & Hoeksema 1995), which adds a second virtual sphere, the cusp surface, between the photosphere and source surface. Above this surface, all magnetic field lines are required to be open, but do not have to be oriented radially. This allows more freedom when modeling the magnetic field.

Slightly more sophisticated models build upon the force-free approach which neglects external forces on a restricted domain near the solar surface. The most general group of these models are the nonlinear force-free models (Aly 1989; Wiegemann 2008). Simplifying this physical model by assuming a current-free domain in addition to it being force-free leads to the PFSS model that allows the extrapolation of the coronal magnetic field using only the line-of-sight component of the photospheric magnetic field configuration (also called a synoptic magnetogram). The photospheric magnetograms can be obtained from direct observations and the procedure has been applied for many decades. While the PFSS model itself makes more simplifying assumptions than the full MHD approach, it relies less on modeled parameters, which can potentially introduce false or inaccurate assumptions to the model.

The assumption that the source surface is spherical simplifies the mathematical framework as well as the computations significantly. Without hints as to exactly what the source surface looks like, as well as a lack of computing power back when this model was created, the only reasonable starting point was to assume a spherical source surface. Also, the very low resolution of available magnetic observations of the photosphere at that time made more accurate model assumptions meaningless.

Since then, several suggestions have been made that question the merit of the spherical source surface. Schulz et al. (1978), Schulz (1997) have developed an algorithm to alter the shape

of the source surface. They proposed surfaces of constant magnetic flux (isogauss) to function as the source surface, and presented a model with a surface that has greater heights above the poles compared to the equator. In this model the free parameter of the PFSS model (the source surface height  $R_{ss}$ ) is substituted for the constant magnetic flux  $B_0$  of the isogauss surface, which is determined by a hypothetical solar internal dipole and the constraint of magnetic field lines to be normal to this surface. The strategy behind this approach is to better match field lines to the predictions of an MHD implementation that produces field lines that are not quite radially oriented at the height of the spherical source surface.

Expanding on this idea Levine et al. (1982) proposed a non-spherical source surface that is determined by three free parameters, the mean height and two parameters defining the shape. Levine et al. (1982) also deviated from the constraint of magnetic field lines that are strictly perpendicular to the source surface, and compared the orientation of computed field lines to total solar eclipse observations.

Riley et al. (2006) computed isosurfaces of  $B_r/|\mathbf{B}| = 0.97$  by employing a magnetohydrodynamic solver and found shapes that resemble prolate spheroids with indentations at the poles. While these isosurfaces do not constitute the source surface, they illustrate the deviation of the magnetic field configuration from spherical symmetry.

The spherical source surface is the simplest assumption and it allows fast computation of the solar magnetic field. However, observations show that the physical conditions of the outer solar coronal plasma depend on longitude as well as latitude, and that polar regions exhibit a more radial orientation of the magnetic field than at the equator (see, e.g., McComas et al. 1998). An oblate elliptical source surface creates a magnetic field that is consistent with this observation, as is discussed in Sect. 2.4.

In the past decades the increase in computing power and space-bound magnetic field observations, have given rise to more intricate models. MHD solvers have allowed a wider array of physical phenomena to be incorporated into the derivation of the solar magnetic field. While potentially more accurate, these models require a larger set of input parameters and model assumptions that are difficult to verify with current observations. The simplicity of the PFSS model allows calculating the rough structure of the solar magnetic field comparably quickly. It is therefore desirable to improve this simple model without adding the complexity of a full MHD approach.

In this work we suggest modifying the classical PFSS model to incorporate elliptical source surfaces. This increases the number of free parameters from one (the source surface height  $R_{ss}$ ) to two (adding the ellipticity or deviation from sphericity of the source surface  $A$ ). In contrast to the approaches mentioned above, we chose to implement a finite difference solver rather than an analytical solver. This allows easier adjustments of the utilized source surface and gives us the possibility to increase solution accuracy by adding more grid points to regions of strong magnetic gradients. We hope that this minor adjustment aids in the modeling of the large-scale structure of the solar magnetic field more accurately and gives insight into the reliability of the PFSS model for different stages of the solar activity cycle.

Evaluating the validity and accuracy of the various existing models is a field of study of its own. Since the phenomena in question cannot be recreated in their entirety in a laboratory environment, the scientific community is forced to browse sparsely available spacecraft data to look for indicators of correctness or lack thereof. In this work we focus on presenting alterations to the classical PFSS model and the computational results produced

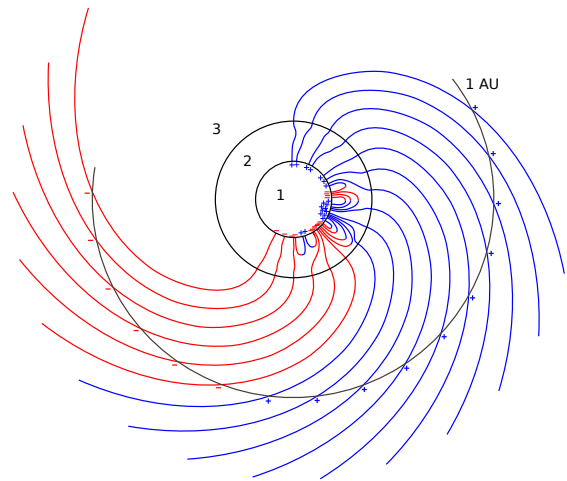


**Fig. 1.** Three regions underlying the PFSS model: region 1 is the inside of the Sun, region 2 is the computational domain between the photosphere and the source surface, and region 3 is the interplanetary space where the solar wind flows radially outward. Figure adapted from Schatten et al. (1969).

by them. In Sect. 4 we discuss options of evaluating the results produced by the different PFSS models.

## 2. Methods

The PFSS model is often used to investigate the link between the interplanetary medium and the solar surface. Because of its simplicity it has strengths and weaknesses, which we investigate here by implementing three different versions of the PFSS. In Sect. 2.1 we give a brief summary of the mathematical framework underlying all the implementations. The first implementation recreates the framework developed by Zhao & Hoeksema (1993) so that subsequent alterations to the model can be compared to a version that has been thoroughly evaluated. This classical implementation is briefly described in Sect. 2.2. We created an implementation of this approach and call it the spherical harmonic coefficient (SHC) version. The second version is a numerical finite differences solver that solves Laplace's Equation (Eq. (1)) on several grid points throughout the computational domain of the PFSS model and is described in Sect. 2.3. The third version is an alteration of the second; it allows for an elliptical source surface and is described in Sect. 2.4. A summary of our treatment of input data as well as the parameters for the computational solver are presented in Sect. 2.5.

### 2.1. The PFSS model

Altschuler & Newkirk (1969) and Schatten et al. (1969) independently proposed a magnetostatic model for the solar corona. They partition the domain of interest into three regions (Fig. 1).

Employing several instruments the magnetic field can be measured at the photosphere, which is the boundary separating regions 1 and 2. Region 2 is the computational domain of the PFSS model. The boundary between regions 2 and 3 is called the source surface. Above the source surface, the solar wind dominates the magnetic field configuration (region 3). At least during the quiet times of the solar activity cycle, and aside from violent

eruptions, the Sun's photosphere displays features that persist for several Carrington rotations. Therefore, in a first approach the lower region of the solar corona (region 2) can be assumed to be electrostatic, or  $\frac{\partial \mathbf{E}}{\partial t} = \mathbf{0}$ . Furthermore, it is assumed that due to the sharp decrease in particle density above the photosphere and with a smaller decrease in magnetic field strength, the electric current density can be neglected to some point, or  $\mathbf{j} = \mathbf{0}$ . Ampère's law then states

$$\nabla \times \mathbf{B} = \mu_0 \left( \mathbf{j} + \epsilon_0 \frac{\partial \mathbf{E}}{\partial t} \right) = \mathbf{0},$$

where  $\mathbf{B}$  is the magnetic flux density,  $\mathbf{E}$  is the electric field,  $\mathbf{j}$  is the electric current density and  $\mu_0$  and  $\epsilon_0$  are the permeability and permittivity of free space, respectively.

A curl-free vector field can be described as the gradient of a scalar potential ( $\nabla \times \nabla f = \mathbf{0}$  for twice the continuously differentiable  $f$ , the curl of a gradient vanishes everywhere). Therefore, we write  $\mathbf{B} = -\nabla\Psi$ , where  $\Psi$  is the scalar magnetic potential. Gauss's law then states

$$\nabla \cdot \mathbf{B} = -\nabla \cdot \nabla\Psi = -\Delta\Psi = 0. \quad (1)$$

Equation (1) can be integrated within region 2, given two boundary conditions, one at the photosphere and one at the source surface. At some height the solar wind carries the magnetic field outward, where it is said to be frozen in. The solar wind is advected outward radially, so at the source region of this flow, the magnetic field lines have to be aligned radially as well. Therefore the upper boundary condition is given by the restriction of the magnetic field lines to be perpendicular to the source surface (Neumann boundary condition). For the lower boundary, the photosphere, the magnetic field configuration is known and is supplied to the algorithms by synoptic (line of sight) magnetograms; therefore, a Dirichlet boundary condition is applied.

For the lower boundary condition, two main approaches are employed regularly by the scientific community, called the radial approach and the line-of-sight approach (Wang & Sheeley 1992; Altschuler & Newkirk 1969). Due to its simplicity and the widespread availability of data for comparison, we employ the radial approach for this study.

## 2.2. Spherical harmonic coefficient implementation

The mathematical framework for the approach to model the solar coronal magnetic field using spherical harmonic coefficients and associated Legendre polynomials can be found in Altschuler & Newkirk (1969) and Chapman & Bartels (1940). All that is necessary to recreate the magnetic field is an implementation of the associated Legendre polynomials  $P_l^m$  as well as the computed harmonic coefficients  $g_{lm}$  and  $h_{lm}$  (for explanations of these symbols, see Chapman & Bartels 1940). The magnetic field configuration at any point in region 2 of the PFSS model can then be acquired by evaluating an analytic expression (see, e.g., Eqs. (8)–(10) in Altschuler & Newkirk 1969).

Today the harmonic coefficients are computed by several groups, including the John M. Wilcox Solar Observatory at Stanford University (Zhao & Hoeksema 1993) and published on their website (Hoeksema 2020). We used synoptic magnetograms from the Wilcox Solar Observatory (Duvall et al. 1977) and compared the results from the Stanford PFSS implementation with our own. Within floating-point precision, our SHC solver produces the same coefficients as published by Stanford.

## 2.3. Grid approach

Instead of fitting the observed photospheric magnetograms to spherical harmonic functions, we have developed a numeric solver that works on a three-dimensional grid and employs finite differences. This allows us to deform the grid in other implementations to incorporate elliptical source surfaces, while also giving us a tool to compare our results with the implementations of other groups.

The computational grid stretches from the photosphere (at  $r = R_\odot$ ) to the source surface in the radial direction, from the northern boundary supplied by the magnetogram to the southern boundary in the meridional direction and around the sphere in the zonal direction without boundaries. Grid spacing is equidistant in zonal direction and follows a sine-latitude distribution in meridional direction, as do the underlying synoptic magnetograms. In the radial direction spacing between grid points increases from the photosphere to the source surface geometrically (see Sect. 2.5 for more details).

The solution method is an explicit time-stepping algorithm that solves Laplace's Eq. (1) at each grid point for the potential field  $\Psi$ . This is done by evaluating the analytic expression utilizing finite differences and solving for the magnetic potential  $\Psi_{ijk}$ , where  $i$ ,  $j$ , and  $k$  denote the radial, meridional, and zonal position in the numerical grid, respectively.

In the initial state, the potential field is set to zero at each grid point except the lowest grid shell which is derived from the synoptic line-of-sight magnetograms. The potential at the uppermost grid shell (at the source surface,  $r = R_{ss}$ ) is kept constant throughout the iteration process, thus implementing the radial boundary condition at the source surface. The potential at each grid point is stored and compared to that obtained in the following time step. Let  $\Psi_{ijk}^t$  denote the magnetic potential at position  $i$ ,  $j$ ,  $k$  in time step  $t$ , and  $\Psi_{ijk}^{t-1}$  the potential computed in the previous time step. The algorithm terminates if the maximum relative deviation to the previous time step at all grid points drops below a specified accuracy threshold  $p$ , or

$$\max_{ijk} (e_{ijk}) = \max_{ijk} \left( \frac{|\Psi_{ijk}^t - \Psi_{ijk}^{t-1}|}{|\Psi_{ijk}^t|} \right) < p. \quad (2)$$

The numerical grid solver produces nearly the same polarity configuration at the source surface as the SHC implementation. Closer to the photosphere the numerical solver can resolve a finer structure than the SHC solver, which is discussed in Sect. 3.

## 2.4. Grid approach with an elliptic source surface

Ideally, an accurate algorithm for the computation of the solar magnetic field would accommodate arbitrary heights of the source surface at every longitudinal and latitudinal position. We propose a small step in this direction by implementing an ellipsoidal source surface controlled by a single parameter  $A$ . An oblate source surface in the PFSS model creates a magnetic field that reaches radial orientation closer above the poles compared to equatorial regions, as can be seen in the renderings in Figs. 2–5. Let  $R_{ss}$  be the source surface height of the classical PFSS model. The actual source surface height  $r_{ss}$  in our model is given by

$$\begin{aligned} \text{oblate case : } & r_{ss,\text{equator}} = A \cdot R_{ss} \\ & r_{ss,\text{poles}} = R_{ss} \\ \text{prolate case : } & r_{ss,\text{equator}} = R_{ss} \\ & r_{ss,\text{poles}} = A \cdot R_{ss}. \end{aligned}$$

As the Sun still needs to be approximated as a sphere, we cannot simply employ a homogeneous elliptical grid. Hence, we created a grid that exhibits spherical symmetry at the photosphere while incrementally deforming higher grid shells to the ellipsoidal shape. A brief explanation of the grid is summarized in Appendix A.

The elliptical implementation works in the same manner as the spherical one by repeatedly solving Laplace's equation at all grid points until the accuracy threshold  $p$  is surpassed at all grid points (see Eq. (2)).

Magnetic field lines are oriented perpendicular to the source surface, which defines an isopotential. In the spherical case, this means field lines are already oriented radially. To obtain the radial orientation of the magnetic field lines in the elliptical model, a spherical surface can be positioned above the source surface, and some form of interpolation technique, for example employing splines, can be applied to "bend" the magnetic field lines into the radial orientation.

### 2.5. Parameters for the grid solver and treatment of input magnetograms

For all model evaluations we employ a source surface at a heliocentric height of  $2.5R_{\odot}$  (minor half-axis in the elliptical version). As input data, we used synoptic magnetograms from the Wilcox Solar Observatory for testing purposes and comparisons with data products published by Hoeksema (2020). Because the resolution of these maps is low, no image processing needs to be applied. For high-resolution grid tests and for the plots presented in this work we employed synoptic magnetograms from the Michelson Doppler Imager (MDI) on board the Solar and Heliospheric Observatory (SOHO; Scherrer et al. 1995). The high-resolution synoptic magnetic maps produced by MDI are scaled down to  $87 \times 175$  pixels using a Lanczos filter. In a second step these magnetograms are corrected for the monopole offset which is introduced by small changes of the photospheric magnetic field during the data acquisition period of about 27 days and for data gaps near the poles.

A well-known difficulty of numerical models is the trade-off between high accuracy and computational demand. After systematically testing and comparing results of several distributions and densities of grid points we chose our numerical grid to have  $35 \times 87 \times 175$  grid points in radial, meridional, and zonal directions. Radial spacing increases geometrically from the photosphere up to the source surface with a geometric factor  $q \approx 3.3\%$ . The radial position of grid points on a height level  $i$  ( $i \in \{1, \dots, N_r - 1\}$ ) in the spherical grid is  $r_i = r_{i-1} + (r_1 - R_{\odot}) \cdot q^{i-1}$ , where  $N_r = 35$  is the number of height levels in the radial direction and  $r_1 - R_{\odot} \approx 18.7$  Mm. For the elliptic case, this height dependence is distorted according to the stretching treatment presented in Appendix A. This geometric increase in radial grid point spacing allows higher accuracy of the solver near the photosphere where magnetic gradients are strongest, while reducing the computational footprint in the higher regions where a lower accuracy is sufficient for acceptable results.

Polar boundaries are introduced by computing virtual values at the poles as being the average value of all northernmost and southernmost grid points at that specific height. The virtual polar points serve as the outermost neighbor for all adjacent grid points that make up its average. This decreases computation time as information of the solution is allowed to directly travel over the poles rather than only in the zonal direction.

As termination criterion (Eq. (2)) we used  $p = 0.01$  which means the value change from one time step to the next is below 1% at all grid points. Magnetic field line tracking is done by employing an adaptive Runge-Kutta-Fehlberg method of fourth order (RKF45), tri-linearly interpolating between computational grid points.

The spherical PFSS model is a special case of the elliptical PFSS model with ellipticity  $A = 1.0$ . The elliptic solver gives the same values at all grid points within floating-point rounding accuracy for this special case compared to the purely spherical solver.

Our implementation has been written in C/C++ and employs the CUDA framework (version 9.2) by NVIDIA. The time-stepping solution process is quite basic and can be sped up significantly by employing more sophisticated solution processes. However, the computation time for one Carrington rotation with the resolution and accuracy presented here takes between 10 and 20 minutes on the NVIDIA GTX Titan which was released in 2013. For the studies presented here, the computation time is sufficiently fast.

## 3. Results

Without answering the question of which parameter for the ellipticity gives the most realistic coronal magnetic field configuration (if any), we illustrate here the qualitative differences between the spherical and elliptical PFSS models. We chose Carrington rotation 2066 during the minimum between solar activity cycles 23 and 24 in early 2008 to illustrate the differences the model parameters incur. There are only a few and weak CMEs registered for this Carrington rotation (Yashiro 2020), and a few coronal holes and active regions (Barra et al. 2009).

Figures 2 and 3 depict the solar coronal magnetic field configuration. The figure consists of a three-dimensional rendering of the magnetic field configuration as seen from the vernal equinox in the first row. The other rows show the magnetic field polarities at different heights between the photosphere and the source surface. For illustrative purposes only, we chose a strong ellipticity ( $A = 2$ ) of the source surface which we assume is higher than a realistic configuration would exhibit.

The three-dimensional renderings consist of two magnetic field line mappings from the source surface down to the photosphere and vice versa. At the specific height (photosphere, source surface), an equidistant two-dimensional grid is spanned in  $\sin(\text{latitude})$  and longitude with  $-14.5/15.0 \leq \sin(\text{latitude}) \leq +14.5/15.0$  and  $0 \leq \text{longitude} < 2\pi$ . Each of these grid points constitutes the starting point of a magnetic field line, which is traced throughout the computational domain. Blue magnetic field lines have a positive sign pointing outwards, while red lines have a negative sign pointing inwards. Closed field lines originating and ending on the photosphere are in cyan. In the renderings,  $15 \times 30$  magnetic field lines are illustrated starting on the source surface and the same number starting on the photosphere.

Similarly, rows 2 to 5 are cuts of magnetic field line mappings originating at intermediate heights but with a higher resolution of  $200 \times 400$  field lines, corresponding to  $200 \times 400$  pixels. The format is similar to synoptic Carrington maps. The uppermost and lowermost pixels again are positioned at  $\sin(\text{latitude}_{\max}) = +14.5/15.0$  and  $\sin(\text{latitude}_{\min}) = -14.5/15.0$ , respectively. Each pixel represents the polarity of the magnetic field line at that pixel center position with the same color scheme as the field lines in the renderings. Due to the sine-latitude spacing pixels near the poles cover a larger area than pixels at the equator, effectively reducing resolution at high latitudes.

## M. Kruse et al.: Elliptic expansion of the PFSS model

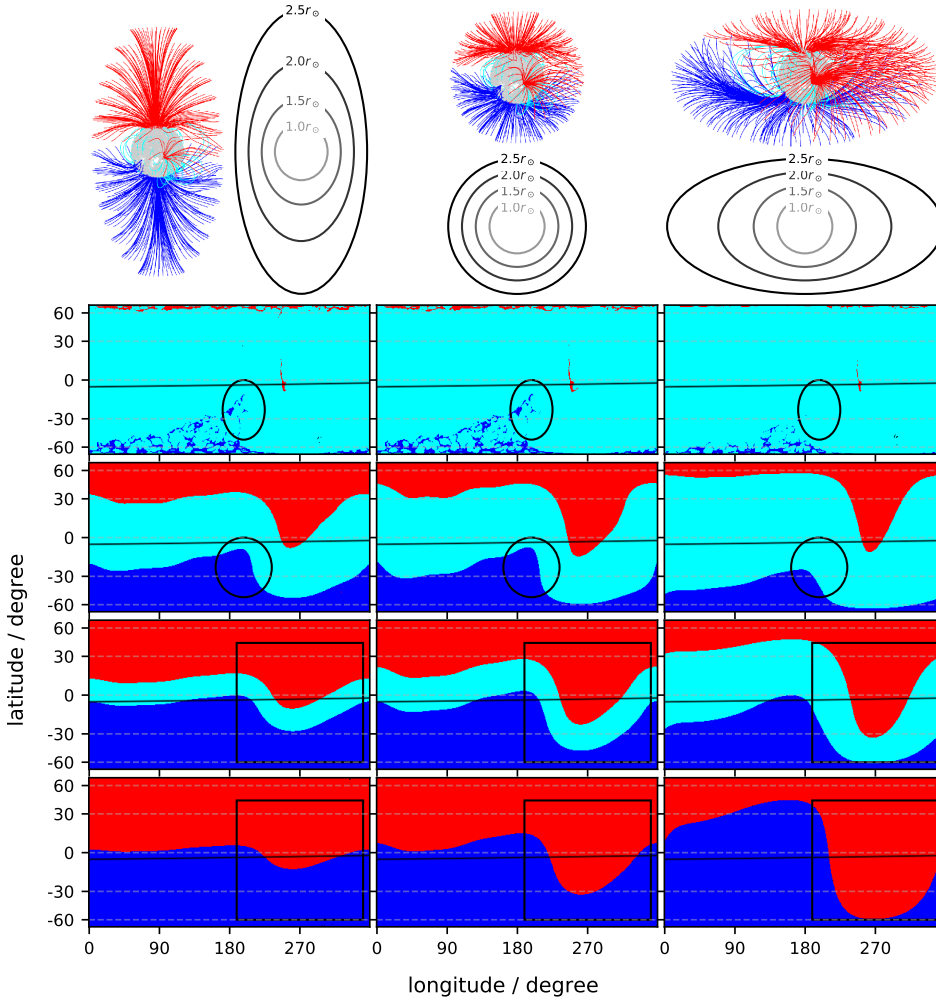


**Fig. 2.** Magnetic field polarity configuration at different heights. Results shown for a prolate ellipsoidal source surface with ellipticity 2.0 (*left column*), for the classical spherical source surface (*center*), and for an oblate ellipsoidal surface again with ellipticity 2.0 (*right*). All figures were created using our grid solver. The source surface height for all models is  $2.5 R_\odot$  (minor half-axis in the ellipsoidal cases). Depicted is Carrington rotation 2066. Data for the lower boundary was obtained from MDI onboard SOHO. *First row:* three-dimensional rendering of a few magnetic field lines for each model as well as a cut through the height levels depicted below. *Rows 2 to 5:* magnetic field polarity configuration at height levels 0%, 33%, 67%, and 100% between the photosphere and source surface. Red magnetic field lines and pixels are directed inward, blue lines are directed outward, and cyan indicates closed field structures. The projection of Earth on the height levels is drawn as a black ascending line near the solar equator. Black ellipses, circles, and squares are inserted to highlight differences in the regimes of interest (see text for details).

In Fig. 2 the intermediate maps correspond to ellipsoidal surfaces which grow in ellipticity, as does the underlying computational grid when approaching the source surface from below. Figure 3 shows intermediate height maps originating on spheres between the two computational boundaries. These represent height levels of  $1.0 R_\odot$ ,  $1.5 R_\odot$ ,  $2.0 R_\odot$ , and  $2.5 R_\odot$  heliocentric distance. We note that the middle column for the spherical model is the same in both figures.

Figure 2 considers global differences among the three presented models. Each height level depicts the magnetic polarity structure at the same relative distance between the boundaries, which correspond to different absolute heliocentric heights for each column. Figure 3 helps to visualize local differences. Each pixel represents the same physical position in all three columns.

While most structures are present in every model, their general appearance can vary greatly. In Figs. 2 and 3 the pronounced current sheet warp (rectangles) at longitude  $270^\circ$ , for example, is less pronounced in the prolate case and extends to lower latitudes in the oblate case compared to the spherical reference model. Another example is the open positive structure slightly south of the equator at longitude  $180^\circ$  (ellipses and circles) which is present in the spherical and prolate models, but missing in the oblate version. Also, closed field structures extend higher in the computational domain in the oblate case, as can be easily seen in the third row of Fig. 2.

Another characteristic that can be computed by only considering magnetic field data is the flux-tube expansion factor  $f_s = B_\odot R_\odot^2 / B_{ss} r_{ss}^2$  (Wang & Sheeley 1990), where  $B_\odot$  is the

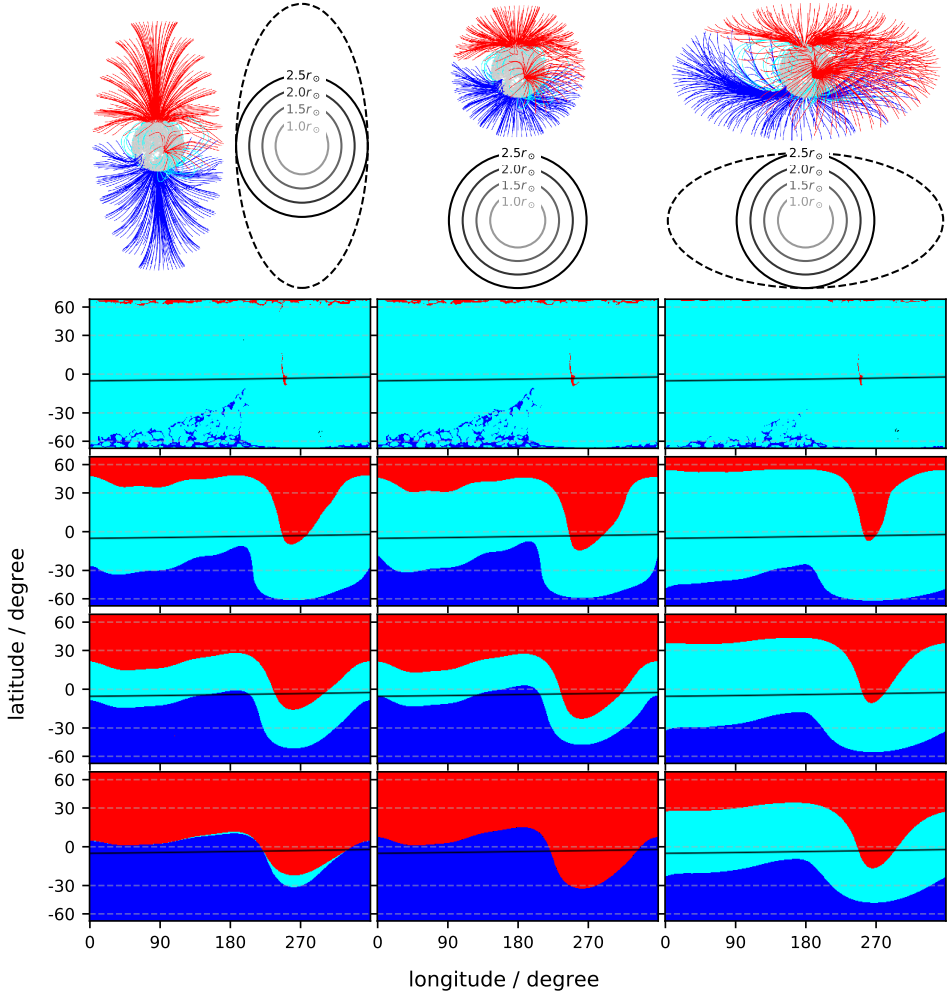


**Fig. 3.** Same as in Fig. 2, but the height levels are spheres. The heights are again  $1.0R_{\odot}$ ,  $1.5R_{\odot}$ ,  $2.0R_{\odot}$ , and  $2.5R_{\odot}$ . The dashed line in the *first row* depicts the source surface, which here is not the same as the uppermost height level examined. The uppermost levels exhibit open field structures in the ellipsoidal cases because the sphere of  $2.5R_{\odot}$  is partially within the source surface and touches it at the equator (prolate case) or the poles (oblate case).

magnetic flux density at the photosphere,  $B_{ss}$  is the magnetic flux density at the source surface,  $R_{\odot}$  is the heliocentric distance of the photosphere, and  $r_{ss}$  is the heliocentric distance of the source surface.

The flux-tube expansion factor is inversely related to solar wind speed and offers a means of comparing model prediction to in situ spacecraft data (*ibid*). In Figs. 4 and 5, we illustrate the expansion factor for the three PFSS models. The format is similar to Figs. 2 and 3, but here each pixel is color-coded with the expansion factor for that specific field line. The oblate PFSS model exhibits higher expansion factors at lower latitudes than the other two models. This suggests lower solar wind speeds in the oblate model, which should be verifiable by analyzing space- craft data.

The expansion factor also illustrates some differences in resolution between the classic implementation employing spherical harmonic coefficients and our grid solver. Figure 6 depicts the expansion factor height levels for the SHC implementation of orders 9 and 20 as well as our implementation. Unsurprisingly,

the middle column, which corresponds to a maximum principle order 20, exhibits more detail than the left column, which corresponds to the classical approach of order 9. Our grid implementation in the right column offers even more detail at the cost of longer computation times. While the classical SHC implementation of order 9 takes less than 1 minute using a single thread on the CPU (Intel Xeon E5-1650), our grid solver takes about 15 minutes employing the massively parallel architecture of a GPU (GTX Titan).

#### 4. Discussion and conclusions

The alteration to the PFSS model to incorporate elliptical source surfaces allows us to tweak the magnetic field computations without needing to employ the full set of MHD assumptions and computational complexity. Only one parameter has been added that needs to be determined and evaluated. In this regard, it is comparable with other improvements of the PFSS model like CSSS, which includes two additional parameters, namely the

## M. Kruse et al.: Elliptic expansion of the PFSS model

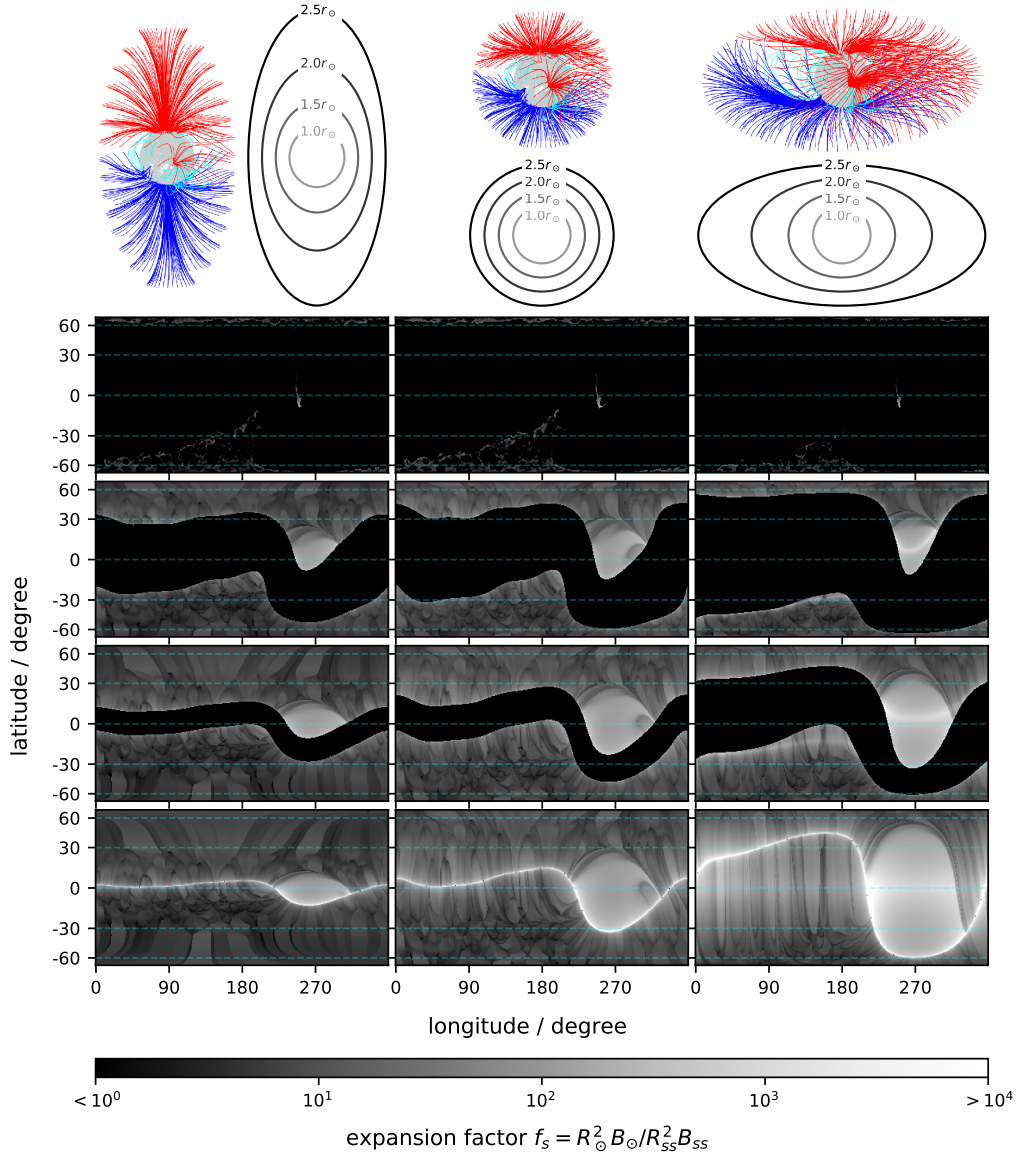


**Fig. 4.** Height levels show the expansion factor. Each pixel again corresponds to one field line, and the color represents its expansion factor between photosphere and source surface.

height of the cusp surface and a length scale of the assumed horizontal electric currents in the corona (Zhao & Hoeksema 1995).

The CESSS model still relies on a spherical symmetry which is a strict constraint for a physical system that we know deviates from this type of symmetry. It is known that the “true” source surface, if it even exists, is most probably not elliptical either (see, e.g., Cohen 2015; Schulz et al. 1978; Riley et al. 2006; Panasenco et al. 2020). It remains to be seen whether the elliptical PFSS approximates the true magnetic field configuration better or worse than the other improvements that have been developed by the community in the past decades. It might also be useful to combine the elliptical source surface with these models, thereby merging possible advantages either model has over the original spherical PFSS model.

The finite difference solver allows more complex shapes to act as source surfaces. For example, the polar indentations found by Riley et al. (2006) may be modeled using the same techniques presented here.

Phenomenologically, there are a few differences between the three grid models presented in this work. In the oblate elliptical model, magnetic field lines tend to bend towards the poles, while in the prolate model they bend away from the poles (see the renderings in Figs. 2–5). Hence, particles traveling along these field lines will have slightly different trajectories. In the oblate case, closed magnetic field structures extend higher relative to the source surface compared to the other two models.

One way to evaluate PFSS models is to compare in situ spacecraft measurements of the heliospheric magnetic field with

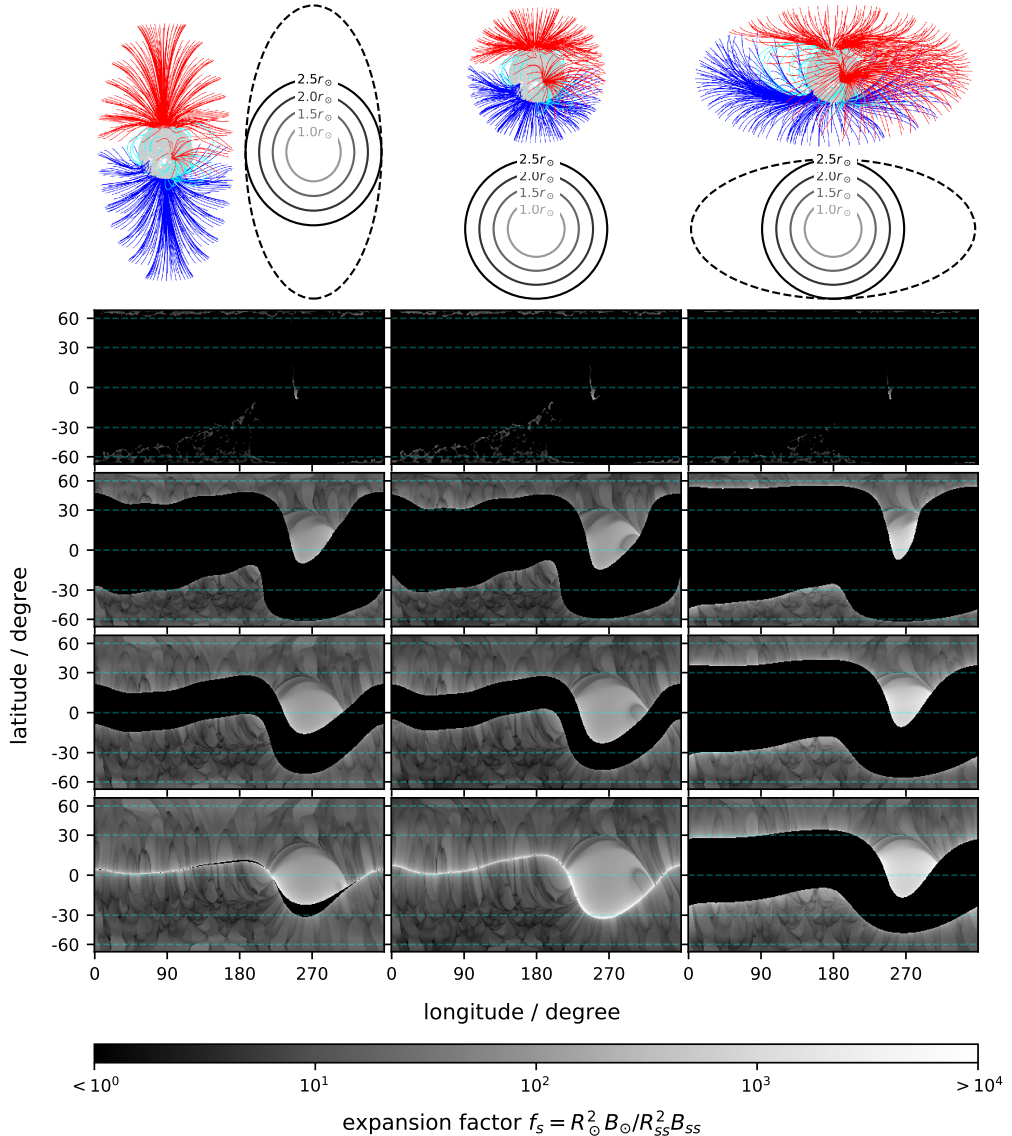


**Fig. 5.** Same as Fig. 4, but for height levels as spheres.

predictions of the PFSS model. After measuring the solar wind speed at the spacecraft, the likely footpoint of the solar wind plasma package on the source surface can be computed by tracing the Parker spiral. The magnetic polarity at the footpoint, as computed by the PFSS implementation, can then be compared to the magnetic field measured at the spacecraft. While there are phenomena above the source surface that might alter the magnetic field orientation as well as inaccuracies in tracing the correct Parker spiral, for example due to solar wind acceleration processes, a better magnetic model of the corona is expected to increase the agreement of spacecraft data with predicted model data.

Going one step further it is possible to track the source surface footpoint of the spacecraft down to the photosphere along

the magnetic field lines computed by the model. The photospheric footpoint positions can then be compared to the appropriate positions in extreme ultraviolet (EUV) images, which originate close to the photosphere. It is generally assumed that open magnetic flux structures map to darker regions in EUV images (Huang et al. 2019). A better magnetic field model should therefore map more often to dark regions in EUV maps than do worse models.

Evaluating predictions of the PFSS models utilizing spacecraft data is complicated due to the distances between spacecraft (typically at heliocentric distances of about 1AU) and the computational domain (below a few  $R_\odot$ ). Connecting spacecraft positions to the source surface introduces errors increasing with distance. Fortunately, two recent missions might help this

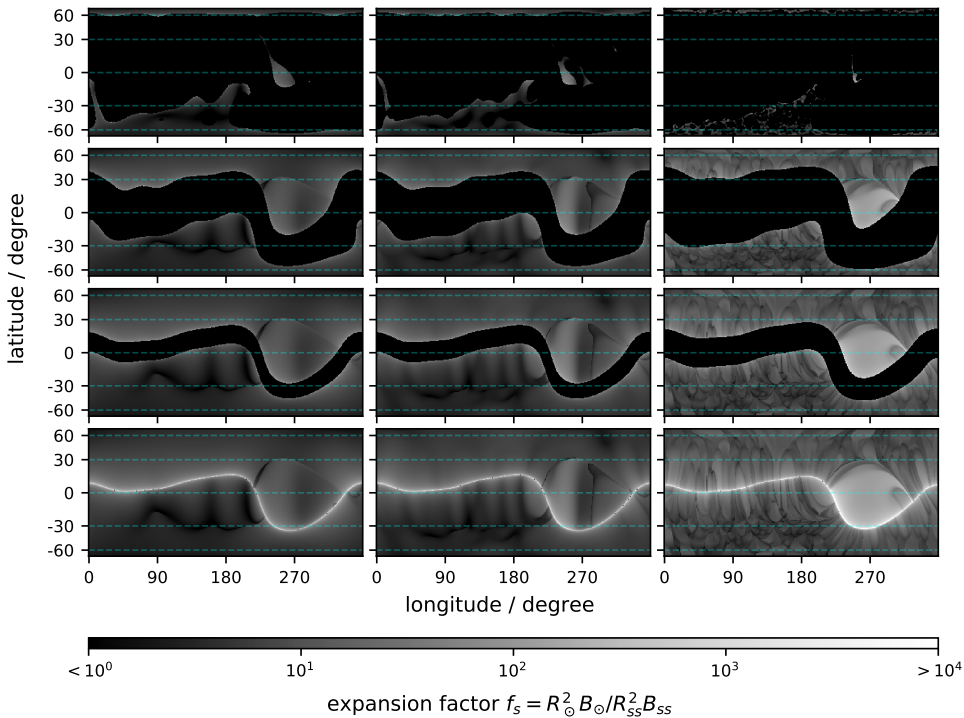


**Fig. 6.** Comparison of expansion height maps for the classical PFSS implementation using spherical harmonic coefficients with order 9 in the left column, with order 20 in the middle column, and our grid solver in the right column. Again Carrington rotation 2066 is depicted. All models employ a spherical source surface at  $2.5R_{\odot}$  heliocentric distance. The height levels in rows 1 to 4 are spheres at heliocentric distances of  $1.0R_{\odot}$ ,  $1.5R_{\odot}$ ,  $2.0R_{\odot}$ , and  $2.5R_{\odot}$ .

endeavor. The Parker Solar Probe (Fox et al. 2016) is already collecting data and Solar Orbiter (Müller & Marsden 2013) was launched in February 2020. The Parker Solar Probe is scheduled to reach a perihelion heliocentric distance of less than  $10R_{\odot}$ , while the Solar Orbiter will go as close as  $60R_{\odot}$ . Solar Orbiter will have a higher ecliptic inclination allowing for measurements closer to the solar poles.

Having instruments close to the computational domain of the PFSS model will help to evaluate the alterations made in this work significantly. Data from both Solar Orbiter as well as the Parker Solar Probe are expected to be available during the 2020s.

Badman et al. (2020) already employed a spherical PFSS model and found that a lower source surface between  $1.3R_{\odot}$  and  $1.5R_{\odot}$  matched the observations better than the traditional source surface height of  $2.5R_{\odot}$ . They also pointed out that this exceptionally low source surface might compensate for washed out small-scale structures due to traditional modeling parameters, which the model alterations presented here might help to alleviate.

**Acknowledgements.** Wilcox Solar Observatory data used in this study was obtained via the web site <http://wso.stanford.edu> at 2019:10:31\_09:49:01 PDT courtesy of J.T. Hoeksema. This work uses data from the Michelson Doppler Imager (MDI) onboard the Solar and Heliospheric Observatory (SOHO). SOHO is a project of international cooperation between ESA and NASA to study the Sun, from its deep core to the outer corona, and the solar wind.

## References

- Altschuler, M. D., & Newkirk, G. 1969, *Sol. Phys.*, **9**, 131
- Aly, J. J. 1989, *Sol. Phys.*, **120**, 19
- Badman, S.T., Bale, S.D., Oliveros, J.C.M., et al. 2020, *ApJS*, **246**, 23
- Barra, V., Delouille, V., Kretzschmar, M., & Hochedez, J.-F. 2009, *A&A*, **505**, 361
- Chapman, S., & Bartels, J. 1940, *Geomagnetism* (Oxford University Press), 1049
- Cohen, O. 2015, *Sol. Phys.*, **290**, 2245
- Duvall, T. L., Wilcox, J. M., Svalgaard, L., Scherrer, P. H., & McIntosh, P. S. 1977, *Sol. Phys.*, **55**, 63
- Fox, N. J., Velli, M. C., Bale, S. D., et al. 2016, *Space Sci. Rev.*, **204**, 7
- Hoeksema, J. 2020, *Wilcox Solar Observatory Web Page*
- Huang, G.-H., Lin, C.-H., & Lee, L.-C. 2019, *ApJ*, **874**, 45
- Levine, R. H., Schulz, M., & Frazier, E. N. 1982, *Sol. Phys.*, **77**, 363
- McComas, D. J., Bame, S. J., Barraclough, B. L., et al. 1998, *Geophys. Res. Lett.*, **25**, 1
- Müller, D., Marsden, R. G., & St. Cyr, O. C., & Gilbert, H. R. 2013, *Sol. Phys.*, **285**, 25
- Panasenco, O., Velli, M., D'Amicis, R., et al. 2020, *ApJS*, **246**, 54
- Piercey, V. I. R. 2007, *The Lamé and Metric Coefficients for Curvilinear Coordinates in R*
- Riley, P., Linker, J. A., Mikić, Z., et al. 2006, *ApJ*, **653**, 1510
- Schatten, K. H., Wilcox, J. M., & Ness, N. F. 1969, *Sol. Phys.*, **6**, 442
- Scherrer, P. H., Bogart, R. S., Bush, R. I., et al. 1995, *Sol. Phys.*, **162**, 129
- Schulz, M. 1997, *Ann. Geophys.*, **15**, 1379
- Schulz, M., Frazier, E. N., & Boucher, D. J. 1978, *Sol. Phys.*, **60**, 83
- Wang, Y. M., & Sheeley, N. R. J. 1990, *ApJ*, **355**, 726
- Wang, Y. M., & Sheeley, N. R. J. 1992, *Astrophysical Journal*, **392**, 310
- Wiegelmann, T. 2008, *J. Geophys. Res. Space Phys.*, **113**, A03S02
- Yashiro, S. 2020, *SOHO LASCO CME Catalog*
- Zhao, X., & Hoeksema, J. T. 1993, *Sol. Phys.*, **143**, 41
- Zhao, X., & Hoeksema, J. T. 1995, *J. Geophys. Res.*, **100**, 19

## Appendix A: Mathematical framework of the elliptical grid solver

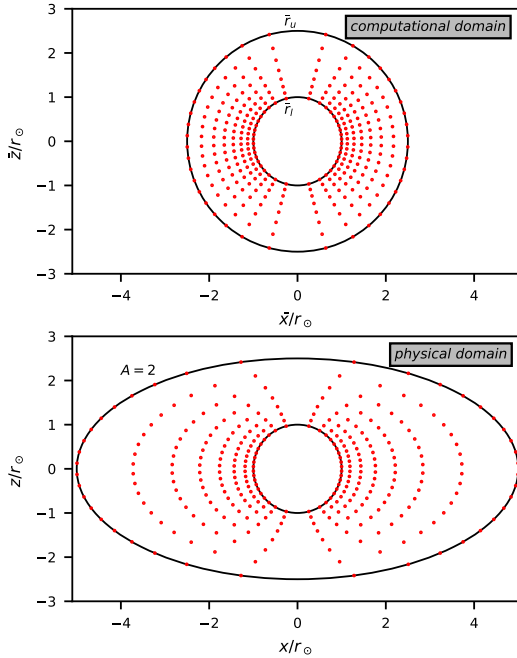


**Fig. A.1.** Cut through the  $\bar{x}/\bar{y}$ - $/x/y$ -plane of the computational and physical domain for an oblate ellipsoidal source surface. The number of grid points shown is considerably reduced to improve clarity. The presented grid has an ellipticity of  $A = 2$  at the source surface, which results in a source surface height of  $2.5R_\odot$  over the poles and of  $5.0R_\odot$  over the equator.

The framework of the employed grid is not trivial, in particular the transition from the spherical configuration at the base to elliptical at the source surface. Here we briefly describe the framework employed for this work. The derivation follows the procedure laid out by [Piercey \(2007\)](#) for non-orthogonal curvilinear coordinate systems.

To simplify the mathematical description, we distinguish between two domains. The first domain is a basic spherical coordinate system on which the algorithm performs its operations. This domain is called the computational domain. By stretching this domain along one or two axes we obtain the physical domain, which corresponds to real-world coordinates that we are interested in. By employing this two-domain approach we circumvent the need for complicated derivations of the mathematical framework by hiding it in a very simple transformation from the computational to the physical domain. Stretching the computational grid along one axis ( $z$ ) produces a prolate ellipsoidal source surface. Stretching the grid along two axes ( $x$  and  $y$ )

produces an oblate ellipsoid. In the following, we concentrate on the oblate case. The prolate version is obtained in an analogous manner.

Figure A.1 shows cuts through the two domains. Coordinates in the computational domain are denoted by bars above the symbols ( $\bar{x}, \bar{y}, \bar{z}, \bar{r}, \bar{\theta}, \bar{\phi}$ ), whereas the same symbols without bars are used for the physical domain ( $x, y, z, r, \theta, \phi$ ). They are in two groups:  $x, \bar{x}, y, \bar{y}, z$  and  $\bar{z}$  are the well-known cartesian coordinates and  $r, \bar{r}, \theta, \bar{\theta}, \phi$ , and  $\bar{\phi}$  are the spherical coordinates in their respective domains. The stretching of the computational grid is performed by an analytic stretching function along the  $\bar{x}$ - and  $\bar{y}$ -axes according to

$$x = a\bar{x} = a_A(\bar{r})\bar{r} \sin \bar{\theta} \cos \bar{\phi}$$

$$y = a\bar{y} = a_A(\bar{r})\bar{r} \sin \bar{\theta} \sin \bar{\phi}$$

$$z = \bar{z} = \bar{r} \cos \bar{\theta}$$

As the stretching function, we chose

$$a_A(\bar{r}) = 1 + \frac{A-1}{\bar{r}_u^2 - \bar{r}_l^2} (\bar{r}^2 - \bar{r}_l^2) = 2\alpha + a_s \bar{r}^2,$$

where  $A$  is the ellipticity parameter at the source surface;  $\bar{r}_u$  and  $\bar{r}_l$  are the radial positions of the upper and lower computational boundaries, respectively;  $\alpha = (1 - a_s \bar{r}_l^2)/2$ ; and  $a_s = (A-1)/(\bar{r}_u^2 - \bar{r}_l^2)$ . We chose the squared dependence on radial distance in the computational domain to decrease the rate of change in the lower region where the algorithm requires a higher computational accuracy compared to the outer region near the source surface.

With these relations between computational and physical domain the gradient basis vectors of the physical coordinate system are

$$\begin{aligned} \mathbf{g}^r &= \frac{1}{a + r \cdot \sin^2 \theta \cdot \frac{\partial a}{\partial r}} \begin{pmatrix} \sin \theta \cos \phi \\ \sin \theta \sin \phi \\ a \cos \theta \end{pmatrix} \\ \mathbf{g}^\theta &= \frac{1}{r(a + r \cdot \sin^2 \theta \cdot \frac{\partial a}{\partial r})} \begin{pmatrix} \cos \theta \cos \phi \\ \cos \theta \sin \phi \\ -\sin \theta (a + r \cdot \frac{\partial a}{\partial r}) \end{pmatrix} \\ \mathbf{g}^\phi &= \frac{1}{a \cdot r \cdot \sin \theta} \begin{pmatrix} -\sin \phi \\ \cos \phi \\ 0 \end{pmatrix}. \end{aligned}$$

With these vectors and a twice continuously differentiable scalar function  $\Psi$ , the Laplace operator in general curvilinear coordinates can be expressed as

$$\nabla^2 \Psi = \frac{1}{\sqrt{g}} \sum_i \sum_j \frac{\partial}{\partial q^i} \left( \sqrt{g} g^{ij} \frac{\partial \Psi}{\partial q^j} \right),$$

where  $g = \det(G)$  is the determinant of the metric coefficient matrix  $G$  with entries  $g^{ij} = \mathbf{g}^i \cdot \mathbf{g}^j$ , and  $i, j \in \{1, 2, 3\}$  corresponding to the coordinates  $r, \theta$ , and  $\phi$ , respectively.

# 6

## EVALUATING THE NEW SOLVER

---

An analysis of the new [PFSS](#) solver's potential merits needs to overcome one major obstacle. There is currently no method available to measure the Sun's large-scale magnetic configuration accurately. Therefore, comparing the three-dimensional output of the [PFSS](#) solver to the near-solar magnetic field is not possible without employing some form of proxy measurement. There are few operational magnetometers throughout the heliosphere which can be utilized for analysis, though most of them are far from the region where the [PFSS](#) model is valid. Only two spacecraft come close to the outer boundary of the [PFSS](#) model. These are the Parker Solar Probe launched in 2018 [[Fox et al., 2016](#)], and Solar Orbiter launched in 2020 [[Müller et al., 2013](#)].

For analyses of extended periods, it is necessary to rely on instruments further away from the domain of interest. The current understanding of the (continuous, quasi-static) solar wind is that the acceleration region is close to the solar surface [see, e.g., [Cranmer, 2005](#); [Nolte and Roelof, 1973](#)]. Above a certain threshold (i.e., where the plasma pressure dominates the magnetic pressure, high  $\beta$ ), the particles stream radially outward, thereby dragging the magnetic field with them through the heliosphere. In the absence of turbulent eruptions, such as [ICMEs](#) or flares, or transport effects, such as Stream Interaction Region ([SIR](#)s), where streams of fast solar wind drive into slow streams, a uniform expansion of solar wind packages can be assumed.

Given the bulk flow velocity of a wind stream measured at some spacecraft, the path of that package can be analytically traced down along the Parker spiral to the source surface height. The magnetic polarity predicted by the model can then be compared to the magnetic configuration measured at the spacecraft. This is just an elementary first test of the model and it does not account for the magnetic orientation below the source surface. Nevertheless, it gives valuable insight into how important the different model parameters are for predicting this simple metric.

This chapter discusses the solar wind's merit as a proxy measurement for the magnetic field configuration near the solar surface. The ballistic back mapping procedure to overcome the measurement divide between spacecraft and model domain is layed out in Sect. 6.1. Sections 6.2 and 6.3 discuss the spacecraft, instrumentation, and periods that are utilized for evaluating the merit of the improved [PFSS](#) solver via the *backmapping polarity measure* presented in Sect. 6.4. The chapter closes with the second publication, which evaluates the newly developed ellipsoidal [PFSS](#) solver in Sect. 6.5.

## 6.1 BALLISTIC BACK MAPPING

By assuming a constant radial flow speed of the solar wind, the trajectory of a plasma parcel measured at some spacecraft can be computed analytically. This allows the solar wind package's origin to be traced down to the source surface along the Parker spiral. A schematic of this method is depicted in Fig. 13. Because the Parker spiral is locked to the rotational axis of the Sun, the Carrington heliographic coordinate system is employed to describe the movement of plasma in the heliosphere. The heliographic position  $x$  is described via the three coordinates radial distance from the Sun's center  $r$ , latitude  $\Theta$ , and longitude  $\Phi$ . Latitude is measured positively towards the solar north pole; longitude is measured in the direction of planetary motion with the prime meridian defined as the one passing through the ascending node of solar rotation on the ecliptic at noon of January 1st, 1854 (Julian Date 2398220.0). A good explanation of this coordinate system can be found, e.g., in Fränz and Harper [2002].

Let  $\Omega_{\odot} = 2.972 \cdot 10^{-6} \frac{\text{rad}}{\text{s}}$  be the rotational speed of the Sun and  $v_{sw}$  the solar wind bulk flow speed measured at the spacecraft. The ballistic footpoint  $(r_{fp}, \theta_{fp}, \phi_{fp})$  of the spacecraft position  $(r_{sc}, \theta_{sc}, \phi_{sc})$  on the source surface at height  $R_{ss}$  can be obtained via

$$r_{fp} = R_{ss} ,$$

$$\theta_{fp} = \theta_{sc} , \text{ and}$$

$$\phi_{fp} = \phi_{sc} + \frac{(r_{sc} - R_{ss}) \cdot \Omega_{\odot}}{v_{sw}} , \quad (67)$$

where a modulo  $2\pi$  operation might need to be applied to the longitudinal coordinate.

## 6.2 SPACECRAFT DATA USED

For the back mapping analysis presented in the following, three spacecraft at a heliocentric distance of 1 AU in the ecliptic were selected to supply in-situ data of the heliospheric environment. They are ACE at L<sub>1</sub> and the two Solar Terrestrial Relations Observatory (STEREO) spacecraft. These spacecraft have collected data for many years and cover different periods of the solar activity cycle.

### 6.2.1 ADVANCED COMPOSITION EXPLORER

The ACE was launched in 1997 and reached its operational orbit around L<sub>1</sub> in early 1998 [Stone et al., 1998]. Its primary mission duration of 5 years has been repeatedly extended and ACE is still in operation as of 2020. The fuel reserves will allow ACE to stay in position until the mid-2020s. The instruments utilized for the analysis presented here are the Solar Wind Electron, Proton and Alpha Monitor (SWEPAM) [McComas et al., 1998a] and Solar Wind Ion Composition Spectrometer (SWICS)

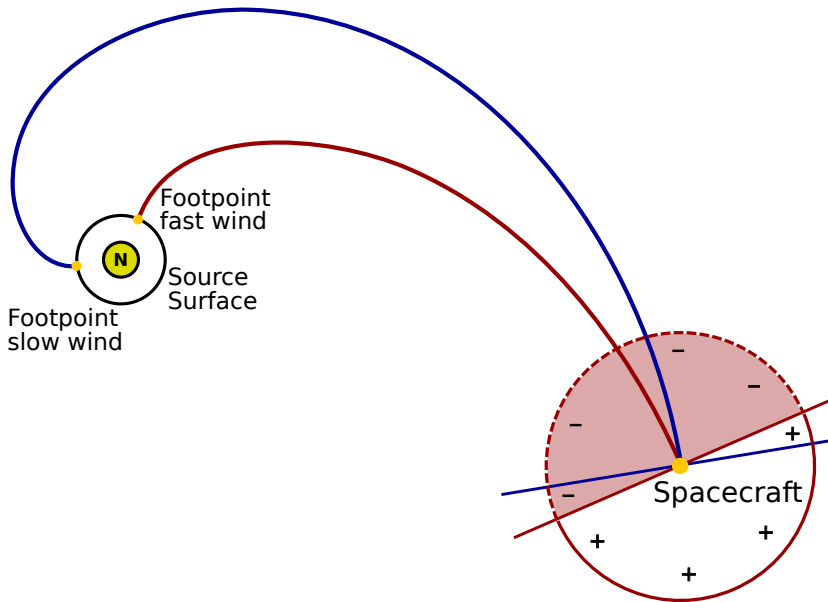


Figure 13: Ballistic traces of a fast (red) and slow (blue) solar wind packages along their respective Parker spirals seen from above the northern solar pole. In the fast solar wind frame, magnetic polarity at the spacecraft is measured positively if the magnetic vector lies in the anti-sunward hemisphere and negatively if it lies in the sunward hemisphere (red shaded). A similar distinction is performed for the slow solar wind frame (not illustrated). The ballistic footpoints for both fast and slow solar wind are marked on the source surface.

[[Gloeckler et al., 1998](#)] for the solar wind bulk flow velocity and the magnetometer (MAG) of the magnetic fields experiment [[Smith et al., 1998](#)].

#### 6.2.2 SOLAR TERRESTRIAL RELATIONS OBSERVATORIES

The twin spacecraft mission [STEREO](#) was launched in 2006 [[Kaiser et al., 2008](#)]. One spacecraft was sent ahead and one behind Earth's orbital position, [STEREO-A](#) and [STEREO-B](#), respectively. The angular separation of each spacecraft is about  $22^\circ$  per year with respect to Earth's position in its orbit. [STEREO-A](#) has a slightly lower orbit than Earth, which in turn has a slightly lower orbit than [STEREO-B](#). The mission objective is to draw a better picture of solar physics by observing the Sun from different positions with the same instruments. Contact with [STEREO-B](#) was lost in 2014, [STEREO-A](#) is still in operation as of 2020. The instruments from the [STEREO](#) system employed in the analysis are the Plasma and Supra-Thermal Ion and Composition instrument ([PLASTIC](#)) [[Galvin et al., 2008](#)] and the magnetometer (MAG) of the In situ Measurements of Particles and CME Transients ([IMPACT](#)) suite [[Luhmann et al., 2008](#); [Acuña et al., 2008](#)].

#### 6.3 SELECTION OF TIME PERIODS AND MAGNETOGRAM DATA

The presented analysis' main objective is to measure the impact of the ellipticity parameter on the results of the [PFSS](#) model to assert if and how strong the ellipsoidal source surface impacts the model predictions. Because the ellipticity is

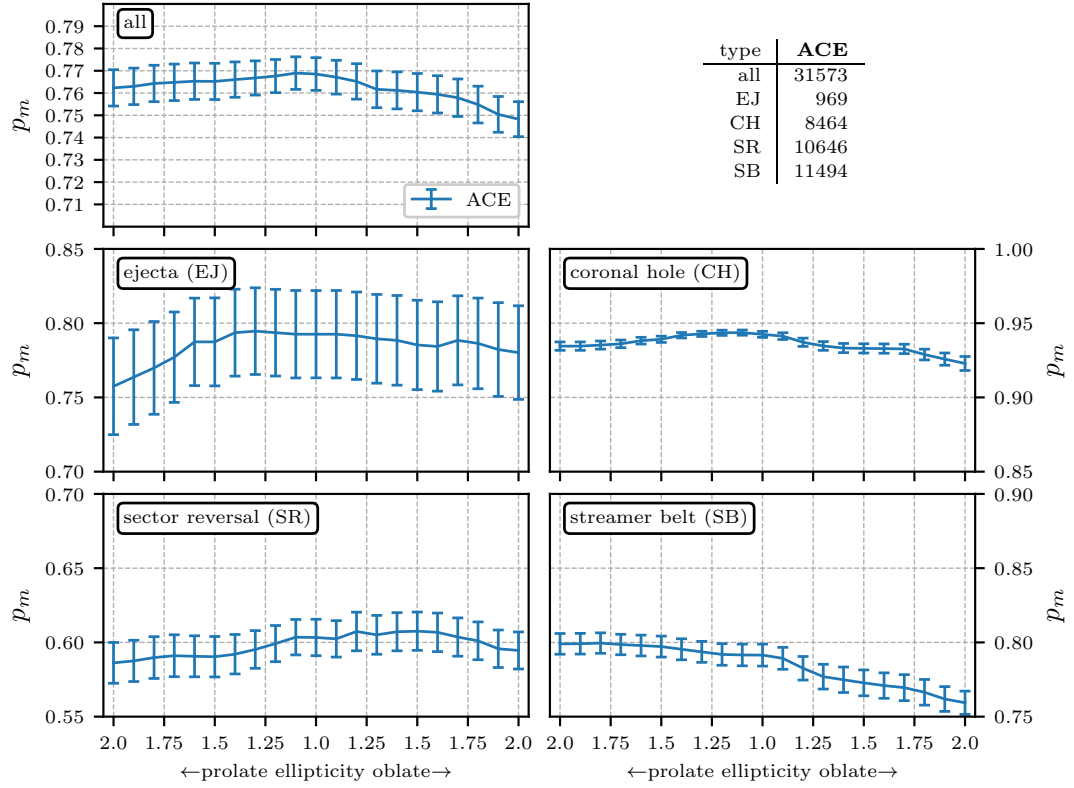


Figure 14: Backmapping polarity measure for all solar wind types during the declining period 1 (CR2041-2055, 2006) measured at [ACE](#). The minimum source surface height is  $R_{ss} = 2.5 \cdot R_\odot$ ; the ellipticity is varied along the x-axis (prolate source surfaces to the left, oblate source surfaces to the right). The number of samples of each solar wind type is listed in the top-right panel.

linked to the parameter of the source surface height (see Sect. 4.1), this parameter has to be evaluated as well. The [PFSS](#) model performs better during the minimum of the solar activity cycle. This is due to the model assumptions being met more often than during solar activity maximum when the coronal environment is more dynamic, violating the quasi-static domain assumption. Therefore, three different periods were chosen during the solar activity cycle to be analyzed. The first period examines the declining solar activity cycle (Carrington rotations 2041-2055) in 2006. Carrington rotations 2044, 2046, 2047, 2050, and 2053 were excluded due to missing data in the magnetograms. For the quiet Sun, the ten Carrington rotations 2066 - 2075 were chosen, starting on January 25th of 2008 and lasting up until October 23rd of the same year. Data from the [MDI](#) magnetometer onboard the [SOHO](#) space-craft have been employed for evaluating the new [PFSS](#) solver during these first two periods. The active Sun is analyzed during Carrington rotations 2133 - 2142 from January 25th to October 25th of 2013. For this period magnetograms from [HMI](#) onboard [SDO](#) have been utilized because [MDI](#) ceased operation in 2010.

#### 6.4 BACK MAPPING POLARITY MEASURE

For the entire period to be analyzed, the five quantities  $B$ ,  $v_{sw}$ ,  $T_p$ ,  $n_p$  and space-craft position  $x_{sc}$  are analyzed. Sampling cadence is 12 minutes for data from [ACE](#)

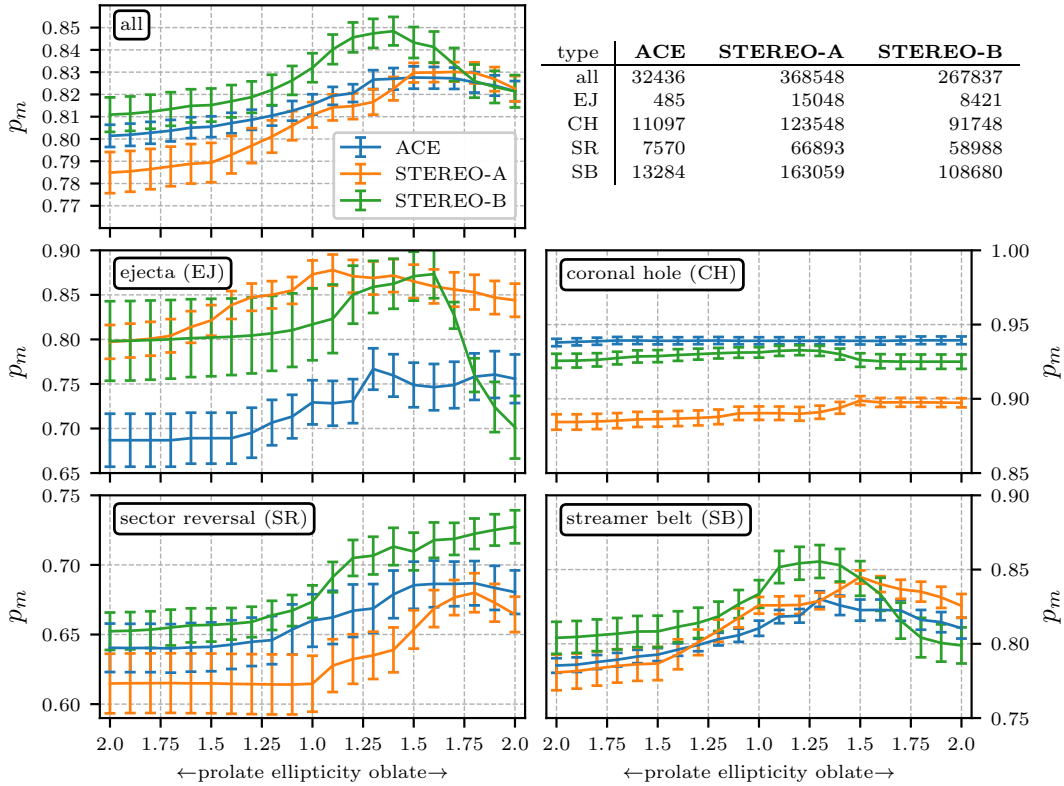


Figure 15: The same as Fig. 14 but with the additional spacecraft STEREO-A/B and for the minimum period 2 (CR2066-2075, 2008).

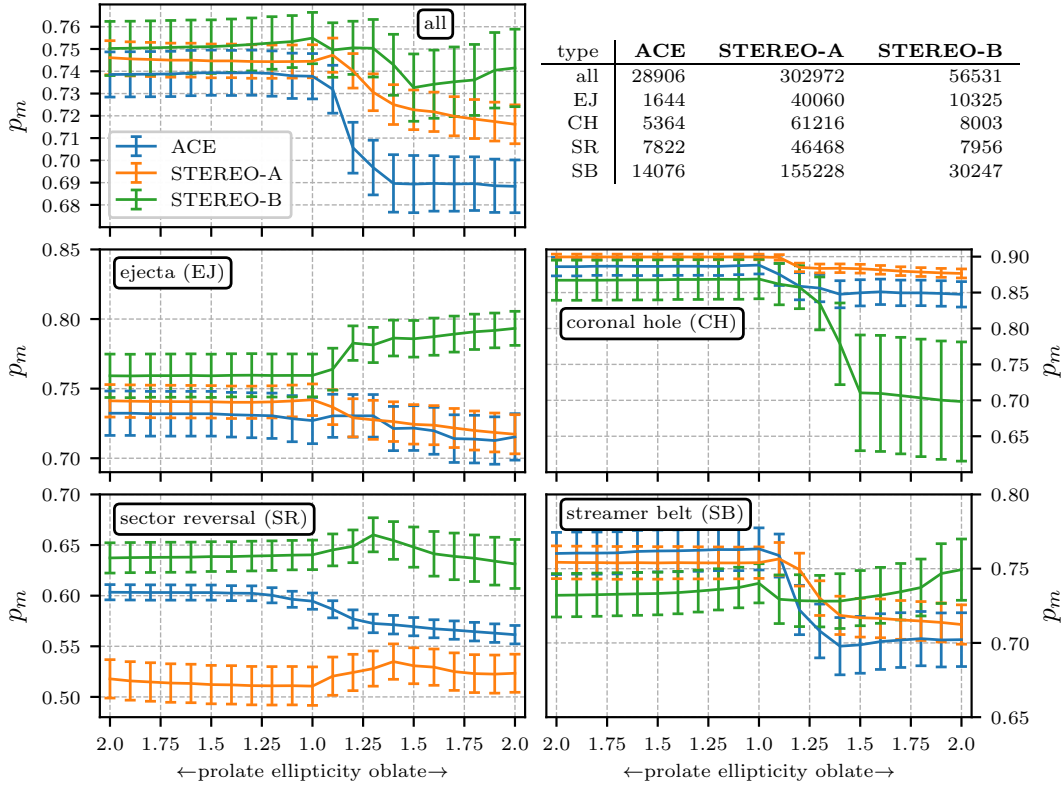


Figure 16: The same as Fig. 15 but for the maximum period 3 (CR2133-2142, 2013).

and 1 minute for data from [STEREO](#). A sample is rejected if one or more quantities are missing. Otherwise, ballistic back mapping down to the source surface is performed by evaluating Eq. 67. The magnetic field measured in-situ is projected onto the Parker spiral (see Fig. 13). The sample is counted as a correct prediction if the projected in-situ magnetic field polarity along the Parker spiral is the same as the computed magnetic field polarity at the source surface. Otherwise, it is counted as a false prediction. The ratio of correctly predicted samples to all valid samples is noted as  $p_m$ . It serves as the evaluation procedure's quality metric and is named the *back mapping polarity measure*.

All valid samples are additionally binned according to the Xu-Borovsky scheme (see Sect. 1.2) so that different solar wind classes can be analyzed separately. This binning is conducted because different wind types provide information of varying quality. For example, the coronal hole wind emanates from regions where no polarity changes are to be expected. Therefore, the parameter of source surface ellipticity is not expected to impact the outcome of the analysis. Contrarily, sector reversal wind emanates from structures near the Heliospheric Current Sheet ([HCS](#)) where magnetic polarity changes are expected. Therefore, the evaluation procedure is sensitive to the model parameters that directly affect the shape of the [HCS](#). The [HCS](#) is a large interplanetary structure and the cause of the radial orientation of the upper coronal magnetic field [Schatten, 1972]. In the [PFSS](#) model paradigm, it is positioned just outside of the source surface at the intersection of the magnetic polarities (see the third column in Fig. 11).

Periods in which [ICMEs](#) have been observed were filtered out from the data set because they originate from turbulent phenomena, which cannot be modeled by the static [PFSS](#) model. For [ICME](#) classification the [Cane and Richardson \[2003\]](#) list for [ACE](#) data and the [Jian et al. \[2018\]](#) list for [STEREO](#) data were employed.

A cross-validation scheme has been performed to estimate the validity of the evaluation procedure: Instead of computing the mean fraction of correctly predicted samples for all 10 Carrington rotations for each period, the mean of 9 Carrington rotations is calculated. By omitting a different Carrington rotation each time, ten such averages can be computed. These ten values can then be averaged, giving a standard deviation of the statistic that serves as the analysis's error estimate. The error is interpreted as a rough estimate for the impact of data from individual Carrington rotations on the study's outcome.

The back mapping polarity measure is applied to three periods of the solar activity cycle to determine its influence on the [PFSS](#) results in addition to the influence of the ellipticity and source surface height parameters. Figures 14 to 16 illustrate the back mapping polarity measure for the three periods and for a minimum source surface height of  $R_{ss} = 2.5 \cdot R_\odot$ . The error bars resemble the standard error of the cross-validation scheme.

Because the assumptions of the [PFSS](#) model are violated more often in periods of the active Sun compared to the quiet times, the back mapping polarity measure produces better results in the minimum period 2 (Fig. 15) compared to the other periods. For the most part, coronal-hole wind contains the best prediction values, which is expected because polarity changes are rare in this solar wind type. This

also explains the relatively flat curve, which shows that the ellipticity parameter has little influence on these wind-type samples. In contrast, sector reversal wind's prediction rate is the lowest of all wind types and shows high variability. This is because samples originating near the HCS are binned into this solar wind type, and therefore magnetic polarity changes are more common. Therefore, the exact position of the HCS, as predicted by the model, substantially impacts the back mapping polarity measure for sector reversal samples. A more thorough analysis co-varying ellipticity and minimum source surface height can be found in Publication 2.

## 6.5 PUBLICATION 2

As part of this work, a new PFSS solver has been developed to incorporate ellipsoidal source surfaces into the model paradigm. The previous chapters are concerned with establishing the mathematical foundation and ensuring the feasibility of implementing a time-efficient solution process. The results of this work, both theoretical and practical, have been addressed and were presented to the scientific community in Publication 1 (see Sect. 5.5). So far, only the model itself and some predicted coronal magnetic configurations have been presented. If this new solver improves the predictions of the decade-old PFSS model had not been answered. To remedy this, real-world data has to be gathered and analyzed for the new solver's predictions. For this purpose, instrumentation data from three spacecraft, ACE and STEREO-A/B, were utilized, and the predictions of the ellipsoidal PFSS solver were compared to the measurements. The evaluation procedure is described in Sect. 6.4 and was performed for three phases of the solar activity cycle. This allows not only to evaluate the advantages of the ellipsoidal source surface compared to the classical, spherical source surface but also to evaluate the prediction quality of the PFSS model in general during the solar activity cycle. The findings have been published in:

**EVALUATION OF A POTENTIAL FIELD SOURCE SURFACE MODEL WITH ELLIPTICAL SOURCE SURFACES VIA BALLISTIC BACKMAPPING OF IN-SITU SPACECRAFT DATA**

M. Kruse, V. Heidrich-Meisner and R. F. Wimmer-Schweingruber, A&A, accepted, in production, reproduced with permission © ESO.

DOI: 10.1051/0004-6361/202039120

Own contribution: 90%

### *Summary*

Following a brief introduction to the [PFSS](#) model and the ellipsoidal modifications from Publication 1, a few methods for evaluating solar magnetic field models and their shortcomings and advantages are presented. After a description of the back mapping polarity measure as the chosen evaluation method, the employed spacecraft and instruments are introduced. The publication concentrates on analyzing three periods during different solar activity cycle stages, a declining, a minimum, and a maximum phase. The publication shows that a model with a slight oblate ellipsoidal source surface performs better than with a spherical source surface. This finding is supported by all three spacecraft utilized for this evaluation procedure. A definitive parameter for best ellipticity is not given because the evaluation procedure can only evaluate the situation in the ecliptic plane. In contrast, data from higher latitudes would be necessary to assert one model's general superiority over another.

In addition to evaluating the merits of employing the ellipsoidal [PFSS](#) model over the spherical model, the publication also illustrates the shortcomings of the [PFSS](#) model in general when it comes to employing it during the active phase of the solar cycle. The conclusion states the data's agreement from the three different sources and suggests further evaluation of the ellipsoidal [PFSS](#) model using synoptic [EUV](#) maps and out-of-ecliptic instrumentation such as onboard Ulysses and Solar Orbiter.

The key results are:

- During the minimum phase of the solar cycle and in the ecliptic, a [PFSS](#) model with an ellipsoidal source surface performs slightly better than the classical model.
- Other evaluation procedures are necessary to assert the general superiority of the ellipsoidal model.
- The [PFSS](#) model, both with spherical and ellipsoidal source surfaces, performs considerably worse during the solar activity maximum phase compared to the minimum phase.

# Evaluation of a potential field source surface model with elliptical source surfaces via ballistic back mapping of in situ spacecraft data

M. Kruse<sup>1</sup>, V. Heidrich-Meisner<sup>1</sup>, and R.F. Wimmer-Schweingruber<sup>1</sup>

University of Kiel, Institute for Experimental and Applied Physics, Leibnizstr. 11, 24118 Kiel  
e-mail: kruse@physik.uni-kiel.de

Received \*\*\*

## ABSTRACT

**Context.** The potential field source surface (PFSS) model is an important tool that helps link the solar coronal magnetic field to the solar wind. Due to its simplicity, it allows for predictions to be computed rapidly and requires little input data, though at the cost of reduced accuracy compared to more complex models. So far, PFSS models have almost exclusively been computed for a spherical outer boundary or "source surface." Changing this to an elliptical source surface holds promise to increase its prediction accuracy without the necessity of incorporating complex computations or additional model assumptions.

**Aims.** The main goal of this work is to evaluate the merit of adding another parameter, namely the ellipticity of the source surface, to the PFSS model. In addition, the applicability of the PFSS model during different periods of the solar activity cycle as well as the impact of the source surface radius are analyzed.

**Methods.** To evaluate the model, in situ spacecraft data are mapped back to the source surface via a ballistic approach. The in situ magnetic field polarity is compared to the magnetic field polarity predicted by the model at the source surface. This method is based on the assumption that better performing models provide better agreements between the prediction and the measured magnetic field polarity. We employ data from the Advanced Composition Explorer (ACE) and the twin Solar Terrestrial Relations Observatory (STEREO) for this analysis.

**Results.** We show that the PFSS model performs slightly better with oblate elliptical source surfaces elongated along the solar equatorial plane, although the best found ellipticity varies for different spacecraft and periods. In addition, it is demonstrated that the performance of the presented analysis degrades during the active times of the solar activity cycle.

**Key words.** Sun: magnetic fields –

## 1. Introduction

The magnetic field of the inner solar corona plays a vital role in the acceleration processes of the solar wind. Due to the sparse availability of in situ measurements, there is a widespread need for computational models to predict the coronal magnetic field based on remote sensing observations. One of the earliest models is the potential field source surface (PFSS) model (Schatten et al. 1969; Altschuler and Newkirk 1969), which requires only synoptic line-of-sight magnetograms of the solar photosphere.

To obtain a configuration of the coronal magnetic field, the PFSS model assumes that there are no electric currents between the photosphere and a second virtual surface, the eponymous source surface, which is located a few solar radii higher. In addition, it is assumed that the magnetic field configuration is stationary for the duration of an entire Carrington rotation. The model, which employs two boundary conditions on the photosphere and the source surface, can produce a magnetic field configuration using a straightforward mathematical framework. The lower boundary condition is realized by deriving values for the magnetic potential from synoptic magnetograms. The upper boundary condition is implemented by keeping the magnetic potential constant throughout the solution process, thereby restricting the magnetic field direction to be perpendicular to the source surface. We refer to Mackay and Yeates (2012) for a more in-

depth explanation of the exact model paradigm and variations of the PFSS models.

Although there are more complex models that offer the computation of a larger set of physical phenomena, namely full magnetohydrodynamic (MHD) models, the PFSS model is still widely used as a first-order approximation of the solar magnetic field for further analyses or where only large-scale magnetic field configurations are of interest. Other models that improve the PFSS model without adding the complexity of full MHD models exist, such as the current sheet source surface (CSSS) model (Zhao and Hoeksema 1995).

Several authors have suggested that deviating from the strict constraint of the source surface being spherical could increase the accuracy of solar magnetic field predictions by the PFSS model (Schulz et al. 1978; Schulz 1997; Levine et al. 1982; Riley et al. 2006). Kruse et al. (2020) altered the well-established spherical PFSS model to employ oblate and prolate elliptical source surfaces, removing the constraint that the magnetic field be radial at the same height at all latitudes. Spherical source surfaces assume an isotropic coronal magnetic orientation, whereas observations (see, e.g., McComas et al. 1998b) show a clear deviation of physical phenomena from this symmetry. An elliptical source surface can account for latitudinal differences of physical phenomena by allowing for different source surface heights and corresponding magnetic orientations.

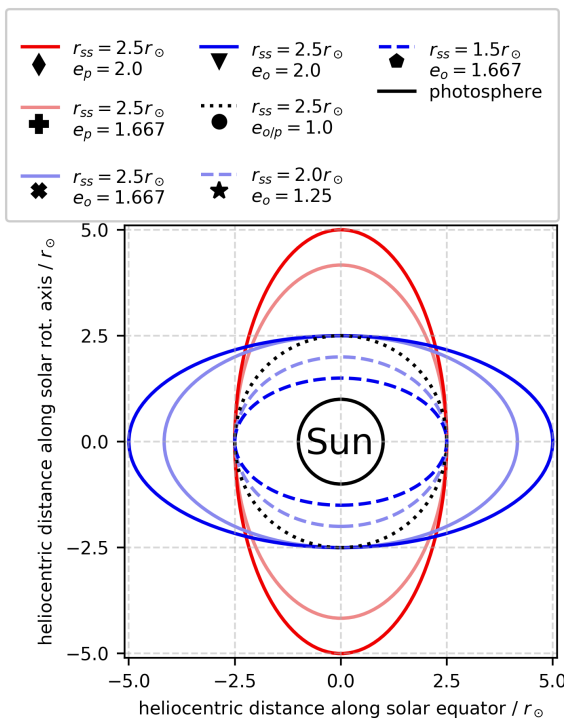


**Fig. 1.** Cuts through several source surfaces used in our PFSS models. Prolate source surfaces (red shapes) resemble zeppelin-shapes aligned with the solar rotation axis elongated along one axis, whereas oblate source surfaces (blue shapes) resemble thick disks elongated along two axes. The classical spherical source surface is drawn with a dotted black line. Various symbols introduced in the legend are used in Figs. 3 to 5, where they are shown at the corresponding positions.

The idea presented by Kruse et al. (2020) is to stretch out the spherical surface either above the solar equator or above the poles to obtain an oblate or prolate ellipsoidal source surface, respectively. Figure 1 shows cuts through various source surfaces of different ellipticities to be used with the new solver. The solar rotation axis is aligned vertically, and the lower boundary (i.e., the photosphere) is the same as in the spherical model.

Evaluating the validity of predictions made by the PFSS model is complicated because the solar magnetic configuration can neither be simply reproduced in a clean laboratory environment nor measured remotely with high accuracy. Instead, the scientific community is forced to work with sparsely available in situ magnetic field spacecraft data (Hoeksema et al. 1983; Hoeksema 1984; Neugebauer et al. 1998; Badman et al. 2020), derive the magnetic field configuration from optical observations of the inner solar corona, such as white-light images or extreme ultraviolet (EUV) maps (Altschuler and Newkirk 1969; Smith and Schatten 1970; Levine et al. 1982; Lee et al. 2011), or compare the results of the PFSS model with the results of more intricate MHD models (Riley et al. 2006; Schulz et al. 1978; Schulz 1997).

The assumptions of the PFSS model are more often violated during the solar activity maximum than during the minimum. Therefore, the model is expected to perform worse during the solar maximum. To quantify this effect and illustrate the shortcomings of the model during the solar activity maximum, we

performed the analysis in different periods of the solar activity cycle.

In the following, we present a method for comparing the magnetic field polarity predictions made by the PFSS model at the source surface to the in situ measurements of the near-Earth interplanetary magnetic field (IMF) taken by three spacecraft, namely the twin Solar Terrestrial Relations Observatory (STEREO-A and STEREO-B) and the Advanced Composition Explorer (ACE). The connection between these two locations is accomplished via ballistic back mapping along the Parker spirals from the spacecraft down to the source surface. We evaluate the two parameters, source surface height and ellipticity, using this back mapping polarity measure.

## 2. Methods

In the absence of laboratory setups, there are two major possibilities for evaluating the quality of solar magnetic field models. The first is an analysis of remote sensing data, such as white-light images of the solar corona or EUV images of the photosphere (see, e.g., Zhao et al. 2017; Huang et al. 2019). The second option is a comparison of in situ measurements of the IMF to values predicted by the model (see, e.g., Bale et al. 2019; Badman et al. 2020). The problem with the former method, due to the absence of high-resolution remote sensing magnetic field measurements above the lower corona, is the necessity of additional assumptions to derive the actual magnetic field configuration from these images. White-light images can be easily computed from predictions of MHD models because these models also compute the particle number density in the computational domain (see, e.g., Mikić et al. 2018). To the contrary, the PFSS model only calculates the magnetic field. Producing an image for comparison to remote sensing images without the knowledge of the particle density is, in our experience, not reliable. Nevertheless, it is feasible to draw magnetic field lines over coronagraph images and compare the overall orientation of magnetic to optical features, though projection effects impede conclusive or quantitative statements when comparing model parameters that might only slightly alter the magnetic field configuration.

Another method of evaluating the merits of solar magnetic field models via remote sensing instrumentation is to analyze the brightness of the synoptic EUV maps of the photosphere (see, e.g., Lee et al. 2011). Open magnetic field lines (i.e., those that reach the source surface) are typically associated with darker regions in the EUV spectrum. Therefore, a better model is expected to, on average, map the footprints of open magnetic field lines to darker spots in the EUV spectrum. While this is a worthwhile analysis, it poses several problems: Depending on the wavelength of the analyzed EUV map, light emission originates in a thin sheet above the photosphere rather than in the photosphere itself. This will lead to some projection effects, similar to but not as strong as with white-light imaging. The average brightness of the EUV maps is dependant on the solar activity cycle; therefore, some form of normalization needs to be applied. Additionally, because the analysis concentrates on the lower boundary of the PFSS model, the upper boundary, where the model differs the most from the spherical model, is not examined.

Due to these shortcomings, we chose to first employ the second method of analyzing in situ measurements for evaluating the PFSS model and will leave the EUV method for another investigation. The problem with in situ measurements is the gap between available measurements (which are mostly obtained near 1 AU) and the regime of interest, which, in the case of the

Spacecraft	Solar Wind Type	Period 1 (declining) CR2041-CR2055			Period 2 (minimum) CR2066-CR2075			Period 3 (maximum) CR2133-CR2142		
		n	$P_{m,s}/P_{m,e}$ (%)	$\sigma_s/\sigma_e$ (%)	n	$P_{m,s}/P_{m,e}$ (%)	$\sigma_s/\sigma_e$ (%)	n	$P_{m,s}/P_{m,e}$ (%)	$\sigma_s/\sigma_e$ (%)
ACE	ejcta	969	79/79	2.9/3.0	485	73/75	2.4/2.6	1644	72/71	1.7/1.7
	coronal hole	8464	94/93	0.2/0.3	11097	94/94	0.2/0.2	5364	89/85	1.2/1.8
	sector reversal	10646	60/60	1.2/1.3	7570	65/69	1.9/1.6	7822	59/57	0.8/0.9
	streamer belt	11494	79/77	0.7/0.9	13284	81/82	0.5/0.7	14076	76/70	1.4/1.9
	overall	31573	76/75	0.7/0.8	32436	82/83	0.5/0.5	28906	74/69	1.0/1.2
STEREO-A	ejcta				15048	87/86	1.6/1.9	40060	74/72	1.1/1.4
	coronal hole				123548	89/90	0.5/0.3	61216	90/88	0.4/0.6
	sector reversal				66893	61/68	2.0/1.2	46468	51/53	1.9/1.8
	streamer belt				163059	83/84	0.6/0.6	155228	75/72	1.1/1.3
	overall				368548	81/83	0.6/0.4	302972	74/72	0.7/0.9
STEREO-B	ejcta				8421	81/85	4.0/2.0	10325	76/79	1.5/1.3
	coronal hole				91748	93/93	0.4/0.5	8003	87/71	2.8/8.1
	sector reversal				58988	67/72	1.2/1.2	7956	64/64	1.5/2.3
	streamer belt				108680	83/82	0.9/1.2	30247	74/73	1.3/1.9
	overall				267837	83/84	0.7/0.7	56531	75/73	1.2/1.6

**Table 1.** Back mapping polarity measure for the spherical source surface at  $2.5r_\odot$ . The first column lists the spacecraft, the second column lists the solar wind types, and columns 3 to 5 show the data for three different periods. Also shown are the sample count (n) and the correctly predicted magnetic field polarity fractions ( $p_{m,s/e}$ ) and standard deviations ( $\sigma_{s/e}$ ) of the evaluation procedure for the standard  $r_{ss} = 2.5r_\odot$  spherical PFSS model (subscript s) and the elliptic model with parameters  $r_{ss} = 2.5r_\odot$  and  $e_o = 1.667$  (subscript e). Data samples were partitioned according to the Xu and Borovsky (2015) scheme into four classes of solar wind types for three periods (columns) and three spacecraft (rows). Analyzing streamer belt wind on the ACE during solar activity minimum shows that there were n = 13284 data samples available, 80.8% (=  $p_{m,s}$ ) of which mapped to correctly predicted magnetic field polarities on the source surface with a standard deviation of  $\sigma_s = 0.5\%$  in the spherical model.

PFSS model, only spans a few solar radii above the photosphere. Therefore, it is necessary to map the in situ measurements of the solar wind parcels to the regime where they originated to have a reliable proxy for the remote magnetic field.

Section 2.1 describes the elliptical PFSS model that is evaluated here. In Sect. 2.2, we discuss the general procedure of tracking in situ measured solar wind packages to the source surface of the PFSS model and comparing predicted and observed magnetic field polarity. To better focus on the most interesting solar wind observations, we describe how to partition the measured solar wind data into meaningful categories according to the four-class Xu-Borovsky-scheme discussed in Sect. 2.3. We perform the analysis for three different periods during solar activity cycles 23 and 24. One period investigates the declining solar activity cycle nearing solar activity minimum, one analyzes the solar activity minimum, and one performs the same method during solar activity maximum. The analyzed periods and utilized instrumentation are discussed in Sect. 2.4.

### 2.1. Elliptical PFSS model

To incorporate elliptical source surfaces into the paradigm of the PFSS model, we need a numerical grid that is spherical at the photosphere and incrementally morphs into the desired elliptical shape with increasing height. The parameter of the source surface height is substituted for the minimum source surface height  $r_{ss}^m$ , and a second parameter (i.e., the ellipticity) is added, which determines the maximum deviation from the spherical shape at the highest position in the numerical grid (i.e., at the source surface). In the oblate case, the minimum source surface height is

found above the poles, while in the prolate case, it is found above the solar equator (see Fig. 1).

The ellipticity parameter defines how the maximum source surface height compares to the minimum source surface height  $r_{ss}^m$ . Because our model employs a case-differentiation for the oblate and prolate ellipsoidal source surfaces, we denote the ellipticity parameter in the oblate case with  $e_o$  and in the prolate case with  $e_p$ . An ellipticity of  $e_o = 2.0$  in the oblate case means that the equatorial source surface height is twice the polar source surface height, and, in the prolate case,  $e_p = 2.0$  denotes a source surface that is twice as high at the poles compared to the equator. In Fig. 1, the two red shapes are prolate ellipsoids with a minimum source surface height of  $r_{ss}^m = 2.5r_\odot$ , where  $r_\odot$  is the solar photospheric radius. A growing prolate ellipticity parameter stretches the grid in the polar direction while the (minimum) equatorial source surface height remains unaltered. Similarly, in the oblate case, the grid is stretched in the equatorial direction with increasing oblate ellipticity while the minimum source surface height above the poles remains the same. Therefore, to keep a constant source surface height above the equator with increasing oblate ellipticity, the minimum source surface height (above the poles) has to be reduced, which is visualized by the blue shapes in Fig. 1.

Our numerical solver utilizes finite differences and an Euler stepping algorithm to obtain a solution to Laplace's equation at all grid points. The grid we use for all analyses presented here has  $35 \times 87 \times 175$  grid points. The grid points are equidistant in the zonal direction, equidistant in sine-latitude in the meridional direction, and have a geometrically increasing spacing in the radial direction. The Laplace operator was derived for general curvi-

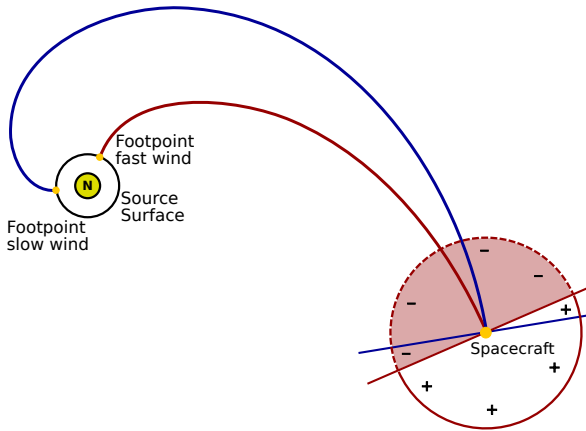


**Fig. 2.** Ecliptic view of the experimental setup (not to scale). Theoretical paths of fast (red) and slow (blue) solar wind packages traced from the spacecraft down to the source surface constitute two coordinate frames. The magnetic polarity is defined by the projection of the magnetic field vector onto the Parker spiral in the respective frame. Two hemispheres are separated by a plane perpendicular to each Parker spiral (colored accordingly). A vector has a positive sign if it lies within the anti-sunward hemisphere (pointing outward, solid half-circle) and has a negative sign if it lies within the sunward hemisphere (pointing inward, dashed half-circle). The depicted hemispheres illustrate the situation in the fast solar wind frame. The slow wind frame has two hemispheres that are defined analogously.

linear coordinates and adjusted for our special case. More information on the technical details of the solver and differences in predicted polarity and heliospheric current sheet locations between the spherical and elliptical solvers is available in Kruse et al. (2020).

## 2.2. Back mapping polarity measure

Because the solar wind flows radially away from the Sun, it carries with it the frozen-in magnetic field, which thus forms an Archimedean spiral. Assuming that the plasma parcel being investigated flows at a constant solar wind speed from the source surface to the observer, the footpoint of the magnetic field line (the Parker spiral) on the source surface is easily calculated. Let  $\Omega_{\odot} = 2.972 \cdot 10^{-6} \frac{\text{rad}}{\text{s}}$  be the rigid rotational speed of the Sun and  $v_p$  the solar wind bulk flow speed measured at the spacecraft. The zonal ballistic footpoint position  $\Phi_{fp}$  of the spacecraft position  $\Phi_{sc}$  on an arbitrary heliocentric height  $r$  can be obtained via the equation

$$\Phi_{fp} = \Phi_{sc} + \frac{(r_{sc} - r) \cdot \Omega_{\odot}}{v_p}, \quad (1)$$

where  $r_{sc}$  is the heliocentric distance of the spacecraft.

Having obtained a position on the source surface, we can then extract the magnetic polarity predicted at that position by our various PFSS implementations and compare it to the magnetic polarity measured aboard the spacecraft down from which the plasma package was traced. Figure 2 shows a schematic of the measurement configuration. If the polarities are the same, we note a correctly predicted sample. If they differ, we note a false

prediction. The overall fraction of correctly predicted samples serves as our quality metric, where higher numbers denote better predictions.

The back mapping polarity measure is noticeably simple, as even just guessing the polarity of a large number of samples would yield a 50% correct prediction rate. A sufficient implementation needs to be significantly better than this 50% threshold. Furthermore, the polarity alone does not give insight into the correctness of the magnetic configuration below the source surface. Nevertheless, this metric allows us to compare different implementations and periods relative to one another: An implementation that does not even get the polarity right is not assumed to perform better in absolute terms compared to one that does.

As a variability measure of this metric, we employed a form of cross-validation using the following method. Each analysis spans several Carrington rotations. Let  $N$  denote the number of full Carrington rotations observed. Instead of computing the fraction of correctly mapped samples for the entire period, we computed  $N$  sets of fractions where, for each set, another Carrington rotation is excluded from the analysis. Let  $p_{m,i}$  denote the fraction of correctly mapped samples where Carrington rotation  $i$  ( $i \in \{0, \dots, N-1\}$ ) is excluded. The final value of this metric is the average over all data sets,  $p_m = 1/N \sum_{i=0}^{N-1} p_{m,i}$ . The standard deviation of this data set,  $\sigma = \sqrt{\frac{1}{N-1} \sum_{i=0}^{N-1} (p_{m,i} - p_m)^2}$ , is used as an error or variability measure of the analysis.

## 2.3. Selection of data samples

Not all solar wind observations give the same insight into the validity of the underlying model of the solar magnetic field. We expect the most interesting results for regions where the polarity of the large-scale magnetic field changes, that is to say, we try to mostly analyze solar wind packages that originated near current sheet crossings.

We partitioned the whole data set according to the Xu and Borovsky (2015) solar wind categorization scheme into four categories. The first is coronal-hole plasma, historically also known as the fast solar wind, which originates above open magnetic structures mostly near high latitudes. The second type is called streamer belt plasma, which is believed to originate near the edges of coronal holes. The third and most interesting type for our analysis is sector reversal plasma, which is likely emitted around helmet streamers where the polarity of the coronal magnetic field changes its polarity. The last type of solar wind is called the ejecta type and is associated with dynamic and short-lived processes like coronal mass ejections. Because the PFSS model is a static model, we do not expect it to be able to predict any dynamic processes; therefore, we omit this wind type from further analysis. We also omit coronal-hole plasma because we do not expect many magnetic polarity changes.

The Xu and Borovsky (2015) scheme requires four types of in situ measurements; they are the proton temperature  $T_p$ , bulk flow velocity  $v_p$ , proton number density  $n_p$ , and magnetic field strength  $B$ . Although the hyperplanes that separate the solar wind types in this four-dimensional space have been derived for the instruments aboard the ACE spacecraft, we also employed this scheme to the twin STEREO spacecraft, which are roughly at the same heliocentric height as ACE and therefore are expected to measure similar characteristics of the solar wind.

Here we mostly concentrate on sector reversal wind and streamer belt wind. This way, we can take a closer look at solar wind streams that feature specific behaviors where this metric might yield the most interesting results, namely, the loca-

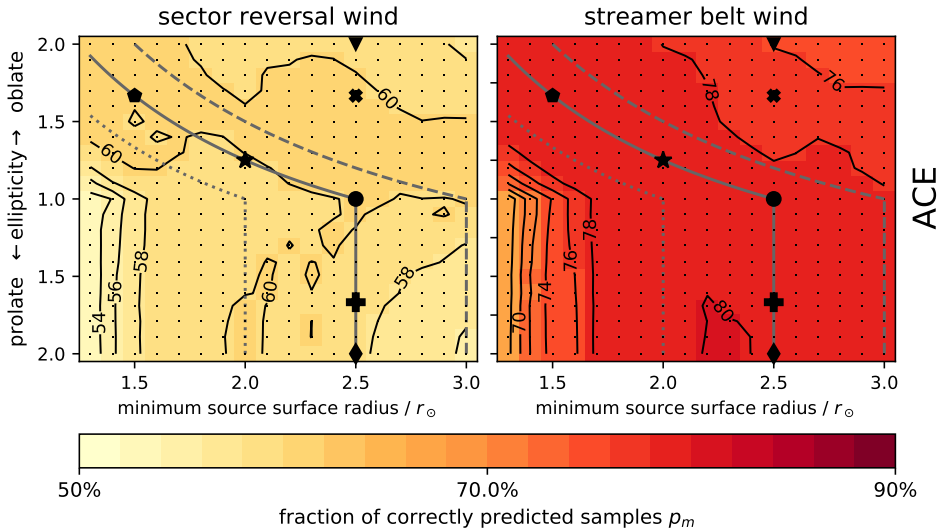


**Fig. 3.** Back mapping polarity measure for streamer belt and sector reversal wind. Ballistic back mapping was performed from ACE to the source surface during period 1 (CR2041–CR2055, 2006, declining solar activity). The colored pixels give the value at their center positions (black dots) in 2% increments. A contour plot bi-linearly interpolating between these values has been drawn on top. Lines marking model parameters of constant equatorial source surface height have been inserted for  $r_{ss,eq} = 2.5r_\odot$  (solid gray line), for  $r_{ss,eq} = 2.0r_\odot$  (dotted gray line), and for  $r_{ss,eq} = 3.0r_\odot$  (dashed gray line). The black symbols mark the parameters for the example source surfaces from Fig. 1.

tions of the current sheet crossings. Furthermore, we excluded plasma packages that were identified to be part of interplanetary coronal mass ejections (ICME) according to the lists of Cane and Richardson (2003), Richardson and Cane (2010), and Jian et al. (2018) as these plasma streams have different characteristics than the previously stated radial expansion of the unperturbed solar wind. They are also inconsistent with the basic assumptions of the PFSS model that demand a static coronal magnetic field configuration.

The Xu-Borovsky scheme is not a perfect partition of the solar wind. Due to the strict boundaries in the four-dimensional parameter space, and without context-sensitive measures, there will always be falsely identified plasma packages. In addition, the solar magnetic field exhibits so-called kinks (see, e.g., Berger et al. 2011), where the overall large-scale polarity is disturbed by short periods of opposite polarity. While a correction of these factors might be beneficial for the analysis, there is the risk of introducing new errors into the data sets by employing an untested correction scheme. We, therefore, chose to accept these minor flaws in the evaluation presented here. We estimate the difference in prediction accuracy due to short-lived polarity reversals in Sect. 3.3.

#### 2.4. Evaluated periods and instrumentation

An analysis of large data sets would be desirable to increase the validity of the obtained results. Unfortunately, high-resolution space-bound photospheric magnetogram data have only been available for less than three decades. It would be preferable to analyze the same stages of the solar activity cycle in different individual cycles, but we only have the three decades' worth of data. Therefore, we chose ten Carrington rotations from a single cycle for each of the three stages of interest. In period 1,

we investigate the declining solar activity phase of solar cycle 23 during Carrington rotations 2041 to 2055 (in 2006), excluding rotations 2044, 2046, 2047, 2050, and 2053. Period 2, which analyzes the minimum between solar activity cycles 23 and 24, consists of Carrington rotations 2066 to 2075 (in 2008), and period 3, which examines the solar activity maximum of cycle 24, is comprised of Carrington rotations 2133 to 2142 (in 2013). Because we want to examine EUV maps in future studies, we excluded some rotations from the declining period that had missing data in either the utilized magnetograms or the corresponding EUV maps. The magnetograms for the minimum and maximum periods 2 and 3 had better coverage, but we also have fewer Carrington rotations to choose from; we therefore decided not to exclude any rotations from these periods.

The utilized photospheric magnetograms for the PFSS computation were obtained from the Michelson Doppler Imager (MDI) (Scherrer 1995) aboard the Solar and Heliospheric Observatory (SOHO) spacecraft for periods 1 and 2 and from the Helioseismic and Magnetic Imager (HMI) (Scherrer et al. 2012) aboard the Solar Dynamics Observatory (SDO), the successor spacecraft to SOHO. Unfortunately, MDI data are not available for the third period. Synoptic magnetograms of complete Carrington rotations were used for the analysis.

For the back mapping analysis, we chose data from ACE (Stone et al. 1998) and the twin STEREO (Kaiser et al. 2008) mission. All three spacecraft operate in the ecliptic plane near Earth's orbit. Solar wind speeds at ACE were measured by the Solar Wind Electron, Proton, and Alpha Monitor (SWEPAM) (McComas et al. 1998a) as well as by the Solar Wind Ion Composition Spectrometer (SWICS) (Gloeckler et al. 1998). We utilized a merged 12-minute SWICS/SWEPAM data set. For the STEREO spacecraft, we used a one-minute data set for solar wind speeds that were measured by the Plasma and Suprathermal

Ion Composition (PLASTIC) instruments (Galvin et al. 2008). In situ measurements of the magnetic field were carried out on the STEREO spacecraft by the In situ Measurements of Particles and CME Transients (IMPACT) suite (Luhmann et al. 2008; Acuña et al. 2008) and by the Magnetic Fields Experiment (MAG) onboard ACE (Smith et al. 1998).

For the back mapping polarity measure, data from the two instruments aboard each spacecraft are required to have the same sampling rates. This means we had to resample the four-minute data set from MAG aboard ACE to match the 12-minute cadence of the merged SWICS/SWEPAM data set. All data sets of instruments aboard the STEREO spacecraft have a cadence of one minute, so resampling was not necessary for the STEREO spacecraft. We also created data sets of the same cadence (12 minutes) to analyze the influence of the sampling rate but found no noticeable difference in the results; we therefore chose to utilize the higher sampling rates of the STEREO instrumentation.

### 3. Results: Magnetic field polarity prediction accuracy

To employ the PFSS model, assumptions about the coronal plasma have to be simplified. This largely refers to the premises that there are no electric currents between the photosphere and the source surface and that there are stable conditions during an entire Carrington rotation. We know that these assumptions are never completely true, but the question remains of whether they are accurate enough during the solar cycle to warrant the usage of the PFSS model for the prediction of the magnetic configuration.

Our findings for the spherical PFSS model with the widely accepted best source surface radius of  $2.5r_{\odot}$  are summarized in Sect. 3.1. We then investigate the impact of the ellipticity of the source surface on the accuracy of the prediction, which we present in Sect. 3.2.

#### 3.1. Accuracy of prediction throughout the solar cycle

Table 1 shows the fraction of samples that have the same polarity measured in situ aboard the spacecraft and at the source surface as predicted by the PFSS implementations. We used our grid implementation of the spherical PFSS model with a radial lower boundary condition (Altschuler and Newkirk 1969) and with a source surface radius of  $2.5r_{\odot}$ .

Solar wind that has been classified as ejecta probably originated in non-current-free regions, for which the basic assumptions of the PFSS model are not valid; therefore, the back mapping will likely not point to the correct source region. Coronal hole wind originates far outside of regions with expected magnetic polarity changes; hence a high fraction of correctly matched polarities is not surprising. Streamer belt and sector reversal wind constitute the most interesting data sets as they originate close to the current sheet where most polarity changes take place. As can be seen in Table 1, polarity prediction during solar maximum is much less accurate compared to the solar minimum. This is not surprising because the basic assumptions that the region below the source surface is current-free and stationary during an entire Carrington rotation are violated more often during solar maximum. Especially for the sector reversal wind, where most current sheet crossings take place, the prediction accuracy drops to almost 50%, illustrating the shortcoming of the PFSS model during the active part of the solar activity cycle.

#### 3.2. Dependence of prediction accuracy on source surface ellipticity

To determine the impact of a nonspherical surface on the coronal magnetic field, we repeated the back mapping analysis while varying the ellipticity and minimum source surface height parameters. In the following, we focus only on the more interesting solar wind types, namely sector reversal and streamer belt. Figure 3 depicts the results for period 1 (CR2041-CR2055) of the declining solar activity cycle. For period 2 (CR2066-CR2075) during solar minimum, the STEREO twin spacecraft mission was operational; therefore, in addition to back mapping from ACE, we have computed the back mapping prediction accuracy from STEREO-A and from STEREO-B in Fig. 4. The active Sun was analyzed during period 3 (CR2133-CR2142), and the results can be found in Fig. 5.

To better illustrate the meaning of the two parameters of our implementation, we depict cuts through various source surfaces in Fig. 1. As can be seen from this figure, increasing the ellipticity in the prolate case does not alter the equatorial source surface height, while in the oblate case, the equatorial height increases with increasing ellipticity. To keep the equatorial height constant with increasing ellipticity, the minimum source surface height  $r_{ss}^m$  has to be decreased. As all measurements from ACE, STEREO-A, and STEREO-B are made near the ecliptic, the equatorial source surface height plays a major role in our back mapping polarity measure. Moving within the figures to higher prolate ellipticities along the negative y-axis has a different effect than moving along the positive y-axis to higher oblate ellipticities. Because the analysis presented here only samples regions near the solar equator, major changes in other regions are not reflected. The most notable changes in the magnetic field configuration in the prolate models are present at higher latitudes, which are not sampled. This has to be kept in mind when interpreting Figs. 3 to 5. It also explains why there are fewer structures depicting the prolate source surfaces in the lower half of these figures. The magnetic field near the solar equator changes more notably with increasing oblate ellipticity than it does with increasing prolate ellipticity.

As can be seen from Figs. 3 to 5, back mapping polarity prediction performs noticeably worse for the active sun period 3 compared to the minimum period 2. This is to be expected as the assumption of a quasi-stationary environment breaks down when the Sun's activity cycle approaches its maximum. Furthermore, when comparing ACE back mapping in the declining and minimum periods 1 and 2, the PFSS model performs slightly better in the minimum period 2, with more pronounced peaks in the parameter space. The differences between the declining and maximum periods 1 and 3 are not as prominent as between the minimum and maximum periods 2 and 3. During the declining period 1 and the activity maximum period 3, the plateaus of best parameters are broader compared to the activity minimum period 2.

During the minimum period 2 (Fig. 4), the best agreement between the three spacecraft can be found in the streamer belt wind. The best prediction ratio of more than 80% for all spacecraft can be found at a minimum source surface radius of slightly above  $r_{ss}^m = 2.0r_{\odot}$  and an oblate source surface ellipticity of about  $e_o = 1.5$ , which amounts to an equatorial source surface radius of roughly  $r_{ss,eq} = 3.0r_{\odot}$ . For the sector reversal wind, the data are less clear. Firstly, the overall prediction ratio is substantially worse compared to the streamer belt wind, which is to be expected as this set contains the interesting current sheet crossings. Secondly, the position of the maximum varies strongly be-

tween the spacecraft. Thirdly, there is no clear single peak; the region of best prediction is broad. The figures suggest the best prediction ratio for slightly lower source surfaces with higher oblate ellipticities compared to the streamer belt data sets.

There are clear differences between the three spacecraft in the minimum and maximum periods 2 and 3. One major distinction is, of course, the instrumentation used for measuring in situ solar wind speed and magnetic configuration. In this regard, STEREO-A and STEREO-B results are at least mutually comparable as both are equipped with near-identical instruments. However, the Xu-Borovsky solar wind categorization scheme was developed using ACE data, so the classification process for the two STEREO spacecraft might be prone to errors, which affects the overall prediction ratios. STEREO-A is slightly closer to the sun than ACE, which is slightly closer than STEREO-B. Therefore, the difference in the position of the maximum in these plots might be attributable to the variation of the respective heliocentric distances, although they are still small compared to 1 AU.

### 3.3. Influence of short-lived polarity reversals

The heliospheric magnetic field exhibits short-lived polarity reversals that are not part of the large-scale magnetic field. The PFSS model is not able to resolve these so-called kinks of the magnetic field because they are local structures that are the result of wave-particle-interaction and turbulent processes. Thus, it would be desirable to filter out these kinks. A simple technique is to compute a running average of the magnetic field, thereby eliminating most of the polarity reversals that have a shorter duration than the window width of the averaging method. The problem with this method is that polarity reversals with a solar origin, which are relevant for the analysis, will be affected as well. Therefore, we chose not to filter the data set and to accept lower overall prediction ratios. The study presented here relies less on the absolute values of the prediction ratio than on relative changes and the position of the maximum in the two-dimensional parameter space. To estimate the impact of short-lived polarity reversals, we repeated the analysis for the minimum period 2 and spacecraft ACE with a running average and a window width of 15 samples, that is, a width of 180 minutes. This leads to a higher maximum in the parameter space of 2% for the sector reversal wind type, 6% for coronal-hole wind, and 8% for streamer belt samples. However, it is important to note that for the streamer belt samples and the sector reversal wind type, this increase in the prediction accuracy is in part caused by removing some of the relevant but particularly difficult polarity reversal with solar origin from the data set. More complex filtering techniques, for example considering the direction of the electron heat flux (Owens et al. 2017), could be applied to increase the prediction ratio without affecting polarity reversals with a solar origin; however, this is beyond the scope of this work.

## 4. Conclusions

We have presented a PFSS model with elliptic source surfaces and the back mapping polarity measure to evaluate it, as well as the data selection procedure to partition in situ solar wind spacecraft data into meaningful categories according to the Xu and Borovsky (2015) scheme. Not surprisingly, our results show that the predictability of the solar magnetic field polarity is better during solar minimum compared to solar maximum. While the fractions of correctly predicted samples  $p_m$  in the sector reversal wind are still slightly above the 50% threshold of pure guess-work, the usefulness of the PFSS model during solar maximum

for prediction of the coronal magnetic configuration is superficial at best. Our findings show that, during solar activity maximum, the most accurate, albeit still unsatisfactory, predictions can be made for source surfaces with an equatorial height of  $2.5r_\odot$ . The ellipticity parameter does not have a strong impact on the back mapping polarity measure during this period.

During the period of the solar activity minimum, our results suggest that the model performs better for slightly oblate elliptical source surfaces compared to the classical spherical model. The resulting equatorial source surface height is about  $r_{ss,eq} = 3r_\odot$ . This result is supported by data from all three spacecraft employed for this analysis in both sector reversal and streamer belt wind, although the exact parameters differ slightly. However, because our analysis was necessarily limited to the equatorial region, a definitive best set of parameters for all regions cannot yet be extracted from these findings. Our findings are also in stark contrast to those of Schulz et al. (1978), Schulz (1997), and Levine et al. (1982), who found that source surfaces with a greater height above the poles compared to the equator match the observations best. We would also like to mention that the visible peaks of the best parameter set stand only slightly higher in the parameter space than the surroundings with respect to the error of the back mapping polarity measure (see Table 1 and Figs. 3 to 5).

For a better prediction of the optimal parameters, a larger data set needs to be analyzed. Back mapping analysis from spacecraft outside of the ecliptic could give valuable insight into the magnetic configuration of elliptical PFSS models at higher latitudes. However, the Xu and Borovsky (2015) scheme was developed for instruments near 1 AU in the ecliptic plane, and therefore another partitioning scheme of solar wind streams is required for the analysis (e.g., Zhao et al. 2017). Ulysses and Solar Orbiter are the only two spacecraft outside the ecliptic that feature the instrumentation needed for this sort of analysis, with Solar Orbiter being the better option due to its lower perihelion distance. The higher heliocentric distance of Ulysses introduces more errors when ballistically mapping to the source surface due to the longer travel time of the plasma packages. Optimal parameters probably differ for different Carrington rotations as well.

We used a comparison of the in situ measured magnetic field polarity with that calculated at the source surface as the test metric and showed that the predictive power of an elliptic PFSS is not much better than that of a spherical PFSS model. We suspect that the elliptical model may hold a more substantial advantage over the spherical model for prediction accuracy in the corona below the source surface. Tracing the solar wind packages downward from the source surface to the photosphere is possible because the charged particles need to follow the magnetic field lines. Analyzing these photospheric footpoints in EUV images might provide another tool for evaluating the merit of nonspherical source surfaces, complementing the analysis presented here.

**Acknowledgements.** This work utilizes data from the Michelson Doppler Imager aboard SOHO. SOHO is a project of international cooperation between ESA and NASA. Magnetograms from HMI aboard SDO are courtesy of NASA/SDO and the AIA, EVE, and HMI science teams. Data from NASA's STEREO and ACE missions were used for this work. We thank the STEREO IMPACT and PLASTIC teams as well as the ACE SWICS,SWEPAM and MAG teams for making the data available to the scientific community.

## References

- Acuña, M. H., Curtis, D., Scheifele, J. L., Russell, C. T., Schroeder, P., Szabo, A., and Luhmann, J. G. (2008). The STEREO/IMPACT magnetic field experiment. *Space Science Reviews*, 136(1-4):203–226.

A&amp;A proofs: manuscript no. output

- Altschuler, M. D. and Newkirk, G. (1969). Magnetic fields and the structure of the solar corona. *Solar Physics*, 9(1):131–149.
- Badman, S. T., Bale, S. D., Martínez Oliveros, J. C., Panasenco, O., Velli, M., Stansby, D., Buitrago-Casas, J. C., Réville, V., Bonnell, J. W., Case, A. W., Dudok de Wit, T., Goetz, K., Harvey, P. R., Kasper, J. C., Korreck, K. E., Larson, D. E., Livi, R., MacDowall, R. J., Malaspina, D. M., Pulupa, M., Stevens, M. L., and Whittlesey, P. L. (2020). Magnetic Connectivity of the Ecliptic Plane within 0.5 au: Potential Field Source Surface Modeling of the First Parker Solar Probe Encounter. *The Astrophysical Journal Supplement Series*, 246(2):23.
- Bale, S. D., Badman, S. T., Bonnell, J. W., Bowen, T. A., Burgess, D., Case, A. W., Cattell, C. A., Chandran, B. D., Chaston, C. C., Chen, C. H., Drake, J. F., de Wit, T. D., Eastwood, J. P., Ergun, R. E., Farrell, W. M., Fong, C., Goetz, K., Goldstein, M., Goodrich, K. A., Harvey, P. R., Horbury, T. S., Howes, G. G., Kasper, J. C., Kellogg, P. J., Klimchuk, J. A., Korreck, K. E., Krasnoselskikh, V. V., Krucker, S., Laker, R., Larson, D. E., MacDowall, R. J., Maksimovic, M., Malaspina, D. M., Martinez-Oliveros, J., McComas, D. J., Meyer-Vernet, N., Moncquet, M., Mozer, F. S., Phan, T. D., Pulupa, M., Raouafi, N. E., Salem, C., Stansby, D., Stevens, M., Szabo, A., Velli, M., Woolley, T., and Wygant, J. R. (2019). Highly structured slow solar wind emerging from an equatorial coronal hole. *Nature*, 576(7786):237–242.
- Berger, L., Wimmer-Scheingruber, R. F., and Gloeckler, G. (2011). Systematic measurements of ion-proton differential streaming in the solar wind. *Physical Review Letters*, 106(15):151103.
- Cane, H. V. and Richardson, I. G. (2003). Interplanetary coronal mass ejections in the near-Earth solar wind during 1996–2002. *Journal of Geophysical Research: Space Physics*, 108(A4).
- Galvin, A. B., Kistler, L. M., Popecki, M. A., Farrugia, C. J., Simunac, K. D., Ellis, L., Möbius, E., Lee, M. A., Boehm, M., Carroll, J., Crawshaw, A., Conti, M., Demaine, P., Ellis, S., Gaidos, J. A., Googins, J., Granoff, M., Gustafson, A., Heirtzler, D., King, B., Knauss, U., Levesque, J., Longworth, S., Singer, K., Turco, S., Vachon, P., Vosbury, M., Widholm, M., Blush, L. M., Karrer, R., Bochsler, P., Daoudi, H., Etter, A., Fischer, J., Jost, J., Opitz, A., Sigrist, M., Wurz, P., Klecker, B., Ertl, M., Seidenschwang, E., Wimmer-Scheingruber, R. F., Koeten, M., Thompson, B., and Steinfeld, D. (2008). The plasma and suprathermal ion composition (PLASTIC) investigation on the STEREO observatories. *Space Science Reviews*, 136(1-4):437–486.
- Gloeckler, G., Cain, J., Ivavich, F. M., Tums, E. O., Bedini, P., Fisk, L. A., Zurbuchen, T. H., Bochsler, P., Fischer, J., Wimmer-Scheingruber, R. F., Geiss, J., and Kallenbach, R. (1998). Investigation of the composition of solar and interstellar matter using solar wind and pickup ion measurements with swics and swims on the ace spacecraft. *Space Science Reviews*, 86(1-4):497–539.
- Hoeksema, J. T. (1984). *Structure and Evolution of the Large Scale Solar and Heliospheric Magnetic Field*. PhD thesis.
- Hoeksema, J. T., Wilcox, J. M., and Scherrer, P. H. (1983). Structure of the Heliospheric Current Sheet: 1978–1982. *Journal of Geophysical Research*, 88(A12):9910–9918.
- Huang, G.-H., Lin, C.-H., and Lee, L.-C. (2019). Examination of the EUV Intensity in the Open Magnetic Field Regions Associated with Coronal Holes. *The Astrophysical Journal*, 874(1):45.
- Jian, L. K., Russell, C. T., Luhmann, J. G., and Galvin, A. B. (2018). STEREO Observations of Interplanetary Coronal Mass Ejections in 2007–2016. *The Astrophysical Journal*, 855(2):114.
- Kaiser, M. L., Kucera, T. A., Davila, J. M., Cyr, O. C., Guhathakurta, M., and Christian, E. (2008). The STEREO mission: An introduction. *Space Science Reviews*, 136(1-4):5–16.
- Kruse, M., Heidrich-Meisner, V., Wimmer-Scheingruber, R. F., and Hauptmann, M. (2020). An elliptic expansion of the potential field source surface model. *Astronomy & Astrophysics*, 638:A109.
- Lee, C. O., Luhmann, J. G., Hoeksema, J. T., Sun, X., Arge, C. N., and de Pater, I. (2011). Coronal Field Opens at Lower Height During the Solar Cycles 22 and 23 Minimum Periods: IMF Comparison Suggests the Source Surface Should Be Lowered. *Solar Physics*, 269(2):367–388.
- Levine, R. H., Schulz, M., and Frazier, E. N. (1982). Simulation of the magnetic structure of the inner heliosphere by means of a non-spherical source surface. *Solar Physics*, 77(1-2):363–392.
- Luhmann, J. G., Curtis, D. W., Schroeder, P., McCauley, J., Lin, R. P., Larson, D. E., Bale, S. D., Sauvaud, J. A., Aoustin, C., Mewaldt, R. A., Cummings, A. C., Stone, E. C., Davis, A. J., Cook, W. R., Kecman, B., Wiedenbeck, M. E., Von Rosenvinge, T., Acuna, M. H., Reichenthal, L. S., Shuman, S., Wortman, K. A., Reames, D. V., Mueller-Mellin, R., Kunow, H., Mason, G. M., Walpole, P., Korth, A., Sanderson, T. R., Russell, C. T., and Gosling, J. T. (2008). STEREO IMPACT investigation goals, measurements, and data products overview. *Space Science Reviews*, 136(1-4):117–184.
- Mackay, D. H. and Yeates, A. R. (2012). The Sun's global photospheric and coronal magnetic fields: Observations and models. *Living Reviews in Solar Physics*, 9.
- McComas, D. J., Bame, S. J., Barker, P., Feldman, W. C., Phillips, J. L., Riley, P., and Griffee, J. W. (1998a). Solar wind electron proton alpha monitor (SWEPAM) for the advanced composition explorer. *Space Science Reviews*, 86(1-4):563–612.
- McComas, D. J., Bame, S. J., Barracough, B. L., Feldman, W. C., Funsten, H. O., Gosling, J. T., Riley, P., Skoug, R., Balogh, A., Forsyth, R., Goldstein, B. E., and Neugebauer, M. (1998b). Ulysses' return to the slow solar wind. *Geophysical Research Letters*, 25(1):1–4.
- Mikić, Z., Downs, C., Linker, J. A., Caplan, R. M., Mackay, D. H., Upton, L. A., Riley, P., Lionello, R., Török, T., Titov, V. S., Wijaya, J., Druckmüller, M., Pasachoff, J. M., and Carlos, W. (2018). Predicting the corona for the 21 August 2017 total solar eclipse. *Nature Astronomy*, 2(11):913–921.
- Neugebauer, M., Forsyth, R. J., Galvin, A. B., Harvey, K. L., Hoeksema, J. T., Lazarus, A. J., Lepping, R. P., Linker, J. A., Mikić, Z., Steinberg, J. T., von Steiger, R., Wang, Y.-M., and Wimmer-Scheingruber, R. F. (1998). Spatial structure of the solar wind and comparisons with solar data and models. *Journal of Geophysical Research*, 103(A7):14587.
- Owens, M. J., Lockwood, M., Riley, P., and Linker, J. (2017). Sunward Strahl: A Method to Unambiguously Determine Open Solar Flux from In Situ Spacecraft Measurements Using Suprathermal Electron Data. *Journal of Geophysical Research: Space Physics*, 122(11):10,980–10,989.
- Richardson, I. G. and Cane, H. V. (2010). Near-earth interplanetary coronal mass ejections during solar cycle 23 (1996 – 2009): Catalog and summary of properties. *Solar Physics*, 264(1):189–237.
- Riley, P., Linker, J. A., Mikić, Z., Lionello, R., Ledvina, S. A., and Luhmann, J. G. (2006). A Comparison between Global Solar Magnetohydrodynamic and Potential Field Source Surface Model Results. *The Astrophysical Journal*, 653(2):1510–1516.
- Schatten, K. H., Wilcox, J. M., and Ness, N. F. (1969). A model of interplanetary and coronal magnetic fields. *Solar Physics*, 6(3):442–455.
- Scherrer, P. (1995). [dataset] MDI. DOI:10.5270/esa-9kpuds2.
- Scherrer, P. H., Schou, J., Bush, R. I., Kosovichev, A. G., Bogart, R. S., Hoeksema, J. T., Liu, Y., Duvall, T. L., Zhao, J., Title, A. M., Schrijver, C. J., Tarbell, T. D., and Tomczyk, S. (2012). The Helioseismic and Magnetic Imager (HMI) Investigation for the Solar Dynamics Observatory (SDO). *Solar Physics*, 275(1-2):207–227.
- Schulz, M. (1997). Non-spherical source-surface model of the heliosphere: A scalar formulation. *Annales Geophysicae*, 15(11):1379–1387.
- Schulz, M., Frazier, E. N., and Boucher, D. J. (1978). Coronal magnetic-field model with non-spherical source surface. *Solar Physics*, 60(1):83–104.
- Smith, C. W., L'Heureux, J., Ness, N. F., Acuña, M. H., Burlaga, L. F., and Scheifele, J. (1998). The ace magnetic fields experiment. *Space Science Reviews*, 86(1-4):613–632.
- Smith, S. M. and Schatten, K. H. (1970). Preliminary comparison of predicted and observed structure of the solar corona at the eclipse of March 7, 1970. *Nature*, 226(5251):1130–1131.
- Stone, E. C., Frandsen, A. M., Mewaldt, R. A., Christian, E. R., Margolies, D., Ormes, J. F., and Snow, F. (1998). The advanced composition explorer. *Space Science Reviews*, 86(1-4):1–22.
- Xu, F. and Borovsky, J. E. (2015). A new four-plasma categorization scheme for the solar wind. *Journal of Geophysical Research: Space Physics*, 120(1):70–100.
- Zhao, L., Landi, E., Lepri, S. T., Gilbert, J. A., Zurbuchen, T. H., Fisk, L. A., and Raines, J. M. (2017). On the Relation between the In Situ Properties and the Coronal Sources of the Solar Wind. *The Astrophysical Journal*, 846(2):135.
- Zhao, X. and Hoeksema, J. T. (1995). Prediction of the interplanetary magnetic field strength. *Journal of Geophysical Research*, 100(A1):19.

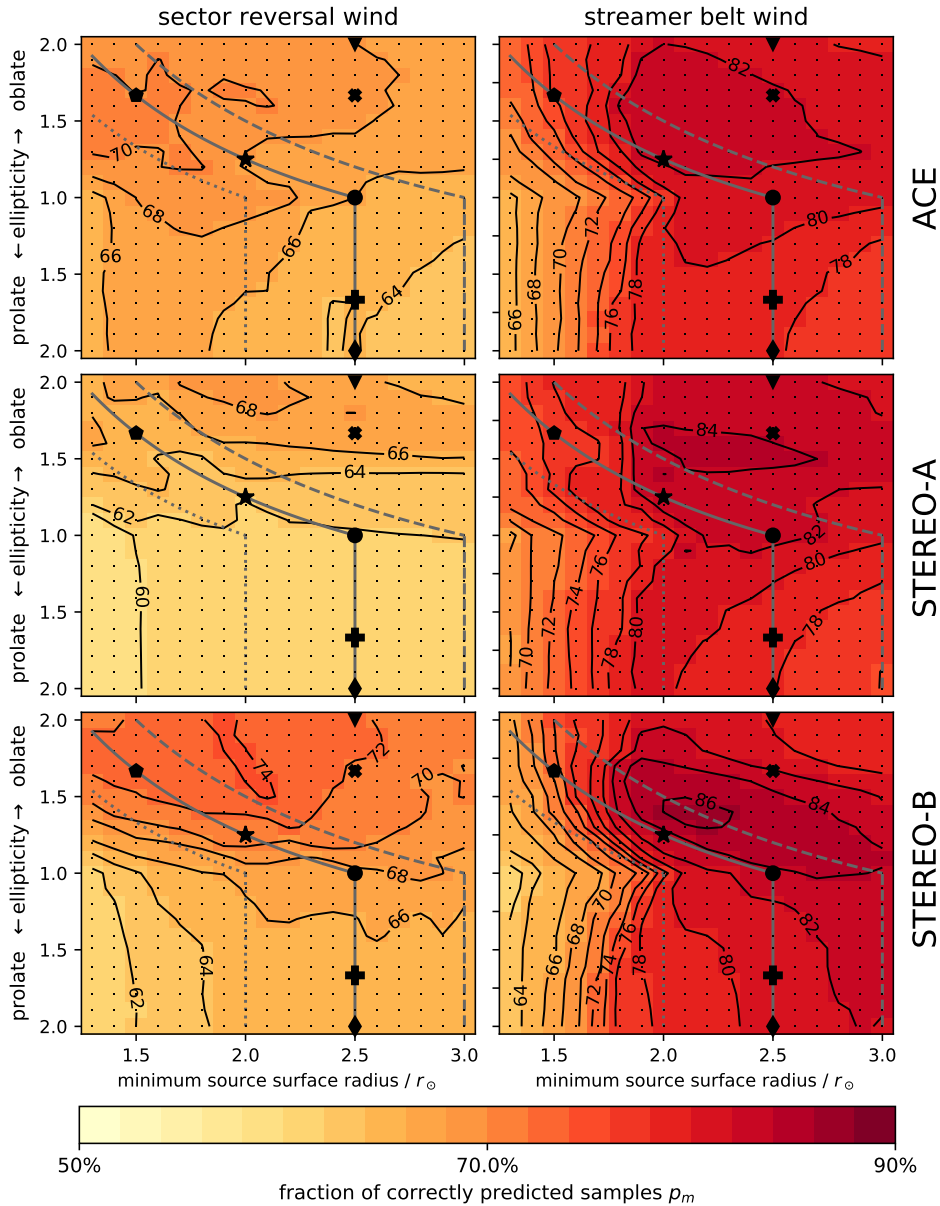


**Fig. 4.** Back mapping polarity measure for period 2 (CR2066-CR2075, 2008, solar activity minimum) for spacecraft ACE, STEREO-A, and STEREO-B. The format is the same as in Fig. 3.

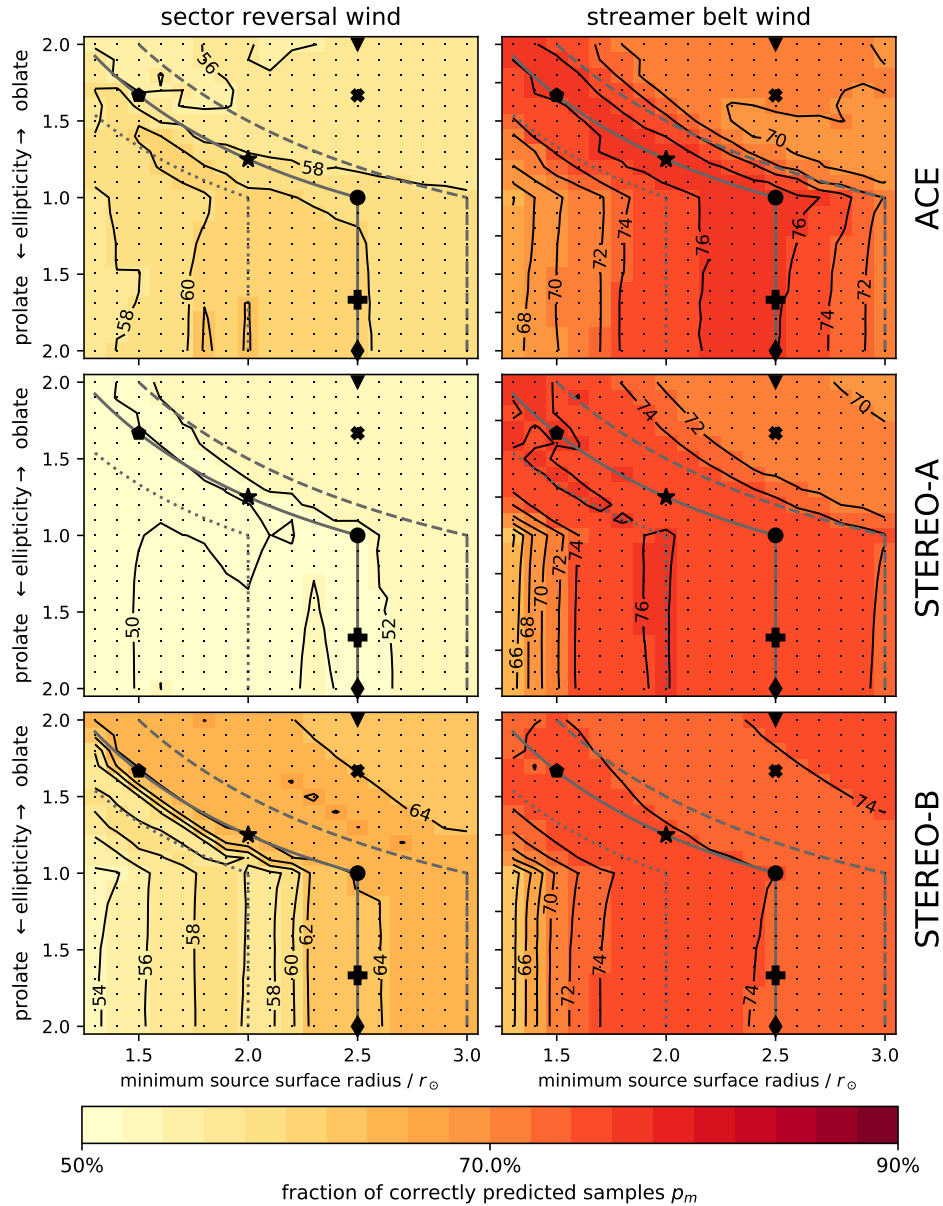


**Fig. 5.** Back mapping polarity measure period 3 (CR2133-CR2142, 2013, solar activity maximum). The format is the same as in Figs. 3 and 4.

## APPLICATIONS

---

Investigations of the solar corona pose considerable obstacles. Due to the hostile environment near our central star, probing the Sun's vicinity via spacecraft travel and in-situ instrumentation is nearly impossible. The closest human-made object to send back information from the upper corona currently is Parker Solar Probe ([PSP](#)), which was launched in 2018 and is planned to achieve the deepest dive of less than 10 solar radii [[Fox et al., 2016](#)]. Another mission to probe the close surroundings of the Sun is Solar Orbiter, which was launched in early 2020 under the participation of the Department of Extraterrestrial Physics at the University of Kiel. Solar Orbiter will achieve a perihelion of about 60 solar radii - further up in the heliosphere compared to [PSP](#) - but with a higher ecliptic inclination of up to 30° [[Müller et al., 2013](#)]. Even though both missions are remarkable scientific and engineering achievements, their closest approach is still a few million kilometers away from the solar photosphere, a neighborhood of abundant physical processes that are not well understood.

To obtain information on the inner corona and close to the photosphere or even below, the scientific community is dependent on remote sensing instrumentation (e.g., eclipse images, coronagraphs, [EUV](#) images) or heliospheric models that can link in-situ measurements of the solar wind plasma further out in the heliosphere to their origin on or close to the solar surface. The [PFSS](#) model predicts the coronal magnetic field from synoptic magnetograms measured by a plethora of observatories, both Earth-bound and in near-Earth space (see Sect. [5.2.1](#)). Due to its simplicity, it is an important tool to link solar wind parcels and investigations of their characteristics to their most-likely source regions in the lower corona or the photosphere. This chapter is concerned with applications of scientific endeavors that rely on the [PFSS](#) model as an integral part of the analysis. For all investigations presented in the following, the semi-numerical grid solver described in Chapter [3](#) was employed with a standard, spherical source surface radius of  $R_{ss} = 2.5 \cdot R_\odot$ .

### 7.1 SOLAR WIND ORIGIN

To better understand the solar wind and its physical properties, the scientific community has been trying to identify its source regions. While it seems clear that some form of fast solar wind originates in coronal holes [e.g., [Wilcox, 1968](#); [Krieger et al., 1973](#); [Cranmer, 2005](#)], the multitude of slow solar wind types cannot be associated with a definitive type of source region. Several candidates have been suggested, such as the edges of coronal-holes, edges of active regions, helmet streamers, and a surface-spanning structure called the S-Web (see Sect. [1.1](#) and references therein).

The task of finding the solar wind's origins is tightly coupled with that of its acceleration mechanism. While most slow and fast solar wind accelerations occur in the lower corona, the acceleration mechanisms can differ considerably. Cramer et al. [2007] have shown that the dissipation of Alfvénic waves can heat and drive the fast solar wind in the open field regime of coronal holes. The abundance enhancement of low First Ionization Potential (FIP) elements in the slow solar wind compared to the photosphere (see Sect. 7.2) suggests that plasma may be trapped and heated in closed magnetic structures above the photosphere before being released later on by dynamic processes such as magnetic reconnection [Woo et al., 2004; Feldman et al., 2005].

Underwood [2004] argue that fast solar wind can also be driven by density gradients above closed magnetic structures. A low FIP bias in the closed regions - suggesting shorter plasma confinement - leads to a steeper radial density gradient and lower coronal base temperatures, increasing solar wind speed in the corona above the closed structures. Contrarily, a high FIP bias hints at longer confinement times, leads to a more shallow density gradient, higher coronal temperature, and resulting in slower solar wind speeds above.

During the solar activity cycle, physical processes and characteristics in the corona change and with them the acceleration mechanisms and locations of the solar wind. Data from Ulysses shows a mostly bimodal solar wind structure during solar activity minimum and a more complex distribution of solar wind streams during solar activity maximum [McComas et al., 2002, 2008; Ebert et al., 2009]. The fast solar wind is observed to be slower during solar activity maximum compared to solar activity minimum [Schwenn and Marsch, 1990; Underwood, 2004].

A contribution to the search for the solar wind origin is presented in Publication 3 (Sect. 7.3) using a combination of remote sensing and in-situ instrumentation aboard Solar Orbiter.

## 7.2 SOLAR WIND TRACERS

In-situ measurements of particular solar wind properties can be used to obtain information about remote regions the solar wind package has passed through. These properties are called *tracers*. If the propagation of the measured solar wind package can be assumed to have been uninterrupted, these tracers can give valuable insights into coronal physical processes. One such tracer is the ionization charge state of the encountered heavy elements.

The *charge-state distribution* of heavy ions is mostly determined by two physical processes, *collisional ionization*, where an electron "knocks out" another electron from an atom, and *radiative recombination*, where an ion captures an electron under emission of light. The former process runs at a rate of  $C_i n_i n_e$ , the latter at a rate of  $R_i n_i n_e$ , where  $n_i$  is the particle density of the ion with charge state  $i$ ,  $n_e$  is the electron density and  $C_i$  and  $R_i$  are the ionization and recombination rates of the ion with charge state  $i$ . The ionization and recombination rates are different for each element species and are functions of the electron temperature. From these rates, an *atomic modification time scale* can be derived as  $\tau_{\text{mod}} = \frac{1}{n_e(C_i + R_{i+1})}$ . The

*expansion time scale* of the solar wind is  $\tau_{\text{exp}} = \frac{\partial/\partial r(n_e)}{n_e v_{sw}}$ , where  $v_{sw}$  is the bulk flow velocity of the plasma parcel. The expansion time scale describes the thinning out of the interplanetary plasma. If the modification time scale exceeds the expansion time scale of the solar wind (i.e.,  $\tau_{\text{mod}} \gg \tau_{\text{exp}}$ ), the plasma thins out faster than the ionization/recombination processes can proceed. The charge-state is said to be frozen-in. More details on this topic can be found in, e.g., [Hundhausen \[1972\]](#).

By measuring the abundance ratios of neighboring ionization charge states, e.g., O<sup>7+</sup>/O<sup>6+</sup> and utilizing the temperature-dependent ionization and recombination rates (i.e., found in an atomic database such as CHIANTI [[Dere et al., 1997](#)]), the respective freeze-in temperature for that plasma package can be deduced. Because of the simplifying assumptions in the freeze-in paradigm (such as assuming a Maxwellian for the electron velocity distribution for the entries in the CHIANTI database or equilibrium conditions between neighboring ionization charge states), this temperature is only an approximation. However, it roughly estimates the temperature conditions at distinct positions of the plasma package's traveled path.

Another interesting tracer is the *average ionization state* of a specific element. It is defined as  $\bar{q}_X = \sum_{i=l}^u i \cdot n_{X^{i+}} / \sum_{i=0}^u n_{X^{i+}}$ , where X is the element in question, l and u are the lower and upper bounds of the ionization state that can be reliably measured by the utilized instrument and  $n_{X^{i+}}$  is the particle number density of the i-th ionization state of element X. Defining a separating boundary allows distinguishing solar wind streams that were subject to different environmental conditions leading to these differing charge-state distributions. An effect related to the average charge state of solar wind streams is expressed by the [FIP bias](#). It describes the observation that elements with a low [FIP](#) are more abundant in the solar wind compared to their photospheric values. Furthermore, this effect is typically stronger in slow compared to fast solar wind streams [[Zhao et al., 2017](#); [Verscharen et al., 2019](#)].

Studies have shown that the proton *collisional age*  $a_c$  is a suitable candidate for separating solar wind classes [[Kasper et al., 2008](#); [Heidrich-Meisner and Wimmer-Schweingruber, 2018](#), and Publications 4 (Sect. 7.4) and 5 (Sect. 7.5)]. It is defined by  $a_c = r / (v_{sw} \cdot \tau_c)$  with r the distance from the sun to the measuring instrument and  $\tau_c$  the time scale for  $\alpha$ -proton energy exchange due to small-angle Coulomb scattering. A low collisional age means that internal plasma collisions were rare during the transit, while a high collisional age signifies a thermalized plasma package due to many internal collisions.

### 7.3 PUBLICATION 3

Several instruments and spacecraft have been utilized to understand solar winds' acceleration processes and identification of the origin regions. One of these spacecraft is the recently launched Solar Orbiter with its [EUV](#) instrument Spectral Imaging of the Coronal Environment ([SPICE](#)) [[Anderson et al., 2020](#)]. The most probable source regions of a solar wind package measured in-situ can be identified by employing a back mapping from the spacecraft to the photosphere. [SPICE](#) can then be pointed to this region to possibly capture the release of the solar wind stream

in question. The back mapping is performed using the [PFSS](#) implementation developed as part of this work. Although this model cannot resolve the dynamic magnetic processes most probably responsible for the slow solar wind, the idea is that this model gives a rough estimate of the surrounding area of the solar wind source region and that the viewing angle of [SPICE](#) suffices to capture the release of the solar wind parcel. The theoretical groundwork for such a procedure identifying and visually capturing the source regions of the solar wind was described and published in:

**ORIGIN OF THE SOLAR WIND: A NOVEL APPROACH TO LINK IN SITU AND REMOTE OBSERVATIONS**

T. Peleikis, M. Kruse, L. Berger and R. F. Wimmer-Schweingruber, *A&A*, A24, 602, 2017, reproduced with permission © ESO.

DOI: [10.1051/0004-6361/201629727](https://doi.org/10.1051/0004-6361/201629727)

Own contribution: 25%

### *Summary*

The publication opens by describing the solar wind's known sources, especially the uncertainties about the slow solar wind's origin. The Solar Orbiter mission is presented as an endeavor to find the slow solar wind origin regions using a combination of in-situ and remote sensing instrumentation. It is further discussed that to point the remote sensing instrument [SPICE](#) to suspected source regions of the solar wind, a two-fold back mapping procedure is required. While the first portion of this back mapping is ballistic and can be performed using only in-situ solar wind measurements by Solar-Orbiter's Solar Wind Analyser ([SWA](#)) suite and an analytical approach, the second and lower portion of the back mapping procedure requires a model for the coronal magnetic field, such as the [PFSS](#) model. A theoretical orbit lasting for 19 Carrington rotations is established employing data from [ACE](#). This orbit is utilized to develop several pointing algorithms for the [SPICE](#) instrument to best capture possible source regions of the slow solar wind.

The key results are:

- A model for the coronal magnetic field, as produced by the [PFSS](#) model, is necessary to achieve a reasonable back mapping accuracy.
- Comparing magnetic field configurations computed by the [PFSS](#) and [CSSS](#) models do not show substantial differences; therefore, the simpler [PFSS](#) model with standard source surface height at  $2.5 \cdot R_{\odot}$  suffices.
- A strategy is proposed that maximizes the chance of observing the slow solar wind's source regions.

## Origin of the solar wind: A novel approach to link in situ and remote observations

### A study for SPICE and SWA on the upcoming Solar Orbiter mission

Thies Peleikis, Martin Kruse, Lars Berger, and Robert Wimmer-Schweingruber

Institut of Experimental and Applied Physics, Christian Albrechts Universitaet Kiel, 24118 Kiel, Germany  
 e-mail: [peleikis@physik.uni-kiel.de](mailto:peleikis@physik.uni-kiel.de)

Received 15 September 2016 / Accepted 27 March 2017

#### ABSTRACT

**Context.** During the last decades great progress has been achieved in understanding the properties and the origin of the solar wind. While the sources for the fast solar wind are well understood, the sources for the slow solar wind remain elusive.

**Aims.** The upcoming Solar Orbiter mission aims to improve our understanding of the sources of the solar wind by establishing the link between in situ and remote sensing observations. In this paper we aim to address the problem of linking in situ and remote observations in general and in particular with respect to ESA's Solar Orbiter mission.

**Methods.** We have used a combination of ballistic back mapping and a potential field source surface model to identify the solar wind source regions at the Sun. As an input we use in situ measurements from the Advanced Composition Explorer and magnetograms obtained from the Michelson Doppler Interferometer on board the Solar Heliospheric Observatory. For the first time we have accounted for the travel time of the solar wind above and also below the source surface.

**Results.** We find that a prediction scheme for the pointing of any remote sensing instrumentation is required to capture a source region not only in space but also in time. An ideal remote-sensing instrument would cover up to  $\approx 50\%$  of all source regions at the right time. In the case of the Spectral Imaging of the Coronal Environment instrument on Solar Orbiter we find that  $\approx 25\%$  of all source regions would be covered.

**Conclusions.** To successfully establish a link between in situ and remote observations the effects of the travel time of the solar wind as well as the magnetic displacement inside the corona cannot be neglected. The predictions needed cannot be based solely on a model, nor on observations alone, only the combination of both is sufficient.

**Key words.** solar wind – Sun: magnetic fields – Sun: corona – space vehicles: instruments

## 1. Introduction

The solar wind which shapes the heliosphere has been intensively studied for many years. Measurements of the solar wind are made by in situ particle detectors on board various spacecraft distributed over different orbits around the Sun. Variations and patterns in the in situ parameters have been used to categorize the solar wind into different types (Geiss et al. 1995). The earliest categorization scheme discerns the solar wind by its velocity into two types, namely the fast and the slow solar wind (Schwenn et al. 1981). Similar discriminations can be made by other parameters such as the density, temperature, charge state and elemental composition. Although the solar wind's in situ parameters have been measured over a long time period, the precise origin of the solar wind is yet elusive, with the exception of lowly charged fast solar wind, which originates from structures in the corona called coronal holes (Krieger et al. 1973). Nevertheless the in situ parameters do contain information about the solar wind's origin. The measured elemental and ionic composition for example are photospheric and coronal signatures, which are assumed to stay unchanged beyond a certain distance above the Sun's surface. The ionic charge states are directly linked to the electron density and temperature in the corona (Bochsler 2000).

The upcoming Solar Orbiter mission intends to determine the source regions of the slow solar wind in the corona. For

that purpose it is planned to combine in situ particle measurements with a solar spectrograph (Hassler et al. 2011), the Spectral Imaging of the Coronal Environment (SPICE) instrument (Fludra et al. 2013). The in situ instruments are the Proton Alpha Sensor (PAS) and the Heavy Ion Sensor (HIS) of the Solar Wind Analyser (SWA) suite. The idea is to link the in situ observations to their coronal origin which are going to be remotely measured by SPICE. A comparable principle has been described by Landi et al. (2012). In the case of SPICE the remote observation is supposed to happen prior to the in situ observation, in order to observe the coronal structure ideally at the time of the solar wind's departure.

A common technique to locate the heliographic origins of in situ measurements is to map the solar wind back onto the solar surface, thereby obtaining heliospheric coordinates for the source region. The back mapping of the solar wind is done in two parts. The first part is a ballistic mapping of the solar wind back to the outer corona and the second part is a magnetic mapping through the corona down to the photosphere. For the first part, the solar wind speed and for the second part, remote magnetograms and a model of the coronal magnetic field based upon the magnetograms are needed.

The basic concept of two-way back mapping has been used before for various spacecraft and instruments, see for example Neugebauer et al. (1998). But compared to former attempts,

Solar Orbiter brings several remarkable advantages. Firstly, like SOHO before it, Solar Orbiter combines in situ and remote instrumentation on one spacecraft. Usually observations from several different spacecraft and observatories were needed for any back mapping studies of the solar wind. Secondly Solar Orbiter will be very close to the Sun with radial distances down to 0.28 AU. On such close distances the ballistic back mapping will be especially effective since the solar wind has undergone less dynamic processing on its way to the spacecraft. Normally this is a major problem when back-mapping from 1 AU.

In this paper we explore different methods for determining the source regions of the solar wind. SPICE will image the source regions of a solar wind package prior to its in situ observation. To ensure that SPICE points at the correct region a predictive forward mapping of the solar wind is needed. This includes a prediction of the solar wind source regions, a prediction of the solar wind speeds prior to its measurement and consequently an estimation of its travel time. Only then can one predict where SPICE has to be pointed at and when it has to take a spectrogram of the Sun's surface. Our goal is to find promising measurement patterns and investigate their feasibility. In order to do so we have looked at the influence of the ballistic as well as the magnetic mapping by simulating the measurement sequence of SPICE. For these simulations we combined real solar wind in situ data measured by the Advanced Composition Explorer (ACE) and real magnetograms from the Michelson Doppler Interferometer (MDI). To validate the different methods, the ability of SPICE to observe the predicted source regions was calculated in each simulation.

## 2. Methods and analysis

In this section, we describe the general procedure of our analysis. During the course of our analysis we applied modifications and improvements to the procedure, but the underlying method is based on the following descriptions.

In Fig. 1 the path of the solar wind from its origin to the spacecraft is sketched for two different solar wind speeds. When traveling from its origin to the spacecraft, the solar wind's path is divided into two distinct regions. First it has to traverse the corona which is dominated by strong magnetic fields. Here, the plasma has to stream along the magnetic field lines. Beyond the source surface in interplanetary space the situation is reversed and the magnetic field has to follow the plasma flow.

Both regions must be considered individually due to their different physics. The second part of the solar wind's path can be calculated via ballistic back mapping under the assumptions that the solar wind velocity does not change between corona and spacecraft and a strictly radial expansion of the solar wind plasma (Krieger et al. 1973). During the solar wind's travel time the Sun continues its rotation which leads to a displacement between spacecraft coordinates and source coordinates. We call this the ballistic displacement.

Unfortunately, the first part of the solar wind's path cannot be simply described by ballistic back mapping. The magnetic pressure inside the corona exceeds the kinetic pressure, therefore the plasma has to follow the magnetic field lines. In order to trace the solar wind further through the corona, the coronal magnetic field line configuration has to be known. Since it is not possible to measure the complete magnetic topology inside the corona directly, one has to introduce a model to simulate the course of the field lines. The Potential Field Source Surface (PFSS) model by Altschuler & Newkirk (1969) or Schatten et al. (1969) is commonly used for this task. It calculates the magnetic field strength

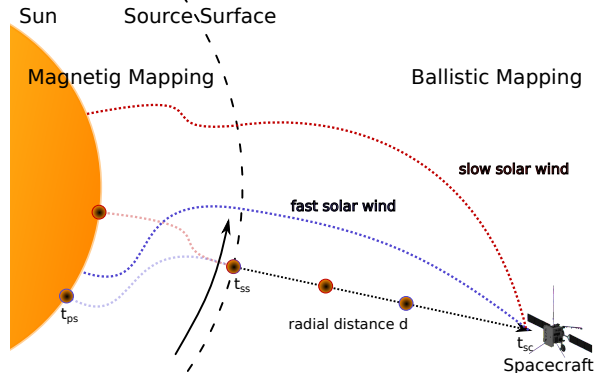


**Fig. 1.** Displacement between the spacecraft's coordinates and the source region's coordinates. The magnetic connection of a fast (blue) and slow (red) solar wind package are shown in the reference frame of the spacecraft. The bending of the field lines below the source surface causes the magnetic displacement, the rotation of the Sun during the travel time from the source surface to the spacecraft causes the ballistic displacement. A solar wind package starts at the time  $t_{ps}$  at the photosphere, reaches the source surface at  $t_{ss}$  and is measured at  $t_{sc}$  by the spacecraft. The colored dashed lines indicate the magnetic connection between spacecraft and the solar wind's sources.

and direction in a region between the photosphere and an artificial surface called the source surface. It needs photospheric magnetograms as input parameter. With the assumption that the solar wind plasma can only flow along the magnetic field lines it can now be traced through the corona to its photospheric origin (Neugebauer et al. 1998). The bending and twisting of the field lines causes an additional displacement between spacecraft and source coordinates. We call this magnetic displacement.

We note that there are other models beside the PFSS model in use. The Current Sheet Source Surface (CSSS) model has been shown to be better than the PFSS model when it comes to solar wind speed predictions (Poduval & Zhao 2014). At the end of this paper we compare the results obtained with the PFSS model with those obtained from a CSSS model.

### 2.1. Ballistic back mapping

For our consideration we assume a spacecraft orbiting the Sun. Its position is given in a heliospheric coordinate system co-rotating with the Sun, that is, the Carrington coordinate system, with  $\lambda_{sc}$  heliospheric or Carrington longitude,  $\phi_{sc}$  heliospheric latitude and its distance to the source surface  $d$ . The source surface is a virtual sphere around the Sun with a radius of typical  $2.5 R_\odot$ . It is the outer boundary for the PFSS model and it marks the point where the magnetic field lines are supposed to radially expand. In our consideration it also marks the point where the plasma no longer has to follow the magnetic field lines. A solar wind package measured by this spacecraft at the time  $t_{sc}$  can be mapped back onto the source surface via ballistic back mapping, hereby determining the ballistic footpoint  $\lambda_{bfp}$  and  $\phi_{bfp}$  of the spacecraft. It can be calculated analytically:

$$\begin{aligned} \lambda_{bfp}(d, v_{sw}) &= \lambda_{sc} + \frac{\omega d}{v_{sw}}, \\ \phi_{bfp} &= \phi_{sc}, \end{aligned} \quad (1)$$

where  $v_{sw}$  is the speed of the measured solar wind package and  $\omega$  is the angular velocity of the Sun. Consequently the time  $t_{ss}$

when the solar wind starts at the source surface calculates to

$$t_{ss}(d, v_{sw}) = t_{sc} - \frac{d}{v_{sw}}. \quad (2)$$

Obviously,  $\lambda_{bfp}$  is a function depending on  $v_{sw}$  and  $d$ . The difference between the spacecraft coordinates and the ballistic footpoint is the afore mentioned ballistic displacement  $\lambda_{dis}^{bm} = \frac{\omega d}{v_{sw}}$  and  $\phi_{dis}^{bm} = 0$ . For a spacecraft traveling between 1 AU and 0.2 AU and observing solar wind with speeds between  $250 \text{ km s}^{-1}$  and  $900 \text{ km s}^{-1}$ ,  $\lambda_{dis}^{bm}$  can reach rather high values of up to  $100^\circ$ . Here the advantage of the Solar Orbiter mission becomes apparent since it will only do its remote observation in regions with  $d \leq 0.4 \text{ AU}$ . Conveniently,  $\lambda_{dis}^{bm}$  is always analytically determined. We note that the latitude  $\phi_{bfp}$  is not affected by the ballistic mapping.

## 2.2. Magnetic mapping

To map from the source surface deeper into the corona to the photosphere the PFSS model has to be applied. It needs photospheric magnetograms as input parameters in order to model the coronal magnetic field. These magnetograms are typically taken over the course of one Carrington Rotation (CR). One of the major problems of the PFSS model lies in the assumption of a current free state in the corona. This is not essentially correct in reality, especially not for the active Sun. Therefore the correctness of the PFSS model strongly depends on the solar activity (Koskela et al. 2015). In general the best feasibility of the model is given for the quiet times of the solar cycle.

With the PFSS model applied each ballistic footpoint is related to the closest open field line on the source surface. We call these field lines source-field lines. They are then traced down to the photosphere. Under the assumption that the solar wind traveled along these source-field lines it has now been mapped magnetically to its photospheric origin. The bending of these field lines introduces an additional displacement  $\lambda_{dis}^{pfss}$  and  $\phi_{dis}^{pfss}$  between the ballistic footpoint on the source surface and the photospheric footpoint of the source-field line. This is the aforementioned magnetic displacement. The coordinates for the photospheric source regions evaluate then to

$$\begin{aligned} \lambda_{sr}(d, v_{sw}, cr) &= \lambda_{sc} + \lambda_{dis}^{bm}(d, v_{sw}) + \lambda_{dis}^{pfss}(cr) \\ \phi_{sr}(cr) &= \phi_{sc} + \phi_{dis}^{pfss}(cr). \end{aligned} \quad (3)$$

Here,  $cr$  depicts the CR used to derive  $\lambda_{dis}^{pfss}(cr)$  and  $\phi_{dis}^{pfss}(cr)$ , that is, magnetic field data from that CR were used as input for the PFSS model. Figure 2 shows an example of the magnetic mapping. Shown are the source surface, the photosphere, the ballistic footpoints and the respective source-field lines. The magnetic displacement induced by the bending of the field lines in heliographic longitude and latitude is apparent.

The time when the solar wind starts at the photosphere calculates to

$$t_{ps}(d, v_{sw}) = t_{sc} - \left( \frac{d}{v_{sw}} + t_{pet} \right). \quad (4)$$

The time  $t_{pet}$  is the plasma escape time, that is, the time the solar wind package needs to travel along the field lines to the source surface. The time  $t_{pet}$  cannot be measured by any means, but it can be estimated by simulating the passage of a solar wind plasma packet through the corona. In order to track a plasma packet through the magnetically dominated lower corona up

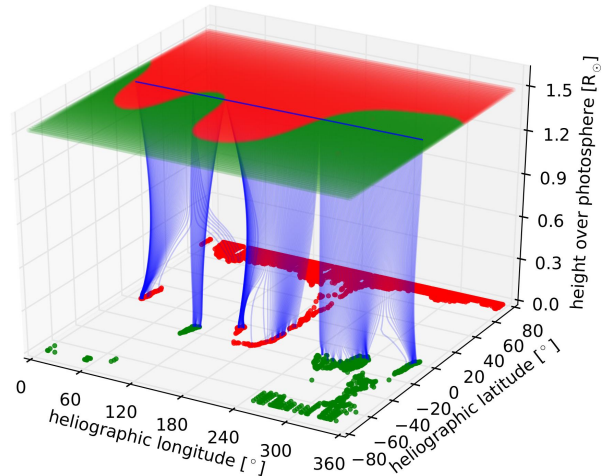


**Fig. 2.** Magnetic field map to illustrate the PFSS mapping. The intersection points with the source surface and foot points of the open magnetic field lines of the PFSS model are shown in red and green, where the colors depict the inward and outward polarities. The determined source-field lines and their course through the corona are shown in blue. The PFSS map corresponds to CR 2050, the underlying magnetogram is based on MDI observations.

**Table 1.** Terminal velocities and travel times from transition region to source surface for different flux tube models.

Model	Terminal velocity [km s <sup>-1</sup> ]	$t_{pet}$ (h)
active	344	17.9
equator	498	14.8
pole	754	4.45
theta12	738	4.32
theta20	696	3.88
theta24	659	3.57
theta25	574	5.82
theta28	550	9.93

**Notes.** Based on Cranmer et al. (2007).

to the source surface, we analyzed several open flux tube geometries computed by Cranmer et al. (2007). Terminal velocities range from  $344 \text{ km s}^{-1}$  for the active region model to  $753 \text{ km s}^{-1}$  for the coronal hole model. We computed the package travel time from the transition region at about  $r = 1.01 R_\odot$  to the source surface at  $r = 2.5 R_\odot$  by reading in the velocity profiles to an equidistant grid and integrating via a Runge-Kutta (RK4) method. Results are shown in Table 1. Unfortunately, the magnetic mapping cannot be analytically calculated since it depends on the magnetic configuration at the Sun. The necessary input magnetograms are taken from the Michelson Doppler Interferometer (MDI; Scherrer et al. 1995) on board of the Solar and Heliospheric Observatory (SOHO) spacecraft.

*Spread and magnitude of the magnetic displacement.* Here, we investigate the spread and magnitude of the magnetic displacement. To achieve this we calculated the magnetic displacements that a spacecraft would encounter on its orbit around the Sun if it were to attempt to back map observed solar wind. This was done with the PFSS model for 19 consecutive CRs from 2040 until 2058. These CRs are well within one of the quiet times of the Sun's activity cycle. This can be seen in Fig. 3. Here a time series of the sunspot number is shown. A high number

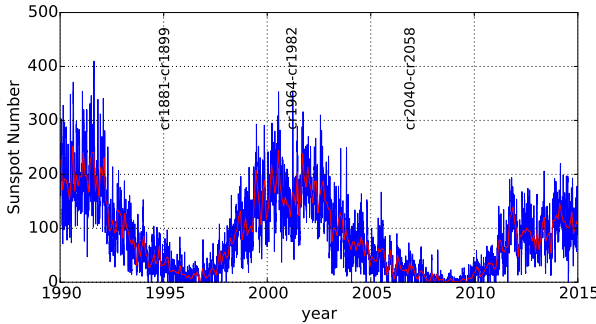


**Fig. 3.** Sunspot number as a function of time. The blue curve gives the actual sunspot number and the red curve the monthly average. The variation in the Sun's activity cycle is easily visible. The green shaded area marks the sequence of CRs we used for this study. The blue and red shaded areas mark sequences of CRs we investigated for comparison, the blue one also happens during the quiet time of the Sun while the red one happens during the active Sun. Data taken from Royal Observatory of Belgium (2016).

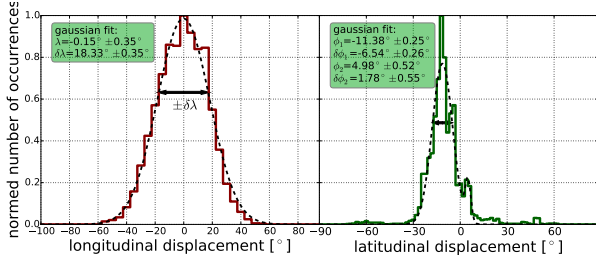


**Fig. 4.** Magnetic induced longitudinal (left) and latitudinal (right) displacement between source surface position and photospheric position. The  $y$  axis gives the number of occurrences for both plots normalized for the maximum. The calculation was made for an equatorial space-craft path over the course of 19 consecutive CRs, each plot also shows a fit with a simple Gaussian (left) or a sum of two Gaussian (right). The fit parameters are given in the respective panels. The arrow marks  $\delta\lambda$ .

of sunspots coincides with the active periods of the Sun and vice versa. The time period from CR 2040 until CR 2058 is marked in the figure, as is a comparable time period in the solar minimum while the red shaded area marks a period during solar maximum.

For each rotation we simulate a full orbit and disregard the ballistic displacement. Since the magnetic configuration is unique for each CR it is reasonable to use many rotations in order to cover the variability of the coronal magnetic field. Figure 4 shows the result of the calculations. All 19 CRs are combined in two histograms, one showing the longitudinal displacement between source surface and photospheric position, the other showing the latitudinal displacement. The longitudinal displacement shows a distribution which can be approximated by a Gaussian distribution with the most likely displacement of  $\lambda = -0.15^\circ \pm 0.35^\circ$  and  $\delta\lambda = 18.33^\circ \pm 0.35^\circ$ . We note that there is no physical motivation for a Gaussian shape. Interestingly, the magnetic mapping as produced by the PFSS model does not seem to have a preferred direction in longitude. The right-hand histogram in Fig. 4 for the latitudinal displacement shows some interesting characteristics. First of all it shows a remarkable north-south asymmetry. Also the distribution itself is more complex compared to the longitudinal displacement. It cannot be described as single Gaussian, but as a sum of two or more Gaussians. In Fig. 4 we fit the histogram with a sum of two

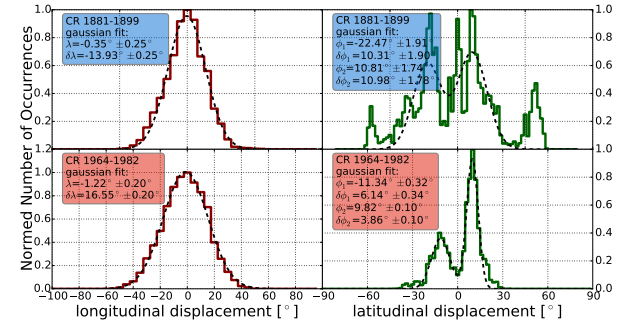


**Fig. 5.** Magnetic displacement for the other two time periods in Fig. 3 in the same manner as in Fig. 4. The period from 1881 until 1899 took place during the quiet phase of the Sun, but the magnetograms are from the Kitt Peak Observatory. The period from 1964 until 1982 took place during the active phase of the Sun where the PFSS model is not reliable.

Gaussian with  $\phi_1 = -11.38^\circ \pm 0.25^\circ$ ,  $\delta\phi_1 = -6.54^\circ \pm 0.26^\circ$ ,  $\phi_2 = 4.98^\circ \pm 0.52^\circ$  and  $\delta\phi_2 = 1.78^\circ \pm 0.55^\circ$ . This means that the majority of the ballistic foot points has been mapped into the southern hemisphere of the Sun and only few have been mapped into the northern hemisphere. Most of the lines originate from a  $-30^\circ$  to  $10^\circ$  band around the equator. This north-south asymmetry is not a numerical artefact but something which is indeed observed (Goel & Choudhuri 2009). In this context it is reassuring that the PFSS model is able to reproduce this asymmetry. There are two minor features around  $\pm 60^\circ$  latitude. These are the infrequent occasions where the equatorial ballistic foot points have been mapped into the polar coronal holes. We also note that the longitudinal distribution is rather broad, which emphasizes how important it is to have knowledge about the magnetic displacement when back mapping. Although the most likely displacement is  $\approx 0$ , the majority of solar wind packages have been displaced by the magnetic field about a value  $\neq 0$ . Therefore it is highly improbable to estimate the photospheric origin of a measured solar wind package without using a PFSS model or a similar tool which can model the magnetic configuration inside the corona.

We repeated the method for two different time periods marked by blue and red shaded regions in Fig. 3 for comparison. The first one from CR 1881 until 1899 was also during solar minimum while the second one from 1964 until 1982 was during solar maximum. The results are shown in Fig. 5. It can be seen that the longitudinal displacement looks similar to Fig. 4 for both time periods. In contrast the latitudinal displacement shows a different behaviour for both time periods. For the time period from CR 1881 until 1899 the distribution looks more disordered, with a broader spread and more source regions mapped into the polar coronal holes. This is most probably the case because for this time period we used input magnetograms from the Kitt Peak National Observatory (KPNT), because at that time, the SOHO mission was not yet launched. In comparison to the MDI magnetograms the magnetograms from KPNP have a lower resolution,  $360 \times 180$  pixel in comparison to  $3600 \times 1080$  pixel. Therefore many fine structures in the equatorial regions are not reproduced. Consequently many field lines are instead mapped into the polar region of the Sun. The longitudinal displacement for CR 1964 until 1982 does show a stronger resemblance to the one shown in Fig. 4. Here the underlying magnetograms are also made by MDI, therefore a stronger similarity is to be expected. Since this period happened during the active Sun, the assumptions of the

T. Peleikis et al.: Origin of the solar wind: A novel approach to link in situ and remote observations

PFSS model may no longer be fulfilled. Especially the assumption of a current free corona can be violated. In the end these are the reasons why we chose the period from CR 2040 until 2058, here we have higher resolution magnetograms and a quiet Sun. Also, Solar Orbiter is expected to operate mainly over a similar time period during the quiet time of the Sun.

### 2.3. Dynamics in the coronal magnetic field

The coronal magnetic field can be a highly dynamic structure with magnetic reconnection occurring between the field lines. Moreover reconnection is a potential source of the slow solar wind, see for example Fisk (2003) and Rappazzo et al. (2012). Therefore to observe magnetic reconnection would be a relevant part of SPICE's investigations.

The reconnection of magnetic field lines alters the footpoint locations of source-field lines and hence affects the study in this paper. Unfortunately neither the PFSS model nor the CSSS model are able to predict or simulate dynamic processes in the magnetic field. Therefore we are not able to include this in the following analysis. In general the shift of a footpoint due to reconnection can be assumed to be confined to the area of one supergranule. Since the area of a supergranule accounts only for  $\sim 4\%$  of SPICE's field of view, it is unlikely that the reconnection of two field lines will shift a source region so that it is no longer covered by the field of view.

### 2.4. Error estimation and uncertainties

Both the ballistic back mapping technique as well as the PFSS model are susceptible to errors. For the ballistic back mapping the errors derive from uncertainties in the solar wind speed measurements and dynamic processes the solar wind undergoes on its way from its source to the spacecraft. In case of the PFSS model the errors stem from uncertainties in the input magnetograms and from the general limitations of the model. For example the model is completely unable to reproduce any dynamic processes inside the corona.

To account for these uncertainties we repeated our analysis several times, at which for each run we introduce artificial statistical errors to the data. From the results for the different runs we then calculated the standard deviation.

For the ballistic back mapping we added noise with a uniform distribution with a magnitude of  $\pm 10^\circ$  to the back mapped longitude  $\lambda_{\text{diss}}^{\text{bm}}$ . This leads to errors which are in agreement with Nolte & Roelof (1973), who proposed an error of  $\Delta\lambda_{\text{diss}}^{\text{bm}} = \pm 10^\circ$ .

The error for the PFSS model is more difficult to tackle. As a first attempt we added noise to the input magnetograms in order to derive different solutions for the model. To each pixel of the magnetogram the value  $\pm 0.1 \times I_p$  is added, where  $I_p$  is the intensity of each respective pixel. This is done according to Liu & Norton (2001) who suggest an error of up to 10% for the magnetic field measurement. In this way we took into account the error of the measurement but not the error of the PFSS model itself, which originates from the overly simplified assumptions. To estimate this intrinsic error of the PFSS model we compare each CR with its preceding and its succeeding rotation. For each source-field line we then calculated the difference  $\Delta\lambda_{\pm} = \lambda_{cr}^{\text{PFSS}} - \lambda_{cr+1}^{\text{PFSS}}$  and the respective  $\Delta\phi_{\pm}$ . For both, the mean is calculated and then added as uniform noise to the respective maps. This does not reflect the actual intrinsic error of the PFSS model but it serves as maximum error estimation.

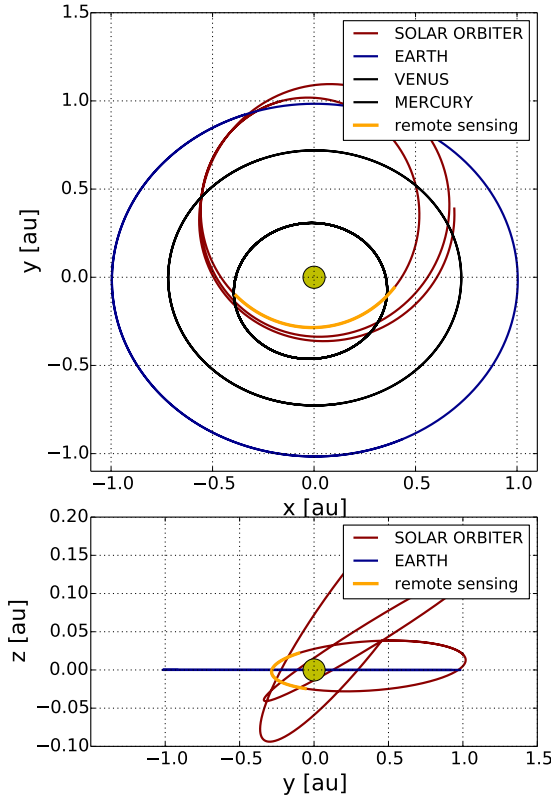


**Fig. 6.** Investigated orbit of Solar Orbiter shown in orange. The  $x$  and  $y$  axes define the ecliptic plane, the  $z$  axis is perpendicular to the ecliptic. The units for the axes are AU. The full Solar Orbiter orbit is shown in red, the orbit of Earth is shown in blue, the Sun is shown as yellow circle. The *upper panel* also contains the orbits of Mercury and Venus as additional reference points. We note that the  $z$  axis in the *lower panel* has a different scale from the  $y$  axis. Hence the out-of-ecliptic extent of the orbit seems exaggerated.

## 3. Solar orbiter forward mapping

Now we begin to focus on the upcoming Solar Orbiter mission. During the actual mission, remote observations are only planned during certain parts of Solar Orbiter's orbit. Those remote sensing windows occur when Solar Orbiter is particularly close to the Sun, that is, the distance between Sun and spacecraft ranges from 0.285 AU to 0.399 AU or at high heliographic latitudes. In Fig. 6 the planned orbit is shown in the  $x$ - $y$  and in the  $y$ - $z$  plane. It begins on the 11th of January, 2022 and ends on the 18th of July, 2023. The part of the orbit which is labeled "remote sensing" does not depict an actual remote sensing window, but marks a part of the orbit which satisfies the spacecraft-Sun distance condition for a remote sensing window.

In Fig. 1 the principle of forward mapping is illustrated. At the time  $t_{ps}$  SPICE has to image the source region of the solar wind package. The solar wind package travels through the corona and reaches the source surface at the time  $t_{ss}$ . From there it travels further through the heliosphere and is now decoupled from the Sun's rotation. At  $t_{sc}$  Solar Orbiter observes the solar wind package in situ. To successfully image each solar wind package with SPICE two parameters are needed, the release time of the solar wind at the photosphere  $t_{ps}$  and its source coordinates

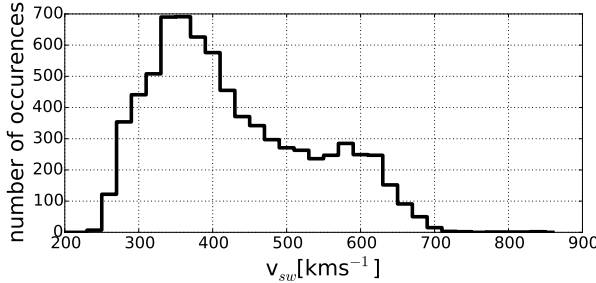


**Fig. 7.** Solar wind speeds used for this study. The solar wind speeds have been measured by ACE/SWEPAM during CRs 2040 to 2058.

$\lambda_{sr}$  and  $\phi_{sr}$ . The release time  $t_{ps}$  is needed in order to determine the specific point in Solar Orbiter's orbit from where SPICE has to image the source coordinates  $\lambda_{sr}$  and  $\phi_{sr}$  to capture the solar wind package at its origin. Both  $t_{ps}$  as well as the source coordinates can be determined by back mapping.

In the following simulations we construct 19 spacecraft orbits for each run. These orbits are intended to emulate the remote sensing windows of Solar Orbiter. The actual remote Sensing windows are planned to last for ten day but we do not have the precise orbit and time information. Therefore we construct them as follows. Each orbit ranges from  $\lambda = 360^\circ$  to  $\lambda = 0^\circ$ , thereby resembling one CR. The radial distance ranges from 0.285 AU to 0.399 AU, equivalent to the remote sensing window. For each of these constructed pseudo orbits we use one magnetogram from CR CR2040 to CR2058 as input parameter for the PFSS model. Hence we end up with 19 CRs each with a different magnetic configuration in the corona. For each orbit the simulation will run according to the following scheme:

1. Simulate the measurement of solar wind by using in situ solar wind data measured by the Solar Wind Electron Proton Alpha Monitor (SWEPAM) on ACE during the exact same CR. See Fig. 7.
2. Determine the actual source regions of the observed solar wind by using Eq. (3). Also determine the release time with Eq. (4).
3. Predict the source regions and the release time using the preceding CR.
4. Simulate the orbit of the spacecraft again with SPICE trying to point at the predicted source regions. Thereby its field of view is projected onto the Sun's surface and it is tested if the actual source region is inside the projection. Figure 8 serves to clarify this concept. The field of view of the spectrograph is adjusted to represent SPICE's actual rectangular field of view of 11 arcmin width and 16 arcmin height (Caldwell 2014). The percentage of observed source regions is calculated, which in return is a measure for the quality of the prediction method.

In the following sections we try different prediction methods for Step 3 of the above numeration and compare the percentage of hit source regions.

### 3.1. Ballistic mapping only

For the first approach the source regions of the solar wind are predicted only by ballistic back mapping, therefore completely ignoring any magnetic displacement inside the corona. This method would be the easiest way to determine the source regions since it does not need any knowledge about the coronal magnetic

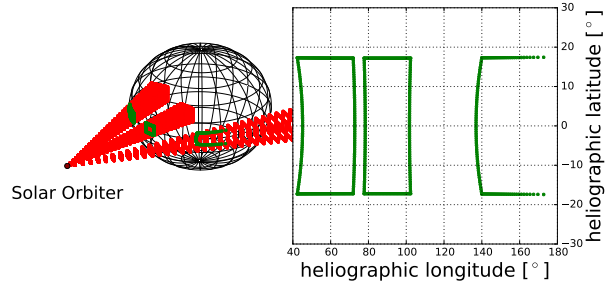


**Fig. 8.** Projection of a field of view on the Sun. The left panel shows Solar Orbiter (dark red point) in orbit around the Sun (black mesh) with SPICE's rectangular field of view (red) projected onto different regions of the Sun's surface (not to scale). The right panel shows the projection on the Sun's surface in heliographic coordinates. This is the actual projection of SPICE's field of view from 0.3 AU, hence the right panel is to scale.

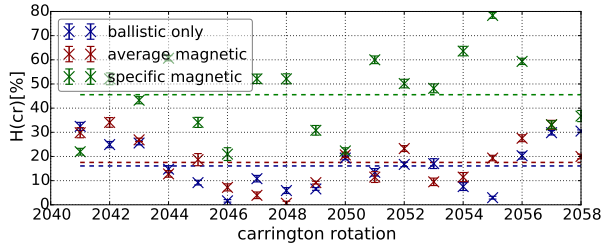


**Fig. 9.** Percentage of hits  $H(cr)$  plotted against the CR. The different colors depict the different methods used. The dashed lines represent the average of  $H(cr)$  for each method. The individual error bars stem from the error estimation described in Sect. 2.4.

structure. For the ballistic back mapping the solar wind speed is needed in order to derive  $\lambda_{dis}^{bm}(d, v_{sw})$  and  $t_{ss}(d, v_{sw})$  according to Eqs. (1) and (2). Unfortunately, at the time the spectrograph has to be pointed at the Sun the in situ solar wind speed has not yet been measured. A solution would be to use the solar wind velocities measured during the preceding CR. At solar minimum the solar wind speeds measured during one CR do not differ too much in comparison to the speeds measured in the preceding CR (see Fig. 11).

Using the solar wind speeds from the preceding CR  $cr - 1$ ,  $\lambda_{sr}$  and  $\phi_{sr}$  for CR  $cr$  can be calculated. The above described is now applied for each CR with the exception of 2040, because here no preceding rotation is available. With the source regions predicted we check if the spectrograph was actually able to hit them. The percentage of successful hits calculates to:

$$H = \frac{N}{5490} \times 100\%. \quad (5)$$

Here  $N$  is the number of observed source regions and 5490 is the total number of observations simulated over 18 CRs. Considering only the ballistic mapping we end up with:

$$H = 16.08 \pm 9.42\%. \quad (6)$$

The error of  $H$  is the standard deviation calculated from the individual  $H(cr)$  for each CR. Additionally the values for individual CRs  $H(cr)$  are displayed in Fig. 9 as blue  $x$ . The errorbars shown here stem from the procedure described in Sect. 2.4. This result shows that ballistic back mapping alone is not sufficient for the prediction of the source regions, since more than 80% are

T. Peleikis et al.: Origin of the solar wind: A novel approach to link in situ and remote observations

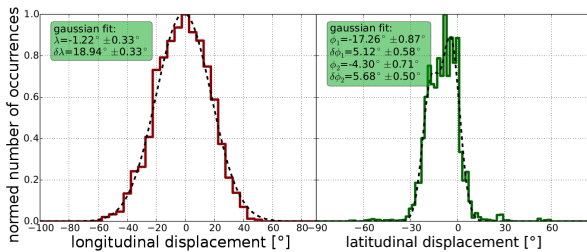


**Fig. 10.** PFSS induced longitudinal (left) and latitudinal (right) displacement between source surface position and photospheric position similar to Fig. 4. The  $y$  axis gives the normed number of occurrences for both plots. The calculation was made for Solar Orbiter's orbit over the course of 19 consecutive CRs, each plot also shows a fit with a simple Gaussian (left) or rather a sum of two Gaussian (right). We note the stronger shift to lower latitudes compared to Fig. 4 due to Solar Orbiter's tilted orbit.

missed. Obviously the magnetic displacement can be expected to have a large influence on the results. There are different ways to include the magnetic displacement which we explore in the next subsections.

### 3.2. Average magnetic mapping

The simplest way to include the magnetic mapping into the simulation and therefore the prediction of the source regions of the solar wind is to assume an overall average magnetic displacement which substitutes the actual magnetic displacement. This can be done under the assumption that displacement distributions like those shown in Fig. 4 are of a general validity.

For that approach we calculated displacement distributions in a similar way as in Sect. 2.2. The results are shown in Fig. 10. We now estimate the percentage of captured source regions, calculating the expected source locations for the solar wind using Eq. (3) with  $\lambda_{\text{dis}}^{\text{pfss}} = -1.22^\circ$  and  $\phi_{\text{dis}}^{\text{pfss}} = -4.3^\circ$  taken from Fig. 10 in addition to the ballistic mapping according to Eq. (3). This approach yields the following result:

$$H = 17.76 \pm 9.76\%. \quad (7)$$

The result is only slightly better than the previous one where only the ballistic back mapping has been considered. The results for the individual CRs are shown as red  $x$  in Fig. 9. The overall average displacement calculated over many CRs does not sufficiently reflect the actual displacement for an individual rotation. Hence, a more sophisticated approach is required.

### 3.3. Specific magnetic mapping

In this approach we calculate the exact photospheric sources including ballistic mapping and magnetic mapping for the orbit of CR  $cr - 1$  and use them for rotation  $cr$ . Of course, they are not exactly the same but similar enough for SPICE's field of view to capture a significant portion of them. The expected source locations for rotation  $cr$  calculate to:

$$\begin{aligned} \lambda_{\text{esr}}(d, v_{\text{sw}}, cr) &= \lambda_{\text{sc}} + \frac{\omega d}{v_{\text{sw}}(cr - 1)} + \lambda_{\text{dis}}^{\text{pfss}}(cr - 1) \\ \phi_{\text{esr}}(cr) &= \phi_{\text{sc}} + \phi_{\text{dis}}^{\text{pfss}}(cr - 1). \end{aligned} \quad (8)$$

The overall result for this method calculates to:

$$H = 45.56 \pm 15.77\%. \quad (9)$$

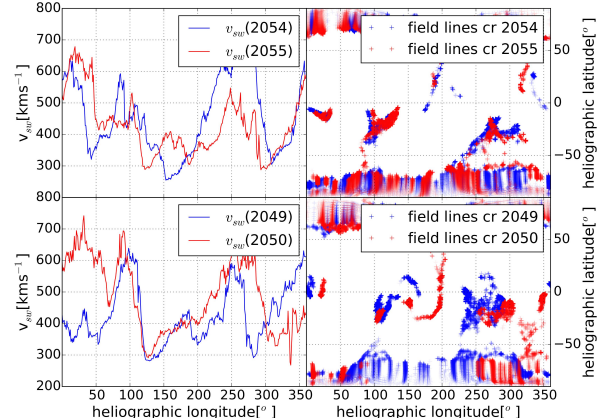


**Fig. 11.** Comparison between consecutive CRs. The *left panels* show the solar wind velocity taken from ACE for the respective CRs while the *right panels* show the PFSS model data of the photospheric foot points of the open magnetic field line. The latter rotations 2055 and 2050 are shown in red, the former rotations 2054 and 2049 are shown in blue. The *upper panels* show the case for CR 2055, where the predictions produced very good results while the *lower panel* show the case for rotation 2050, where only very poor results were produced.

The results for the individual CRs are shown in Fig. 9 as green  $x$ . This is a more satisfying result than the two derived before. But if we look at the individual CRs in Fig. 9 there is a notable degree of variation, ranging from 75% of the source regions captured, for example, CR2055, down to only around 30%, for example, CR2050. To understand this variation we compared the mentioned examples with their respective preceding CR which was used to determine  $\lambda_{\text{esr}}(d, v_{\text{sw}}, cr)$  and  $\phi_{\text{esr}}(cr)$ . This is done in Fig. 11. It is evident that the differences between CR 2054 and 2055 are rather small, hence the specific deviation method was able to produce such good results. The opposite is true for the rotations 2050 and 2049. Here the differences are considerable. Therefore it is only reasonable that the hit percentage is very low for CR 2050 and high for rotation 2047. From Figs. 11 and 9 it can be inferred that the correct prediction of the source regions depends critically on the similarity between consecutive CRs. If the similarities are not sufficient, the predictions made become unreliable.

In the case of SPICE constantly imagining the source regions for every step in Solar Orbiter's orbit the method to specifically predict the source regions could be considered a satisfactory method since it leads to many cases where the source regions are successfully captured. SPICE will also be used for different purposes, therefore it will only image the solar wind's source regions for certain selected points during its orbit. With only a small number of images the risk of not capturing even one source region becomes considerable. This renders the procedure discussed in this chapter rather unfavorable in the end. A different and more reliable method is discussed in the next section.

### 3.4. Leading stripe mapping

Instead of predicting each solar wind source region individually one could point the spectrograph at the sun with or without a certain leading angle while also trying to maximise the covered area on the Sun's surface. Six observations per day can be vertically stacked in order to increase the instruments field of view. This increased field of view has a height of 96 arcmin and

completely covers the Sun in terms of latitude. In this section we analyze the feasibility of such an approach. Solar Orbiter's orbit and the observation of solar wind is simulated in the same manner as before. For each point in its orbit SPICE takes an image of the Sun's surface with a fixed leading angle  $\lambda_{la}$ , pointing at

$$\lambda = \lambda_{sc} + \lambda_{la}. \quad (10)$$

With this configuration SPICE is able to capture virtually any source region on the Sun's surface, but not necessarily at the actual solar wind release time. For each CR we calculate the coordinates of the solar wind's source position and for every source coordinate we also determine the solar wind release time  $t_{ps}$ . The orbit is then simulated as described above ten times for different leading angles  $\lambda_{la}$  ranging from  $-50^\circ$  to  $40^\circ$ . Due to the rotation of the Sun, source regions enter the projection of the field of view coming from lower longitudes. As soon as a source region is located in the center of SPICE's field of view it counts as observed. For each observed source region the remote observation time  $t_{obs}$  is listed. Due to the rotation of the Sun the source region enters the field of view on the left side, that is, at lower longitudes. The field of view then sweeps over the source region until it is no longer covered. A source region stays roughly between 40 and 90 h inside the field of view, depending on the leading angle. In order to analyze this simulation we calculate the time difference between the release time of the solar wind package  $t_{ps}$  and the observation time  $t_{obs}$  for every source region:

$$\Delta t = t_{ps} - t_{obs}. \quad (11)$$

The results are shown in Fig. 12. Each panel shows the results for a different leading angle, starting with the upper left panel at  $\lambda_{la} = -50^\circ$  and ending with the lower right panel at  $\lambda_{la} = 40^\circ$ . The histograms are normalized to their respective sum. The  $y$  axis therefore gives the probability per bin. The differently colored histograms show source regions with measured solar wind speeds below  $350 \text{ km s}^{-1}$ , only source regions with speeds above  $600 \text{ km s}^{-1}$ , and intermediate speeds with  $350 \text{ km s}^{-1} < v_{sw} < 600 \text{ km s}^{-1}$ . On the  $x$  axis  $\Delta t$  is shown. A negative value for  $\Delta t$  means that a particular source region has been observed by SPICE after the solar wind package was released, a positive value means the source region has been observed before the solar wind package departed. The area taking the extent of the field of view into account is marked. As stated above, a source region needs 40 to 90 h to traverse the field of view. With SPICE's intention to observe a source region during the release of the solar wind, the area between the dashed lines marks the optimal observation time. We call the portion of source regions which are optimally covered  $\Gamma_{oc}$ .

If we now analyze the shown distributions of  $\Delta t$  it is evident that it shifts from right to left with increasing leading angle. With a leading angle of  $\lambda_{la} = -50^\circ$  the majority of solar wind packages are observed before the release of the solar wind package. Then again, a leading angle of  $\lambda_{la} = 30^\circ$  and greater means the observation of nearly all source regions happens after the solar wind is released. We note that the difference between fast and slow solar wind is small. On the one hand the ballistic displacement leads to a systematic separation between the distributions of the fast and slow solar wind, since it depends on the solar wind speed. The magnetic displacement on the other hand does not depend on  $v_{sw}$  and therefore leads to a broadening of both distributions and therefore to a distinctive overlap.

Since SPICE's goal is to find the source regions of the slow solar wind we will focus on the red histograms in Fig. 12. The optimal solution would be a leading angle which enables SPICE

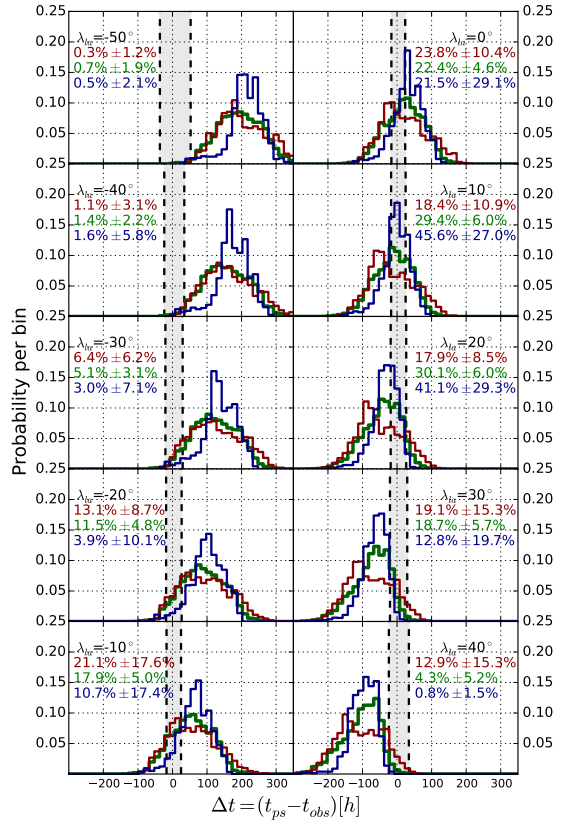


**Fig. 12.** Results for the leading stripe mapping. The  $x$  axis shows the time difference  $\Delta t = t_{ps} - t_{obs}$  between the time when a source region is observed by the spectrograph and when it releases its solar wind package. The  $y$  axis shows the probability per bin. The red curves show only source regions with a measured solar wind speed below  $350 \text{ km s}^{-1}$ , the green curves represent intermediate speeds from  $350 \text{ km s}^{-1}$  to  $600 \text{ km s}^{-1}$  and the blue curves with speeds above  $600 \text{ km s}^{-1}$ . Each panel shows the result for a different leading angle. The dashed vertical lines mark the area where a source regions would be observed at the moment of the solar wind's release. The colored numbers show  $\Gamma_{oc}$  in percent with the corresponding errors. The errors are the statistical errors originating from the variation between individual CRs.

to observe the solar wind's source region at the moment when the solar wind is released, that is, when  $\Gamma_{oc}$  becomes maximal. This is the case for a leading angle  $\lambda_{la} \approx 0^\circ$ , as can be seen in the respective panel in Fig. 12. To examine this in more detail we repeat the simulation for leading angles ranging from  $-8^\circ$  to  $2^\circ$ . The results are shown in Table 2. It can be seen that the best results are achieved for leading angles  $\lambda_{la}$  between  $-6^\circ$  and  $-4^\circ$ . For the study of fast and intermediate solar wind a leading angle of  $\lambda_{la} = 10^\circ$  would be optimal.

The errors shown in Fig. 12 derive from the variation between the individual CRs. These statistical errors are considerably larger than the ones derived from the method described in Sect. 2.4, which are of the order of 0.5% and smaller. From that we conclude that the uncertainties from the ballistic and magnetic mapping play only a secondary role in comparison to the statistical error.

**Table 2.**  $\Gamma_{oc}$  for solar wind with speeds  $<350 \text{ km s}^{-1}$ , as function of the leading angle.

Leading angle [°]	$\Gamma_{oc}$ [%]
-8	$23.6 \pm 18.1$
-7	$24.3 \pm 17.4$
-6	$24.8 \pm 16.2$
-5	$24.7 \pm 14.8$
-4	$24.8 \pm 12.4$
-3	$24.4 \pm 11.4$
-2	$24.4 \pm 10.8$
-1	$24.0 \pm 10.0$
0	$23.8 \pm 10.4$
1	$23.1 \pm 12.6$

#### 4. Comparison with the CSSS model

As stated in Sect. 2, the CSSS model has been shown to predict solar wind speed nearly twice better than the PFSS model. The details of the CSSS model and the method adopted for the prediction technique can be found in Poduval & Zhao (2014) and Poduval (2016). In order to test if a different input model alters the results of our analysis we repeated the analysis of the former section but using the CSSS model for the calculation of the magnetic mapping. Additionally we adjust the radius of the source surface to  $15 R_\odot$ , as this is the case for the CSSS model. Since we have only a smaller subset of CRs computed with the CSSS model we also used the same smaller subset of rotations computed with the PFSS model for the comparison. The results are shown in Fig. 13. The histograms shown here cover the same solar wind speed window as the red histogram in Fig. 12. The differences from Fig. 12 are because of the smaller subset of CRs used. In Fig. 13 we can see that both results show the same behaviour. Although the absolute numbers differ slightly both histograms show that the optimal value for  $\Gamma_{oc}$  is obtained for  $\lambda_{la} = -10^\circ$ . This analysis shows that the CSSS results are comparable to those of the well-established PFSS model. Therefore, for the present analysis both the CSSS and PFSS models seem equally applicable.

#### 5. Summary and conclusion

One of the aims of the upcoming Solar Orbiter mission is to directly identify the source regions of solar wind by linking remote and in situ observations. The novelty of Solar Orbiter's instrumentation lies in the capability of measuring solar wind in situ and remotely at the same time and very close to the Sun. The challenge to establish the link is not only to find the spatial displacement between in situ observed solar wind and its source region on the Sun but also to take into account the temporal displacement between these two observations. This means that we need to point the remote-sensing instrument on the right place at the Sun and at the right time. In order to do so the terminal solar wind speed as well as the magnetic configuration inside the corona must be known. Both cannot be known in real time, for example, the terminal solar wind speed cannot be obtained from remote sensing but only by in situ measurements. Thus, a prediction of the solar wind speed which will be measured in situ in the future is needed to point the spectrograph at the right place at present.

In this study we investigated the spatial and temporal displacement between in situ observed solar wind and its source region on the Sun. In addition we tested different methods to

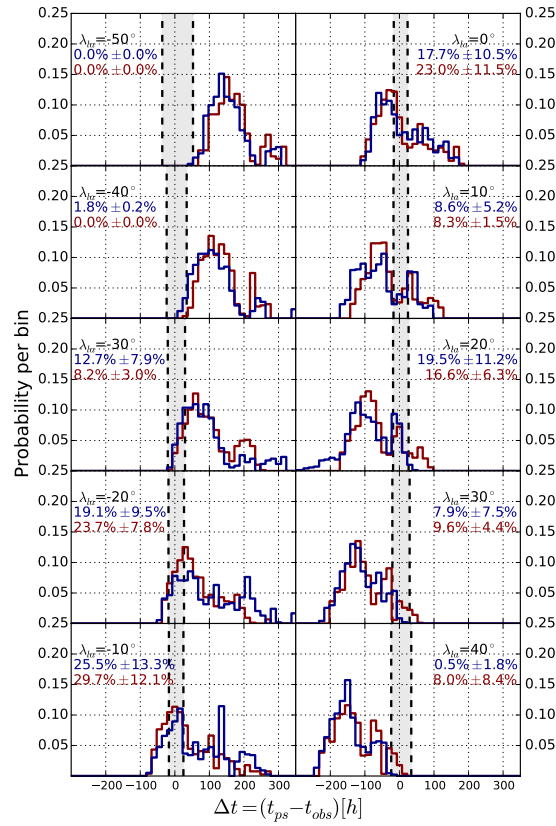


**Fig. 13.** Comparison of the leading stripe mapping between the PFSS (red histograms) and the CSSS (blue histograms) model. The axes are the same as in Fig. 12. Note that the subset of CRs used for this comparison only includes four rotations. The solar wind speed window covers the range from 0 to  $350 \text{ km s}^{-1}$ . The errors given are the statistical errors originating from the variation between the CRs.

predict the optimal pointing of SPICE with respect to source region coverage and temporal displacement. The spatial displacement is found by tracking the solar wind from its source region out to the spacecraft. Above the source surface we applied classic ballistic back mapping, resulting in a ballistic displacement. Inside the corona we applied a PFSS model which yields a magnetic displacement, and a model by Cranmer et al. (2007) from which we derive the coronal escape time.

We find that it is important to consider the magnetic mapping in addition to the ballistic mapping for the prediction of the solar wind's source regions. For the prediction of the solar wind's release time, that is, the time when the instrument has to do its observation, the plasma escape time has to be added to the ballistic travel time of the plasma package. For an instrument to track the source regions in real time, a prediction scheme that uses the solar wind speeds and magnetic configuration of the preceding CR yields a probability of  $45.56 \pm 15.77\%$  to observe the source region at the time of the solar wind's release at the photosphere.

SPICE will only be able to make one raster per day, that is, SPICE will not be able to track the source regions at all times, but the in situ instrument (HIS) will measure at all time. To account for this a leading stripe forward mapping was devised, where six snapshots are vertically stacked to form a stripe which covers the whole Sun in latitude. Virtually any source region will be

detected eventually, but typically not at the time of the plasma release at the Sun. For each source region covered by the leading stripe the time difference between remote observation and solar wind release can be calculated. To optimize the number of observations done at the right time the leading angle of the stripe can be varied. We tested this for various angles ranging from  $-50^\circ$  to  $40^\circ$  and three different solar wind speed regimes. This results in an optimal leading angle  $\approx -6^\circ$  for the study of slow solar wind ( $250 \text{ km s}^{-1} < v_{\text{sw}} < 350 \text{ km s}^{-1}$ ),  $\approx 20^\circ$  for intermediate ( $350 \text{ km s}^{-1} < v_{\text{sw}} < 600 \text{ km s}^{-1}$ ) and  $\approx 10^\circ$  for fast solar wind ( $600 \text{ km s}^{-1} < v_{\text{sw}} < 900 \text{ km s}^{-1}$ ).

Additionally we repeated the leading stripe method while using CSSS maps for the magnetic mapping in order to compare the results. The comparison did not lead to different results, hence we concluded that the PFSS model is sufficient for the presented analysis. In particular these small leading angles and the corresponding almost optimal line of sights are advantageous for the quality of the SPICE measurements. Although the focus of our study was on the upcoming Solar Orbiter mission and the SPectral Imaging of the Coronal Environment instrument, the methods described are generally applicable.

**Acknowledgements.** This work uses magnetograms obtained from the MDI instrument in board the SOHO spacecraft. SOHO is a project of international cooperation between ESA and NASA. Additionally this work uses SOLIS data obtained by the NSO Integrated Synoptic Program (NISP), managed by the National Solar Observatory, which is operated by the Association of Universities for Research in Astronomy (AURA), Inc. under a cooperative agreement with the National Science Foundation. The authors would like to thank Dr Bala Poduval for her valuable support with the CSSS model and the computations contributed to this work. R.f.W.S. acknowledges constructive discussions with the

Solar Orbiter SPICE steering committee and the Solar Orbiter Science Working Team and the German Space Agency, DLR for grant 50OT1202. L.B. was supported by DLR grant 50OC1501.

## References

- Altschuler, M. D., & Newkirk, G. 1969, *Sol. Phys.*, **9**, 131
- Bochsler, P. 2000, *Rev. Geophys.*, **38**, 247
- Caldwell, M. 2014, SPICE Instrument User Manual
- Crammer, S. R., van Ballegooijen, A. A., & Edgar, R. J. 2007, *ApJS*, **171**, 520
- Fisk, L. A. 2003, *J. Geophys. Res. (Space Physics)*, **108**, 1157
- Fludra, A., Griffin, D., Caldwell, M., et al. 2013, in Solar Physics and Space Weather Instrumentation V, *Proc. SPIE*, **8862**, 88620F
- Geiss, J., Gloeckler, G., & von Steiger, R. 1995, *Space Sci. Rev.*, **72**, 49
- Goel, A., & Choudhuri, A. R. 2009, *Res. Astron. Astrophys.*, **9**, 115
- Hassler, D. M., Deforest, C., & Spice Team 2011, AGU Fall Meeting Abstracts
- Koskela, J. S., Virtanen, I. I., & Mursula, K. 2015, AGU Fall Meeting Abstracts
- Krieger, A. S., Timothy, A. F., & Roelof, E. C. 1973, *Sol. Phys.*, **29**, 505
- Landi, E., Gruesbeck, J. R., Lepri, S. T., & Zurbuchen, T. H. 2012, *ApJ*, **750**, 159
- Liu, Y., & Norton, A. 2001, Mdi measurement errors: the magnetic perspective, SOI technical note, Tech. Rep., Stanford University
- Neugebauer, M., Forsyth, R. J., Galvin, A. B., et al. 1998, *J. Geophys. Res.*, **103**, 14587
- Nolte, J. T., & Roelof, E. C. 1973, *Sol. Phys.*, **33**, 241
- Poduval, B. 2016, *ApJ*, **827**, L6
- Poduval, B., & Zhao, X. P. 2014, *ApJ*, **782**, L22
- Rappazzo, A. F., Matthaeus, W. H., Ruffolo, D., Servidio, S., & Velli, M. 2012, *ApJ*, **758**, L14
- Royal Observatory of Belgium, B. 2016, <http://sidc.be/silso/home>
- Schatten, K. H., Wilcox, J. M., & Ness, N. F. 1969, *Sol. Phys.*, **6**, 442
- Scherrer, P. H., Bogart, R. S., Bush, R. I., et al. 1995, *Sol. Phys.*, **162**, 129
- Schwenn, R., Mohlhauser, K. H., & Rosenbauer, H. 1981, in Solar Wind 4, ed. H. Rosenbauer, 118

## 7.4 PUBLICATION 4

Although fast solar wind streams originating in coronal-hole regions are well understood, they are not necessarily homogeneous in their composition. Compared to the slow solar wind, average charge states of oxygen and carbon are usually low in fast solar wind streams. Data samples measured aboard [ACE](#) using the [SWICS](#) instrument during the years 2004 and 2006 were selected according to their average oxygen and carbon charge-states and their collisional age. The average iron charge-state distribution was compared for the two periods, and the streams were classified as either FE-hot or FE-cold. The new [PFSS](#) solver was used to determine the individual solar wind streams' footpoints in the photosphere and the corresponding locations of stream boundaries. The results were published in:

**OBSERVATIONS OF HIGH AND LOW FE CHARGE STATES IN INDIVIDUAL SOLAR WIND STREAMS WITH CORONAL-HOLE ORIGIN**

V. Heidrich-Meisner, T. Peleikis, M. Kruse, L. Berger and R. F. Wimmer-Schweingruber, *A&A*, A70, 593, 2016, reproduced with permission © ESO.

DOI: [10.1051/0004-6361/201527998](https://doi.org/10.1051/0004-6361/201527998)

Own contribution: 25%

*Summary*

A brief introduction to solar wind streams' characteristics is followed by a description of ion charge states, the collisional age metric, the proton solar wind speed, and their role in classifying different solar wind types. The [ACE](#) mission and instrumentation are presented as a data source for performing the publication's analysis. After a thorough overview of the boundaries for classification of solar wind streams, especially the distinction between Fe-cold (low average Fe-ion charge state) and Fe-hot (high average Fe-ion charge state) streams, the publication discusses several individual solar wind streams and their transitions from one to another with respect to the aforementioned classification during 2004 and 2006. The photospheric source regions of the individual streams are computed using a combination of ballistic and magnetic back mapping employing a [PFSS](#) model for the lower coronal magnetic field. This mapping distinguishes between polar coronal hole origin (mostly Fe-hot) and equatorial coronal hole (mostly Fe-cold) origin.

The key results are:

- Coronal hole wind is not uniform in its properties; utilizing the appropriate measure permits developing a more fine-grained classification.
- Fe-hot and Fe-cold streams originate both in equatorial regions and close to each other.
- The distribution between Fe-hot and Fe-cold streams might depend on the solar cycle, though more data is required to assert this assumption.

## Observations of high and low Fe charge states in individual solar wind streams with coronal-hole origin

Verena Heidrich-Meisner, Thies Peleikis, Martin Kruse, Lars Berger, and Robert Wimmer-Schweingruber

Christian Albrechts University at Kiel, 24118 Kiel, Germany  
 e-mail: [heidrich@physik.uni-kiel.de](mailto:heidrich@physik.uni-kiel.de)

Received 18 December 2015 / Accepted 18 July 2016

### ABSTRACT

**Context.** The solar wind originating from coronal holes is comparatively well-understood and is characterized by lower densities and average charge states compared to the so-called slow solar wind. Except for wave perturbations, the average properties of the coronal-hole solar wind are passably constant.

**Aims.** In this case study, we focus on observations of the Solar Wind Ion Composition Spectrometer (SWICS) on the Advanced Composition Explorer (ACE) of individual streams of coronal-hole solar wind that illustrate that although the O and C charge states are low in coronal-hole wind, the Fe charge distribution is more variable. In particular, we illustrate that the Fe charge states in coronal-hole solar wind are frequently as high as in slow solar wind.

**Methods.** We selected individual coronal-hole solar wind streams based on their collisional age as well as their respective O and C charge states and analyzed their Fe charge-state distributions. Additionally, with a combination of simple ballistic back-mapping and the potential field source surface model, transitions between streams with high and low Fe charge states were mapped back to the photosphere. The relative frequency of high and low Fe charge-state streams is compared for the years 2004 and 2006.

**Results.** We found several otherwise typical coronal-hole streams that include Fe charge states either as high as or lower than in slow solar wind. Eight such transitions in 2006 were mapped back to equatorial coronal holes that were either isolated or connected to the northern coronal-hole. Attempts to identify coronal structures associated with the transitions were so far inconclusive.

**Key words.** solar wind – Sun: heliosphere – Sun: magnetic fields

### 1. Introduction

The steady solar wind is typically divided into two dominant types, fast and slow solar wind. However, the differences in their properties are better ordered by elemental and charge-state abundances rather than by solar wind speed. Here, we focus on fast solar wind. It has been uniquely identified as originating from coronal holes and the release mechanism is well understood (i.e. Tu et al. 2005). Therefore, in the following, we use the term coronal-hole wind instead of fast solar wind. Aside from fluctuations caused by waves (mainly Alfvénic waves), its plasma and compositional properties are constant (e.g. von Steiger et al. 2000). Both the elemental and charge-state compositions of the solar wind reflect the conditions in the respective solar source regions. In particular, the charge-state distribution for each solar wind ion species is (almost completely) determined in the corona. For each ion pair the recombination and ionization rates are temperature dependent and the hot corona allows high ionization states to occur. For a pair of adjacent ionization states  $i \leftrightarrow i+1$ , this can be expressed by a temperature dependent charge modification time scale  $\tau_{\text{mod},i}(T) = \frac{1}{n_e(C_i + R_{i+1})}$ , where  $T$  denotes the electron temperature in K,  $n_e$  the electron density,  $C_i$  the ionization rate of the  $i$ th ionization state, and  $R_{i+1}$  the recombination rate of the  $(i+1)$ th to the  $i$ th ionization state. But the ionization state is not only temperature dependent. A sufficiently high electron density is required to allow recombination. Thus, a simple model to explain the observed solar wind speeds and charge states assumes that the charge state can change along

the solar-wind flux tube until the expansion time scale (which depends on the electron density profile in the corona) is of the same order as the charge modification time scale of an ion pair. Beyond this point the charge-state distribution remains “frozen-in” as the solar wind propagates further outwards.

The coronal-hole wind is known for comparatively low O and C charge states and corresponding freeze-in temperatures. They are particularly low compared to those of the slow solar wind. The O charge-state distribution can be considered as a tracer for the solar wind type. The ratio  $n_{O^{7+}}/n_{O^{6+}}$  of the densities of  $O^{7+}$  to  $O^{6+}$  (denoted with  $n_{O^{7+}}$  and  $n_{O^{6+}}$ , respectively) has been frequently used in solar wind categorization schemes (e.g. Zurbuchen et al. 2002; Zhao et al. 2009) to differentiate between fast (coronal hole) and slow solar wind. In accordance with the cool O and C signatures in coronal-hole wind, the charge-state distributions of other ions, for example Fe, could also be expected to be cooler in the coronal-hole wind than in the slow solar wind. However, that is clearly not necessarily the case. While the Ulysses observations in von Steiger et al. (2000), Richardson (2014) and Zhao & Landi (2014, as well as the ACE observations in Zhao & Landi 2014) show on average higher Fe charge states in the fast solar wind than in the slow solar wind (see for example Plate 5 in von Steiger et al. 2000), the STEREO results (Galvin et al. 2009) indicate lower Fe charge states in coronal-hole wind. For example, for the solar-wind speed bin  $650\text{--}700 \text{ km s}^{-1}$  the average Fe charge state in coronal-hole wind observed with PLASTIC on STEREO A from 2007–2009 is given as 9.25, which is lower than for all slow

solar wind bins considered in that article. For all other high speed bins, the average Fe charge state is even lower. Zhao & Landi (2014) compared long-term properties of coronal-hole wind at different solar minima and identified two subcategories, coronal-hole wind originating from polar coronal holes and coronal-hole wind originating from the equatorial region. Lower Fe charge states were observed in equatorial coronal-hole wind than in polar coronal holes and additionally lower charge states were found in the second solar minimum. A gradual charge-state decrease for O, C, and Fe from solar maximum to the following solar minimum in solar cycle 23 has been discussed in Lepri et al. (2013) and Zhao & Fisk (2010) underlines differences in the composition of the slow solar wind between the two consecutive solar minima in solar cycles 22 and 23.

Instead of focusing on the statistics of charge-state parameters gathered over long time periods, we discuss several case studies of individual streams within the ACE/SWICS data that show regions of high and low Fe charge states with a clear transition between these regions. We then map these streams back to their coronal sources and assess whether there are any coronal structures that may be associated with these transitions.

## 2. Data analysis and event selection

The SWICS instrument on ACE (Gloeckler et al. 1998) combines a time-of-flight mass spectrometer and energy-per-charge analyzer with an energy measurement. A detailed and extensive description of the data analysis procedure applied to the pulse height amplitude (PHA) data is given in the PhD thesis Berger (2008) and has been applied in, e.g. Berger et al. (2011).

The proton density  $n_p$  (from the Solar Wind Electron, Proton and Alpha Monitor (SWEPAM) on ACE, McComas et al. 1998), and the densities of  $O^{6+}$ ,  $O^{7+}$ ,  $C^{5+}$ , and  $C^{6+}$  are used for the characterization of solar-wind plasma as coronal-hole wind. We selected coronal-hole-wind streams based on four-hour resolution data from SWICS and SWEPEPAM and the following three criteria: (1) Low O and C charge-state ratios ( $n_{O^{7+}}/n_{O^{6+}}$  and  $n_{C^{6+}}/n_{C^{5+}}$ , respectively) are considered as the decisive property for identifying coronal-hole wind. Zhao et al. (2009) proposed an upper limit of  $n_{O^{7+}}/n_{O^{6+}} < 0.145$  for coronal-hole wind. To avoid potential contamination with inter-stream solar wind, we apply  $n_{O^{7+}}/n_{O^{6+}} < 0.1$  which was also used in Zurbuchen et al. (2002). For C, we adopted an upper threshold of  $n_{C^{6+}}/n_{C^{5+}} < 1$ . (2) Based on the observations in Kasper et al. (2008), we additionally require a low collisional age  $a_{\text{col}} = \frac{r}{v_p \tau_{\text{col}}} < 0.1$ , with  $r$  as the distance from the Sun to ACE,  $v_p$  the solar-wind proton speed, and  $\tau_{\text{col}}$  the time scale for  $\alpha$  to proton energy exchange due to small-angle Coulomb scattering, where  $\tau_{\text{col}} \sim n_p T_p^{-3/2}$ . The collisional age is defined by the ratio of expansion and collisional time scales. Although the proton-proton collisional age is not representative for the collisional properties of the entire solar-wind plasma, we consider the proton-proton collisional age as a representative marker for the solar-wind stream type. (3) Only streams that remained within the respective same categorization regimes of the average O and C charge states and collisional age for at least half a day were considered. Fluctuations in  $a_{\text{col}}$ ,  $n_{O^{7+}}/n_{O^{6+}}$ ,  $n_{C^{6+}}/n_{C^{5+}}$ , or the average Fe charge-state on smaller time scales than the four hours were permitted as long as the average value (averaged over four hours) remained in the respective range.

As a comparison baseline we also require pure slow solar wind. In this context, pure slow solar wind is characterized by high O charge states  $n_{O^{7+}}/n_{O^{6+}} > 0.1$ , high C charge states

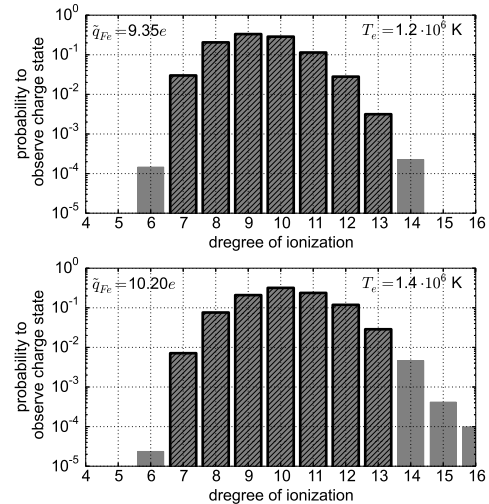


**Fig. 1.** Top panel: Fe charge-state distribution at  $T = 1.2 \times 10^6$  K taken from the CHIANTI database. Bottom panel: Fe charge-state distribution at  $T = 1.4 \times 10^6$  K from the CHIANTI. The black borders indicate the Fe charge states considered in this work. In both panels, the mean Fe charge-state  $\bar{q}_{\text{Fe}}$  is given as inset on the left.

$n_{C^{6+}}/n_{C^{5+}} > 1$ , and high collisional age  $a_{\text{col}} > 0.4$ . This characterization of slow solar wind is not directly complementary to the criteria for identifying coronal-hole wind as described above in order to reduce the contamination of each wind type by transition regions that exhibit a mixture of properties of slow and coronal-hole wind.

In this study, we are interested in the Fe charge-state distribution in coronal-hole wind. The densities of the Fe charge states are provided by ACE/SWICS. In particular, since the most abundant Fe charge states are well isolated from all other ions in the SWICS  $m/m/q$  diagram, we focus on these, namely  $Fe^{7+}$ ,  $Fe^{8+}$ ,  $Fe^{9+}$ ,  $Fe^{10+}$ ,  $Fe^{11+}$ ,  $Fe^{12+}$ , and  $Fe^{13+}$ . In the following the average Fe charge-state  $\bar{q}_{\text{Fe}}$  is defined as  $\bar{q}_{\text{Fe}} = \sum_{c=7}^{13} cn_{\text{Fe}^{c+}} / \sum_{c=7}^{13} n_{\text{Fe}^{c+}}$ .

Figure 1 shows the Fe charge-state distribution for two electron temperatures  $T = 1.2 \times 10^6$  K (top) and  $T = 1.4 \times 10^6$  K (bottom) as provided by the atomic database CHIANTI (Dere et al. 1997; Landi et al. 2013). The temperatures are chosen from the typical range of observed electron temperatures in the corona (see e.g. Ko et al. 1997; Wilhelm 2012). The charge states considered here ( $Fe^{7+}$ ,  $Fe^{8+}$ ,  $Fe^{9+}$ ,  $Fe^{10+}$ ,  $Fe^{11+}$ ,  $Fe^{12+}$ , and  $Fe^{13+}$ ) are highlighted by hatched bars and black borders around the respective bars and are at the relevant temperatures the most prominent charge states.

Based on the CHIANTI data displayed in Fig. 1 and under the assumptions that the freeze-in temperature  $T_{f,\text{Fe}}$  for all Fe ions is the same and that  $T_{f,\text{Fe}} \sim 1.2 \times 10^6$  K, Fig. 1 also illustrates that  $q_{\text{Fe}} = 9$  would be the most likely charge state, with a mean charge state of 9.35. For  $T = 1.4 \times 10^6$  K a mean charge state of 10.2 would be expected. However, since the assumption that all Fe ions freeze-in at the same temperature is not accurate, this provides only a rough guideline. Furthermore CHIANTI makes the assumption of a Maxwellian distribution for the electron velocity distribution function which is known not to be the appropriate choice for the solar corona and the solar wind (see for example, Marsch 2006). Instead our notion of high or low average Fe charge state is based on a comparison

of Fe charge states in coronal-hole wind to those observed in selected samples of slow solar wind.

For 2004 the median of the average Fe charge-state of pure slow solar wind was  $\tilde{q}_{\text{Fe,slow}} = 9.87$ . The  $1\sigma$ -level is bounded below by  $\tilde{q}_{\text{Fe,slow}} - \sigma = 9.54$ . These values are used to define our notion of high and low Fe charge states. We consider the average Fe charge state  $\tilde{q}_{\text{Fe,CH}}$  of a coronal-hole-wind stream as low and the stream as Fe-cool if  $\tilde{q}_{\text{Fe,CH}} < \tilde{q}_{\text{Fe,slow}} - \sigma$ . Analogously, we consider a coronal-hole-wind stream to be Fe-hot if its average Fe charge-state is within one  $\sigma$  of the average Fe charge state of pure slow solar wind for that year or higher:  $\tilde{q}_{\text{Fe,CH}} > \tilde{q}_{\text{Fe,slow}} - \sigma$ . Thus for 2004, the threshold value is  $\tilde{q}_{\text{Fe,slow}} - \sigma = 9.54$  and for 2006  $\tilde{q}_{\text{Fe,slow}} - \sigma = 9.71$ .

To ensure that the selected coronal-hole-wind streams are not contaminated with interplanetary coronal mass ejections (ICMEs), we cross-referenced the [Jian et al. \(2006, 2011\)](#) and [Richardson & Cane \(2010\)](#) ICME lists and the Large Angle and Spectrometric Coronagraph (LASCO) CME list and excluded all time periods with ICMEs from our times of interest. For four days after each halo CME in the LASCO list ([Yashiro et al. 2004; Gopalswamy et al. 2009](#)) that does not have a counterpart in the ICME lists, we verified that no ICME signatures were contained in the coronal-hole-wind stream candidates. Also, to reduce the effect of inter-stream regions, time periods with enhanced proton density and magnetic field strength which indicate stream interaction-regions ([Jian et al. 2006, 2011](#)) were excluded as well. With this method, 4660 12-min observations were selected as coronal-hole wind in 2004, accumulating to 38.8 days of combined coronal-hole wind, and 8346 observations corresponding to 69.5 days of combined coronal-hole wind in 2006. For the sake of an unbiased representation, we randomly chose three transitions from two different years between Fe-cool and Fe-hot coronal-hole wind from the available data set to be discussed in detail in the following section: day of year (DoY) 2–14 in 2004 and DoY 158–162 and DoY 212–215 in 2006. Six additional transitions in 2006 are mentioned briefly.

### 3. Fe charge states of individual coronal-hole-wind streams

We now focus on the Fe charge-state distribution of individual coronal-hole-wind streams and relate the average Fe charge state of these to the average Fe charge-state of all slow solar wind streams of the same year.

Figure 2 summarizes the solar wind properties for 12 days in 2004. From top to bottom, the panels in Fig. 2 show the collisional age  $a_{\text{col}}$ , the ratios  $n_{\text{O}^{7+}}/n_{\text{O}^{6+}}$  and  $n_{\text{C}^{6+}}/n_{\text{C}^{5+}}$ , the corresponding freeze-in temperatures  $T_{f,\text{O}^{7+}/\text{O}^{6+}}$  and  $T_{f,\text{C}^{6+}/\text{C}^{5+}}$ , the magnetic field strength  $B$  and angles  $B_\phi$ ,  $B_\theta$ , and in the bottom panel the proton speed  $v_p$  (left  $y$ -axis) and proton density  $n_p$  (right  $y$ -axis). A coronal-hole stream (DoY 3.5–6.5) is followed by an interface region with a higher-speed stream and an ICME beginning on DoY 9. The ICME period is marked with gray hatching. From DoY 3.5 to DoY 6.5,  $n_{\text{O}^{7+}}/n_{\text{O}^{6+}}$  and  $n_{\text{C}^{6+}}/n_{\text{C}^{5+}}$  are low and, in particular, are below their respective thresholds for coronal-hole wind. The collisional age  $a_{\text{col}}$  is below its threshold value of 0.1 for coronal-hole wind as well. Thus, according to the criteria described in Sect. 2, this suffices to categorize this stream as fast, that is, as coronal-hole wind. This is supported by the additional data products shown in Fig. 2. Although there is some variability in the solar-wind proton speed  $v_p$ , the minimal value is still unlikely to be produced by slow solar wind. The freeze-in temperatures are derived under the assumption of an

equilibrium state that allows us to relate the observed abundance ratio of two adjacent ions to the respective ionization and recombination rates:  $n_i/n_{i+1} = R_{i+1}(T_f)/C_i(T_f)$ . Since they depend on the density ratios  $n_{\text{O}^{7+}}/n_{\text{O}^{6+}}$  and  $n_{\text{C}^{6+}}/n_{\text{C}^{5+}}$  it is not surprising that the freeze-in temperatures are low during the coronal-hole-wind stream as well.

Although still below the threshold for coronal-hole wind defined above, the  $n_{\text{O}^{7+}}/n_{\text{O}^{6+}}$  ratio and the collisional age are higher from DoY 3.5 to DoY 4.25 than in the following period. To prevent any interference by other processes, we focus on the part of the coronal-hole-wind stream from DoY 4.5–6.5 where both density ratios are safely below their respective categorization thresholds. Based on these considerations, the time period from DoY 4.5–6.5 (which is indicated with the gray shaded area in Fig. 2) contains only typical, quiet coronal-hole wind.

The ICME period exhibits a much larger variability in all data products; in particular, the  $n_{\text{O}^{7+}}/n_{\text{O}^{6+}}$  and the collisional age are much higher. The magnetic-field angles show a smooth rotation indicating a magnetic cloud as part of the ICME. Thus, this ICME can easily be distinguished from the coronal-hole-wind stream.

Figure 3 focuses on the highlighted part of the coronal-hole-wind stream (DoY 4.5–6.5) from Fig. 2. For this time period of interest, Fig. 3 examines how the individual Fe charge states behave during DoY 4.5–5.6 and DoY 5.6–6.5. The motivation for this partition is detailed in Fig. 4. The upper five panels of Fig. 3 show the density ratios of C, O, and Fe ion pairs within these two parts of the coronal-hole-wind stream of interest, and the bottom panel provides examples of the charge-state distributions of C, O, and Fe for two selected observations. The vertical lines in the upper panels indicate the corresponding times used in the bottom panel. The horizontal lines in each panel give the mean density ratio in the left and right interval, respectively. All Fe ion density ratios shown here are higher in the first part of the stream than in the second part. Comparing the two charge-state distribution examples at the bottom, in the example on the left, not only is the maximum of the Fe charge-state distribution shifted from  $\text{Fe}^{9+}$  to  $\text{Fe}^{10+}$  as compared to the second example, but the complete distribution is shifted to higher charge states. Thus, a change in the mean charge-state cannot be explained by a single enhanced or depleted charge-state. Instead all considered charge states are affected.

As a continuous representation of the charge-state distributions in the bottom panel of Fig. 3, Fig. 4 shows a time series of the Fe charge-state distribution (considering only  $\text{Fe}^{7+}$  to  $\text{Fe}^{13+}$ ) in the first panel. The three bottom panels provide the solar-wind proton speed  $v_p$ , proton density  $n_p$ , and the ratio  $n_{\text{O}^{7+}}/n_{\text{O}^{6+}}$  as reference. During DoY 4.5–5.6 the charge-state distribution of Fe is shifted to higher charge states more similar to those observed in slow solar wind. A transition between Fe-hot and Fe-cool coronal-hole wind (marked with a vertical black line) occurs at DoY 5.6. After the transition, at 5.6–6.5, lower Fe charge states are observed. Both the characterization as Fe-cool or Fe-hot wind and the resulting transition point are defined on four-hour resolution data. The same transition divides the left and right parts of the five top panels in Fig. 3. It is interesting to note that the Fe-hot part of the stream coincides with an average solar wind speed below  $600 \text{ km s}^{-1}$ , whereas the Fe-cool interval shows an average solar wind speed higher than  $600 \text{ km s}^{-1}$ . This hints at a potential stream boundary between two high-speed streams that coincides with the transition between Fe-hot and Fe-cool coronal-hole wind as a possible explanation for the observed transition.

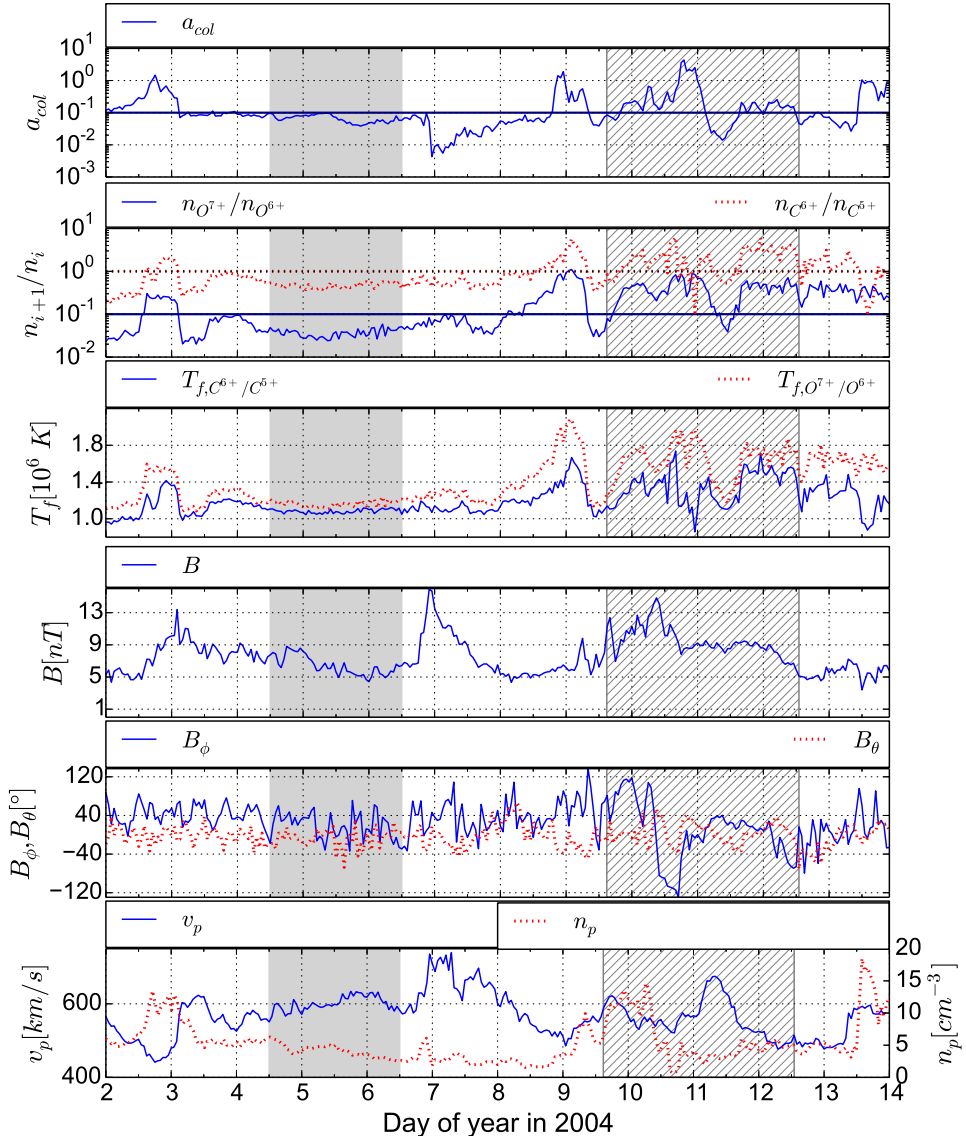


**Fig. 2.** Solar wind properties for 12 days in 2004. The collisional age  $a_{\text{col}}$  is displayed in the first panel. The second panel shows the density ratios  $n_{\text{O}^{7+}}/n_{\text{O}^{6+}}$  and  $n_{\text{C}^{6+}}/n_{\text{C}^{5+}}$ . The horizontal lines in the first two panels indicate the respective selection thresholds for  $a_{\text{col}} = 0.1$ ,  $n_{\text{C}^{6+}}/n_{\text{C}^{5+}} = 1$ , and  $n_{\text{O}^{7+}}/n_{\text{O}^{6+}} = 0.1$ . The third panel contains the freeze-in temperatures  $T_f$  corresponding to the ion density ratios  $n_{\text{O}^{7+}}/n_{\text{O}^{6+}}$  and  $n_{\text{C}^{6+}}/n_{\text{C}^{5+}}$ . The fourth panel gives the magnitude of the magnetic field  $B$  and the azimuthal ( $B_\phi$ ) and polar ( $B_\theta$ ) angles of the magnetic field are shown in the fifth panel. The sixth panel shows the solar-wind proton speed (left y-axis) and proton density (right y-axis) as measured by SWEPM. All data products are displayed with 1h time resolution. The gray shaded area marks a pure coronal-hole-wind stream, while the hatched area highlights an ICME.

Figure 5 shows observations for a solar wind stream in 2006 which exhibits a transition from Fe-cool CH wind to Fe-hot CH wind. In the top panel of Fig. 5, a time series of the charge-state distribution is shown (in the same way as in Fig. 4). An increase of the average Fe charge state is visible at DoY 160.4 thus indicating a transition from Fe-cool coronal-hole wind to Fe-hot coronal-hole wind. The panels below show the solar-wind proton speed, proton density, and the  $n_{\text{O}^{7+}}/n_{\text{O}^{6+}}$  ratio measured at ACE. To allow a direct comparison with the model polarity in Fig. 6, the bottom panel gives additionally the magnetic-field polarity observed with ACE/MAG (Smith et al. 1998) for the same time

period. In order to determine the in-situ magnetic-field polarity, we first derive the nominal magnetic-field direction  $B_\phi^{\text{nom}}$ , that is, the angle between the field line and the radial direction:  $B_\phi^{\text{nom}} = \arccos\left(\sqrt{\frac{1}{1+(\omega r \sin(\theta)/v_p)^2}}\right)$ . Here,  $\omega$  is the solar angular velocity,  $r$  is the Sun-spacecraft distance,  $\theta$  is the heliographic latitude and  $v_p$  is the in-situ solar-wind proton speed. Next, we subtract the nominal magnetic field angle  $B_\phi^{\text{nom}}$  from the in-situ measured angle  $B_\phi$ . If the absolute difference is greater than 90 deg, the magnetic-field polarity is inwardly ( $\otimes$ , red) directed; otherwise it is outwardly ( $\odot$ , green) directed. A switch from outwardly

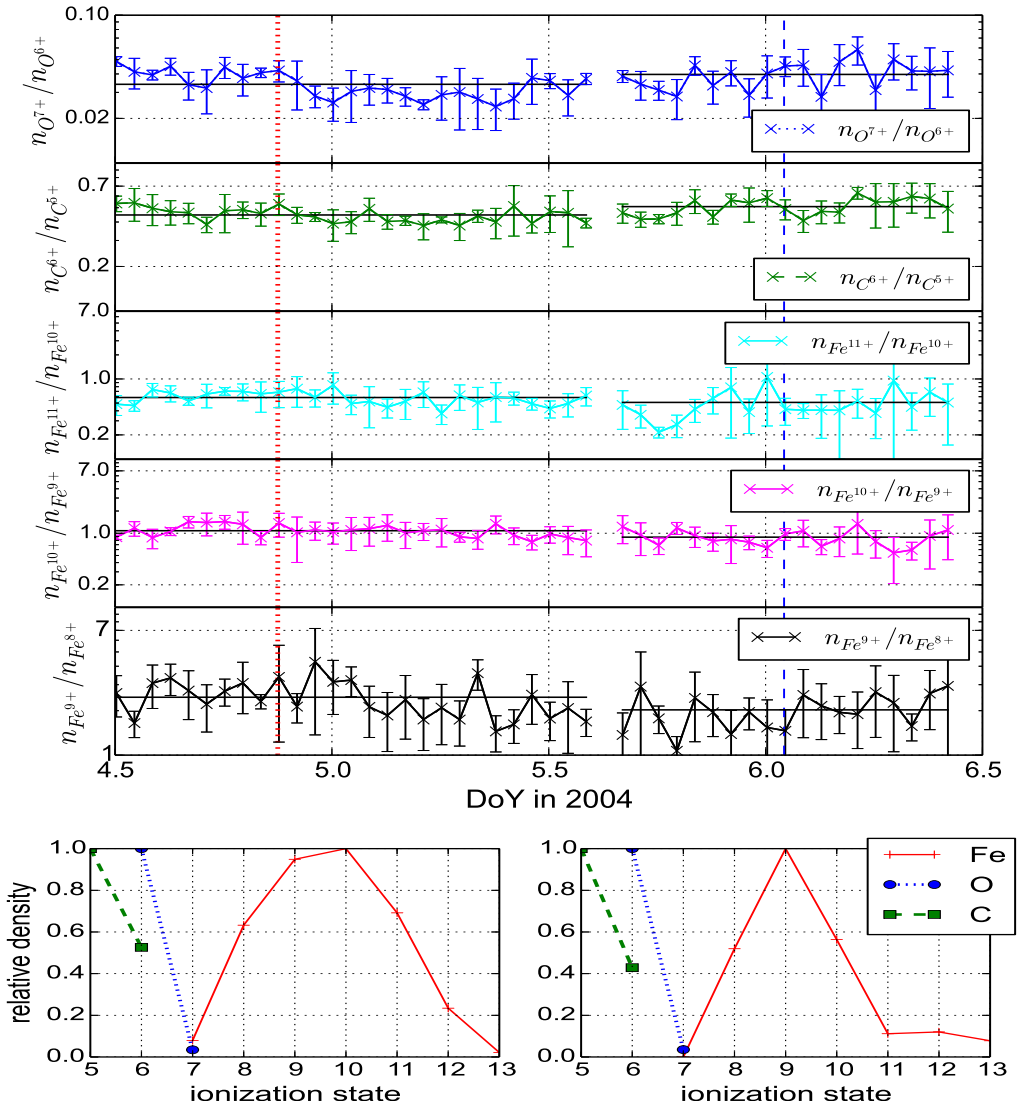


**Fig. 3.** Ion density ratios for the highlighted part of the coronal-hole-wind stream from Fig. 2. The five top panels show the density ratios of ion pairs, namely  $n_{O^{7+}}/n_{O^{6+}}$ ,  $n_{C^{6+}}/n_{C^{5+}}$ ,  $n_{Fe^{11+}}/n_{Fe^{10+}}$ ,  $n_{Fe^{10+}}/n_{Fe^{9+}}$ ,  $n_{Fe^{9+}}/n_{Fe^{8+}}$ . Each curve is divided into two parts. This partition is based on the mean Fe charge-state as illustrated in Fig. 4. The horizontal lines in each panel give the mean density ratio in the left and right interval, respectively. The vertical lines in the five top panels indicate the points in times for which examples of charge-state distributions normalized to the maximum density for C, O, and Fe are shown in the bottom panel. The dotted line corresponds to the left bottom panel and the dashed line to the right panel. (Although  $C^{4+}$  is more abundant than  $C^{6+}$  it is omitted here because it tends to be contaminated with adjacent O ions in ACE/SWICS.) Each data point represents a one-hour average and the error bars reflect the error from the counting statistics.

pointing (i.e.  $\odot$ , green) polarity to inwardly pointing polarity (i.e.  $\otimes$ , red) occurs at DoY 157.3. From DoY 157.3 onwards, the polarity remains inwardly pointing ( $\otimes$ , red) with some exceptions. We verified that the exceptions are caused by kinks in the magnetic field which can be seen by a reversal of the ion-proton differential streaming (Berger et al. 2011). In particular, the polarity does not change on DoY 160 which includes the transition from Fe-cool coronal-hole wind to Fe-hot coronal-hole wind.

With a combination of ballistic back-mapping and a potential field source surface (PFSS, Schatten et al. 1969; Altschuler & Newkirk 1969) model, the photospheric source

region of the ACE observations from DoY 158–163 can be estimated. Based on the in-situ solar wind speed, the solar rotation, and the heliographic coordinates of ACE, the position of ACE in heliographic coordinates is mapped back to the source surface. Here, a simple PFSS model takes over and allows us to track the field lines down to the photosphere. A uniform grid with  $1^\circ$  resolution is assumed at the source surface. Peleikis et al. (2015) gives a more detailed description of the method applied here. The accuracy of this approach is limited by the varying age of different parts of the underlying magnetograms that are composites of images from 27 days. In the following, this back-mapping is used to test whether the observed coronal-hole wind can be

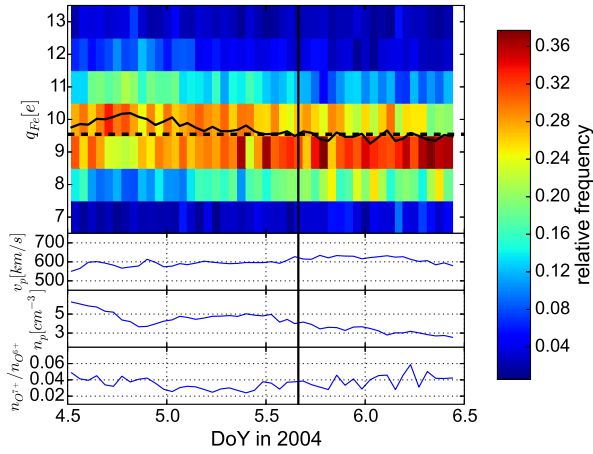


**Fig. 4.** Time series of Fe charge-state distributions (first panel) for the highlighted time period from Fig. 2, that is, DoY 4.5–6.5 in 2004, in one-hour time resolution. In black, the average charge-state (that is,  $\tilde{q}_{Fe} = \sum_{c=7}^{13} cn_{Fe^{c+}} / \sum_{c=7}^{13} n_{Fe^{c+}}$ ) is shown in units of the elementary electric charge  $e$ . Each charge-state distribution is normalized to the sum. Below, the solar wind proton speed (second panel) and proton density (third panel) are given as reference. In the bottom panel the ratio  $n_{O^{+}}/n_{O^{6+}}$  is shown as well. The threshold value between Fe-cool and Fe-hot wind is shown as a horizontal dashed line and the transition between Fe-hot and Fe-cool coronal-hole wind is marked with a vertical black line in all panels.

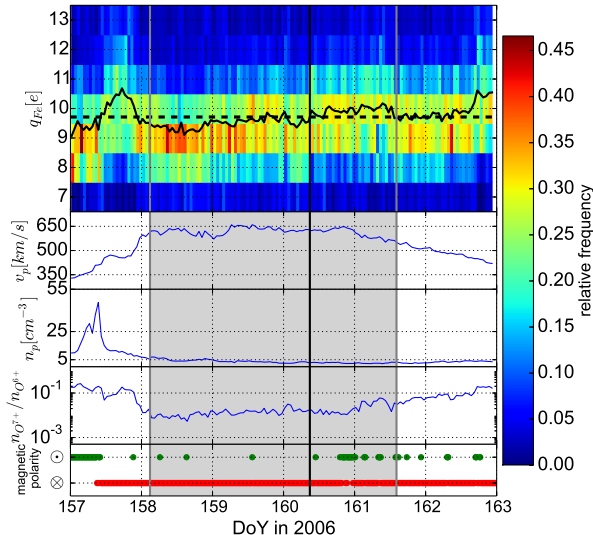


**Fig. 5.** Time series of the charge-state distributions of Fe for six days in 2006 with a one-hour time resolution and in the same format as in Fig. 4, with an additional panel for the magnetic-field polarity. Here, red indicates inwards pointing polarity ( $\otimes$ ) and green indicates outwards-pointing polarity ( $\odot$ ).

associated with an open field line region in the photosphere and to investigate what kind of coronal structures are related to the transitions between Fe-cool and Fe-hot coronal-hole wind. Although only parts of the resulting heliographic maps are shown here, we examined the complete Carrington map in each case.

In Fig. 6, each cross in the lower panel represents a footpoint of a magnetic field line mapped back from the source

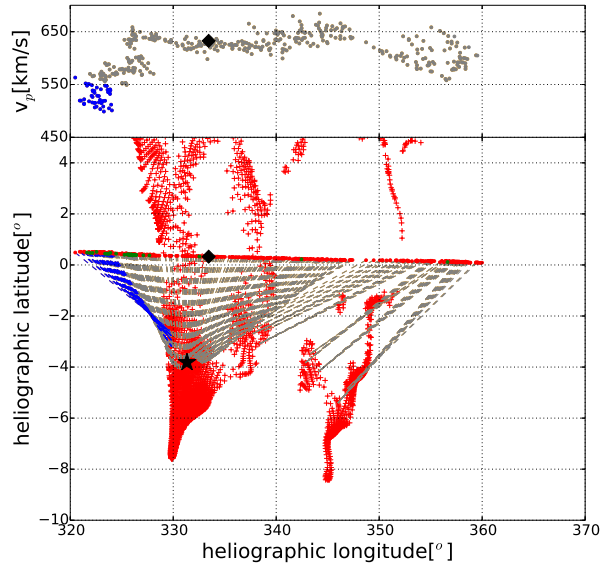


**Fig. 6.** Section of a heliographic map based on MDI magnetograms for Carrington rotation 2044. The first part of the highlighted part of the stream in Fig. 5 is omitted because it is part of the previous Carrington rotation. The top panel shows the solar-wind proton speed ( $v_p$ ) plotted against the mapped back heliographic longitude on the source surface. Below, the dotted line shows the corresponding footpoints of ACE for DoY 158.4–162 on the source surface in heliographic coordinates. The color of each footpoint on the source surface corresponds to the magnetic-field polarity observed at ACE. The polarity is plotted in 12-min time resolution. These footpoints are then traced down to the photosphere with a PFSS model. The dashed lines connect the positions of the ACE footpoints on the source surface to the corresponding footpoints on the photosphere. Footpoints of open field lines in the photosphere are indicated with + symbols (red). The transition between the Fe-hot coronal-hole wind and the Fe-cool coronal-hole wind is marked with a black diamond on the source surface (and in the first panel) and with a black star on the photosphere.

surface down to the photosphere. Additionally for the corresponding Carrington rotation 2044, the footpoints of ACE are shown over this Carrington map derived from a PFSS model based on magnetograms from the Michelson Doppler Imager (MDI, Scherrer et al. 1991) on the Solar and Heliospheric Observatory (SOHO). Figure 6 shows only the area to which the observations in the stream of interest in Fig. 5 are mapped back by the PFSS model. This area is an extension of the northern polar coronal hole to equatorial regions with – according to the PFSS model – red, inwardly pointing polarity. The dashed lines connecting the footpoints on the source surface and the photosphere corresponding to the coronal-hole-wind stream from DoY 158.12–161.59 are colored gray and the start of the subsequent declining phase of the stream (DoY 161.59–162) is colored blue. The border between the Fe-cool coronal-hole wind and the Fe-hot coronal-hole wind is indicated with a black diamond on the source surface and with a black star on the photosphere. The beginning of the period of interest belongs to the preceding Carrington rotation. Thus, for mapping the corresponding footpoints a different Carrington map would need to be considered. Since the transition itself occurs later in the stream and for the sake of clarity this first part of the stream is therefore omitted in Fig. 6. The remaining part of the coronal-hole-wind stream of interest, including the transition between the Fe-cool and the

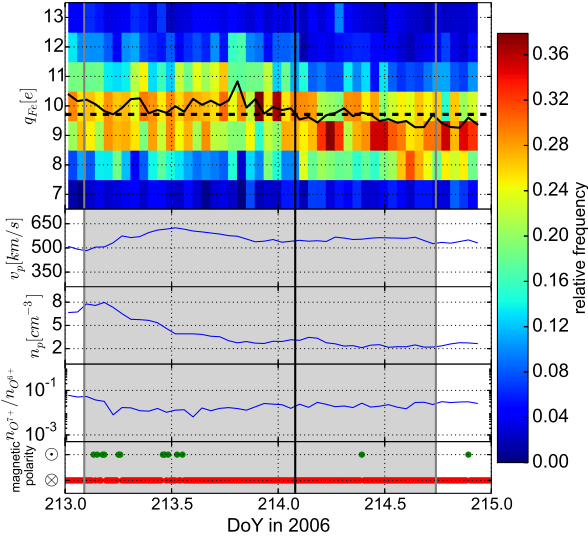


**Fig. 7.** Time series of the charge-state distributions of Fe for two days in 2006, with a one-hour time resolution (first panel) in the same format as in Fig. 5.

Fe-hot stream, and the following stream are mapped to a small scale region with open field lines in the equatorial region which is, as we verified on the complete Carrington map, connected to the northern polar coronal hole. For the whole time period and in particular, around the transition between the Fe-cool and Fe-hot stream, the in-situ observed polarities match (inwards pointing with the exception of the aforementioned kinks) the polarities predicted by the PFSS model. However, due to the limitations on the accuracy of the back-mapping caused by the requirement to derive the magnetic field lines from a complete Carrington rotation, the possibility that the transition occurs at an edge of this open field line region cannot be ruled out.

A second transition, DoY 213–215 in 2006, in this case from an Fe-hot to an Fe-cool stream, is shown as a charge-state distribution time series in Fig. 7. The Fe-hot part of this stream includes the beginning of the trailing edge of the high-speed stream as defined in Borovsky & Denton (2016). The transition from Fe-cool to Fe-hot wind, however, occurs 12 h earlier and is thus unlikely to be affected by the trailing edge. It is interesting to note that the Fe-hot part of the stream of interest includes faster solar wind than the Fe-cool part of the stream. However, the change in solar wind speed occurs >5 h earlier than the transition from Fe-hot to Fe-cool wind. Since the transition boundary is defined on four-hour averages, shifting the temporal bins cannot make the two changes coincide exactly but they might be closer, as it appears here. As shown in Fig. 8, which provides a part of the photospheric map for the relevant Carrington rotation 2046, the transition between the Fe-hot and Fe-cool coronal-hole-wind streams is situated within a larger region (compared to the case in Fig. 6) of open field lines. Inspection of the heliographic map for the complete Carrington rotation (not shown here) indicates that this region was not connected to a polar coronal hole. In the following, we refer to such a region of open field lines which is not connected to a polar coronal hole as isolated. Within the accuracy of the back-mapping approach, the transition lies within a region of open field lines. However, within this region, the field line density is not uniform; for example west of the transition (to the right of the star in Fig. 8) the field line density is decreasing at

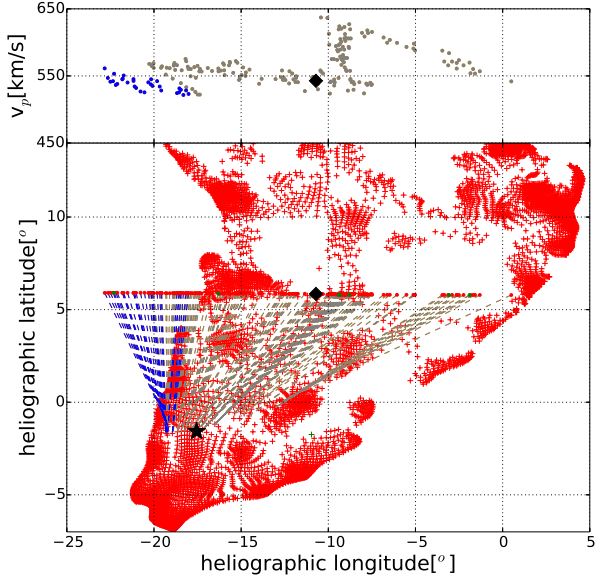


**Fig. 8.** A section of a heliographic map based on an MDI magnetogram for Carrington rotation 2046. The format is the same as in Fig. 6.

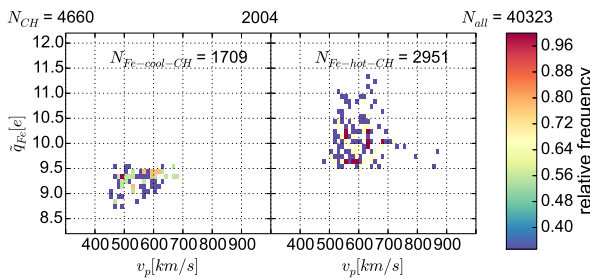
the photosphere. This fine-structure could be related to the transition. The in-situ magnetic polarity again matches the polarity predicted by the PFSS model with a few exceptions that can be explained as kinks in the magnetic field as well. For both transition examples in Figs. 6 and 8, both streams, in particular also the Fe-hot stream, originate in the equatorial region.

Table 1 summarizes the properties of eight transitions in 2006. The first column gives the start and end times of the part of the coronal-hole-wind stream containing the transition in DoY and the corresponding Carrington rotation is noted in the second column. An \* in the first column indicates the transitions shown in Figs. 5–8. The transition time is listed in the third column. To indicate the latitudinal and longitudinal position of the back-mapped foot points of each coronal-hole-wind stream, the highest and lowest back-mapped foot point is given in heliographic latitude in the fourth column, and the respective heliographic longitude in the fifth column. The last column indicates whether the stream is mapped to an isolated open field line region or whether the corresponding open field line region is connected to the northern polar coronal hole (NPCH). All these coronal-hole-wind streams have inwardly pointing magnetic polarity as indicated by the symbol  $\otimes$  in the last column. All eight transitions are mapped back to low latitudes and the longitudinal spread is at most  $18^\circ$ . As listed in Table 1, four out of eight transitions between Fe-cool and Fe-hot coronal-hole wind in 2006 were mapped back to isolated coronal holes in the equatorial region. The remaining three transitions were observed in the equatorial region as well, but the respective coronal holes were connected to the northern polar coronal hole. With respect to the long-term behavior, Zhao & Landi (2014) observed that wind from polar coronal holes is predominantly Fe-hot, while equatorial coronal-hole wind is predominantly Fe-cool. The case study shown here illustrates that, independently of their connection to a polar coronal hole, Fe-hot coronal-hole-wind streams are hidden within the mainly Fe-cool equatorial coronal-hole wind.

A possible explanation for the change in the Fe charge states at transitions between Fe-cool and Fe-hot coronal-hole wind is

**Table 1.** Eight transitions between Fe-cool and Fe-hot coronal-hole-wind streams in 2006.

Stream of interest [DoY in 2006]	CR	Transition time [DoY in 2006]	Latitude [°]	Longitude [°]	Isolated or connected
51.6–53.2	2040	51.4	-10.8	to -5.7	320.2 to 331.6 ⊗ isolated
104.9–107.0	2042	105.7	-5.0	to -4.0	317.5 to 320.9 ⊗ connected to NPCH
131.5–134.4	2043	133.4	-7.7	to -2.9	326.7 to 343.9 ⊗ connected to NPCH
* 158.1 – 161.6	2044	160.4	-5.4	to -2.4	329.8 to 348.5 ⊗ connected to NPCH
186.2–188.1	2045	187.4	-4.9	to -1.4	331.1 to 343.5 ⊗ connected to NPCH
* 213.1–214.5	2046	214.1	-1.7	to -2.9	341.0 to 351.7 ⊗ isolated
240.1–241.7	2047	241.0	-0.1	to 3.6	354.4 to 3.3 ⊗ isolated
294.0–296.0	2049	295.0	5.2	to 5.7	4.9 to 5.7 ⊗ isolated



**Fig. 9.** Average charge-state ( $\bar{q}_{\text{Fe}}$ ) versus solar wind proton speed for Fe-cool and Fe-hot coronal-hole type wind for 2004. The color gradient indicates the frequency of observing each charge-state-solar wind speed pair in 2004 and is normalized to the maximum in each panel. Each data point represents a four-hour average. The inset in each panel gives the number of data points in 12-min resolution that contributed to the averages in this figure. The number ( $N_{\text{all}}$ ) of all 12-min resolution data points in 2004 is given on the top right and the number ( $N_{\text{CH}}$ ) of all data points categorized as pure coronal-hole wind, in the top left.

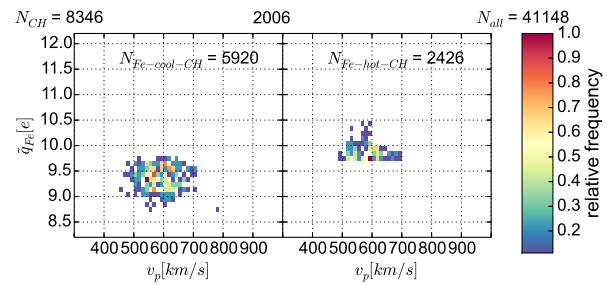


**Fig. 10.** Average charge-state ( $\bar{q}_{\text{Fe}}$ ) versus solar wind proton speed for Fe-cool and Fe-hot coronal-hole wind for 2006 in the same format as in Fig. 9.

that they coincide with stream interfaces between two distinct coronal-hole-wind streams. This is supported by the coinciding increase in solar wind speed and the decrease in proton density  $n_p$  in the 2004 example in Fig. 4. However, in Figs. 5 and 7, no clear change in the proton density  $n_p$  is visible at the transition. Furthermore, although the average solar wind speeds in the DoY 213–215 example in 2006 differ before and after the transition, the change in the solar wind speed does not coincide with the transition but occurs more than five hours earlier. Within the accuracy of the back-mapping approach, the back-mapped positions of the transitions in Figs. 6 and 8 might be consistent with stream interfaces at the transition times but this is not conclusive. Therefore, this explanation can neither be proved nor ruled out by the observations here.

To put the case studies presented above into some perspective, Figs. 9 and 10 illustrate how frequently Fe-cool and Fe-hot coronal-hole-wind streams were observed in 2004 and 2006, respectively. Figure 9 shows the frequency of the average charge-state versus the solar wind proton speed for all Fe-cool coronal-hole wind in 2004 (left panel) and all Fe-hot coronal-hole wind in 2004 (right panel). The inset in each panel indicates the number of data points in 12-min resolution of Fe-cool ( $N_{\text{Fe-cool-CH}}$ ) and Fe-hot coronal-hole wind ( $N_{\text{Fe-hot-CH}}$ ) included in each panel. For reference, the number  $N_{\text{all}}$  of all 12-min resolution data points in 2004 is given on the top right and the number  $N_{\text{CH}}$  of all data points categorized as pure coronal-hole wind in the top left. In the same way, Fig. 10 shows Fe-cool and

Fe-hot coronal-hole wind for the year 2006. With respect to the solar wind speed, the distributions of both the Fe-cool and Fe-hot components of the coronal-hole wind overlap to a large extent in both years. In particular in 2004, the Fe-cool component contains slower solar wind than the Fe-hot component and the overlap is smaller than in 2006. The question under which conditions each type of coronal-hole wind is prevalent in other years is left for a later study. However, comparing the years 2004 (Fig. 9) and 2006 (Fig. 10) allows some observations. Firstly, while in 2004, 1709 individual observations can be identified as Fe-cool coronal-hole wind and 2951 as Fe-hot coronal-hole wind, the 2006 data contains 5920 Fe-cool coronal-hole wind observations and 2426 Fe-hot coronal-hole wind observations. This illustrates that in 2004 the Fe-hot wind is more frequent than the Fe-cool coronal-hole wind. In 2006, however, the opposite is the case: Fe-cool coronal-hole wind is more frequent than Fe-hot coronal-hole wind. Secondly, not only does the frequency of each wind type change but the Fe-hot coronal-hole wind is less variable in its average Fe charge state and the overall average Fe charge states are lower in 2006 than in 2004. (Although not shown here, this effect is not only visible for Fe but also for O.) Both observations hint at a solar-cycle dependence as observed for O and C in Kasper et al. (2012), Schwadron et al. (2011). Additionally, an overall drop of O and C charge states as observed in 2006, at the transition to the long solar minimum at the end of solar cycle 23 (e.g. Lepri et al. 2013; Richardson 2014), is probably superimposed on the Fe charge-state distribution as well. This aspect requires further investigation.

The 2004 data in Fig. 9 exhibits an interesting feature with respect to a possible solar-wind proton speed dependence of the average Fe charge state. The average Fe charge state of the Fe-cool component (left panel) of the coronal-hole wind shows a possible dependence on the solar-wind speed. However, this is

not visible in the Fe-hot component in the right panel which instead manifests a larger variability in the average Fe charge state for each solar-wind speed. For the 2006 example, this feature is not visible.

#### 4. Conclusions

Complementing the observations of the long-term behavior of the Fe charge states in von Steiger et al. (2000), Galvin et al. (2009), Richardson (2014), Lepri et al. (2013), Kasper et al. (2012), Schwadron et al. (2011), Zhao & Landi (2014), we present a case-study of individual solar-wind streams that can be clearly identified as coronal-hole wind, with either high or low Fe charge states compared to the charge states in slow solar wind. Streams with either property occur in the same year and we also observe direct transitions between them. This indicates that the steady coronal-hole wind is less uniform in terms of Fe charge states than with respect to O and C charge states. In particular, solar-wind streams with high Fe charge states are Fe-hot and C/O-cool at the same time. Under the assumption that the charge-state distribution is frozen-in in the corona, a higher Fe charge state implies a higher freeze-in temperature for the same cool O freeze-in temperature and thus, a qualitatively different temperature profile in the corona.

The back-mapping of transitions between Fe-cool and Fe-hot coronal-hole-wind streams finds the origin of both streams in equatorial regions and close to each other. Thus, streams with consistently high or low Fe charge states can originate in the same region. A more systematic investigation of the origin of all individual Fe-hot and Fe-cool coronal-hole-wind streams is beyond the scope of this case-study. In addition, we have seen that in 2004 Fe-hot coronal-hole wind is more frequent, while in 2006 Fe-cool coronal-hole wind is predominantly observed. A possible solar-cycle dependence of the frequency of Fe-hot and Fe-cool coronal-hole wind – as it has been observed for O and C in Schwadron et al. (2011) and for Fe as well over solar cycle 23 in Lepri et al. (2013) – is one possibility to explain the changes in the frequency of Fe-hot and Fe-cool coronal-hole wind between 2004 and 2006. The details of a solar-cycle dependence, the evolution of the respective coronal structures over consecutive Carrington rotations, and the implications of these observations for the temperature profile in coronal holes require further investigation.

*Acknowledgements.* Part of this work was supported by the Deutsche Forschungsgemeinschaft (DFG) project number Wi-2139/10-1. We very gratefully acknowledge the diligent work of the anonymous referee who provided very detailed and helpful suggestions and comments.

#### References

- Altschuler, M. D., & Newkirk, G. 1969, *Sol. Phys.*, **9**, 131
- Berger, L. 2008, Ph.D. Thesis, Kiel, Christian-Albrechts-Universität
- Berger, L., Wimmer-Schweingruber, R., & Gloeckler, G. 2011, *Phys. Rev. Lett.*, **106**, 151103
- Borovsky, J. E., & Denton, M. H. 2016, *J. Geophys. Res.: Space Phys.*, **121**, 5055
- Dere, K., Landi, E., Mason, H., Fossi, B. M., & Young, P. 1997, *A&AS*, **125**, 149
- Galvin, A., Popecki, M., Simunac, K., et al. 2009, *Ann. Geophys.*, **27**, 3909
- Gloeckler, G., Cain, J., Ipavich, F., et al. 1998, in The Advanced Composition Explorer Mission (Springer), 497
- Gopalswamy, N., Yashiro, S., Michalek, G., et al. 2009, *Earth, Moon, and Planets*, **104**, 295
- Jian, L., Russell, C., Luhmann, J., & Skoug, R. 2006, *Sol. Phys.*, **239**, 393
- Jian, L., Russell, C., & Luhmann, J. 2011, *Sol. Phys.*, **274**, 321
- Kasper, J., Lazarus, A., & Gary, S. 2008, *Phys. Rev. Lett.*, **101**, 261103
- Kasper, J., Stevens, M., Korreck, K., et al. 2012, *ApJ*, **745**, 162
- Ko, Y.-K., Fisk, L. A., Geiss, J., Gloeckler, G., & Guhathakurta, M. 1997, *Sol. Phys.*, **171**, 345
- Landi, E., Young, P., Dere, K., Del Zanna, G., & Mason, H. 2013, *ApJ*, **763**, 86
- Lepri, S., Landi, E., & Zurbuchen, T. 2013, *ApJ*, **768**, 94
- Marsch, E. 2006, *Liv. Rev. Sol. Phys.*, **3**, 1
- McComas, D., Bame, S., Barker, P., et al. 1998, in The Advanced Composition Explorer Mission (Springer), 563
- Peleikis, T., Kruse, M., Berger, L., Drews, C., & Wimmer-Schweingruber, R. F. 2015, in Solar Wind 14: Proc. of the fourteenth international Solar wind Conf., AIP Conf. Proc., 1720, 020003
- Richardson, I. 2014, *Sol. Phys.*, **289**, 3843
- Richardson, I., & Cane, H. 2010, *Sol. Phys.*, **264**, 189
- Schatten, K., Wilcox, J., & Ness, N. 1969, *Sol. Phys.*, **6**, 442
- Scherrer, P., Hoeksema, J., & Bush, R. 1991, *Adv. Space Res.*, **11**, 113
- Schwadron, N., Smith, C., Spence, H. E., et al. 2011, *ApJ*, **739**, 9
- Smith, C. W., L'Heureux, J., Ness, N. F., et al. 1998, in The Advanced Composition Explorer Mission (Springer), 86, 613
- Tu, C., Zhou, C., Marsch, E., et al. 2005, *Science*, **308**, 519
- von Steiger, R. V., Schwadron, N., Fisk, L., et al. 2000, *J. Geophys. Res.: Space Phys.*, **105**, 27217
- Wilhelm, K. 2012, *Space Sci. Rev.*, **172**, 57
- Yashiro, S., Gopalswamy, N., Michalek, G., et al. 2004, *J. Geophys. Res.: Space Phys.*, **109**
- Zhao, L., & Fisk, L. 2010, in SOHO-23: Understanding a Peculiar Solar Minimum, ASP Conf. Ser., 428, 229
- Zhao, L., & Landi, E. 2014, *ApJ*, **781**, 110
- Zhao, L., Zurbuchen, T. H., & Fisk, L. A. 2009, *Geophys. Res. Lett.*, **36**, L14104
- Zurbuchen, T., Fisk, L., Gloeckler, G., & von Steiger, R. 2002, *Geophys. Res. Lett.*, **29**, 66

## 7.5 PUBLICATION 5

During the minimum phases of the solar activity cycle, surface features like coronal holes can remain stable for several Carrington rotations. This allows for an analysis of the structure's slow evolution and the accompanying solar wind which emerges from them. Because of the solar rotation, the solar wind sector structure sweeps over instruments mounted on the spacecraft ACE positioned at L1, which scans the emitted plasma horizontally from one border of the sector to the next. A radial probe of the sector can be accomplished by utilization of the freeze-in paradigm described in Sect. 7.2. By measuring particle density ratios of neighboring charge states of heavy elements, the corresponding freeze-in temperature can be determined, and an approximate radial temperature profile of the sector can be obtained. Mapping the in-situ data samples to the photosphere is performed by utilizing a PFSS model and connects the in-situ measurements to the photospheric source structures from which they most likely originated. This analysis was published in:

**EVOLUTION OF AN EQUATORIAL CORONAL HOLE STRUCTURE AND THE RELEASED CORONAL HOLE WIND STREAM: CARRINGTON ROTATIONS 2039 TO 2050**

V. Heidrich-Meisner, T. Peleikis, M. Kruse, L. Berger and R. F. Wimmer-Schweingruber, A&A, A84, 603, 2017, reproduced with permission © ESO.

DOI: 10.1051/0004-6361/201730574

Own contribution: 15%

### *Summary*

The introductory section briefly explains the photospheric phenomenon of coronal holes, their longevity during the minimum phase of the solar activity cycle, and their role as the origin of solar wind streams. The concept of a temperature-dependent freeze-in effect of the ratio of ions with neighboring charge states is described. Heavy-ion charge state ratios, freeze-in-conditions, and orders are discussed and presented as tracers of coronal temperature. Following the brief recapitulation of these basic phenomena, the instrument selection and data samples are presented that were utilized during the publication's studies. Following an in-depth explanation of the region of interest (i.e., the coronal hole and its surroundings), several characteristics of the solar wind plasma emanating from this region are presented. It is discussed how the in-situ measured ion charge state ratios of several elements combined with a modeled coronal temperature profile can be used to infer the heliocentric freeze-in points. Furthermore, a method is developed to probe the heliocentric temperature profile of the respective stream qualitatively without the need for additional models by just examining the charge-state ratios measured in-situ at [ACE](#). In this study, the [PFSS](#) model is used to link in-situ measurements to their probable source regions on the photosphere. It also shows magnetic fine-structures near the photospheric region of interest and gives insight into phenomena that might impact the analysis presented in this publication.

The key results are:

- During the solar activity minimum, the [PFSS](#) model gives a reasonable means to link in-situ spacecraft measurements to their photospheric source regions.
- Coronal sub-streams can be classified according to their average charge-state ratios of several elements.
- A qualitative temperature profile of a solar wind stream can be extracted from in-situ measurements of ion densities and their ratios to each other.

## Evolution of an equatorial coronal hole structure and the released coronal hole wind stream: Carrington rotations 2039 to 2050

Verena Heidrich-Meisner, Thies Peleikis, Martin Kruse, Lars Berger, and Robert F. Wimmer-Schweingruber

Christian Albrechts University at Kiel, 24118 Kiel, Germany  
 e-mail: [heidrich@physik.uni-kiel.de](mailto:heidrich@physik.uni-kiel.de)

Received 7 February 2017 / Accepted 24 March 2017

### ABSTRACT

**Context.** The Sun is a highly dynamic environment that exhibits dynamic behavior on many different timescales. Variability is observed both in closed and in open field line regions in the solar corona. In particular, coronal holes exhibit temporal and spatial variability. Signatures of these coronal dynamics are inherited by the coronal hole wind streams that originate in these regions and can effect the Earth's magnetosphere. Both the cause of the observed variabilities and how these translate to fluctuations in the in situ observed solar wind is not yet fully understood.

**Aims.** During solar activity minimum the structure of the magnetic field typically remains stable over several Carrington rotations (CRs). But how stable is the solar magnetic field? Here, we address this question by analyzing the evolution of a coronal hole structure and the corresponding coronal hole wind stream emitted from this source region over 12 consecutive CRs in 2006.

**Methods.** To this end, we link in situ observations of Solar Wind Ion Composition Spectrometer (SWICS) onboard the Advanced Composition Explorer (ACE) with synoptic maps of Michelson Doppler imager (MDI) on the Solar and Heliospheric Observatory (SOHO) at the photospheric level through a combination of ballistic back-mapping and a potential field source surface (PFSS) approach. Together, these track the evolution of the open field line region that is identified as the source region of a recurring coronal hole wind stream. Under the assumptions of the freeze-in scenario for charge states in the solar wind, we derive freeze-in temperatures and determine the order in which the different charge state ratios of ion pairs appear to freeze-in. We call the combination of freeze-in temperatures derived from in situ observed ion density ratios and freeze-in order a minimal electron temperature profile and investigate its variability.

**Results.** The in situ properties and the PFSS model together probe the lateral magnetic field configuration, the minimal temperature profiles allow to constrain the radial structure. We find that the shape of the open field line region and to some extent also the solar wind properties are influenced by surrounding more dynamic closed loop regions. We show that the freeze-in order can change within a coronal hole wind stream on small timescales and illustrate a mechanism that can cause changes in the freeze-in order. The inferred minimal temperature profile is variable even within coronal hole wind and is in particular most variable in the outer corona.

**Key words.** solar wind – Sun: corona – Sun: magnetic fields

### 1. Introduction

In situ observations of the solar wind often show recurring structures that are interpreted as the footprint of stable coronal structures at the Sun. This is supported by remote sensing observations that show coronal structures that remain stable over several Carrington rotations (CRs; [Benevolenskaya et al. 2001](#); [Russell et al. 2010](#)). These stable structures are typically observed during solar minimum conditions. Under these conditions, when the Sun is less active, the solar magnetic field changes less rapidly than during the solar activity maximum; fewer active regions, fewer sunspots, and from a heliospheric point of view most importantly fewer coronal mass ejections (CMEs) occur during solar minimum than during solar maximum ([Gopalswamy 2006](#); [Robbrecht et al. 2009](#)). The quiet Sun leads to a less variable heliospheric structure as well. But the Sun is never completely quiet even during deep solar minimum. Although the large scale changes occur more slowly, the Sun is nevertheless still a highly dynamic environment and the magnetic configuration continues to evolve during solar minimum. A recurring stable structure on the Sun can be considered as a test bed to investigate the comparatively slow evolution of this region and the solar wind streaming into the heliosphere from

this source region. Except for the influence of wave activity and stream interaction regions, the fine structure of in situ observed solar wind properties can be linked back to the evolving conditions at the solar source regions. The solar wind speed, temperature, ion, and charge state composition, as well as the magnetic field are all influenced by the conditions in the respective source region of a solar wind stream.

The average magnetic field configuration at the photospheric level is captured by synoptic maps based on magnetograms from, for example, the Michelson Doppler imager (MDI, [Scherrer et al. 1991](#)) on the Solar and Heliospheric Observatory (SOHO). The corresponding coronal structure of the magnetic field can be derived with a potential field source surface approach (PFSS, [Schatten et al. 1969](#); [Altschuler & Newkirk 1969](#)). This procedure requires the magnetic configuration on the complete solar surface as an input, such as MDI synoptic maps. These combine observations from a complete CR into an average map. As a result the derived magnetic field configuration cannot reflect dynamic changes on timescales faster than a CR and is best applied during solar minimum conditions. This limits the eligibility of PFSS models. However, in this case study, we are especially interested in the scenario PFSS models are best suited for: we are looking for changing fine structure features in

the photosphere, solar corona, and in situ observations that vary on the timescale of CRs.

The PFSS model enables us to track magnetic field lines from the photosphere to the source surface which is conventionally but arbitrarily assumed to be at 2.5 solar radii ( $R_\odot$ ). Under the assumption that the solar wind speed is constant from the source surface to the location of the spacecraft, in our case the Advanced Composition Explorer (ACE) at L1, a solar wind package can be tracked ballistically from the spacecraft to the source surface. However, stream interaction regions obviously violate the assumption of constant solar wind speed. Moreover, especially the fast solar wind is likely to experience ongoing acceleration much further out in the corona (Cranmer 2009; Fisk et al. 1999). This type of combination of ballistic back-mapping and the PFSS model has frequently been used to investigate the source regions of solar wind (Fazakerley et al. 2016; Gómez-Herrero et al. 2011; Thompson et al. 2011).

The combination of in situ observations and the back-mapping method enables us to trace the fine structure at the photospheric level for each CR. The comparison between CRs enables us to track the temporal evolution of these structures. This can be considered as a lateral (or horizontal) probing of the evolution of magnetic structures in the photosphere. The aim of this study is to investigate variability inside coronal hole wind flows. Thus, we focus mainly on one recurring coronal hole wind stream per CR. This stream has another interesting property with respect to its Fe charge state composition. Heidrich-Meisner et al. (2016) has shown that coronal hole wind streams with either low Fe charge states (Fe-cool) or Fe charge states comparable to those observed in slow solar wind (Fe-hot) are observed in equatorial coronal hole wind. In particular, transitions from Fe-cool to Fe-hot coronal hole wind or vice versa were observed. Our coronal hole wind stream of interest shows transitions between Fe-hot and Fe-cool coronal hole wind. In the context of this investigation, the average Fe charge state thus provides an additional tool to investigate the fine structure of a coronal hole wind stream.

Tracking the radial evolution of the magnetic field line configuration in the solar atmosphere is more difficult. Without invoking a more or less complete model of the solar atmosphere it is, for example, not possible to derive a radial temperature profile of the solar atmosphere solely from in situ observations. However, we argue that even without an additional model, in situ derived freeze-in temperatures (Hundhausen et al. 1968; Ogilvie & Vogt 1980; Owocki et al. 1983; Geiss et al. 1995) can give some insights on radial structures and their variability. In the freeze-in image, charge states can change freely as long as the charge modification timescale is smaller than the expansion timescale. For different ion species this condition is met at different heights in the solar atmosphere. In particular, the order in which the charge states of each ion pair freezes is constrained by the local electron density and – through the recombination and ionization rates – by the electron temperature. The charge modification timescale is sensitive to the relative influence of ionization compared to recombination. This can also change the order in which ion pairs freeze-in, as illustrated in Sect. 4. We combine the information on the order in which the charge states freeze in with the freeze-in temperatures into what we call a minimal temperature profile. These minimal temperature profiles can be considered as a tracer of radial (or vertical) structures in the solar atmosphere. Their temporal evolution can provide insights on the variability and radial evolution of coronal structures without requiring a complete model of the solar atmosphere.

This article is structured as follows: Sect. 2 describes our data selection and the back-mapping procedure. In Sect. 3, we investigate the variability of our coronal structure of interest from a photospheric and in situ perspective. We then discuss minimal temperature profiles and their variability in Sect. 4. In Sect. 5, we present our conclusions.

## 2. Data selection, solar wind characterisation, and methods

We combine in situ observations from ACE/SWICS (Gloeckler et al. 1998), ACE/MAG (Smith et al. 1998) and the Solar Wind Electron, Proton and Alpha Monitor (ACE/SWEPAM; McComas et al. 1998) with synoptic maps based on magnetograms from SOHO/MDI (Scherrer et al. 1991). The analysis procedure applied to the raw ACE/SWICS data is described in detail in Berger (2008) and has been applied in, for example, Berger et al. (2011) and Heidrich-Meisner et al. (2016).

To characterize observed solar-wind packages by type, we use the categorisation scheme from Xu & Borovsky (2015). This scheme defines four categories of solar wind: coronal hole wind plasma, ejecta plasma, and two slow solar wind categories, namely sector-reversal region plasma and streamer-belt plasma. Here, we combine the latter two into a single category for slow solar wind. The ejecta category is intended to cover plasma from interplanetary coronal mass ejections (ICMEs). However, this category can be problematic because it frequently and possibly incorrectly interprets parts of cool, very slow solar wind streams as ejecta plasma. Therefore, we instead rely on the Jian et al. (2006, 2011) ICME list for identifying ICMEs in the in situ observations. The Xu & Borovsky scheme is applied to data with the native 12-min resolution of ACE/SWICS.

We chose twelve consecutive CRs in 2006 as a case study to investigate the evolution of the source region of a recurring coronal hole wind stream. This stream and these CRs were selected not only because the coronal hole wind stream is observed repeatedly but also because it exhibits an interesting feature with respect to its average Fe charge state (Heidrich-Meisner et al. 2016). These streams show transition between coronal hole wind with low Fe charge states (called Fe-cool coronal hole wind) and coronal hole wind with high Fe charge states (Fe-hot coronal hole wind). The distinction between Fe-hot and Fe-cool coronal hole wind streams is based on a comparison of the average Fe-charge state  $\bar{q}_{\text{Fe}} = \sum_{c=7}^{13} c n_{\text{Fe}^c} / \sum_{c=7}^{13} n_{\text{Fe}^c}$  in coronal hole wind streams to the average Fe charge state of all (pure) slow solar wind in the same year. As in Heidrich-Meisner et al. (2016), to avoid both compression and rarefaction regions between slow and coronal wind streams the proton-proton collisional age  $a_c$  (Kasper et al. 2008; Heidrich-Meisner et al. 2016) is used as an additional criterion for solar wind classification. In particular, an upper bound  $a_c < 0.1$  is applied for choosing pure coronal hole wind for the coronal hole wind streams of interest and a lower bound  $a_c > 0.4$  for pure slow solar wind as reference for defining the notion of high (Fe-hot) and low (Fe-cool) Fe charge states. Thus, solar wind plasma that has been categorized as coronal hole wind by the Xu & Borovsky scheme is considered to be so-called pure coronal hole wind if, additionally, the collisional age is low,  $a_c < 0.1$ , and solar wind plasma that has been categorized as slow solar wind in the Xu & Borovsky scheme is considered to be pure slow solar wind if the collisional age is high,  $a_c > 0.4$ . These two categories (pure coronal hole wind and pure slow solar wind, respectively) are only used for the

V. Heidrich-Meisner et al.: Evolution of an equatorial coronal hole structure and wind

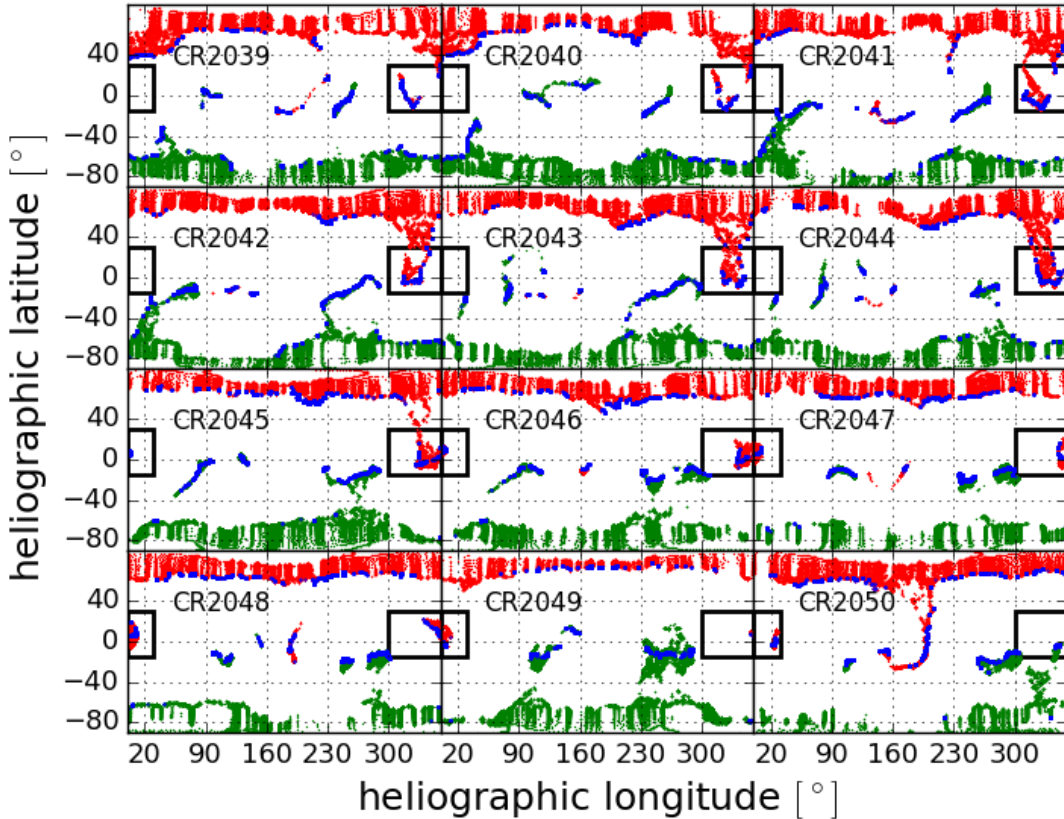


**Fig. 1.** Heliographic map at the photospheric level for CRs 2039–2050 derived from a numerical PFSS approach. The maps are sorted *row-wise* by CR with CR 2039 at the top left and CR 2050 at the bottom right. Only foot points of open field lines are shown. Inwards directed magnetic polarity is indicated with red dots and outwards directed polarity with green dots. The blue dots refer to the foot points of ACE mapped down to the photosphere. The black boxes indicate the region of interest for which a zoom-in is shown in the following Fig. 2.

definition of Fe-hot and Fe-cool coronal hole wind and are applied on observations with 4h time resolution. We use the modified Xu & Borovsky scheme here instead of the categorization of slow and fast solar wind used in Heidrich-Meisner et al. (2016) to test how sensitive the characterization of Fe-hot or Fe-cool coronal hole wind is to the particular solar wind categorization scheme. As a result of the different underlying solar wind categorization scheme, the threshold value for the average Fe charge state that differentiates between Fe-cool and Fe-hot coronal hole wind changes for the year 2006 from  $\bar{q}_{\text{Fe,slow},2006} = 9.71$  (which was used in Heidrich-Meisner et al. 2016) to  $\bar{q}_{\text{Fe,slow},2006} = 9.66$  (which is used here). Consequently, the start and end times of each stream change slightly and, in some cases, more transitions occur. Nevertheless, the presence of Fe-cool and Fe-hot coronal hole wind streams and the existence of transitions between them is unaffected by the particular solar wind categorization scheme. The mean of all average Fe charge states in Fe-hot coronal hole wind is during CR 2039–2050  $\bar{q}_{\text{Fe-hot}} = 9.75$  and for the same CRs in Fe-cool coronal hole wind the respective mean value is  $\bar{q}_{\text{Fe-cool}} = 9.65$ .

To link the in situ observations with the photosphere, we apply a combination of ballistic back-mapping and the PFSS model (Schatten et al. 1969; Altschuler & Newkirk 1969). The same approach has been applied in Heidrich-Meisner et al. (2016) and Peleikis et al. (2016), Peleikis et al. (2017). Firstly, a solar wind

package is mapped back ballistically to the source surface at  $2.5 R_{\odot}$  under the assumption that the solar wind speed is constant between the source surface and the observer. Secondly, a grid of open field lines is distributed over the source surface. The resolution in heliographic latitude is latitude-dependent with a finer grid at the equator ( $0.63^{\circ}$ ) than in polar regions ( $2.2^{\circ}$ ). The longitudinal grid is uniform with  $1^{\circ}$  resolution. Thirdly, based on a numerical PFSS approach on this grid with 50 radial grid points, each open field line is traced down to the photosphere. The PFSS model requires a synoptic map of the complete photospheric surface as a boundary condition. This limits the applicability of this approach. The PFSS model is most reliable during solar minimum when the magnetic field configuration changes only slowly and few or no ICMEs are observed. However, this is exactly the situation we are interested in in this case. Thus, the influence of averaging the solar magnetic field over a complete CR still limits the accuracy of the back-mapping but less so than under different conditions. The assumption of a constant solar wind speed that is required by the ballistic back-mapping is invalid for stream interaction regions. As a result, the back-mapping is distorted for stream-interaction regions. This effect can be reduced by the upwind back-mapping algorithm in Riley & Lionello (2011). However, since we are mainly interested in coronal hole wind streams, the upwind back-mapping algorithm was not applied here.

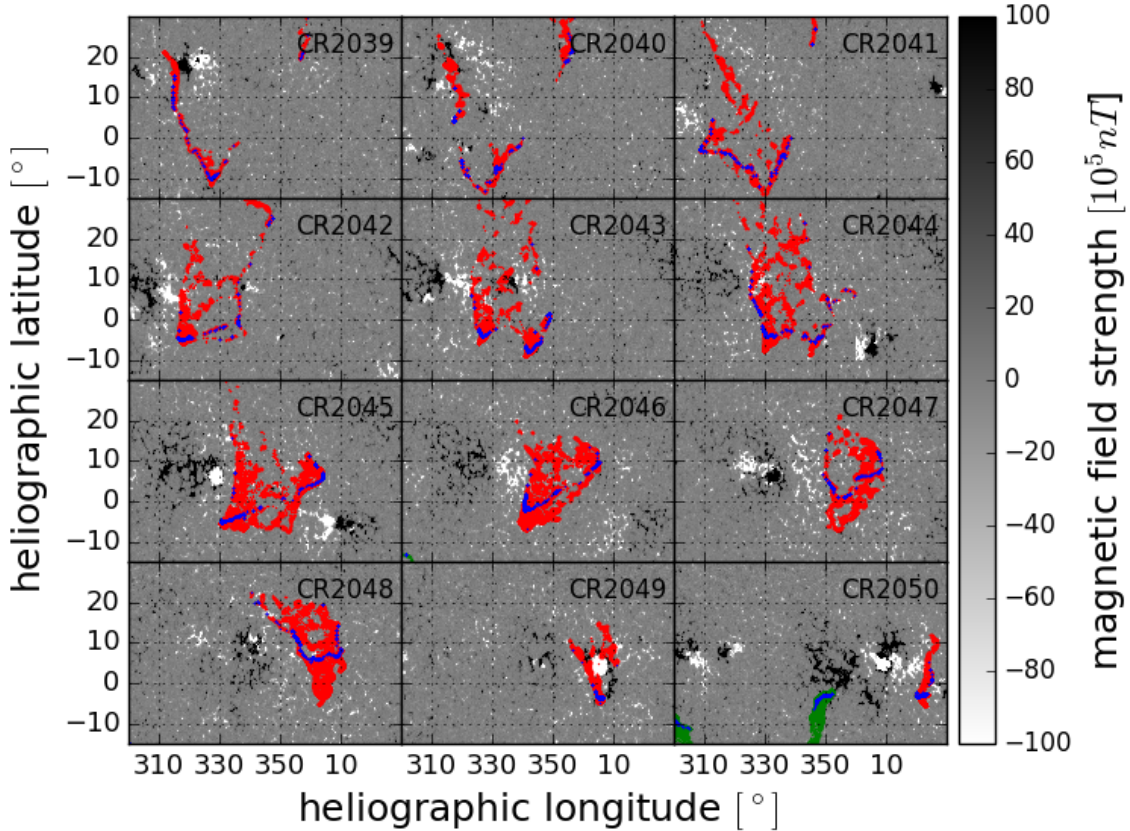


**Fig. 2.** Zoom of the heliographic map at the photospheric level for CRs 2039–2050. In addition to the foot points of open field lines as in Fig. 1, the respective MDI synoptic maps that were used as input to the PFSS model are shown in the background.

### 3. A recurring coronal structure

We look at our structure of interest, which is mainly the first coronal hole wind stream in each CR, from two perspectives: a photospheric perspective and an in situ perspective. The PFSS model directly provides an overview on the magnetic configuration at the photospheric level. With the help of backmapping the photospheric source regions of the in situ observed solar wind can be identified. Each solar wind package originates from a different position in the photosphere. Together, the source regions of consecutive observation trace a curve in the photosphere. Thus, temporal variations in the in situ data translate to lateral variations in the photospheric source region. Therefore, the photospheric perspective provided by the PFSS model and the in situ observed solar wind parameters both contribute to a picture of the lateral structure of the source region in the photosphere. Comparing the properties of our structure of interest between different CRs gives an indication of their evolution on the timescale of CRs.

#### 3.1. Properties of a recurring coronal hole wind stream: photospheric perspective

An overview over the complete heliographic maps derived with our back-mapping approach for CRs 2039–2050 is given in Fig. 1. Only the foot points of open field lines are shown in

the heliographic map as colored dots. The color depends on the magnetic polarity as derived by the PFSS model. Consecutive maps differ most obviously in equatorial regions. Although their shapes and sizes vary, several regions with open field lines appear in all considered CRs. In particular, two regions with outwards pointing magnetic polarity (green in Fig. 1) are persistent through all CRs at heliographic latitude  $-40^\circ < \theta < 40^\circ$  and heliographic longitudes,  $40^\circ < \phi < 120^\circ$  and  $230^\circ < \phi < 310^\circ$ . With inwards pointing polarity (red in Fig. 1) we find one recurring region of open field lines at heliographic latitude  $-15^\circ < \theta < 30^\circ$  and heliographic longitude  $300^\circ < \phi < 30^\circ$ . The shape of the border of open field line regions at the poles also changes slowly.

In the following, we focus on the source region of a recurring coronal hole wind stream. The respective region is already outlined with black boxes in Fig. 1. In Fig. 2, only this region is shown. The respective open field line region is located at the western edge in the first CRs, moves further to the west and south until the center of gravity of the open field line region has reached low longitudes. Although the open field line region is present in all considered CRs, its shape and structures evolves from thin elongated structures (CRs 2039–2041) to increasingly larger regions of open field lines (CRs 2042–2048) back to small but dense regions (CRs 2049–2050). Additionally to the foot points of open field lines (in red for inwards pointing and in green for outwards-pointing polarity) the field lines

V. Heidrich-Meisner et al.: Evolution of an equatorial coronal hole structure and wind

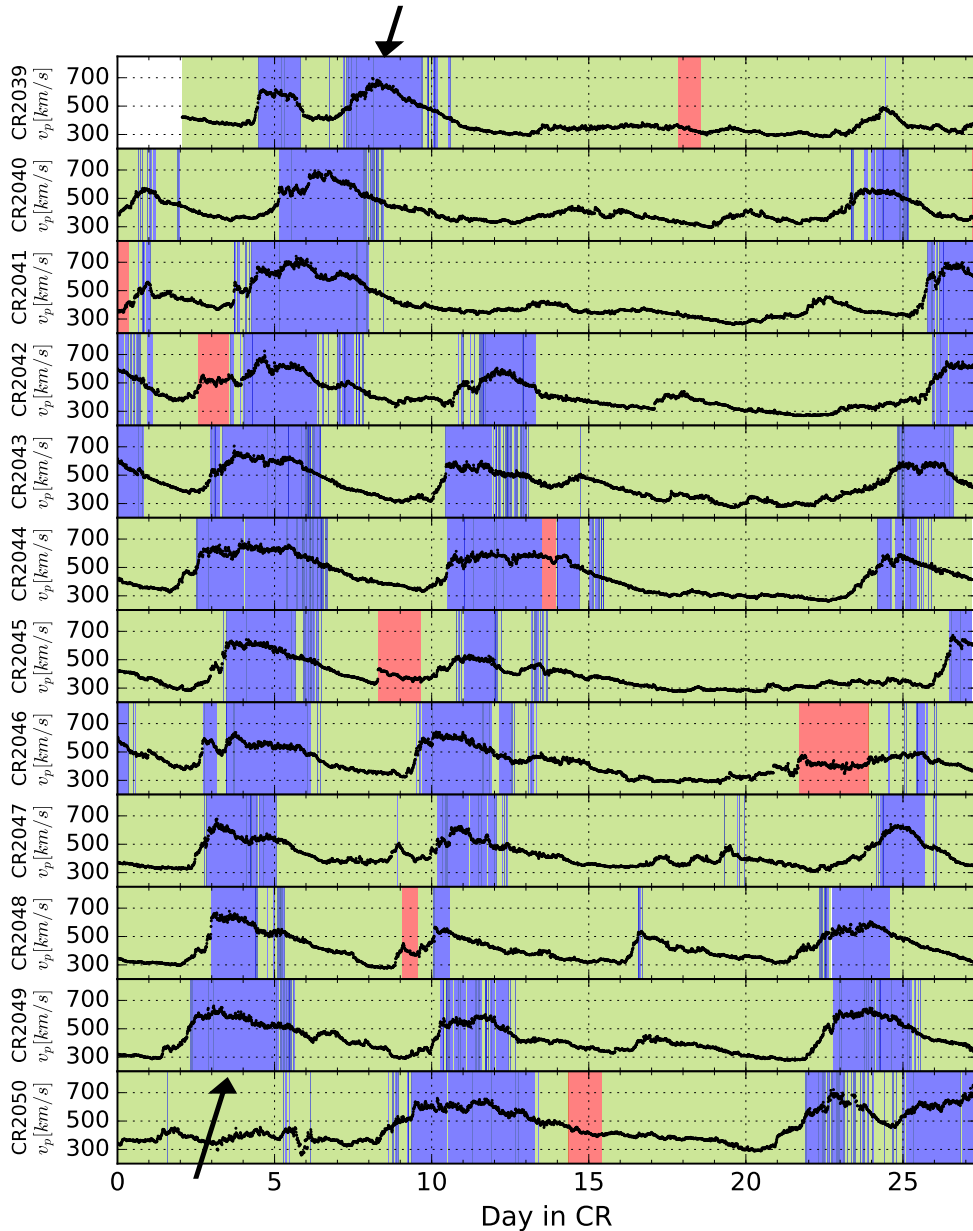


**Fig. 3.** Solar wind speed over time for CRs 2039–2050. Coronal hole wind is highlighted in blue and slow solar wind in green based on the Xu & Burovsky scheme. ICMEs from the Jian ICME catalog are indicated in red. The arrows indicate our coronal hole wind stream of interest.

that were identified as the foot points of ACE are shown in blue. The netlike, filigree structure of the open field line region in particular in CR 2041 resembles, albeit on a larger scale, the intricate connected coronal hole structures that make up the S-web. However, unlike the S-web, which is considered to be a potential source for slow solar wind (Antiochos et al. 2011), in this case, clearly solar wind with coronal hole wind properties is emitted by this sparse structure.

Figure 2 also shows the respective part of the corresponding MDI synoptic maps. In these synoptic maps, the magnetic field strength is coded in grayscale with negative values with high

absolute value in white (for inwards pointing polarity), high positive values in black (for outwards pointing polarity) and values close to zero in gray. In this representation, closed loops are visible as paired clusters of high magnetic field strength with opposite polarity. Since these indicate regions with closed magnetic field lines, a coronal hole as a region with open magnetic field lines naturally cannot be in the same place. As also discussed in Wang et al. (2010), Fig. 2 shows regions with probably closed magnetic field lines in close proximity to the predicted foot points of open magnetic field lines. In most cases (except for CR 2048) the open field line region is situated between at least

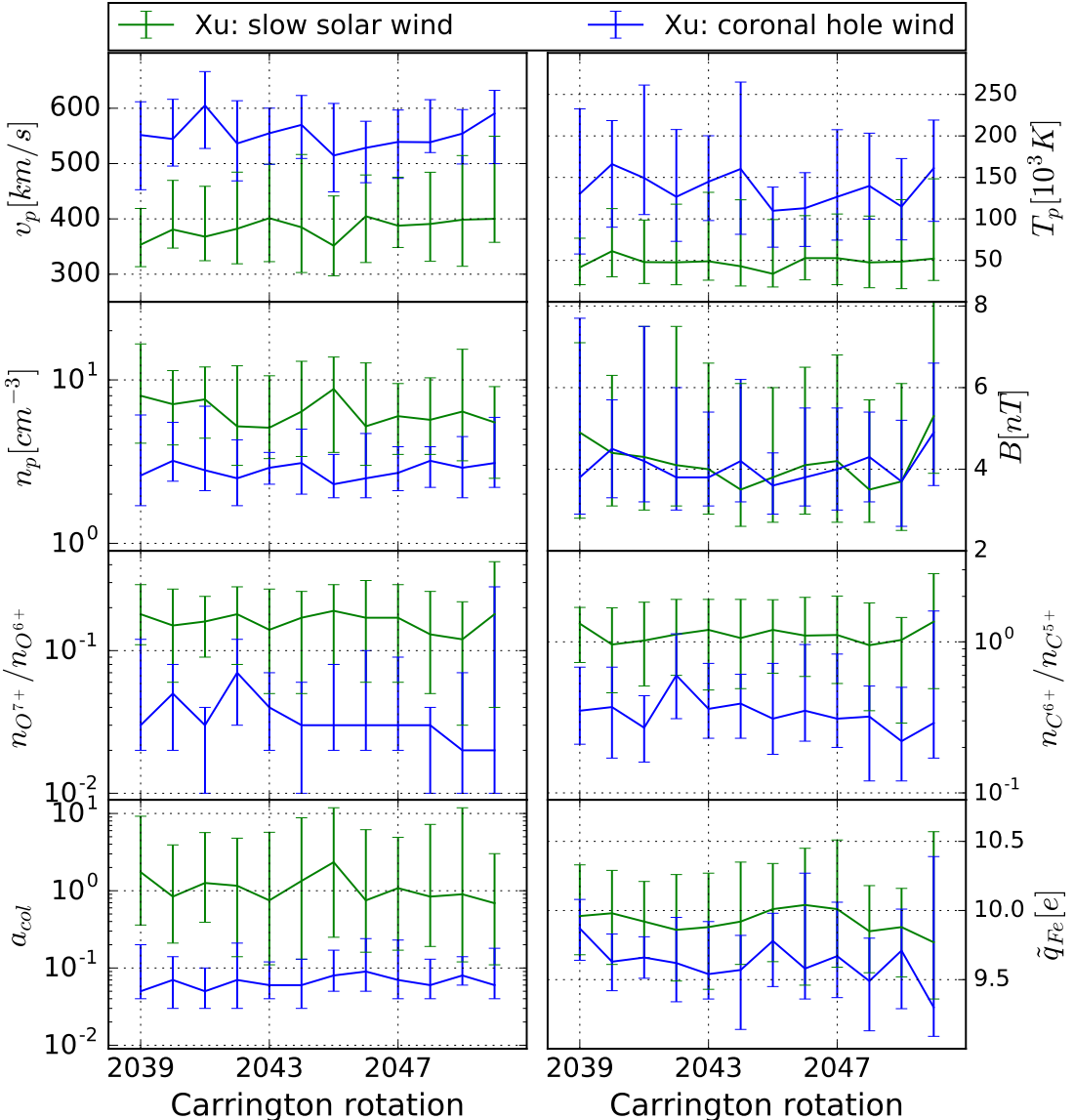


**Fig. 4.** Solar wind properties per solar wind type based on the Xu & Burovsky scheme (coronal hole wind (blue) and slow solar wind (green)), averaged over the respective CRs. In each panel, the median of all 4h bins of the respective solar wind type is shown, as well as the true variability of the 4h-resolution observations as indicated by the 15.9th and 84.1th percentiles. Row-wise from top left to bottom right: proton solar wind speed  $v_p$ , proton temperature  $T_p$ , proton density  $n_p$ , magnetic field strength  $B$ , O charge state ratio  $n_{O^{7+}}/n_{O^{6+}}$ , C charge state ratio  $n_{C^{6+}}/n_{C^{5+}}$ , collisional age  $a_{col}$ , and average Fe charge state  $\tilde{q}_{Fe}$ .

two such clusters of foot points of closed field lines. In particular, in CRs 2044–2048 more space is available between the active region candidates and, at the same time, the open field line region that is the source region of our coronal hole wind stream of interest is larger and the foot points are distributed more uniformly. In the other cases, the closed field line regions constrain the shape of the likely coronal hole more strongly. CR 2049 is an interesting special case. Compared to the previous CR, a new closed field line region has appeared within the previously open field line region. As a result, the open field lines in CR 2049 are very dense and are mapped very close to this active region. An additional complication is caused by the location of this region.

It is located around zero degrees longitude. Thus, it sits at the interface between the oldest and the newest observations that contributed to the underlying MDI synoptic map. Therefore, the PFSS model here is particularly vulnerable to the effect of dynamic changes. That open field lines apparently emerge very close or even from within a closed loop region is probably both a signature of the dynamic change that occurred here and the limitations of the PFSS model. The emergence of this active region which (if it is indeed the same one) is larger in CR 2050 is a possible reason for the disappearance of the coronal hole wind stream of interest in CR 2050. We have verified that (with the exception of CR 2049) the open field line regions predicted by

V. Heidrich-Meisner et al.: Evolution of an equatorial coronal hole structure and wind

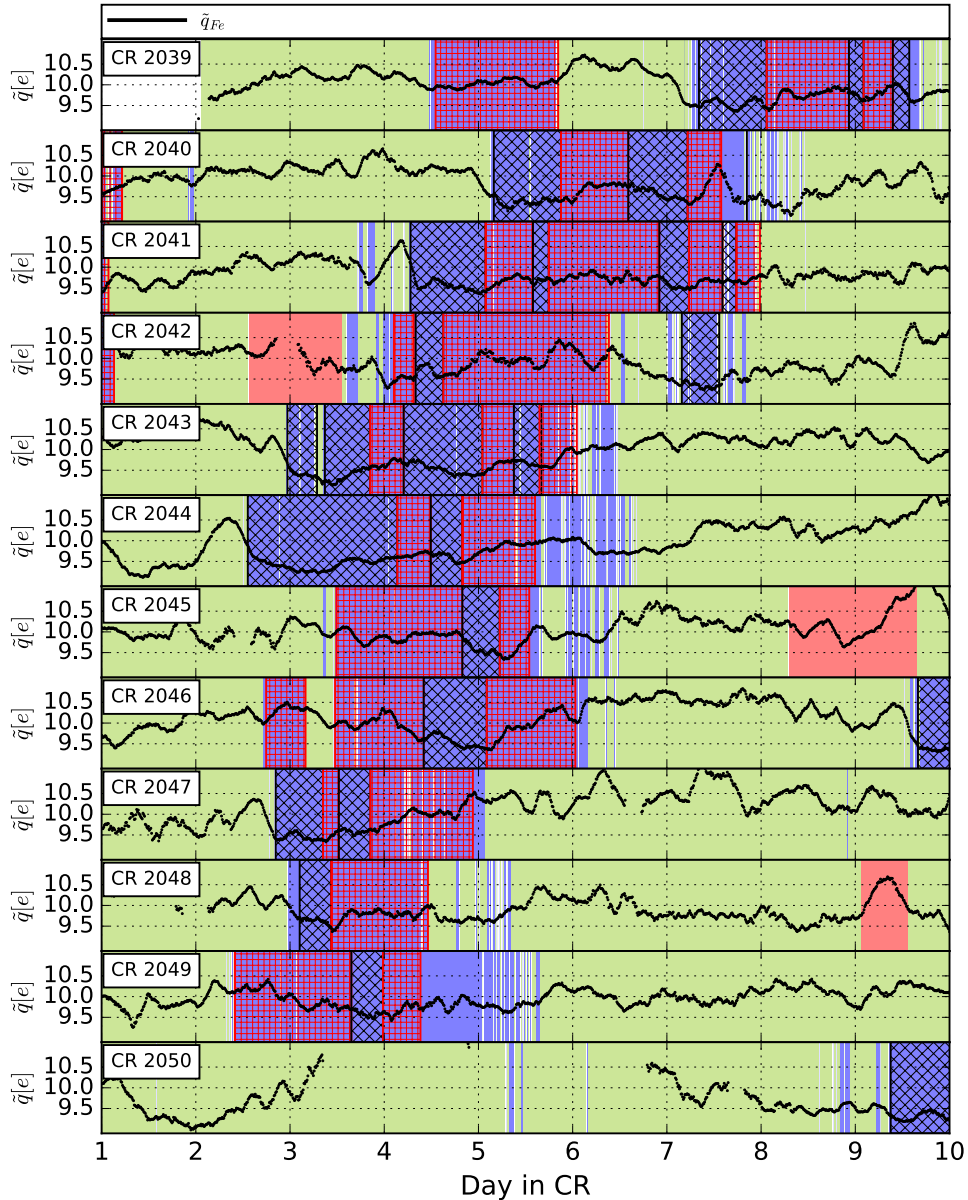


**Fig. 5.** Average Fe charge state over time for CRs 2039–2050. The solar wind type is indicated in the same way as in Fig. 3. Periods with high and low Fe charge states in coronal hole wind are highlighted: Fe-hot (red, +–hatched) and Fe-cool (black, ×–hatched).

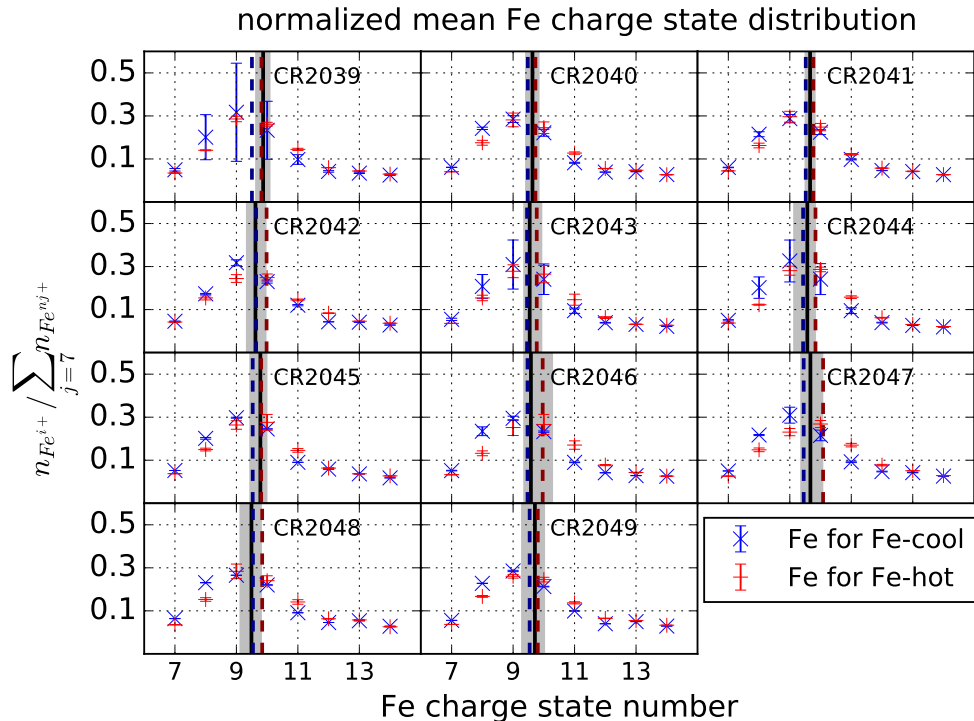
the PFSS model match reasonably well with dark regions visible in the synoptic maps from the Extreme ultraviolet Imaging Telescope (EIT, Delaboudiniere et al. 1995) on SOHO. In all cases, the shape of the open field line region is constrained by the proximity to closed magnetic field line loops and the evolution of the shape of the coronal hole can be considered a result of changes that are due to more dynamic phenomena such as active regions.

Figure 2 also shows that the open field line region associated with our coronal hole wind stream of interest is moving to the south-west. This is a result of the differential rotation of the Sun (Thompson et al. 1996). Since the region of interest lies at lower latitudes than the region used to determine the beginning and end

of each CR, this region rotates faster and thus moves to the west and south on the heliographic map.

### 3.2. Properties of a recurring coronal hole wind stream: *in situ* perspective

A time series of the solar wind proton speed is given in Fig. 3 for each CR. The highlighting indicates the solar wind type wherein green means slow solar wind, blue identifies coronal hole wind, and red shows ICMEs. There is a data gap at the beginning of CR 2039. Each CR contains two or three distinct coronal hole wind streams. One of these, indicated by the arrows above the



**Fig. 6.** Normalized mean charge distributions for Fe sorted by CR (in the same order as in Fig. 1) averaged separately over the Fe-hot and Fe-cool parts of the first recurring coronal hole stream during CR 2030–2049. CR 2050 is omitted because the coronal hole wind stream is not observed any more in that CR. The black vertical line marks the median of the average Fe charge state for each CR as given in Fig. 4 and the gray shaded areas indicate the corresponding  $1\sigma$  interval. The median of the average Fe charge state in Fe-hot is indicated by a red dashed vertical line and the median of the average Fe charge state in Fe-cool coronal hole wind is given in blue. The error bars indicate the error of the mean. In the cases where the error bars are not visible, they are hidden behind the respective symbol for the mean. Each distribution is normalized to its sum.

first and in the last panel reoccurs in all CRs except the last one. The coronal hole wind stream moves to the left, i.e. earlier in the CR. This again illustrates the differential rotation of the source region. A total of eight ICMEs is included in the Jian ICME list for this time period.

Figure 4 summarizes the average properties of slow solar wind and coronal hole wind for CRs 2039–2050. Each parameter is given as the median of all 4h time resolution data points of the corresponding wind type. In addition, the 15.9th and 84.1th percentile are provided as error bars to indicate the variability of each property. In the case of the Fe charge state, we first compute the average Fe charge state  $\bar{q}_{\text{Fe}} = \sum_{c=7}^{13} c n_{\text{Fe}^{c+}} / \sum_{c=7}^{13} n_{\text{Fe}^{c+}}$  and then use the median to obtain a temporal averaging. For all solar wind parameters the variability of the 4h observations is high. The variability of the proton temperature  $T_p$  is higher in coronal hole wind than in slow solar wind. For the proton density  $n_p$ ,  $n_{\text{O}^{7+}}/n_{\text{O}^{6+}}$ , and  $n_{\text{C}^{6+}}/n_{\text{C}^{5+}}$  the variability is larger in slow solar wind. This is not surprising and well known (Bame et al. 1977; McComas et al. 2000; Dasso et al. 2005). Although the temporal median of the average Fe charge state is lower in coronal hole wind than in slow solar wind, the temporal median of the average Fe charge state for coronal hole wind is within one standard deviation of that of slow solar wind. In coronal hole wind the average Fe charge state changes depending on whether Fe-hot or Fe-cool coronal hole wind is dominant. The median of the O charge state ratio remains remarkably constant during CRs 2044–2048. For CRs 2045–2048 the median of the C charge state ratio behaves similarly. This coincides with the CRs that are

least restrained in their shape by surrounding regions with closed magnetic field lines. For all other CRs the median of the O and C charge state ratios are more variable. However, the variability of the observations as indicated by the error bars is large for all CRs. Nevertheless, this could indicate that the coronal hole wind stream in CRs 2045–2048 represents undisturbed coronal hole wind whereas, in the other cases, not only the shape of the coronal hole is affected by the surrounding active regions, but also in the same way, the composition. This could be caused by reconnection that mixes small amounts of active region plasma into the coronal hole wind stream. Another possibility is that because of the constraints on the open field lines, individual fluxtubes interact more strongly, which could lead to a more variable solar wind plasma.

Figure 5 shows an overview on the average Fe charge state for each CR. The average Fe charge state is variable in all considered solar wind types. As described in Heidrich-Meisner et al. (2016), the Fe charge states in coronal hole wind can be as high as in slow solar wind. This motivated the distinction between Fe-cool coronal hole wind with average Fe charge states smaller than those in most slow solar wind observations and Fe-hot coronal hole wind with average Fe charge states comparable to those observed in slow solar wind. Periods with Fe-hot (red, +hatched) and Fe-cool (black, x-hatched) coronal hole wind are highlighted. Several of the coronal hole wind streams shown here exhibit at least one transition between Fe-hot and Fe-cool coronal hole wind. The first coronal hole wind stream in each CR persists from CR 2039–2049 but is not present anymore

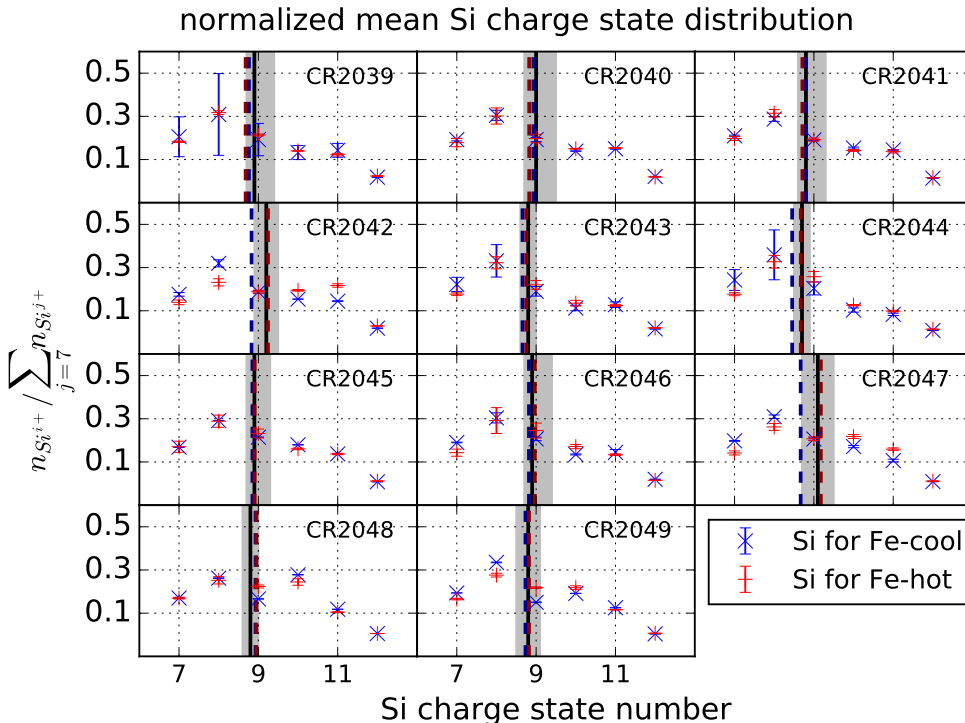


**Fig. 7.** Normalized mean charge distributions for Si sorted by CR (in the same order and format as in Fig. 1) for the Fe-hot and Fe-cool parts of the first recurring coronal hole stream during CR 2030–2049.

in CR 2050. Since this stream recurs most frequently and exhibits at least one transition from Fe-hot to Fe-cool coronal hole wind in CR 2040–2049, as is shown in Fig. 5, we focus on this recurring coronal hole wind stream in the following. While for CRs 2039–2041, 2043, 2044, 2047, and 2048 first a Fe-cool and then a Fe-hot coronal hole wind is observed, for CR 2042, 2045, 2046, and 2049 this is reversed. In some cases this switches back and forth. The end of the first coronal hole wind stream in CR 2040 shows a distinct peak in the average Fe charge state. This could be a signature of a hidden ICME that is not included in the Jian ICME list.

#### 4. Implications for temperature profiles

Figure 6 shows the average charge state distributions for the Fe-hot and Fe-cool parts of the recurring coronal hole wind stream for each CR for Fe. Figure 7 shows the same for Si. As reference the median of the average Fe charge state of all coronal hole wind is shown as a black vertical line, its variability is indicated with gray shading, the median of the average Fe charge state in Fe-hot coronal wind is shown with a red vertical line and for Fe-cool coronal hole wind with a blue vertical line. This illustrates that the Fe charge state distribution is consistently shifted to higher charge states in Fe-hot coronal hole wind compared to Fe-cool coronal hole wind. For Si this is not necessarily the case. For example for CRs 2042, 2043, 2047, and 2049 the complete Si charge state distribution is shifted to higher charge states in Fe-hot wind compared to Fe-cool wind as well. However, for the remaining CRs the Si charge state distribution in Fe-hot wind is similar to that in Fe-cool wind. Since this is coronal hole wind, the corresponding streams are all O and C cool at the same time.

In the freeze-in scenario, the charge states of two neighboring ions can change freely in the corona through recombination and ionization processes until the charge modification timescale  $\tau_{\text{mod},i}(T) = \frac{1}{n_e(C_i + R_{i+1})}$  is of the same order as the expansion time scale  $\tau_{\text{exp}} = \frac{H}{v_p}$ . Here,  $C_i$  denotes the ionization rate of the  $i$ th charge state,  $R_{i+1}$  the recombination rate from charge state  $i+1$  to  $i$ ,  $n_e$  the electron density,  $H$  the electron density scale height and  $v_p$  the proton bulk solar wind speed. After this point is reached, the electron density is too small and recombination does not have a significant effect anymore. Thus, the charge states of the considered ion pair is frozen-in and remains unchanged. Under the assumption of ionization equilibrium the electron temperature at the freeze-in point ( $T_f$ , also called freeze-in temperature) can be estimated from the in situ observed ion densities,  $n_i$  for the density of the  $i$ th charge state and  $n_{i+1}$  for the  $(i+1)$ th charge state:

$$n_i/n_{i+1} = R_{i+1}(T_f)/C_i(T_f). \quad (1)$$

Thus, in this model, pairs of charge states freeze in at different temperatures. However, this simple point of view can be misleading. If, for example, the ratio  $n_{\text{Fe}^{11+}}/n_{\text{Fe}^{10+}}$  is already frozen in but  $n_{\text{Fe}^{10+}}/n_{\text{Fe}^{9+}}$  has not yet reached its freeze-in point the density  $n_{\text{Fe}^{10+}}$  can still change. This would also affect the already frozen-in ratio  $n_{\text{Fe}^{11+}}/n_{\text{Fe}^{10+}}$  unless the transition  $\text{Fe}^{11+} \leftrightarrow \text{Fe}^{10+}$  continues to be in ionization equilibrium until its neighboring charge state pairs have frozen in as well.

From the in situ observations, only freeze-in temperatures can be inferred directly but not the radial position of the freeze-in point. For this, a model of the solar corona is required. A variety of different models with varying complexity is available.

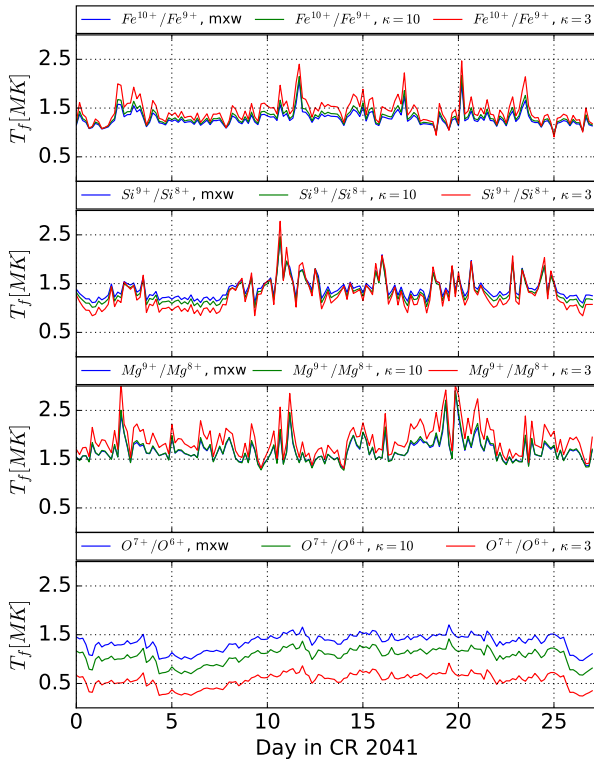


**Fig. 8.** Time series of freeze-in temperatures for selected ion pairs ( $T_{f,\text{Fe}^{10+}/\text{Fe}^{9+}}$ ,  $T_{f,\text{Si}^{9+}/\text{Si}^{8+}}$ ,  $T_{f,\text{Mg}^{9+}/\text{Mg}^{8+}}$ , and  $T_{f,\text{O}^{7+}/\text{O}^{6+}}$ ) based on different electron velocity distribution functions in 4-hour time resolution. In each panel the freeze-in temperatures based on a Maxwellian (mxw, blue),  $\kappa$ -distribution with  $\kappa = 10$  (green), and  $\kappa$ -distribution with  $\kappa = 3$  (red) as electron velocity distribution function are shown.

For example, a qualitative electron temperature profile with unspecified radial dependence is derived from the in situ observed freeze-in temperature in Geiss et al. (1995). The declining slope of the electron temperature profile, as well as the electron density and solar wind speed in the same region, are approximated with power laws for slow solar wind in Aellig et al. (1997). The coronal model of Ko et al. (1997) also derives a simple model for the electron temperature, density, and solar wind speed, but covers a larger part of the electron temperature profile, including the coronal maximum of the electron temperature. The self-consistent model of the solar corona described in Cranmer et al. (2007) of course also includes a detailed temperature profile. However, these models differ in the shape, maximum value, and radial position of the maximum of the electron temperature profile. Unfortunately, it is difficult to verify which of these models describes the conditions in the solar atmosphere most accurately. This very complex issue is beyond the scope of the work presented here. Instead, we focus on the information contained directly in the in situ data and add as few assumptions as possible. A strong assumption is required to translate the in situ observed ion densities into freeze-in temperatures: the assumption of (local) ionization equilibrium. Since the ionization and recombination rates depend on it, we also have to make an assumption on the shape of the electron velocity distribution. Under thermal equilibrium, a Maxwellian distribution would be the appropriate choice. However, the solar corona is highly

dynamic and thus most likely not in thermal equilibrium in the relevant regions (Contesse et al. 2004; Poppenhaeger et al. 2013; Singh et al. 2006). Thus, a non-Maxwellian distribution is more realistic. This can be approximated for example by a  $\kappa$ -distribution (Dzifčáková et al. 2015; Dzifčáková & Dudík 2013). The parameter  $\kappa$  controls the shape of the distribution. For  $\kappa \rightarrow \infty$ , the  $\kappa$ -distribution converges to a Maxwellian distribution.

Figure 8 shows time series of the freeze-in temperature of four ion pairs, namely  $T_{f,\text{Fe}^{10+}/\text{Fe}^{9+}}$ ,  $T_{f,\text{Si}^{9+}/\text{Si}^{8+}}$ ,  $T_{f,\text{Mg}^{9+}/\text{Mg}^{8+}}$ , and  $T_{f,\text{O}^{7+}/\text{O}^{6+}}$ , for recombination and ionization rates based on a Maxwellian and  $\kappa$ -distributions with  $\kappa = 3$  and  $\kappa = 10$  as electron velocity distribution functions. The rates based on a Maxwellian electron velocity distribution function are taken from CHIANTI (Dere et al. 1997; Landi et al. 2013) and the rates based on  $\kappa$ -distributions are taken from the KAPPA package for CHIANTI as described in Dzifčáková et al. (2015). While the freeze-in temperatures  $T_{f,\text{Mg}^{9+}/\text{Mg}^{8+}}$  and  $T_{f,\text{Fe}^{10+}/\text{Fe}^{9+}}$  are increased the further the electron velocity distribution deviates from the Maxwellian case, the opposite is the case for  $T_{f,\text{O}^{7+}/\text{O}^{6+}}$ . The  $T_{f,\text{Si}^{9+}/\text{Si}^{8+}}$  case represents a mixture of both. For freeze-in temperatures below 1.5 MK the most strongly superthermal electron velocity distribution function with  $\kappa = 3$  leads to lower freeze-in temperatures than the Maxwellian case, while for higher freeze-in temperatures the  $\kappa = 3$  scenario results in higher freeze-in temperatures than for a Maxwellian electron velocity distribution function. Under model assumptions that lead to similar freeze-in radii for O and C, Owocki & Ko (1999) argue that both should also have comparable freeze-in temperatures. This can be achieved not only by a non-Maxwellian electron velocity distribution function but also by taking differential streaming into account. As illustrated in Fig. 8, the different ion pairs are affected differently by different assumptions on the shape of the underlying electron velocity distribution function. Since differential streaming (Esser & Edgar 2001) is observed in the solar wind and is observed in coronal hole wind (Berger et al. 2011; Janitzek et al. 2016), a combination of both differential streaming and an extremely superthermal  $\kappa$  distribution might be unrealistic. Thus, we chose  $\kappa = 10$  as a compromise that results in a significant, but not extreme deviation from the Maxwellian case.

#### 4.1. Freeze-in order: examples based on the Cranmer 2007 model

In Figs. 9 and 10, we illustrate the freeze-in scenario with the help of the Cranmer et al. (2007) model. We take the temperature profile, mass density, and bulk solar wind speed for the coronal hole scenario from Cranmer et al. (2007), derive the electron density with the help of the ionization fraction that is given there as well (see Fig. 9), and compute the expansion time scale  $\tau_{\exp}$ , as well as the charge modification time scales  $\tau_{\text{mod}}$  for selected Si and Fe ion pairs (upper subpanels in Fig. 10). Then we modify the temperature profile to show how this affects the charge modification timescales and, in particular, the order in which charge states of the ion pairs freeze in. The recombination and ionization rates were again taken from the KAPPA package for CHIANTI and are shown in the bottom panels. In both figures, we consider four cases: the original temperature profile from Cranmer et al. (2007; top left), a temperature profile with steeper slopes (top right), a down-scaled temperature profile (bottom left), and the combination of both, down-scaled temperature profile with steeper slopes (bottom right). For all three modified temperature profiles, we leave the other quantities at their original values to focus solely on the effect of the shape

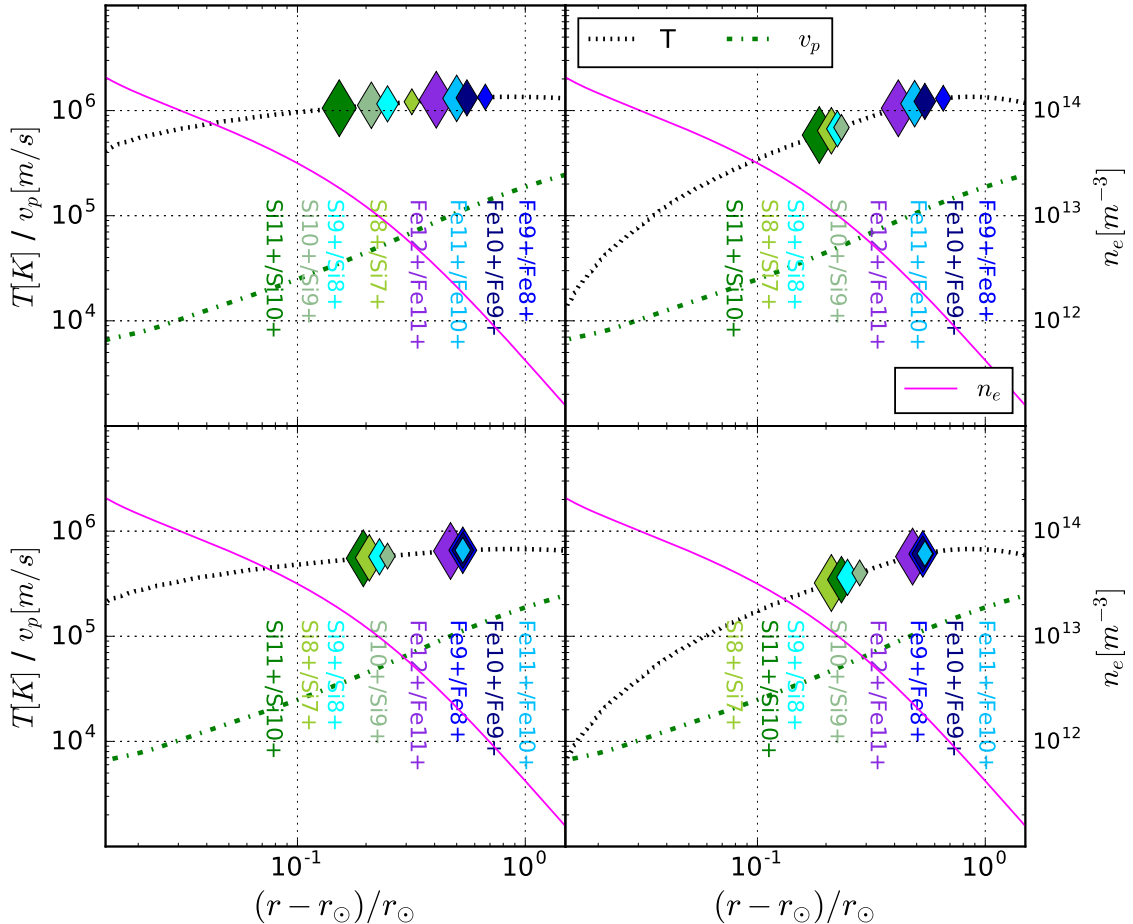


**Fig. 9.** Freeze-in temperatures based on the Cranmer et al. (2007) model. Each panel shows the top the temperature, electron density and bulk solar wind flow speed over the radius. Four different temperature profiles are considered: unmodified (*top left*), steeper increasing and declining slopes (*top right*), lower maximum temperature (*bottom left*), lower maximum temperature and steeper slopes (*bottom right*). The freeze-in points were derived based on ionization and recombination rates for  $\kappa$ -distributed electron velocity functions with  $\kappa = 10$ .

of temperature profile on the freeze-in order. For all four cases, the freeze-in points are indicated in Fig. 10 as colored diamond-shaped symbols.

These scenarios only serve as illustrations of how freeze-in order can depend on the temperature profile. In the unmodified case, the Si and Fe charge state freeze-in in the expected order: The highest-order Si charge state pair  $\text{Si}^{11+}/\text{Si}^{10+}$  freezes in first, followed by  $\text{Si}^{10+}/\text{Si}^{9+}$ , then  $\text{Si}^{9+}/\text{Si}^{8+}$ , and finally  $\text{Si}^{8+}/\text{Si}^{7+}$ . The same is the case for the Fe charge states: 1st  $\text{Fe}^{12+}/\text{Fe}^{11+}$ , 2nd  $\text{Fe}^{11+}/\text{Fe}^{10+}$ , 3rd  $\text{Fe}^{10+}/\text{Fe}^{9+}$ , and 4th  $\text{Fe}^{9+}/\text{Fe}^{8+}$ . If the temperature profile has steeper slopes (top right in Figs. 9 and 10) the Fe ion pairs still freeze in in the same order, but for Si the freeze-in order has changed to: 1st  $\text{Si}^{11+}/\text{Si}^{10+}$ , 2nd  $\text{Si}^{8+}/\text{Si}^{7+}$ , 3rd  $\text{Si}^{9+}/\text{Si}^{8+}$ , and 4th  $\text{Si}^{10+}/\text{Si}^{9+}$ . The lower sub-panels in Fig. 10 show the sum of the ionization and recombination rates as solid lines for each ion pair, the ionization rate as dashed lines, and the recombination rate as dotted lines. The order reversal is caused by the more localized transition from a recombination-dominated charge modification timescale at lower temperatures to an ionization-dominated charge modification timescale at higher temperatures. The only other factor in

the charge modification timescale is the electron density, which is kept unchanged between the different scenarios. Thus, at their freeze-in point, some ion pairs are still dominated by recombination, while others are ionization-dominated at their respective freeze-in points. This leads to a variation of the freeze-in order. If, instead, the temperature profile is down-scaled, the freeze-in order of the Si ion pairs remains unchanged, but three of the Fe ion pair charge states,  $\text{Fe}^{11+}/\text{Fe}^{10+}$ ,  $\text{Fe}^{10+}/\text{Fe}^{9+}$ , and  $\text{Fe}^{9+}/\text{Fe}^{8+}$ , freeze in very close together, with very similar freeze-in radii and freeze-in temperatures. This means that the apparent order in which they freeze-in is determined by small fluctuations and would be expected to vary frequently in the in situ derived freeze-in temperatures. We note that the assumption that each ion pair remains in ionization equilibrium at least until its neighboring ion pairs have also frozen in is, in this case, fulfilled intrinsically for  $\text{Fe}^{10+}/\text{Fe}^{9+}$  because its neighbors freeze-in at the same place. The last case, in the bottom right, is the combination of both effects: the temperature profile is down-scaled and steeper compared to the original one. Here, the freeze-in order of the Si ion pairs is changed to: 1st  $\text{Si}^{8+}/\text{Si}^{7+}$ , 2nd  $\text{Si}^{11+}/\text{Si}^{10+}$ , 3rd  $\text{Si}^{9+}/\text{Si}^{8+}$ , and 4th  $\text{Si}^{10+}/\text{Si}^{9+}$ . At the same time,

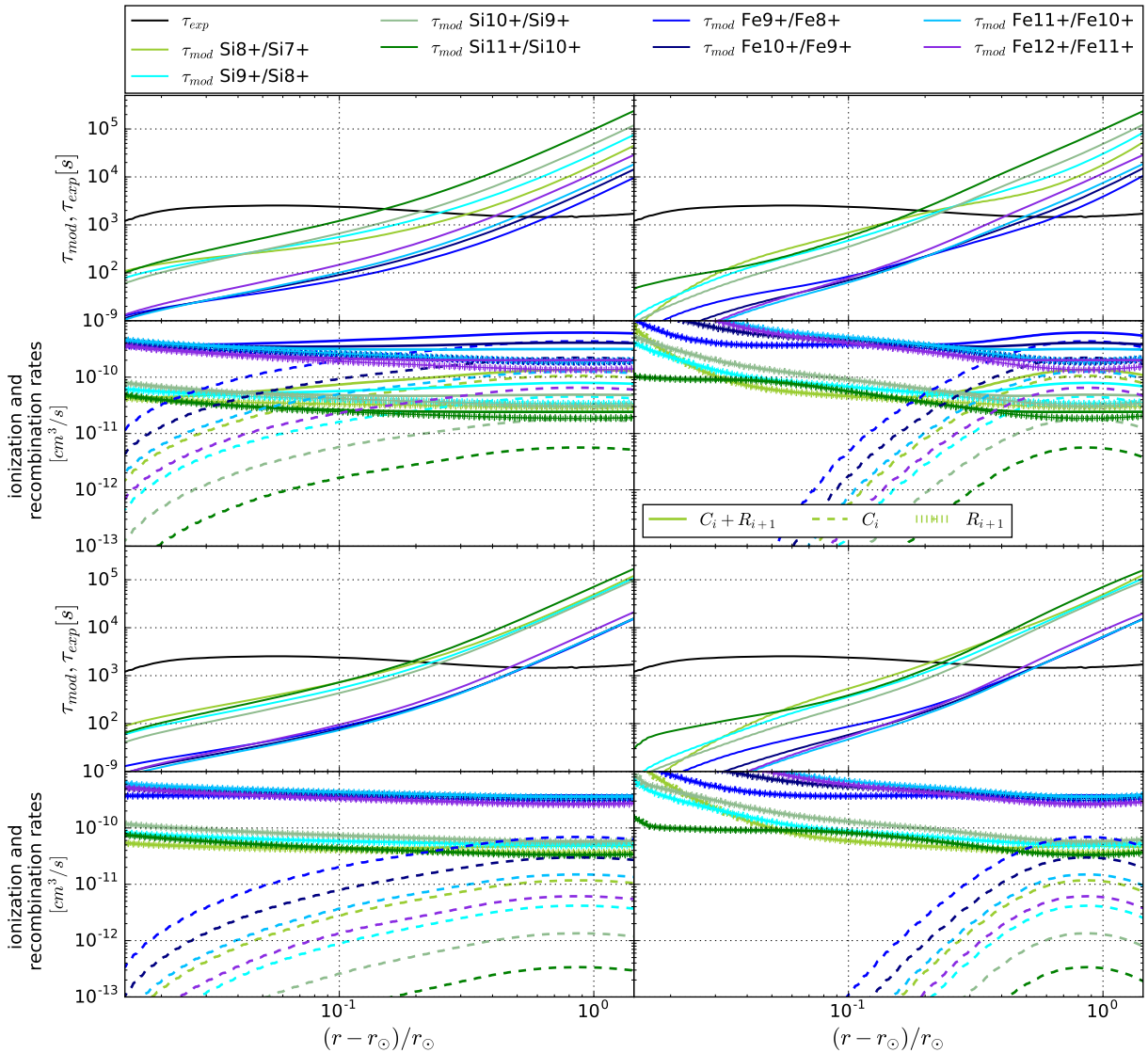


**Fig. 10.** Charge modification and expansion timescales for Si and Fe ions based on the Cranmer et al. (2007) model (top left) and for modified temperature profiles: steeper increasing and declining slopes (top right), lower maximum temperature (bottom left), lower maximum temperature and steeper slopes (bottom right). The first and third rows show the expansion and charge modification timescales. The other panels show for each ion pair the ionization and recombination rates, as well as their sum. The ionization and recombination rates are based on  $\kappa$ -distributed electron velocity functions with  $\kappa = 10$ .

while  $\text{Fe}^{12+}/\text{Fe}^{11+}$  still freezes in first, the other three Fe ion pairs again freeze in very close together, i.e. their freeze-in order is just about to change.

#### 4.2. Minimal temperature profiles

Before we can compare the in situ derived freeze-in temperatures and freeze-in orders, a concise representation of this data is needed. We derive minimal temperature profiles as defined in the following. The aim of this representation is to exploit all information that is provided by the in situ observed ion density data without relying on models for the electron temperature,

electron density, and solar wind speed in the relevant regions of the Sun. As long as the underlying assumption required to derive freeze-in temperatures is valid, that is that the local environment in which the ion pairs freeze in is approximately in local ionization equilibrium and that the electron velocity distribution function is well-represented by a  $\kappa$ -distribution, models for electron temperature, density, and solar wind speed profiles should be consistent with the observations shown here. From in situ observations of ACE/SWICS, the densities of the several O, C, Mg, Si, and Fe ions are available. With Eq. (1) and the recombination and ionization rates from CHIANTI and the KAPPA package, freeze-in temperatures can be inferred for each pair of adjacent ions. We estimate the freeze-in order based on

## V. Heidrich-Meisner et al.: Evolution of an equatorial coronal hole structure and wind

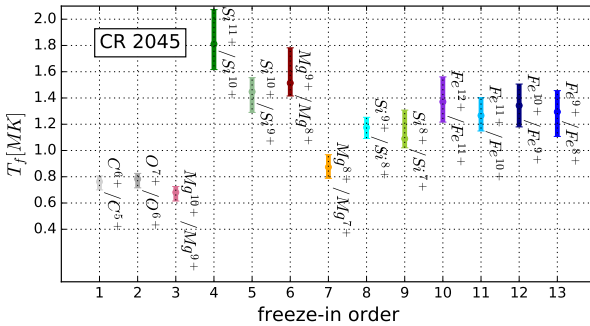


**Fig. 11.** Minimal temperature profile averaged over the first coronal hole stream in CR 2045. The freeze-in temperatures are derived from in situ observed ion ratios and the median over the coronal hole stream is shown together with the 15.9th and 84.1th percentile as error bars. The freeze-in order is determined by the median of the recombination and ionization rates  $C_i(T_f) + R_{i+1}(T_f)$  at the freeze-in points. The recombination and ionization rates are based on a  $\kappa$ -function as electron velocity distribution with  $\kappa = 10$ .

the sum of recombination and ionization rates at the respective freeze-in temperatures. In this way, the recombination and ionization rates at the freeze-in temperature additionally provide the order in which the ion pairs freeze in (see also Fig. 10). Figure 11 shows a so-called minimal temperature profile averaged over one coronal hole wind stream (the first in CR 2045). The x-axis gives the averaged freeze-in order for 13 O, C, Mg, Si, and Fe ion pairs from low (left) to high (right) in the solar atmosphere as defined by the sum of the respective recombination and ionization rates. From models like the Cranmer et al. (2007) model a single maximum in this minimal temperature profile would be expected. The averaged minimal temperature profile in Fig. 11 shows an additional local minimum for  $T_{f,Mg^{8+}/Mg^{7+}}$ . This is probably caused by the combination of two effects: 1) As a result of the variability in the freeze-in order, averaging the freeze-in order can be misleading. This is therefore avoided in the following. 2) In ACE/SWICS ions with a similar mass-to-charge ratio can influence each other. We believe that this is the reason that the densities  $n_{Mg^{8+}}$  and  $n_{Mg^{10+}}$  are systematically underestimated and therefore the freeze-in temperatures  $T_{f,Mg^{10+}/Mg^{9+}}$  and  $T_{f,Mg^{8+}/Mg^{7+}}$  are also underestimated, while  $T_{f,Mg^{9+}/Mg^{8+}}$  is overestimated.

Figure 12 combines all in situ available information into a time series plot. Each color in Fig. 12 identifies an ion pair. For each temporal bin, a minimal temperature profile is shown by stacking the freeze-in temperatures for the considered ion pairs on top of each other. They are again ordered by the sum of their recombination and ionization rates (at the respective temperature) from lowest (and thus deepest in the solar atmosphere) to highest (which corresponds to a freeze-in radius higher in the solar atmosphere). In this way, each stack approximates a temperature profile from lowest in the atmosphere (bottom) to highest in the atmosphere (top) without giving the actual radial distance. The location of each freeze-in point requires some kind of model of the corona (as for example Aellig et al. 1997; Geiss et al. 1995; Cranmer et al. 2007). We now avoid using an additional model and focus on conclusions based directly on the in situ observations. To ensure comparable statistics in each bin, a variable bin size is used. For each bin and beginning with the native 12-min resolution of ACE/SWICS, the bin size is increased until at least 100 total counts per element are reached. The average bin size in all minimal temperature profiles shown here lies between

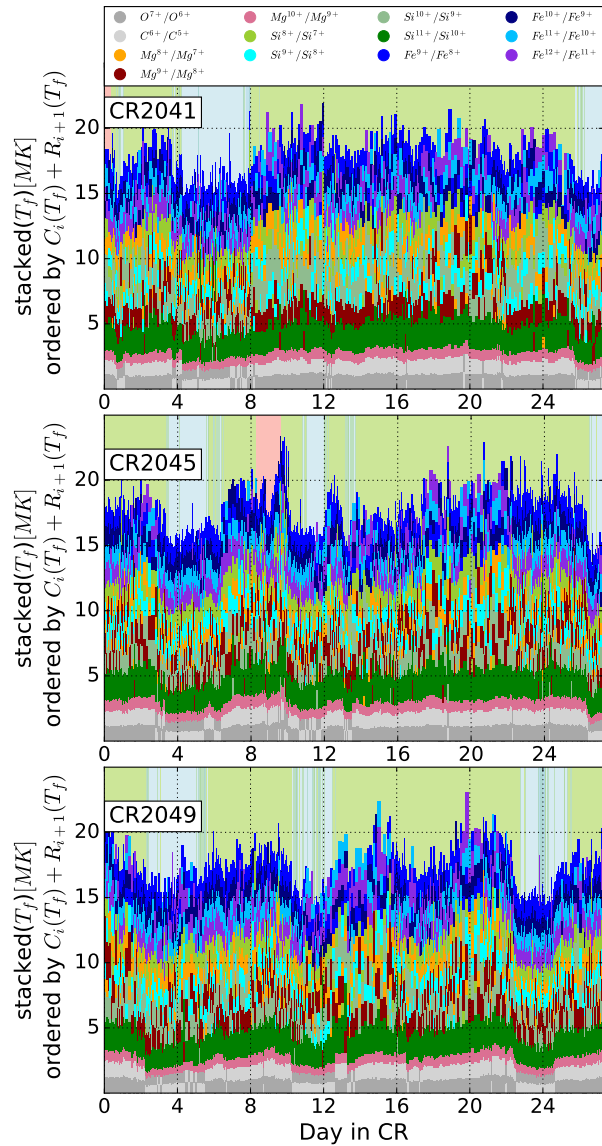


**Fig. 12.** Minimal temperature profiles: freeze-in temperatures for selected ion pairs ordered by the sum of recombination and ionization rates and over time for CR 2041 (top), CR 2045 (middle) and CR 2049 (bottom). The bin size is adaptive to ensure comparable statistics in each bin. For each element, at least 100 total counts are contained per bin. The maximum bin size is 4 h. All panels refer to a  $\kappa$ -function with  $\kappa = 10$  as the electron velocity distribution function. Each ion pair is identified by color. Their order (from bottom to top) is determined by their recombination and ionization rates  $C_i(T_f) + R_{i+1}(T_f)$ .

1h and 1.5h and the maximum allowed bin size of 4h is used for at most 20 bins in all the following figures.

Figure 12 shows a time series of such minimal temperature profiles for CRs 2041, 2045, and 2049. These three CRs were chosen as representatives of coronal hole streams that are mapped back to a thin sparse open field line region (CR 2041, see Fig. 2), to an open field line region with foot points distributed more uniformly over a larger area (CR 2045), and the special

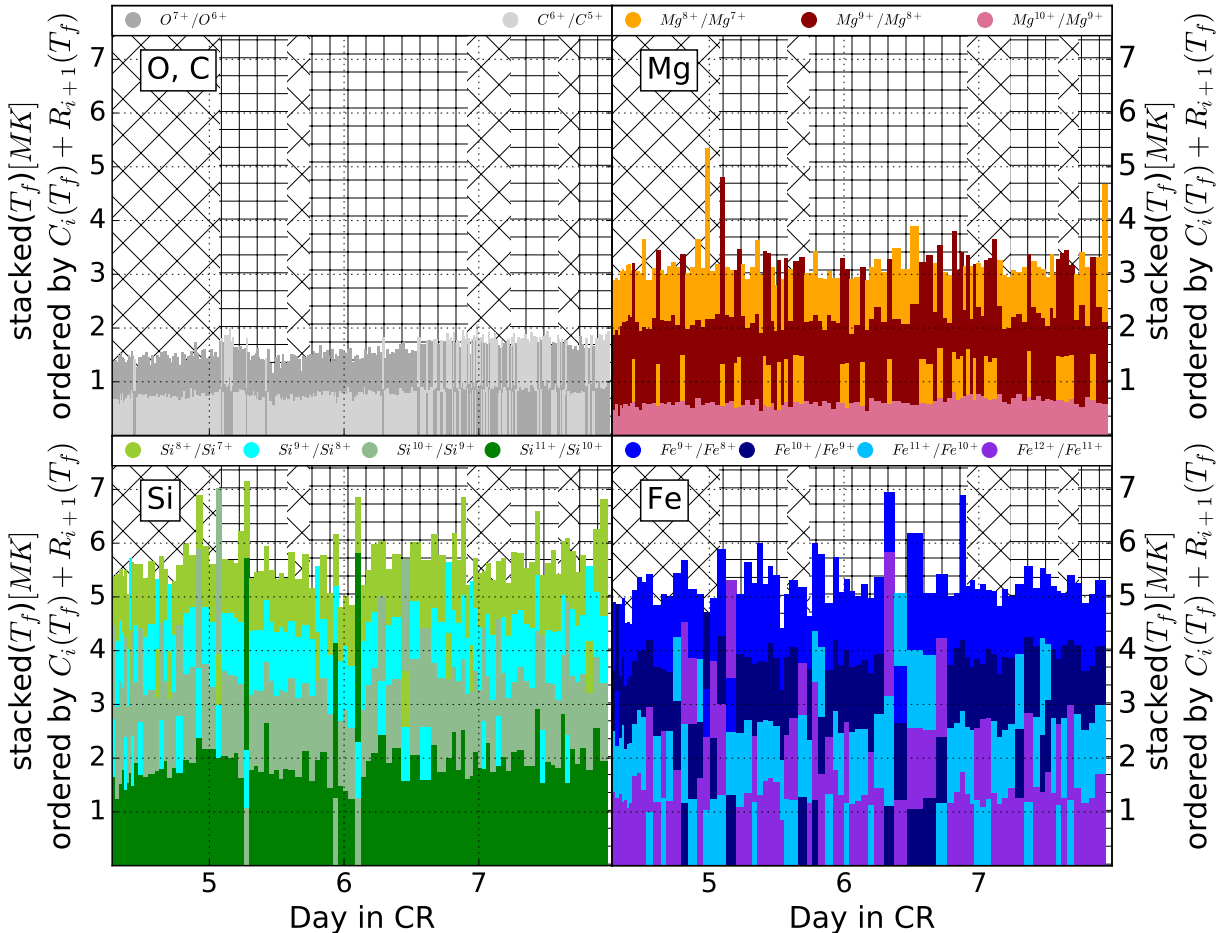


**Fig. 13.** Time series of minimal temperature profiles with adaptive bin size for the first recurring coronal hole wind stream in CR 2041 and in the same format as in Fig. 12. *Top left:* O and C ion pairs, *top right:* Mg ion pairs, *bottom left:* Si ion pairs, and *bottom right:* Fe ion pairs. All panels refer to a  $\kappa$ -function with  $\kappa = 10$  as the electron velocity distribution function. Fe-hot and Fe-cool coronal hole wind streams are marked with +-shaped hatching (Fe-hot) and x-shaped hatching (Fe-cool).

case of very dense and compact open field line region very close to an active region (CR 2049). In the background, the solar wind type is indicated in the same way as in Figs. 3 and 5. Although not shown here, we compared the time series of minimal temperature profiles based on a Maxwellian distribution with that based on a  $\kappa$ -distribution with  $\kappa = 10$ . We verified that the resulting minimal temperature profiles for the Maxwellian and  $\kappa$  cases are similar but not identical. In particular, both show comparable changes in the freeze-in order.

Keeping a simplified sketch of the expected shape of the electron temperature profile in mind, for example as in Fig. 5 in Geiss et al. (1995), helps to interpret our minimal temperature profiles. O and C ion pairs are expected to freeze in lower in the corona, in particular below the maximum of the electron temperature profile. Mg and Si ion pairs have freeze-in points around the maximum and Fe ion pairs are expected to freeze-in at higher distances and thus on the declining slope of the temperature profile. It is notable that the example from the Cranmer et al. (2007) model in Fig. 9 differs from the idealized sketch in so far as all ion pairs freeze in on the increasing slope of the temperature profile, whereas in the ACE/SWICS data (as is discussed in the

following) the maximum freeze-in temperature is typically observed for  $T_{f,\text{Si}^{11+}/\text{Si}^{10+}}$ . Smaller O and C freeze-in temperatures indicate a steeper increase towards the maximum of the temperature profile. The Si and Mg freeze-in temperatures are assumed to be distributed around the maximum of the temperature profile and thus estimate the maximum height of the profile. The Fe ion pairs freeze-in on the declining slope of the temperature profile and for example high Fe freeze-in temperatures indicate therefore a slowly decreasing slope of the temperature profile outside of the maximum.

Mainly because of the smaller O and C freeze-in temperatures, the sum of all temperatures in coronal hole wind in Fig. 12 is smaller than in slow solar wind. This reflects the different conditions in the respective source regions. In all three selected CRs, the minimal temperature profile of slow solar shows high variability.

Figures 13–15 have the same format as Fig. 12, but show a smaller subset of ion pairs and zoom in on the time period of our coronal hole wind stream of interest. The bin size is again adaptive and therefore differs between the different subplots. Fe-hot and Fe-cool coronal hole wind streams are marked

V. Heidrich-Meisner et al.: Evolution of an equatorial coronal hole structure and wind

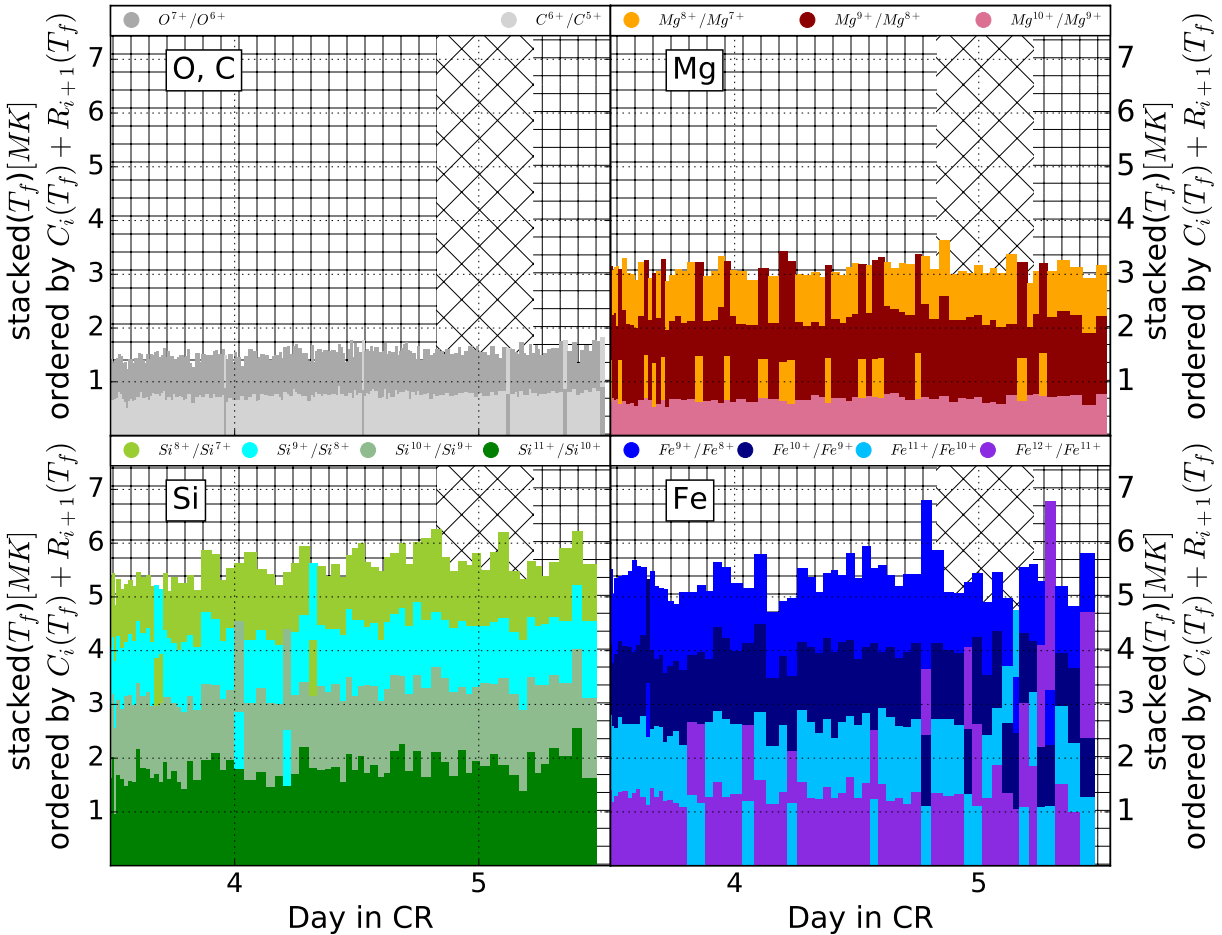


**Fig. 14.** Time series of minimal temperature profiles with adaptive bin size for the first recurring coronal hole wind stream in CR 2045 and in the same format as in Fig. 13. *Top left:* O and C ion pairs, *top right:* Mg ion pairs, *bottom left:* Si ion pairs, and *bottom right:* Fe ion pairs. All panels refer to a  $\kappa$ -function with  $\kappa = 10$  as the electron velocity distribution function.

with +-shaped hatching (Fe-hot) and  $\times$ -shaped hatching (Fe-cool). The  $y$ -axis scale is, for all three figures, the same in all subplots. The comparison between the summed freeze-in temperatures for the different elements shows that the Si ion pairs have (most of the time) higher freeze-in temperatures than the Fe ion pairs. In particular in most bins,  $T_{f, Si^{11+}/Si^{10+}}$  shows the highest observed freeze-in temperature. Thus, the Si ion pairs are indeed most representative of the maximum of the temperature profile. The combined Fe freeze-in temperatures are however similar. This can indicate a slow decline of the temperature profile in the corona. The inner part of the temperature profile, as estimated by the O and C freeze-in temperatures, shows little variability for CR 2045 but, in CRs 2041 and 2049, the O and C freeze-in temperatures and, in particular, the freeze-in order are more variable. In all three CRs in some time bins, the ratio  $n_{O^{7+}}/n_{O^{6+}}$  freezes in lower in the corona than  $n_{C^{6+}}/n_{C^{5+}}$ . The Mg ion pairs show no difference between the Fe-hot and Fe-cool coronal hole wind streams in all three CRs. The freeze-in order of  $Mg^{9+}/Mg^{8+}$  and  $Mg^{8+}/Mg^{7+}$  change more frequently in CR 2041 and CR 2045 than in CR 2049. The Si ion pairs that are closest to the maximum of the temperature profile is more variable in CRs 2041 and 2049. In particular, the order in which

the Si ion pairs freeze in changes frequently. Because, most of the time, they have similar freeze-in temperatures, this can also indicate that these charge states freeze-in in close radial proximity. There are a few interesting cases (for example for the Si ion pairs at DoY 78.67 and for the Fe ions at DoY 79.90) where the minimal temperature profiles exhibit more than one local maximum. Although the adaptive bin-size reduces the effects of varying statistics this could still be an effect of insufficient statistics for some of the relevant ion pairs. But it can also be interpreted as an indication for a more complex structure within the corona. The Fe-part of the temperature profile, which probably represents the declining slope at higher radial distances, is also variable, both in terms of freeze-in temperatures and in terms of the order in which the Fe ion pairs freeze in. In particular, while in Fe-cool coronal hole wind  $n_{Fe^{12+}}/n_{Fe^{11+}}$  ratio (purple in Figs. 13–15) freezes as the first Fe ion pair in some cases, in others this is the last Fe ion pair to freeze in (at least of those shown here). However, this correlates only weakly with Fe-hot and Fe-cool coronal hole wind. Thus, although the average Fe charge state is different in Fe-cool and in Fe-hot coronal hole wind, this is not clearly reflected in the respective minimal temperature profiles. In CR 2045,  $n_{Fe^{12+}}/n_{Fe^{11+}}$  ratio freezes in first both in Fe-hot

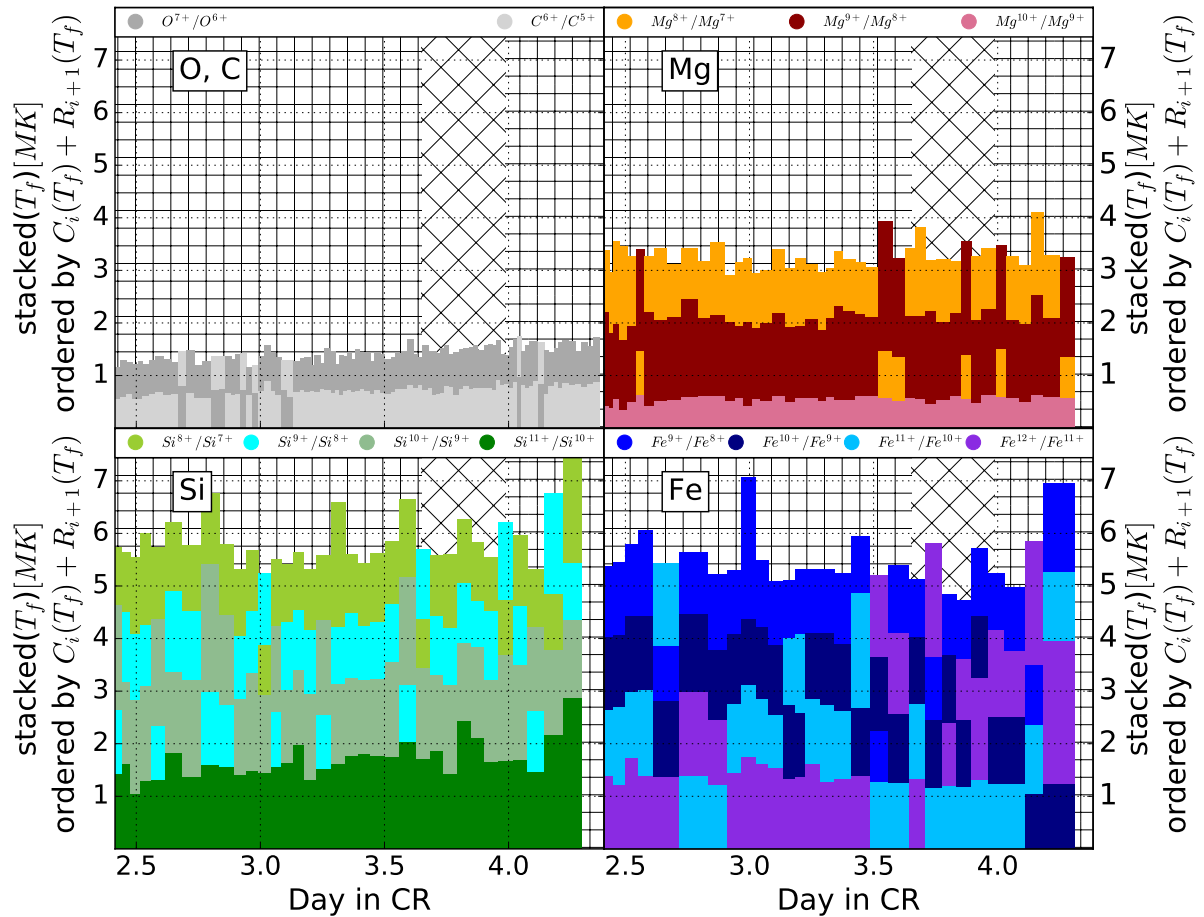


**Fig. 15.** Time series of minimal temperature profiles with adaptive bin size for the first recurring coronal hole wind stream in CR 2049 and in the same format as in Fig. 13. Top left: O and C ion pairs, top right: Mg ion pairs, bottom left: Si ion pairs, and bottom right: Fe ion pairs. All panels refer to a  $\kappa$ -function with  $\kappa = 10$  as the electron velocity distribution function.

and in Fe-cool wind, in CRs 2041 and 2049 this ion pair freezes in at higher radial distances than the other Fe ion pairs mainly in Fe-hot coronal hole wind. In all three CRs, the Fe freeze-in temperatures are similar for all Fe ion pairs. If this was solely influenced by the form of the temperature profile, according to the considerations based on Fig. 10, this hints at a locally comparatively low electron temperature at the freeze-in point of these Fe ion pairs. In the case of CR 2045 the minimal temperature profile shows less variability than in CR 2041 and CR 2049. Although not shown here, this is also the case for CRs 2044, and 2046–2048. This supports the observation that our coronal hole wind stream of interest in CR 2045 as an example for an open field line region that is less strongly constrained by surrounding active regions shows undisturbed and quiet coronal hole wind.

## 5. Discussion and conclusions

We have combined in situ solar wind observations from ACE with a ballistic back-mapping and a numerical PFSS to trace the evolution of a coronal hole structure and the coronal hole wind stream originating there over 11 CRs in 2006 (in CR 2050 the coronal hole wind stream is not observed in situ anymore). We have shown that the equatorial coronal hole shows high

variability on small scales, both with respect to its shape and to its Fe charge state composition. In each CR, the in situ observations trace a different lateral path through the coronal hole. Therefore, although solar wind from the same recurring coronal hole is observed multiple times, its properties can be expected to vary even if the source region itself would remain unchanged. As illustrated by the PFSS model output, the shape of the open field line region varies from CR to CR. This is probably influenced by the more dynamic neighboring coronal loop structures. These closed field line regions constrain the available space the open field line region can extend to. Interestingly, during the CRs where the open field line region is most uniformly filled with field lines, also the median O and C charge state ratios observed in situ are mostly similar. This could imply that in the CRs where the surrounding regions with closed field lines impose stronger constraints on the shape of the open field line region, their proximity also influences the compositional properties. This could be caused by reconnection effects or by inducing stronger interactions between neighboring individual flux tubes within the coronal hole wind stream.

The average Fe charge state exhibits an interesting variability within this recurring coronal hole wind stream. Except for the case of CR 2050, where the coronal hole wind stream is not

## V. Heidrich-Meisner et al.: Evolution of an equatorial coronal hole structure and wind

observed in situ any more, each CR shows transitions between Fe-hot and Fe-cool coronal hole wind. But their order (from Fe-hot to Fe-cool or vice versa) and length is different between CRs. This illustrates that a (recurring) coronal hole wind stream carries additional fine structure features. It is possible that the Fe-hot and Fe-cool property of a coronal hole wind stream is caused or enhanced by wave-plasma interactions. This topic requires further investigation that is beyond the scope of this study.

We probed the coronal temperature profile based on in situ derived freeze-in temperatures. We illustrated that the freeze-in order of Si and Fe ion pairs can change depending on the respective influence of ionization versus recombination at the freeze-in point. Together with the freeze-in order determined by the sum of ionization and recombination rates the freeze-in temperatures constitute what we call a minimal temperature profile. Minimal temperature profiles can be derived without a model of the solar atmosphere. Although the radial position of the freeze-in points is not defined by the minimal temperature profiles, they nevertheless constrain the shape of the coronal electron temperature profile. We found signatures of variability of the temperature profile within coronal holes. While, in the inner part of the electron temperature profile and thus in the lower atmosphere, the shape of the temperature profile shows only small variations within the considered coronal hole wind streams, this is different higher in the corona. The probable maximum value of the electron temperature profile can change on timescales of hours, even in coronal hole wind. The declining slope of the electron temperature profile is variable as well. This implies that the conditions in the solar corona also change on relatively small scales within a coronal hole wind stream. This variability in the electron temperature profile could be a signature of individual flux tubes. Whether it is related to turbulence remains to be investigated. The order in which the different ion pairs freeze in is here determined by the combination and ionization rates at the derived freeze-in temperature. It is sensitive to the precise conditions in the coronal hole wind stream. For models that are compatible with the assumptions necessary to derive our minimal temperature profiles, that is local ionization equilibrium and Maxwellian or  $\kappa$ -distributions for the underlying electron velocity distribution functions, our minimal temperature profiles can be a suitable tool for the comparison with model predictions and thus help to distinguish between different such models.

The variability and lack thereof of the coronal hole wind properties and of the shape of the corresponding open field line region are tracers of the lateral structure of a coronal hole within the photosphere. The minimal temperature profile based on the charge state composition complements this with a probe of the radial structure of the coronal hole. For CRs 2045–2048, both the lateral and radial variability between CRs is lower than for the other CRs. This indicates that during these CRs 2045–2048, the respective coronal hole wind stream probably represents undisturbed coronal hole wind.

**Acknowledgements.** Part of this work was supported by the Deutsche Forschungsgemeinschaft (DFG) project number Wi-2139/10-1. We are very grateful for the detailed and helpful suggestions provided by the anonymous referee.

## References

- Aellig, M., Grünwaldt, H., Bochsler, P., et al. 1997, in Fifth SOHO Workshop: The Corona and Solar Wind Near Minimum Activity, [ESA SP, 415, 27](#)
- Altschuler, M. D., & Newkirk, G. 1969, *Sol. Phys.*, **9**, 131
- Antiochos, S., Mikić, Z., Titov, V., Lionello, R., & Linker, J. 2011, *ApJ*, **731**, 112
- Bame, S., Asbridge, J., Feldman, W., & Gosling, J. 1977, *J. Geophys. Res.*, **82**, 1487
- Benevolenskaya, E., Kosovichev, A., & Scherrer, P. 2001, in Recent Insights into the Physics of the Sun and Heliosphere: Highlights from SOHO and Other Space Missions, IAU Symp., 203, 251
- Berger, L. 2008, Ph.D. Thesis, Christian-Albrechts-Universität, Germany
- Berger, L., Wimmer-Schweingruber, R., & Gloeckler, G. 2011, *Phys. Rev. Lett.*, **106**, 151103
- Contesse, L., Koutchmy, S., & Viladrich, C. 2004, *Ann. Geophys.*, **22**, 3055
- Cranmer, S. R. 2009, *Liv. Rev. Sol. Phys.*, **6**, 1
- Cranmer, S. R., Van Ballegooijen, A. A., & Edgar, R. J. 2007, *ApJSS*, **171**, 520
- Dasso, S., Milano, L., Matthaeus, W., & Smith, C. 2005, *ApJ*, **635**, L181
- Delaboudinière, J.-P., Artzner, G., Brunaud, J., et al. 1995, in The SOHO Mission (Springer), 291
- Dere, K., Landi, E., Mason, H., Fossi, B. M., & Young, P. 1997, *A&AS*, **125**, 149
- Dzifčáková, E., & Dudík, J. 2013, *ApJSS*, **206**, 6
- Dzifčáková, E., Dudík, J., Kotrč, P., Fárník, F., & Zemanová, A. 2015, *ApJS*, **217**, 14
- Esser, R., & Edgar, R. J. 2001, *ApJ*, **563**, 1055
- Fazakerley, A., Harra, L., & van Driel-Gesztelyi, L. 2016, *ApJ*, **823**, 145
- Fisk, L., Schwadron, N., & Zurbuchen, T. 1999, *J. Geophys. Res.: Space Phys.*, **104**, 19765
- Geiss, J., Gloeckler, G., Von Steiger, R., et al. 1995, *Science*, **268**, 1033
- Gloeckler, G., Cain, J., Ipavich, F., et al. 1998, in The Advanced Composition Explorer Mission (Springer), 497
- Gómez-Herrero, R., Kartavykh, Y., Klassen, A., & Dresing, N. 2011, in *Int. Cosmic Ray Conf.*, **10**, 201
- Gopalswamy, N. 2006, *JA&A*, **27**, 243
- Heidrich-Meisner, V., Peleikis, T., Kruse, M., Berger, L., & Wimmer-Schweingruber, R. 2016, *A&A*, **593**, A70
- Hundhausen, A., Gilbert, H., & Bame, S. 1968, *ApJ*, **152**, L3
- Janitzek, N., Taut, A., Berger, L., et al. 2016, in SOLAR WIND 14: Proc. 14th Int. Solar Wind Conf., AIP Conf. Proc., 1720, 040006
- Jian, L., Russell, C., Luhmann, J., & Skoug, R. 2006, *Sol. Phys.*, **239**, 393
- Jian, L., Russell, C., & Luhmann, J. 2011, *Sol. Phys.*, **274**, 321
- Kasper, J., Lazarus, A., & Gary, S. 2008, *Phys. Rev. Lett.*, **101**, 261103
- Ko, Y.-K., Fisk, L. A., Geiss, J., Gloeckler, G., & Guhathakurta, M. 1997, *Sol. Phys.*, **171**, 345
- Landi, E., Young, P., Dere, K., Del Zanna, G., & Mason, H. 2013, *ApJ*, **763**, 86
- McComas, D., Bame, S., Barker, P., et al. 1998, in The Advanced Composition Explorer Mission (Springer), 563
- McComas, D., Barracough, B., Funsten, H., et al. 2000, *J. Geophys. Res.: Space Phys.*, **105**, 10419
- Ogilvie, K. W., & Vogt, C. 1980, *Geophys. Res. Lett.*, **7**, 577
- Owocki, S., & Ko, Y. 1999, in The Solar Wind Nine Conf., AIP Conf. Proc., **471**, 263
- Owocki, S., Holzer, T., & Hundhausen, A. 1983, *ApJ*, **275**, 354
- Peleikis, T., Kruse, M., Berger, L., Drews, C., & Wimmer-Schweingruber, R. F. 2016, in AIP Conf. Ser., 1720, 020003
- Peleikis, T., Kruse, M., Berger, L., & Wimmer-Schweingruber, R. 2017, *A&A*, **602**, A24
- Poppenhaeger, K., Günther, H., Beiersdorfer, P., et al. 2013, *Astron. Nachr.*, **334**, 101
- Riley, P., & Lionello, R. 2011, *Sol. Phys.*, **270**, 575
- Robbrecht, E., Berghmans, D., & Van der Linden, R. 2009, *ApJ*, **691**, 1222
- Russell, C., Luhmann, J., & Jian, L. 2010, *Rev. Geophys.*, **48**, RG2004
- Schatten, K., Wilcox, J., & Ness, N. 1969, *Sol. Phys.*, **6**, 442
- Scherrer, P., Hoeksema, J., & Bush, R. 1991, *Adv. Space Res.*, **11**, 113
- Singh, J., Sakurai, T., Ichimoto, K., Munneer, S., & Raveendran, A. 2006, *Sol. Phys.*, **236**, 245
- Smith, C. W., L'Heureux, J., Ness, N. F., et al. 1998, in The Advanced Composition Explorer Mission (Springer), 613
- Thompson, M., Toomre, J., Anderson, E., Antia, H., et al. 1996, *Science*, **272**, 1300
- Thompson, B. J., Gibson, S. E., Schroeder, P. C., et al. 2011, *Sol. Phys.*, **274**, 29
- Wang, Y.-M., Robbrecht, E., Rouillard, A., Sheeley Jr, N., & Thernisien, A. 2010, *ApJ*, **715**, 39
- Xu, F., & Borovsky, J. E. 2015, *J. Geophys. Res.: Space Phys.*, **120**, 70



# 8

## SUMMARY & OUTLOOK

---

As part of this work, the well-established Potential Field Source Surface ([PFSS](#)) model has been re-implemented employing both the classical Spherical Harmonic Coefficient ([SHC](#)) (Sect. 2.3) and the finite-difference approach (Chapter 3). While the [SHC](#) solver mainly serves as a tool for comparing alterations to the [PFSS](#) model structure with the classical, established model, the semi-analytical finite difference solver serves as a basis for advancing the [PFSS](#) model paradigm. In this version, it already provides several advantages over the classical implementations that are presented in this work:

- Depending on the modeler's requirements, it can provide an improved numerical accuracy or a decrease in computation time by increasing or decreasing the overall grid point density, respectively.
- The finite-differencing scheme allows altering the employed source surface's geometry by implementing an appropriate coordinate transformation with an accompanying set of coordinate basis vectors.
- Because the computation procedure is the same at all grid points, it allows for the utilization of massively parallel processing structures such as Graphics Processing Unit ([GPU](#)), thereby decreasing computation time by one to two orders of magnitude.
- The utilization of a finite-difference approach based on non-equidistant grid points allows increasing the grid point density selectively in regions of strong magnetic gradients. This improves the overall prediction accuracy without the need to increase computational efforts in the entire computational domain, as is the case with the classical implementations.

Based on the developed finite-difference [PFSS](#) solver, a modified version has been implemented that allows incorporating prolate and oblate source surfaces in the model paradigm (Chapter 4). While from a theoretical (model) standpoint, the number of free parameters has increased by only one (i.e., the ellipticity of the source surface), several computational parameters, such as the number of grid points, distribution of grid points, scaling algorithm for the input data, and interpolation procedure of the output data, are required to obtain accurate results. These parameters are thoroughly discussed and evaluated in Chapter 5. The new ellipsoidal [PFSS](#) implementation was presented to the scientific community in Publication 1 (Sect. 5.5).

Following the solver's technical description, a newly developed evaluation procedure named the back mapping polarity measure is presented in Chapter 6. The theoretical considerations of numerical accuracy and solution process stability are important parts of the development process. However, the predictions of a new

model have to withstand experimental data's reality to confirm or reject its merits compared to the established models. For this purpose, in-situ spacecraft data from several sources measured near Earth's orbit are linked to the source surface, and the measured magnetic field polarity is compared to the polarity predicted by the new [PFSS](#) solver. A slight performance increase of the new solver compared to the classical implementation is found by employing the back mapping polarity measure presented in Sect. 6.4. This evaluation procedure's findings were made public in Publication 2 (Sect. 6.5).

The magnetic field configurations predicted by the [PFSS](#) model are frequently used as a basis for studies on the solar wind phenomenon. Chapter 7 demonstrates the need for a heliospheric magnetic field model to address various fundamental research questions. In particular, the [PFSS](#) model is employed to further studies focusing on the search for the origin of solar wind streams (Publication 3, Sect. 7.3) as well as solar wind composition and classification (Publications 4 and 5, Sects. 7.4 and 7.5). The [PFSS](#) solvers presented in this work enable researchers to quickly and accurately produce a prediction of the magnetic configuration according to a well-established model. They also enhance the magnetic prediction accuracy, which improves the quality of subsequent studies relying on the heliospheric magnetic configuration.

The model's evaluation procedure presented in Sect. 6.4 has a few drawbacks. It only employs the predicted magnetic field's polarity at the source surface rather than directional information of the magnetic configuration in the computational domain below. Also, because the utilized spacecraft data were measured near the ecliptic, the method only evaluates a very narrow latitude range. This is especially detrimental for evaluating prolate source surfaces, which affect the magnetic configuration mostly at higher latitudes. Therefore, additional evaluations should be performed that utilize model information from below the source surface and from a broader range of latitudes.

Analysis of Extreme Ultra-Violet ([EUV](#)) maps might provide the desired information. Because of the high ratio of plasma to magnetic pressure (high  $\beta$ ) below the source surface, charged particles are forced to travel along the magnetic field lines, whereas at some point above, the situation is reversed, and charged particles "drag" the magnetic field radially outward. Brightness in the [EUV](#) maps is determined by a combination of plasma temperature and density or, more accurately, the emission measure [see, e.g., [Li et al., 2020](#)]. Coronal hole wind streams are associated with source regions that appear less bright in [EUV](#) images [[Lee et al., 2011](#)] because the plasma can escape along open magnetic field lines, thereby "cooling" the coronal hole. Therefore, the footpoints of open magnetic field lines (i.e., magnetic field lines extending from the photosphere to the source surface) should be mapped to darker [EUV](#) regions compared to closed magnetic field lines. An evaluation method might vary the model parameters source surface height and ellipticity and compute the average open field line footpoint brightness ratio to closed field line footpoint brightness. A more accurate model is expected to feature a lower ratio than a model with lower prediction accuracy. This method would consider the entire computational domain at all latitudes up to the magnetograms' polar boundaries. A considerable problem with this method is the normalization of the

[EUV](#) maps. The general appearance of [EUV](#) maps changes throughout the solar activity cycle and for different instruments. Also, while [EUV](#) maps are typically associated with the lower boundary, the emission of light with specific wavelengths occurs in a non-zero width sheet above the photosphere, thereby introducing projection effects in the analysis.

If this second evaluation procedure upholds the finding that the ellipsoidal [PFSS](#) model only slightly improves the merit of the prediction, the application of another source surface shape might be necessary to improve the model substantially. With the solver presented in Chapter 4, more complicated source surfaces require analytical expressions for the coordinate transformations. A better solution would be to re-implement the model as a purely numerical solver. If a numerical grid generation technique is employed to fit the computational grid to an arbitrarily shaped source surface, the governing equations will be transformed similarly. The lengthy derivation of the co- and contravariant coordinate basis vectors and the Laplace operator performed in Chapter 4 would be substituted for finite-difference expressions that can be computed automatically. The drawback of this method and the reason this has not been done in the first place is that finding a suitable algorithm to perform the grid generation is an involved task. Sharp edges, varying grid point density, numerical instabilities at the boundaries, and other factors have to be automatically controlled to ensure that the resulting grid allows for a stable and converging solution process. While producing a grid that fits an arbitrary source surface shape is easy, proving that the solver can utilize this grid with high or even sufficient accuracy is not. Nevertheless, the ability to compute the [PFSS](#) model for arbitrary source surface shapes is worth striving for because it allows for another degree of freedom when modeling the solar magnetic field.

Another refinement of the [PFSS](#) implementation can be achieved by including an adaptive solution process or an adaptive grid. The solver presented in this work utilizes a primitive Euler solver, which treats every grid point at each solution step identically. While this procedure permits distributing the workload over the massively parallel computing architecture of the [GPU](#) efficiently, it also requires computations at grid points, where computational convergence might already be achieved. By breaking up this requirement and allowing a more intelligent solution process to terminate at individual grid points at different time steps, the overall computation time can be reduced even further. While this approach only speeds up the solution process, the specific treatment of grid regions could also enhance the [PFSS](#) model paradigm. The source surface height, for example, could be determined by another model for separate grid regions during run time. The one-dimensional flux tube model of [Cranmer et al. \[2007\]](#), could be employed to estimate a source surface height, which could be fed to the numerical [PFSS](#) solver and in turn resulting in a refinement of the flux tube parameters. A rotating solution process between the [PFSS](#) and the flux tube model might achieve an even better magnetic configuration prediction. The implementation employed for this work already supports non-equidistant grid spacing, and the grid is not required to be static during the solution process.



# A

## IMPLEMENTATION DETAILS AND RUN TIME MEASUREMENTS

---

As part of this work, the new semi-numerical solver has been implemented in C++ [ISO, 2017] and Nvidia's parallel computing platform CUDA [NVIDIA et al., 2020]. The CUDA programming framework permits the utilization of GPUs as massively parallel computing platforms. GPUs consist of hundreds or thousands of inexpensive processing units that are capable of performing a *single instruction* on *multiple data* (SIMD). The typical graphics processing pipeline requires the same instructions to be computed for the different pixels (i.e., different input data) for a computer graphics output. This paradigm can be employed for the new PFSS solver: At each time-step, the instruction to be computed is the same for all grid points.

Development of the program began in 2013 and was optimized for the hardware of that time (CUDA compute capability 3.5 / CUDA SDK version 5.5). The CUDA computing platform has changed considerably since then (as of 2020: CUDA compute capability 8.6 / CUDA SDK version 10.2). Due to backward compatibility, the program runs on all current-generation Nvidia GPUs, but the program makes no use of the new hardware's modern capabilities. Therefore, the run times presented in this section reflect the unoptimized state of the unpublished program. A publication of the program code in open-source format is intended.

The program can be either used in an accelerated form with CUDA hardware or in standard C++ form without the need for specific GPUs. The run time measurements presented here were obtained on an in-use office computer, and the single-threaded Central Processing Unit (CPU) version has been instanced up to six times in parallel. The GPU version has been running alongside the CPU version. Therefore, the values presented are merely approximations of the run times that would be obtained in an isolated environment. Some variability in the run times is to be expected.

For the CPU version, an AMD Ryzen9 3900X CPU (released in 2019) was used. For the GPU version, an Nvidia GTX 1080 GPU (released in 2016), and an Nvidia RTX 2080 Super (released in 2019) were employed.

The measured quantities are denoted as follows: The number of iteration steps of the solver N, the run time of the CPU version  $t_0$ , the run time of the GPU version on the GTX 1080  $t_1$  and on the RTX 2080 Super  $t_2$ . The speedup for both GPUs is defined by  $s_1 = t_0/t_1$  and  $s_2 = t_0/t_2$ . If not stated otherwise, the programs were compiled using single-precision floating-point accuracy. Increasing the accuracy to double-precision does not change the results considerably. The relative differences of the resulting scalar potential at the grid points typically amount to less than 0.1%. The measurements are listed in Tables 2 - 5.

CR	SphericA = 1.00			EllipsoidA = 1.01 oblate			EllipsoidA = 1.67 oblate			EllipsoidA = 2.00 oblate		
	N ( $\times 1000$ )	$t_0/t_1/t_2$ (s)	$s_1/s_2$	N ( $\times 1000$ )	$t_0/t_1/t_2$ (s)	$s_1/s_2$	N ( $\times 1000$ )	$t_0/t_1/t_2$ (s)	$s_1/s_2$	N ( $\times 1000$ )	$t_0/t_1/t_2$ (s)	$s_1/s_2$
1972	17.4	11839/747/88	15.8/135	16.5	-/738/88	-/-	15.9	10706/685/84	15.6/127	15.3	-/656/82	-/-
1973	16.6	10662/711/84	15.0/127	15.8	-/676/84	-/-	14.1	9503/607/75	15.7/127	12.8	-/552/69	-/-
1974	17.0	11745/729/86	16.1/137	17.7	-/759/93	-/-	18.3	-/824/97	-/-	15.6	-/670/83	-/-
1975	15.8	10736/677/80	15.9/134	17.2	-/736/91	-/-	15.4	9700/621/77	15.6/126	14.5	-/623/77	-/-
1976	16.0	11099/687/82	16.2/135	17.3	-/743/92	-/-	16.9	11525/725/90	15.9/128	13.8	-/593/74	-/-
1977	17.6	11935/754/89	15.8/134	16.6	-/712/88	-/-	15.2	8628/670/81	12.9/107	15.4	-/661/82	-/-
1978	16.6	11404/713/85	16.0/134	15.6	-/671/83	-/-	16.0	11055/687/85	16.1/130	13.7	-/589/74	-/-
1979	14.3	9865/613/73	16.1/135	14.4	-/618/77	-/-	15.0	-/672/80	-/-	14.7	-/631/78	-/-
1980	17.0	11626/728/86	16.0/135	16.5	-/709/87	-/-	16.4	11228/704/87	15.9/129	16.8	-/721/89	-/-
1981	16.1	10890/690/82	15.8/133	17.4	-/746/92	-/-	14.5	9925/623/77	15.9/129	14.8	-/637/79	-/-
mean	16.4	11180/705/84	15.9/134	16.5	-/711/88	-/-	15.8	10284/682/83	15.5/125	14.7	-/633/79	-/-

Table 2: Run times and speedup for solar maximum. Michelson Doppler Imager ([MDI](#)) magnetograms were used.

CR	SphericA = 1.00			EllipsoidA = 1.01 oblate			EllipsoidA = 1.67 oblate			EllipsoidA = 2.00 oblate		
	N (×1000)	t <sub>0</sub> /t <sub>1</sub> /t <sub>2</sub> (s)	s <sub>1</sub> /s <sub>2</sub>	N (×1000)	t <sub>0</sub> /t <sub>1</sub> /t <sub>2</sub> (s)	s <sub>1</sub> /s <sub>2</sub>	N (×1000)	t <sub>0</sub> /t <sub>1</sub> /t <sub>2</sub> (s)	s <sub>1</sub> /s <sub>2</sub>	N (×1000)	t <sub>0</sub> /t <sub>1</sub> /t <sub>2</sub> (s)	s <sub>1</sub> /s <sub>2</sub>
2066	17.3	11641/738/87	15.8/134	16.6	11765/712/87	16.5/135	19.1	13281/820/107	16.2/124	17.6	11237/755/92	14.9/122
2067	16.8	10979/718/84	15.3/131	16.6	11264/712/87	15.8/129	18.5	12298/802/119	15.3/103	18.3	12477/785/97	15.9/129
2068	17.4	11352/747/90	15.2/126	18.6	12840/799/97	16.1/132	19.0	12651/858/102	14.7/124	15.8	10807/678/84	15.9/129
2069	15.6	10229/667/78	15.3/131	16.0	10858/687/84	15.8/129	15.9	10640/682/101	15.6/105	15.0	10271/644/80	15.9/128
2070	17.3	10859/739/87	14.7/125	17.4	12131/746/91	16.3/133	16.6	11359/711/106	16.0/107	15.7	10279/674/83	15.3/124
2071	16.9	10703/722/85	14.8/126	15.0	10060/644/79	15.6/127	15.7	10200/674/100	15.1/102	15.8	10807/678/84	15.9/129
2072	16.7	10766/713/84	15.1/128	16.5	11488/708/87	16.2/132	15.6	10453/669/96	15.6/109	15.1	10575/649/80	16.3/132
2073	17.5	11448/747/88	15.3/130	16.3	11049/700/86	15.8/128	15.9	11611/682/101	17.0/115	16.4	11577/704/87	16.4/133
2074	15.6	10219/666/78	15.3/131	15.6	10598/670/82	15.8/129	15.6	10661/669/100	15.9/107	15.0	10877/644/80	16.9/136
2075	17.8	11614/738/89	15.7/130	16.4	11002/704/86	15.6/128	15.7	10494/674/107	15.6/98	14.5	9903/623/77	15.9/129
mean	16.9	10981/720/85	15.3/129	16.5	11306/708/87	16.0/130	16.8	11365/724/104	15.7/109	15.9	10881/683/84	15.9/129

Table 3: Run times and speedup for solar minimum. MDI magnetograms were used.

CR	SphericA = 1.00			EllipsoidA = 1.01 oblate			EllipsoidA = 1.67 oblate			EllipsoidA = 2.00 oblate		
	N ( $\times 1000$ )	$t_0/t_1/t_2$ (s)	$s_1/s_2$	N ( $\times 1000$ )	$t_0/t_1/t_2$ (s)	$s_1/s_2$	N ( $\times 1000$ )	$t_0/t_1/t_2$ (s)	$s_1/s_2$	N ( $\times 1000$ )	$t_0/t_1/t_2$ (s)	$s_1/s_2$
2133	19.3	12831/829/98	15.5/131	18.9	-/811/99	-/-	19.7	13369/844/103	15.8/130	18.3	-/785/97	-/-
2134	18.4	12455/788/94	15.8/133	19.2	-/823/100	-/-	20.0	13610/904/105	15.1/130	21.6	-/925/112	-/-
2135	19.6	13168/841/99	15.7/133	16.9	-/725/90	-/-	15.7	10555/674/84	15.7/126	14.5	-/623/78	-/-
2136	20.9	14086/897/106	15.7/133	16.9	-/725/90	-/-	19.8	13294/849/104	15.7/128	20.0	-/857/105	-/-
2137	18.9	13173/810/96	16.3/137	17.5	-/751/92	-/-	19.3	12038/827/101	14.6/119	17.2	-/738/91	-/-
2138	16.9	11403/724/86	15.8/133	17.0	-/730/90	-/-	15.8	10848/723/84	15.0/129	14.4	-/619/77	-/-
2139	19.4	13033/832/98	15.7/133	17.3	-/742/92	-/-	17.9	12160/768/94	15.8/129	16.2	-/695/86	-/-
2140	19.3	12912/828/98	15.6/132	18.9	-/810/99	-/-	20.0	13730/857/105	16.0/131	20.5	-/879/107	-/-
2141	16.5	11081/708/83	15.7/134	16.6	-/712/88	-/-	18.0	12111/773/95	15.7/127	16.3	-/700/87	-/-
2142	13.8	9401/592/71	15.9/132	13.6	-/585/73	-/-	16.6	11156/732/88	15.2/127	15.4	-/661/82	-/-
mean	18.3	12354/785/93	15.7/133	17.3	-/741/91	-/-	18.3	12287/795/96	15.5/128	17.4	-/748/92	-/-

Table 4: Run times and speedup for solar minimum. Helioseismic and Magnetic Imager ([HMI](#)) magnetograms were used.

CR	SphericA = 1.00 double precision			EllipsoidA = 1.01 prolate			EllipsoidA = 1.67 prolate			EllipsoidA = 2.00 prolate		
	N ( $\times 1000$ )	$t_0/t_1/t_2$ (s)	$s_1/s_2$	N ( $\times 1000$ )	$t_2$ (s)	N ( $\times 1000$ )	$t_2$ (s)	N ( $\times 1000$ )	$t_0/t_2$ (s)	$s_2$		
2066	17.5	11744/-/109	-/108	16.9	89	19.9	103	21.6	14521/113	129		
2067	16.8	11265/775/104	14.5/108	16.4	86	20.1	109	19.7	13449/103	131		
2068	17.4	11586/800/107	14.5/108	16.4	86	19.8	103	20.4	14144/106	133		
2069	15.6	10720/737/97	14.5/111	15.6	83	17.6	92	19.9	13701/104	132		
2070	16.8	11220/-/104	-/108	16.8	88	20.2	105	19.7	13281/103	129		
2071	16.9	11537/826/105	14.0/110	16.8	89	19.5	102	19.7	13658/103	133		
2072	16.7	11209/-/104	-/108	16.8	88	17.9	94	18.7	12645/98	129		
2073	17.5	11753/-/109	-/108	16.2	86	19.5	102	18.8	12941/99	131		
2074	15.6	10456/-/97	-/108	16.2	86	17.9	94	20.7	13950/108	129		
2075	17.9	12120/867/111	14.0/109	16.0	85	19.4	102	20.5	13997//107	131		
mean	16.9	11361/801/105	14.3/109	16.4	87	19.2	101	20.0	13629/104	131		

Table 5: Run times for double precision computing and prolate source surfaces. MDI magnetograms were used.



## BIBLIOGRAPHY

---

- M. H. Acuña, D. Curtis, J. L. Scheifele, C. T. Russell, P. Schroeder, A. Szabo, and J. G. Luhmann. The STEREO/IMPACT magnetic field experiment. *Space Science Reviews*, 136(1-4):203–226, 2008. ISSN 00386308. doi: 10.1007/s11214-007-9259-2.
- M. D. Altschuler and G. Newkirk. Magnetic fields and the structure of the solar corona. *Solar Physics*, 9(1):131–149, sep 1969. ISSN 0038-0938. doi: 10.1007/BF00145734. URL <http://www.springerlink.com/index/10.1007/BF00145734>.
- M. Anderson, T. Appourchaux, F. Auchère, R. Aznar Cuadrado, J. Barbay, F. Baudin, S. Beardsley, K. Bocchialini, B. Borgo, D. Bruzzi, E. Buchlin, G. Burton, V. Büchel, M. Caldwell, S. Caminade, M. Carlsson, W. Curdt, J. Davenne, J. Davila, C. E. DeForest, G. Del Zanna, D. Drummond, J. Dubau, C. Dumesnil, G. Dunn, P. Eccleston, A. Fludra, T. Fredrik, A. Gabriel, A. Giunta, A. Gottwald, D. Griffin, T. Grundy, S. Guest, M. Gyo, M. Haberreiter, V. Hansteen, R. Harrison, D. M. Hassler, S. V. H. Haugan, C. Howe, M. Janvier, R. Klein, S. Koller, T. A. Kucera, D. Koulache, E. Marsch, A. Marshall, G. Marshall, S. A. Matthews, C. McQuirk, S. Meining, C. Mercier, N. Morris, T. Morse, G. Munro, S. Parenti, C. Pastor-Santos, H. Peter, D. Pfiffner, P. Phelan, A. Philippon, A. Richards, K. Rogers, C. Sawyer, P. Schlatter, W. Schmutz, U. Schühle, B. Shaughnessy, S. Sidher, S. K. Solanki, R. Speight, M. Spescha, N. Szwee, C. Tamiatto, L. Teriaca, W. Thompson, I. Tosh, S. Tustain, J.-C. Vial, B. Walls, N. Waltham, R. Wimmer-Schweingruber, S. Woodward, P. Young, A. De Groof, A. Pacros, D. Williams, and D. Müller. The Solar Orbiter SPICE instrument. *Astronomy & Astrophysics*, 642:A14, oct 2020. ISSN 0004-6361. doi: 10.1051/0004-6361/201935574. URL <https://www.aanda.org/10.1051/0004-6361/201935574>.
- S. K. Antiochos, J. A. Linker, R. Lionello, Z. Mikić, V. Titov, and T. H. Zurbuchen. The structure and dynamics of the corona-heliosphere connection. *Space Science Reviews*, 172(1-4):169–185, 2012. ISSN 00386308. doi: 10.1007/s11214-011-9795-7.
- H. W. Babcock. The Solar Magnetograph. *The Astrophysical Journal*, 118:387, nov 1953. ISSN 0004-637X. doi: 10.1086/145767. URL <http://adsabs.harvard.edu/doi/10.1086/145767>.
- S. T. Badman, S. D. Bale, J. C. Martínez Oliveros, O. Panasenco, M. Velli, D. Stansby, J. C. Buitrago-Casas, V. Réville, J. W. Bonnell, A. W. Case, T. Dudok de Wit, K. Goetz, P. R. Harvey, J. C. Kasper, K. E. Korreck, D. E. Larson, R. Livi, R. J. MacDowall, D. M. Malaspina, M. Pulupa, M. L. Stevens, and P. L. Whittlesey. Magnetic Connectivity of the Ecliptic Plane within 0.5 au: Potential Field Source Surface Modeling of the First Parker Solar Probe Encounter. *The Astrophysical Journal Supplement Series*, 246(2):23, 2020. ISSN 1538-4365. doi: 10.3847/1538-4365/ab4da7. URL <http://arxiv.org/abs/1912.02244> <http://dx.doi.org/10.3847/1538-4365/ab4da7>.

- L. Biermann. Kometenschweife und solare Korpuskularstrahlung. *Zeitschrift fur Astrophysik*, 29(274-286):274–286, 1951. URL <http://adsabs.harvard.edu/full/1951ZA.....29..274B>.
- L. Biermann. Solar corpuscular radiation and the interplanetary gas. *The Observatory*, 77:109–110, 1957. URL <http://onlinelibrary.wiley.com/doi/10.1002/cbdv.200490137/abstract><http://adsabs.harvard.edu/full/1957Ob.....77.109B>.
- K. Birkeland. A Possible Connection Between Magnetic and Meteorologic Phenomena. *Monthly Weather Review*, 42(4):211–211, apr 1914. ISSN 0027-0644. doi: 10.1175/1520-0493(1914)42<211a:apcbma>2.0.co;2. URL <http://journals.ametsoc.org/doi/abs/10.1175/1520-0493{281914}{2942}{3C211a}{3AAPCBMA}{3E2.0.C0}{3B2}>.
- W. Burger and M. J. Burge. *Principles of Digital Image Processing*. Undergraduate Topics in Computer Science. Springer London, London, 2009. ISBN 978-1-84800-194-7. doi: 10.1007/978-1-84800-195-4. URL <http://link.springer.com/10.1007/978-1-84800-195-4>.
- H. V. Cane and I. G. Richardson. Interplanetary coronal mass ejections in the near-Earth solar wind during 1996–2002. *Journal of Geophysical Research: Space Physics*, 108(A4), 2003. ISSN 21699402. doi: 10.1029/2002JA009817.
- R. C. Carrington. Description of a Singular Appearance seen in the Sun on September 1, 1859. *Monthly Notices of the Royal Astronomical Society*, 20(1):13–15, nov 1859. ISSN 0035-8711. doi: 10.1093/mnras/20.1.13. URL <https://academic.oup.com/mnras/article-lookup/doi/10.1093/mnras/20.1.13>.
- S. Chapman. On the times of sudden commencement of magnetic storms. *Proceedings of the Physical Society of London*, 30(1):205–214, dec 1917. ISSN 14787814. doi: 10.1088/1478-7814/30/1/317. URL <https://iopscience.iop.org/article/10.1088/1478-7814/30/1/317>.
- S. Chapman. The Viscosity and Thermal Conductivity of a Completely Ionized Gas. *The Astrophysical Journal*, 120:151, jul 1954. ISSN 0004-637X. doi: 10.1086/145890. URL <http://adsabs.harvard.edu/doi/10.1086/145890>.
- S. Chapman and J. Bartels. *Geomagnetism*. Oxford University Press, 1940.
- S. R. Cranmer. Why is the Fast Solar Wind Fast and the Slow Solar Wind Slow? A Survey of Geometrical Models. *Proceedings of Solar Wind 11/SOHO-16: Connecting Sun and Heliosphere*, pages 1–6, jun 2005. URL <http://arxiv.org/abs/astro-ph/0506508>.
- S. R. Cranmer, A. A. van Ballegooijen, and R. J. Edgar. Self-consistent Coronal Heating and Solar Wind Acceleration from Anisotropic Magnetohydrodynamic Turbulence. *The Astrophysical Journal Supplement Series*, 171(2):520–551, aug 2007. ISSN 0067-0049. doi: 10.1086/518001. URL <http://stacks.iop.org/0067-0049/171/i=2/a=520>.

- K. P. Dere, E. Landi, H. E. Mason, B. C. Monsignori Fossi, and P. R. Young. CHIANTI - an atomic database for emission lines. *Astronomy and Astrophysics Supplement Series*, 125(1):149–173, oct 1997. ISSN 0365-0138. doi: 10.1051/aas:1997368. URL <http://aas.aanda.org/10.1051/aas:1997368>.
- H. Drolon. FreeImage webpage, n.d., accessed 2020-10-28. URL <https://freeimage.sourceforge.io/>.
- B. Dunbar. NASA Pioneer 10/11 Mission Summary, 2017. URL <https://web.archive.org/web/20201125102020/https://www.nasa.gov/centers/ames/missions/archive/pioneer.html>.
- T. L. Duvall, J. M. Wilcox, L. Svalgaard, P. H. Scherrer, and P. S. McIntosh. Comparison of H $\alpha$  synoptic charts with the large-scale solar magnetic field as observed at Stanford. *Solar Physics*, 55(1):63–68, nov 1977. ISSN 00380938. doi: 10.1007/BF00150874. URL <http://link.springer.com/10.1007/BF00150874>.
- R. W. Ebert, D. J. McComas, H. A. Elliott, R. J. Forsyth, and J. T. Gosling. Bulk properties of the slow and fast solar wind and interplanetary coronal mass ejections measured by Ulysses: Three polar orbits of observations. *Journal of Geophysical Research: Space Physics*, 114(A1):n/a–n/a, jan 2009. ISSN 01480227. doi: 10.1029/2008JA013631. URL <http://doi.wiley.com/10.1029/2008JA013631>.
- A. S. Eddington. The Envelopes of Comet Morehouse (1908 c). *Monthly Notices of the Royal Astronomical Society*, 70(5):442–458, 1910. ISSN 0035-8711. doi: 10.1093/mnras/70.5.442.
- E. Fehlberg. Low order classical Runge Kutta formulas with stepwise control and their application to some heat transfer problems. Technical Report July, ~, 1969.
- U. Feldman, E. Landi, and N. A. Schwadron. On the sources of fast and slow solar wind. *Journal of Geophysical Research: Space Physics*, 110(A7):A07109, 2005. ISSN 21699402. doi: 10.1029/2004JA010918. URL <http://www.agu.org/pubs/crossref/2005/2004JA010918.shtml>.
- X. Feng, L. Yang, C. Xiang, C. Jiang, X. Ma, S. T. Wu, D. Zhong, and Y. Zhou. Validation of the 3D AMR SIP-CESE Solar Wind Model for Four Carrington Rotations. *Solar Physics*, 279(1):207–229, jul 2012. ISSN 0038-0938. doi: 10.1007/s11207-012-9969-9. URL <http://link.springer.com/10.1007/s11207-012-9969-9>.
- N. J. Fox, M. C. Velli, S. D. Bale, R. Decker, A. Driesman, R. A. Howard, J. C. Kasper, J. Kinnison, M. Kusterer, D. Lario, M. K. Lockwood, D. J. McComas, N. E. Raouafi, and A. Szabo. The Solar Probe Plus Mission: Humanity’s First Visit to Our Star. *Space Science Reviews*, 204(1-4):7–48, dec 2016. ISSN 15729672. doi: 10.1007/s11214-015-0211-6. URL <http://link.springer.com/10.1007/s11214-015-0211-6>.
- M. Fränz and D. Harper. Heliospheric coordinate systems. *Planetary and Space Science*, 50(2):217–233, feb 2002. ISSN 00320633. doi: 10.1016/S0032-0633(01)00119-2. URL <https://linkinghub.elsevier.com/retrieve/pii/S0032063301001192>.

- K. Fujiki, M. Hirano, M. Kojima, M. Tokumaru, D. Baba, M. Yamashita, and K. Hakamada. Relation between solar wind velocity and properties of its source region. *Advances in Space Research*, 35(12):2185–2188, jan 2005. ISSN 02731177. doi: 10.1016/j.asr.2005.05.057. URL <https://linkinghub.elsevier.com/retrieve/pii/S0273117705006587>.
- A. B. Galvin, L. M. Kistler, M. A. Popecki, C. J. Farrugia, K. D. Simunac, L. Ellis, E. Möbius, M. A. Lee, M. Boehm, J. Carroll, A. Crawshaw, M. Conti, P. Demaine, S. Ellis, J. A. Gaidos, J. Googins, M. Granoff, A. Gustafson, D. Heirtzler, B. King, U. Knauss, J. Levasseur, S. Longworth, K. Singer, S. Turco, P. Vachon, M. Vosbury, M. Widholm, L. M. Blush, R. Karrer, P. Bochsler, H. Daoudi, A. Etter, J. Fischer, J. Jost, A. Opitz, M. Sigrist, P. Wurz, B. Klecker, M. Ertl, E. Seidenschwang, R. F. Wimmer-Schweingruber, M. Koeten, B. Thompson, and D. Steinfeld. The plasma and suprathermal ion composition (PLASTIC) investigation on the STEREO observatories. *Space Science Reviews*, 136(1-4):437–486, apr 2008. ISSN 00386308. doi: 10.1007/s11214-007-9296-x. URL <http://link.springer.com/10.1007/s11214-007-9296-x>.
- B. Gilding. A numerical grid generation technique. *Computers & Fluids*, 16(1):47–58, jan 1988. ISSN 00457930. doi: 10.1016/0045-7930(88)90038-2. URL <https://linkinghub.elsevier.com/retrieve/pii/0045793088900382>.
- G. Gloeckler, J. Cain, F. M. Ipavich, E. O. Tums, P. Bedini, L. A. Fisk, T. H. Zurbuchen, P. Bochsler, J. Fischer, R. F. Wimmer-Schweingruber, J. Geiss, and R. Kallenbach. Investigation of the composition of solar and interstellar matter using solar wind and pickup ion measurements with swics and swims on the ace spacecraft. *Space Science Reviews*, 86(1-4):497–539, 1998. ISSN 00386308. doi: 10.1007/978-94-011-4762-0\_18.
- P. Hackenberg, E. Marsch, and G. Mann. On the origin of the fast solar wind in polar coronal funnels. *Astonomy & Astrophysics*, 360(3):1139–1147, 2000.
- J. W. Harvey, F. Hill, R. P. Hubbard, J. R. Kennedy, J. W. Leibacher, J. A. Pintar, P. A. Gilman, R. W. Noyes, A. M. Title, J. Toomre, R. K. Ulrich, A. Bhatnagar, J. A. Kennewell, W. Marquette, J. Patron, O. Saa, and E. Yasukawa. The Global Oscillation Network Group (GONG) Project. *Science*, 272(5266):1284–1286, may 1996. ISSN 0036-8075. doi: 10.1126/science.272.5266.1284. URL <https://www.sciencemag.org/lookup/doi/10.1126/science.272.5266.1284>.
- R. L. Heacock. The Voyager Spacecraft. *Proceedings of the Institution of Mechanical Engineers*, 194(1):211–224, jun 1980. ISSN 0020-3483. doi: 10.1243/PIME\_PROC\_1980\_194\_026\_02. URL [http://journals.sagepub.com/doi/10.1243/PIME\\_{ }PROC\\_{ }1980\\_{ }194\\_{ }026\\_{ }02](http://journals.sagepub.com/doi/10.1243/PIME_{ }PROC_{ }1980_{ }194_{ }026_{ }02).
- V. Heidrich-Meisner and R. F. Wimmer-Schweingruber. Solar Wind Classification Via k -Means Clustering Algorithm. In *Machine Learning Techniques for Space Weather*, pages 397–424. Elsevier, 2018. doi: 10.1016/B978-0-12-811788-0.00016-0. URL <https://linkinghub.elsevier.com/retrieve/pii/B9780128117880000160>.

- V. Heidrich-Meisner, T. Peleikis, M. Kruse, L. Berger, and R. Wimmer-Schweingruber. Observations of high and low Fe charge states in individual solar wind streams with coronal-hole origin. *Astronomy and Astrophysics*, 593: 1–9, 2016. ISSN 14320746. doi: 10.1051/0004-6361/201527998.
- V. Heidrich-Meisner, T. Peleikis, M. Kruse, L. Berger, and R. F. Wimmer-Schweingruber. Evolution of an equatorial coronal hole structure and the released coronal hole wind stream: Carrington rotations 2039 to 2050. *Astronomy and Astrophysics*, 603, 2017. ISSN 14320746. doi: 10.1051/0004-6361/201730574.
- P. Hick, B. V. Jackson, S. Rappoport, G. Woan, G. Slater, K. Strong, and Y. Uchida. Synoptic IPS and Yohkoh soft X-ray observations. *Geophysical Research Letters*, 22(5):643–646, mar 1995. ISSN 19448007. doi: 10.1029/95GL00011. URL <http://doi.wiley.com/10.1029/95GL00011>.
- J. Hoeksema. WSO magnetograms, n.d., accessed 2020-10-27, a. URL <http://wso.stanford.edu/synoptic1.html>.
- J. Hoeksema. Wilcox Solar Observatory Web Page, n.d., accessed 2020-10-27, b. URL <http://wso.stanford.edu>.
- J. Hoeksema and P. Scherrer. The Solar Magnetic Field Since 1976. Technical report, UAG-94, WDC-A, 1986.
- J. T. Hoeksema. *Structure and Evolution of the Large Scale Solar and Heliospheric Magnetic Field*. PhD thesis, 1984.
- A. J. Hundhausen. *Coronal Expansion and Solar Wind*, volume 5 of *Physics and Chemistry in Space*. Springer Berlin Heidelberg, Berlin, Heidelberg, 1972. ISBN 978-3-642-65416-9. doi: 10.1007/978-3-642-65414-5. URL <http://link.springer.com/10.1007/978-3-642-65414-5>.
- ISO. *ISO\IEC 14882:2017 Information technology — Programming languages — C++*. Fifth edition, 2017. URL <https://www.iso.org/standard/68564.html>.
- L. K. Jian, C. T. Russell, J. G. Luhmann, and A. B. Galvin. STEREO Observations of Interplanetary Coronal Mass Ejections in 2007–2016. *The Astrophysical Journal*, 855(2):114, mar 2018. ISSN 1538-4357. doi: 10.3847/1538-4357/aab189. URL <http://dx.doi.org/10.3847/1538-4357/aab189> <http://stacks.iop.org/0004-637X/855/i=2/a=114?key=crossref>. e96df4290d9efde47e1adead1eb67560.
- M. L. Kaiser, T. A. Kucera, J. M. Davila, O. C. Cyr, M. Guhathakurta, and E. Christian. The STEREO mission: An introduction. *Space Science Reviews*, 136(1-4):5–16, apr 2008. ISSN 00386308. doi: 10.1007/s11214-007-9277-0. URL <http://link.springer.com/10.1007/s11214-007-9277-0>.
- J. C. Kasper, A. J. Lazarus, and S. P. Gary. Hot Solar-Wind Helium: Direct Evidence for Local Heating by Alfvén-Cyclotron Dissipation. *Physical Review Letters*, 101(26):261103, dec 2008. ISSN 0031-9007. doi: 10.1103/PhysRevLett.101.261103. URL <https://link.aps.org/doi/10.1103/PhysRevLett.101.261103>.

- J. H. King. Availability of IMP-7 And IMP-8 data for the IMS period. In *The IMS Source Book: Guide to the International Magnetospheric Study Data Analysis*, pages 10–20. American Geophysical Union, Washington, D. C., 1982. doi: 10.1029/SP020p0010. URL <http://doi.wiley.com/10.1029/SP020p0010>.
- C. E. Kohlhase and P. A. Penzo. Voyager mission description. *Space science reviews*, 21(2):77–101, 1977.
- A. S. Krieger, A. F. Timothy, and E. C. Roelof. A coronal hole and its identification as the source of a high velocity solar wind stream. *Solar Physics*, 29(2):505–525, 1973. ISSN 00380938. doi: 10.1007/BF00150828.
- M. A. Kruse, V. Heidrich-Meisner, and R. Wimmer-Schweingruber. Evaluation of a potential field source surface model with elliptical source surfaces via ballistic backmapping of in situ spacecraft data. *Astronomy & Astrophysics*, nov 2020a. ISSN 0004-6361. doi: 10.1051/0004-6361/202039120. URL <https://www.aanda.org/10.1051/0004-6361/202039120>.
- M. A. Kruse, V. Heidrich-Meisner, R. F. Wimmer-Schweingruber, and M. Hauptmann. An elliptic expansion of the potential field source surface model. *Astronomy & Astrophysics*, 638:A109, jun 2020b. ISSN 0004-6361. doi: 10.1051/0004-6361/202037734. URL <https://www.aanda.org/10.1051/0004-6361/202037734>.
- E. Landi, R. L. Alexander, J. R. Gruesbeck, J. A. Gilbert, S. T. Lepri, W. B. Manchester, and T. H. Zurbuchen. Carbon Ionization Stages as a Diagnostic of the Solar Wind. *The Astrophysical Journal*, 744(2):100, jan 2012. ISSN 0004-637X. doi: 10.1088/0004-637X/744/2/100. URL <https://iopscience.iop.org/article/10.1088/0004-637X/744/2/100>.
- L. E. Lasher. Pioneer 10 and 11 missions. In *Encyclopedia of Planetary Science*, pages 579–582. Kluwer Academic Publishers, Dordrecht, 1997. doi: 10.1007/1-4020-4520-4\_306. URL [http://link.springer.com/10.1007/1-4020-4520-4\\_{ }306](http://link.springer.com/10.1007/1-4020-4520-4_{ }306).
- C. O. Lee, J. G. Luhmann, J. T. Hoeksema, X. Sun, C. N. Arge, and I. de Pater. Coronal Field Opens at Lower Height During the Solar Cycles 22 and 23 Minimum Periods: IMF Comparison Suggests the Source Surface Should Be Lowered. *Solar Physics*, 269(2):367–388, 2011. ISSN 00380938. doi: 10.1007/s11207-010-9699-9.
- S. T. Lepri, E. Landi, and T. H. Zurbuchen. Solar Wind Heavy Ions over Solar Cycle 23: ACE/SWICS Measurements. *The Astrophysical Journal*, 768(1):94, apr 2013. ISSN 0004-637X. doi: 10.1088/0004-637X/768/1/94. URL <https://iopscience.iop.org/article/10.1088/0004-637X/768/1/94>.
- R. H. Levine, M. Schulz, and E. N. Frazier. Simulation of the magnetic structure of the inner heliosphere by means of a non-spherical source surface. *Solar Physics*, 77(1-2):363–392, apr 1982. ISSN 00380938. doi: 10.1007/BF00156118. URL <http://link.springer.com/10.1007/BF00156118>.

- Z.-F. Li, S.-H. Hu, X. Cheng, and M.-D. Ding. Synthesising solar radio images from Atmospheric Imaging Assembly extreme-ultraviolet data. *Research in Astronomy and Astrophysics*, 20(2):18, 2020.
- P. C. Liewer, M. Neugebauer, and T. Zurbuchen. Characteristics of active-region sources of solar wind near solar maximum. *Solar Physics*, 223(1-2):209–229, sep 2004. ISSN 0038-0938. doi: 10.1007/s11207-004-1105-z. URL <http://link.springer.com/10.1007/s11207-004-1105-z>.
- J. A. Linker, Z. Mikić, D. A. Biesecker, R. J. Forsyth, S. E. Gibson, A. J. Lazarus, A. Lecinski, P. Riley, A. Szabo, and B. J. Thompson. Magnetohydrodynamic modeling of the solar corona during Whole Sun Month. *Journal of Geophysical Research: Space Physics*, 104(A5):9809–9830, may 1999. ISSN 01480227. doi: 10.1029/1998JA900159. URL <http://doi.wiley.com/10.1029/1998JA900159>.
- R. Lionello, J. A. Linker, and Z. Mikić. Multispectral Emission of the Sun During the First Whole Sun Month: Magnetohydrodynamic Simulations. *The Astrophysical Journal*, 690(1):902–912, jan 2009. ISSN 0004-637X. doi: 10.1088/0004-637X/690/1/902. URL <https://iopscience.iop.org/article/10.1088/0004-637X/690/1/902>.
- S. Liu and J. T. Su. Multi-channel observations of plasma outflows and the associated small-scale magnetic field cancellations on the edges of an active region. *Astrophysics and Space Science*, 351(2):417–425, jun 2014. ISSN 0004-640X. doi: 10.1007/s10509-014-1853-7. URL <http://link.springer.com/10.1007/s10509-014-1853-7>.
- W. C. Livingston, J. Harvey, A. K. Pierce, D. Schrage, B. Gillespie, J. Simmons, and C. Slaughter. Kitt Peak 60-cm vacuum telescope. *Applied Optics*, 15(1):33, jan 1976. ISSN 0003-6935. doi: 10.1364/AO.15.000033. URL <https://www.osapublishing.org/abstract.cfm?URI=ao-15-1-33>.
- J. G. Luhmann, D. W. Curtis, P. Schroeder, J. McCauley, R. P. Lin, D. E. Larson, S. D. Bale, J. A. Sauvaud, C. Aoustin, R. A. Mewaldt, A. C. Cummings, E. C. Stone, A. J. Davis, W. R. Cook, B. Kecman, M. E. Wiedenbeck, T. Von Rosenvinge, M. H. Acuna, L. S. Reichenthal, S. Shuman, K. A. Wortman, D. V. Reames, R. Mueller-Mellin, H. Kunow, G. M. Mason, P. Walpole, A. Korth, T. R. Sanderson, C. T. Russell, and J. T. Gosling. STEREO IMPACT investigation goals, measurements, and data products overview. *Space Science Reviews*, 136(1-4):117–184, apr 2008. ISSN 00386308. doi: 10.1007/s11214-007-9170-x. URL <http://link.springer.com/10.1007/s11214-007-9170-x>.
- D. H. Mackay and A. R. Yeates. The Sun’s global photospheric and coronal magnetic fields: Observations and models. *Living Reviews in Solar Physics*, 9, 2012. ISSN 16144961. doi: 10.12942/lrsp-2012-6.
- E. Marsch and A. K. Richter. Distribution of solar wind angular momentum between particles and magnetic field: Inferences about the Alfvén critical point from Helios observations. *Journal of Geophysical Research*, 89(A7):5386, 1984. ISSN 0148-0227. doi: 10.1029/JA089iA07p05386. URL <http://doi.wiley.com/10.1029/JA089iA07p05386>.

- E. Marsch, H. Tian, J. Sun, W. Curdt, and T. Wiegemann. Plasma Flows Guided by Strong Magnetic Fields in the Solar Corona. *The Astrophysical Journal*, 685(2):1262–1269, oct 2008. ISSN 0004-637X. doi: 10.1086/591038. URL <https://iopscience.iop.org/article/10.1086/591038>.
- R. G. Marsden, K. Wenzel, and E. J. Smith. The Ulysses Mission. *Astronomy & Astrophysics Supplement Series*, 92, 1992. doi: 10.1007/978-94-009-4612-5\_54. URL [http://link.springer.com/10.1007/978-94-009-4612-5\\_{\\_}54](http://link.springer.com/10.1007/978-94-009-4612-5_{_}54).
- D. J. McComas, S. J. Bame, P. Barker, W. C. Feldman, J. L. Phillips, P. Riley, and J. W. Griffee. Solar wind electron proton alpha monitor (SWEPAM) for the advanced composition explorer. *Space Science Reviews*, 86(1-4):563–612, 1998a. ISSN 00386308. doi: 10.1007/978-94-011-4762-0\_20.
- D. J. McComas, S. J. Bame, B. L. Barraclough, W. C. Feldman, H. O. Funsten, J. T. Gosling, P. Riley, R. Skoug, A. Balogh, R. Forsyth, B. E. Goldstein, and M. Neugebauer. Ulysses' return to the slow solar wind. *Geophysical Research Letters*, 25(1):1–4, 1998b. ISSN 00948276. doi: 10.1029/97GL03444.
- D. J. McComas, P. Riley, J. T. Gosling, A. Balogh, and R. Forsyth. Ulysses' rapid crossing of the polar coronal hole boundary. *Journal of Geophysical Research: Space Physics*, 103(A2):1955–1967, feb 1998c. ISSN 2169-9402. doi: 10.1029/97ja01459. URL <http://doi.wiley.com/10.1029/97JA01459>.
- D. J. McComas, H. A. Elliott, J. T. Gosling, D. B. Reisenfeld, R. M. Skoug, B. E. Goldstein, M. Neugebauer, and A. Balogh. Ulysses' second fast-latitude scan: Complexity near solar maximum and the reformation of polar coronal holes. *Geophysical Research Letters*, 29(9):4-1–4-4, may 2002. ISSN 00948276. doi: 10.1029/2001GL014164. URL <http://doi.wiley.com/10.1029/2001GL014164>.
- D. J. McComas, R. W. Ebert, H. A. Elliott, B. E. Goldstein, J. T. Gosling, N. A. Schwadron, and R. M. Skoug. Weaker solar wind from the polar coronal holes and the whole Sun. *Geophysical Research Letters*, 35(18):L18103, sep 2008. ISSN 0094-8276. doi: 10.1029/2008GL034896. URL <http://doi.wiley.com/10.1029/2008GL034896>.
- D. Müller, R. G. Marsden, O. C. St. Cyr, and H. R. Gilbert. Solar Orbiter: Exploring the Sun-Heliosphere Connection. *Solar Physics*, 285(1-2):25–70, jul 2013. ISSN 00380938. doi: 10.1007/s11207-012-0085-7. URL <http://link.springer.com/10.1007/s11207-012-0085-7>.
- M. Neugebauer and C. W. Snyder. Solar plasma experiment. *Science*, 138(3545):1095–1097, dec 1962. ISSN 00368075. doi: 10.1126/science.138.3545.1095-a. URL <https://www.sciencemag.org/lookup/doi/10.1126/science.138.3545.1095-a>.
- M. Neugebauer, R. J. Forsyth, a. B. Galvin, K. L. Harvey, J. T. Hoeksema, a. J. Lazarus, R. P. Lepping, J. a. Linker, Z. Mikic, J. T. Steinberg, R. von Steiger, Y.-M. Wang, and R. F. Wimmer-Schweingruber. Spatial structure of the solar wind and comparisons with solar data and models. *Journal of Geophysical Research*, 103(A7):14587, 1998. ISSN 0148-0227. doi: 10.1029/98JA00798.

- M. Neugebauer, P. C. Liewer, E. J. Smith, R. M. Skoug, and T. H. Zurbuchen. Sources of the solar wind at solar activity maximum. *Journal of Geophysical Research: Space Physics*, 107(A12):SSH 13–1–SSH 13–15, dec 2002. ISSN 01480227. doi: 10.1029/2001JA000306. URL <http://doi.wiley.com/10.1029/2001JA000306>.
- G. Newkirk. Structure of the Solar Corona. *Annual Review of Astronomy and Astrophysics*, 5(1):213–266, sep 1967. ISSN 0066-4146. doi: 10.1146/annurev.aa.05.090167.001241. URL <http://www.annualreviews.org/doi/10.1146/annurev.aa.05.090167.001241>.
- J. T. Nolte and E. C. Roelof. Large-scale structure of the interplanetary medium. *Solar Physics*, 33, 1973. doi: <https://doi.org/10.1007/BF00152435>.
- NVIDIA, P. Vingelmann, and F. H. P. Fitzek. CUDA, release: 10.2.89, 2020. URL <https://developer.nvidia.com/cuda-toolkit>.
- O. Panasenco and M. Velli. Coronal pseudostreamers: Source of fast or slow solar wind? pages 50–53, 2013. doi: 10.1063/1.4810987. URL <http://aip.scitation.org/doi/abs/10.1063/1.4810987>.
- O. Panasenco, M. Velli, R. D’Amicis, C. Shi, V. Réville, S. D. Bale, S. T. Badman, J. Kasper, K. Korreck, J. W. Bonnell, T. D. de Wit, K. Goetz, P. R. Harvey, R. J. MacDowall, D. M. Malaspina, M. Pulupa, A. W. Case, D. Larson, R. Livi, M. Stevens, and P. Whittlesey. Exploring Solar Wind Origins and Connecting Plasma Flows from the Parker Solar Probe to 1 au: Nonspherical Source Surface and Alfvénic Fluctuations. *The Astrophysical Journal Supplement Series*, 246(2):54, feb 2020. ISSN 1538-4365. doi: 10.3847/1538-4365/ab61f4. URL <https://iopscience.iop.org/article/10.3847/1538-4365/ab61f4>.
- E. N. Parker. Dynamics of the Interplanetary Gas and Magnetic Fields. *The Astrophysical Journal*, 128:664, nov 1958. ISSN 0004-637X. doi: 10.1086/146579. URL <http://adsabs.harvard.edu/doi/10.1086/146579>.
- K. I. Paularena and J. H. King. NASA’s IMP 8 Spacecraft. In *Interball in the ISTP Program*, pages 145–154. Springer Netherlands, Dordrecht, 1999. doi: 10.1007/978-94-011-4487-2\_11. URL [http://link.springer.com/10.1007/978-94-011-4487-2\\_{\\_}11](http://link.springer.com/10.1007/978-94-011-4487-2_{_}11).
- T. Peleikis, M. Kruse, L. Berger, and R. Wimmer-Schweingruber. Origin of the solar wind: A novel approach to link in situ and remote observations: A study for SPICE and SWA on the upcoming Solar Orbiter mission. *Astronomy and Astrophysics*, 602:A24, 2017. ISSN 14320746. doi: 10.1051/0004-6361/201629727. URL <http://www.aanda.org/10.1051/0004-6361/201629727>.
- M. M. P. Petrou and C. Petrou. *Image Processing: The Fundamentals*. John Wiley & Sons Ltd, 2010.
- V. I. Piercy. The Lamé and Metric Coefficients for Curvilinear Coordinates in R, 2007. URL <http://odessa.phy.sdsmt.edu/{~}andre/homework/Phys481/Lame.pdf>.

- R. F. Pinto and A. P. Rouillard. A Multiple Flux-tube Solar Wind Model. *The Astrophysical Journal*, 838(2):89, 2017. ISSN 1538-4357. doi: 10.3847/1538-4357/aa6398.
- R. H. Pletcher, J. C. Tannenhill, and D. Anderson. *Computational Fluid Mechanics and Heat Transfer*. Taylor and Francis Group, 2012. ISBN 9781591690375.
- G. W. Pneuman. Some general properties of helmeted coronal structures. *Solar Physics*, 3(4):578–597, apr 1968. ISSN 0038-0938. doi: 10.1007/BF00151939. URL <http://link.springer.com/10.1007/BF00151939>.
- G. W. Pneuman and R. A. Kopp. Gas-magnetic field interactions in the solar corona. *Solar Physics*, 18(2):258–270, jun 1971. ISSN 0038-0938. doi: 10.1007/BF00145940. URL <http://www.springerlink.com/index/10.1007/BF00145940>.
- B. Poduval and X. P. Zhao. Validating solar wind prediction using the current sheet source surface model. *Astrophysical Journal Letters*, 782(2):L22, feb 2014. ISSN 20418205. doi: 10.1088/2041-8205/782/2/L22. URL <http://stacks.iop.org/2041-8205/782/i=2/a=L22?key=crossref.54e3a72e4c8a168a4e34b83505ca2b97>.
- H. Porsche. HELIOS mission: Mission objectives, mission verification, selected results. In *Solar System and its Exploration*, volume 164, 1981.
- M. P. Rast. The Scales of Granulation, Mesogranulation, and Supergranulation. *The Astrophysical Journal*, 597(2):1200–1210, nov 2003. doi: 10.1086/381221. URL <https://doi.org/10.1086/381221>.
- P. Riley, J. A. Linker, Z. Mikić, R. Lionello, S. A. Ledvina, and J. G. Luhmann. A Comparison between Global Solar Magnetohydrodynamic and Potential Field Source Surface Model Results. *The Astrophysical Journal*, 653(2):1510–1516, dec 2006. ISSN 0004-637X. doi: 10.1086/508565. URL <http://stacks.iop.org/0004-637X/653/i=2/a=1510>.
- C. Runge. Ueber die numerische Auflösung von Differentialgleichungen. *Mathematische Annalen*, 46(2):167–178, 1895. ISSN 00255831. doi: 10.1007/BF01446807.
- D. M. Rust. Magnetic Fields in Quiescent Solar Prominences. II. Photospheric Sources. *The Astrophysical Journal*, 160:315, apr 1970. ISSN 0004-637X. doi: 10.1086/150429. URL <http://adsabs.harvard.edu/doi/10.1086/150429>.
- K. Schatten. Current sheet magnetic model for the solar corona. *Cosmical Electrodynamics*, 2:232, 1971. URL [https://ntrs.nasa.gov/search.jsp?R=19730002037%0Ahttp://www.osti.gov/energycitations/product.biblio.jsp?osti{\\_}id=4722444](https://ntrs.nasa.gov/search.jsp?R=19730002037%0Ahttp://www.osti.gov/energycitations/product.biblio.jsp?osti{_}id=4722444).
- K. H. Schatten. *Current Sheet Magnetic Model for the Solar Corona*, volume 308, page 44. 1972.
- K. H. Schatten, J. M. Wilcox, and N. F. Ness. A model of interplanetary and coronal magnetic fields. *Solar Physics*, 6(3):442–455, mar 1969. ISSN 0038-0938. doi: 10.1007/BF00146478. URL <http://www.springerlink.com/index/10.1007/BF00146478>.

- P. H. Scherrer, J. M. Wilcox, L. Svalgaard, T. L. Duvall, P. H. Dittmer, and E. K. Gustafson. The mean magnetic field of the Sun: Observations at Stanford. *Solar Physics*, 54(2):353–361, oct 1977. ISSN 0038-0938. doi: 10.1007/BF00159925. URL <http://link.springer.com/10.1007/BF00159925>.
- P. H. Scherrer, R. S. Bogart, R. I. Bush, J. T. Hoeksema, A. G. Kosovichev, J. Schou, W. Rosenberg, L. Springer, T. D. Tarbell, A. Title, C. J. Wolfson, and I. Zayer. The Solar Oscillations Investigation - Michelson Doppler Imager. *Solar Physics*, 162 (1-2):129–188, 1995. ISSN 00380938. doi: 10.1007/BF00733429.
- P. H. Scherrer, J. Schou, R. I. Bush, A. G. Kosovichev, R. S. Bogart, J. T. Hoeksema, Y. Liu, T. L. Duvall, J. Zhao, A. M. Title, C. J. Schrijver, T. D. Tarbell, and S. Tomczyk. The Helioseismic and Magnetic Imager (HMI) Investigation for the Solar Dynamics Observatory (SDO). *Solar Physics*, 275(1-2):207–227, jan 2012. ISSN 0038-0938. doi: 10.1007/s11207-011-9834-2. URL <http://link.springer.com/10.1007/s11207-011-9834-2>.
- M. Schulz. Non-spherical source-surface model of the heliosphere: A scalar formulation. *Annales Geophysicae*, 15(11):1379–1387, 1997. ISSN 09927689. doi: 10.1007/s00585-997-1379-1.
- M. Schulz, E. N. Frazier, and D. J. Boucher. Coronal magnetic-field model with non-spherical source surface. *Solar Physics*, 60(1):83–104, nov 1978. ISSN 0038-0938. doi: 10.1007/BF00152334. URL <http://www.springerlink.com/index/10.1007/BF00152334.html>.
- R. Schwenn and E. Marsch, editors. *Physics of the Inner Heliosphere I*. Springer Berlin Heidelberg, Berlin, Heidelberg, 1990. ISBN 978-3-642-75363-3. doi: 10.1007/978-3-642-75361-9. URL <http://link.springer.com/10.1007/978-3-642-75361-9>.
- P. K. Seidelmann. *Explanatory Supplement to the Astronomical Almanac. A revision to the Explanatory Supplement to the Astronomical Ephemeris and the American Ephemeris and Nautical Almanac*. University Science Books, 1992. ISBN 0-935702-68-7.
- K. Shoemake. Animating rotation with quaternion curves. In *Proceedings of the 12th annual conference on Computer graphics and interactive techniques - SIGGRAPH '85*, volume 19, pages 245–254, New York, New York, USA, 1985. ACM Press. ISBN 0897911660. doi: 10.1145/325334.325242. URL <http://portal.acm.org/citation.cfm?doid=325334.325242>.
- C. W. Smith, J. L'Heureux, N. F. Ness, M. H. Acuña, L. F. Burlaga, and J. Scheifele. The ace magnetic fields experiment. *Space Science Reviews*, 86(1-4):613–632, 1998. ISSN 00386308. doi: 10.1023/A:1005092216668.
- W. Smith. NASA History Division, Explorer Series of Spacecraft, 2006. URL <https://web.archive.org/web/20201021085332/https://history.nasa.gov/explorer.html>.

- M. Stakhiv, E. Landi, S. T. Lepri, R. Oran, and T. H. Zurbuchen. On the Origin of Mid-Latitude Fast Wind: Challenging the Two-State Solar Wind Paradigm. *The Astrophysical Journal*, 801(2):100, mar 2015. ISSN 1538-4357. doi: 10.1088/0004-637X/801/2/100. URL <https://iopscience.iop.org/article/10.1088/0004-637X/801/2/100>.
- E. C. Stone, A. M. Frandsen, R. A. Mewaldt, E. R. Christian, D. Margolies, J. F. Ormes, and F. Snow. The advanced composition explorer. *Space Science Reviews*, 86(1-4):1–22, 1998. ISSN 00386308. doi: 10.1007/978-94-011-4762-0\_1.
- L. Strachan, R. Suleiman, A. V. Panasyuk, D. A. Biesecker, and J. L. Kohl. Empirical Densities, Kinetic Temperatures, and Outflow Velocities in the Equatorial Streamer Belt at Solar Minimum. *The Astrophysical Journal*, 571(2):1008–1014, jun 2002. ISSN 0004-637X. doi: 10.1086/339984. URL <https://iopscience.iop.org/article/10.1086/339984>.
- X. Sun. Notes on PFSS Extrapolation, 2009. URL <http://wso.stanford.edu/words/pfss.pdf>.
- A. Szabo, D. Larson, P. Whittlesey, M. L. Stevens, B. Lavraud, T. Phan, S. Wallace, S. I. Jones-Mecholsky, C. N. Arge, S. T. Badman, D. Odstrcil, N. Pogorelov, T. Kim, P. Riley, C. J. Henney, S. D. Bale, J. W. Bonnell, A. W. Case, T. Dudok de Wit, K. Goetz, P. Harvey, J. C. Kasper, K. E. Korreck, A. Koval, R. Livi, R. J. MacDowall, D. M. Malaspina, and M. Pulupa. The Heliospheric Current Sheet in the Inner Heliosphere Observed by the Parker Solar Probe. *The Astrophysical Journal Supplement Series*, 246(2):47, feb 2020. ISSN 1538-4365. doi: 10.3847/1538-4365/ab5dac. URL <https://iopscience.iop.org/article/10.3847/1538-4365/ab5dac>.
- J. F. Thompson, Z. U. A. Warsi, and C. W. Mastin. *Numerical Grid Generation: Foundations and Applications*. Elsevier North-Holland, Inc., 1985.
- H. Tian, S. W. McIntosh, S. R. Habbal, and J. He. Observation of high-speed outflow on plume-like structures of the quiet sun and coronal holes with Solar Dynamics Observatory / Atmospheric Imaging Assembly. *The Astrophysical Journal*, 736(2):130, aug 2011. ISSN 0004-637X. doi: 10.1088/0004-637X/736/2/130. URL <https://iopscience.iop.org/article/10.1088/0004-637X/736/2/130>.
- G. Tóth, B. Van Der Holst, and Z. Huang. Obtaining potential field solutions with spherical harmonics and finite differences. *Astrophysical Journal*, 732(2), 2011. ISSN 15384357. doi: 10.1088/0004-637X/732/2/102. URL <http://arxiv.org/abs/1104.5672>.
- C.-Y. Tu, C. Zhou, E. Marsch, L.-D. Xia, L. Zhao, J.-X. Wang, and K. Wilhelm. Solar wind origin in coronal funnels. *Science (New York, N.Y.)*, 308(5721):519–23, apr 2005. ISSN 1095-9203. doi: 10.1126/science.1109447. URL <http://www.ncbi.nlm.nih.gov/pubmed/15845846>.
- K. Underwood. FPGAs vs. CPUs: Trends in peak floating-point performance. *ACM/SIGDA International Symposium on Field Programmable Gate Arrays - FPGA*, 12:171–180, 2004.

- D. Verscharen, K. G. Klein, and B. A. Maruca. The multi-scale nature of the solar wind. *Living Reviews in Solar Physics*, 16(1):5, dec 2019. ISSN 16144961. doi: 10.1007/s41116-019-0021-0. URL <http://link.springer.com/10.1007/s41116-019-0021-0>.
- R. von Steiger, N. A. Schwadron, L. A. Fisk, J. Geiss, G. Gloeckler, S. Hefti, B. Wilken, R. R. Wimmer-Schweingruber, and T. H. Zurbuchen. Composition of quasi-stationary solar wind flows from Ulysses/Solar Wind Ion Composition Spectrometer. *Journal of Geophysical Research: Space Physics*, 105(A12):27217–27238, dec 2000. ISSN 01480227. doi: 10.1029/1999JA000358. URL <http://doi.wiley.com/10.1029/1999JA000358>.
- Y.-M. Wang and J. Sheeley, N. R. Solar wind speed and coronal flux-tube expansion. *The Astrophysical Journal*, 355:726, jun 1990. ISSN 0004-637X. doi: 10.1086/168805. URL <http://adsabs.harvard.edu/doi/10.1086/168805>.
- T. Wiegmann and T. Sakurai. Solar force-free magnetic fields. *Living Reviews in Solar Physics*, 9, 2012. ISSN 16144961. doi: 10.12942/lrsp-2012-5.
- J. Wilcox. The interplanetary magnetic field. Solar origin and terrestrial effects. *Space Science Reviews*, 8(2), apr 1968. ISSN 0038-6308. doi: 10.1007/BF00227565. URL <http://link.springer.com/10.1007/BF00227565>.
- R. Woo and J. M. Martin. Source regions of the slow solar wind. *Geophysical Research Letters*, 24(20):2535–2538, oct 1997. ISSN 00948276. doi: 10.1029/97GL02598. URL <http://doi.wiley.com/10.1029/97GL02598>.
- R. Woo, S. R. Habbal, and U. Feldman. Role of Closed Magnetic Fields in Solar Wind Flow. *The Astrophysical Journal*, 612(2):1171–1174, sep 2004. ISSN 0004-637X. doi: 10.1086/422799. URL <https://iopscience.iop.org/article/10.1086/422799>.
- F. Xu and J. E. Borovsky. A new four-plasma categorization scheme for the solar wind. *Journal of Geophysical Research: Space Physics*, 120(1):70–100, jan 2015. ISSN 21699380. doi: 10.1002/2014JA020412. URL <http://doi.wiley.com/10.1002/2014JA020412>.
- L. Zhao and L. Fisk. Comparison of Two Solar Minima: Narrower Streamer Stalk Region and Conserved Open Magnetic Flux in the Region Outside of Streamer Stalk. mar 2010. URL <http://arxiv.org/abs/1003.4336>.
- L. Zhao, T. H. Zurbuchen, and L. A. Fisk. Global distribution of the solar wind during solar cycle 23: ACE observations. *Geophysical Research Letters*, 36(14):L14104, jul 2009. ISSN 0094-8276. doi: 10.1029/2009GL039181. URL <http://doi.wiley.com/10.1029/2009GL039181>.
- L. Zhao, E. Landi, T. H. Zurbuchen, L. A. Fisk, and S. T. Lepri. The evolution of 1 Au equatorial solar wind and its association with the morphology of the heliospheric current sheet from solar cycles 23 to 24. *Astrophysical Journal*, 793(1):44, sep 2014. ISSN 15384357. doi: 10.1088/0004-637X/793/1/44. URL <https://iopscience.iop.org/article/10.1088/0004-637X/793/1/44>.

- L. Zhao, E. Landi, S. T. Lepri, J. A. Gilbert, T. H. Zurbuchen, L. A. Fisk, and J. M. Raines. On the Relation between the In Situ Properties and the Coronal Sources of the Solar Wind. *The Astrophysical Journal*, 846(2):135, sep 2017. ISSN 1538-4357. doi: 10.3847/1538-4357/aa850c. URL <https://iopscience.iop.org/article/10.3847/1538-4357/aa850c>.
- X. Zhao and J. T. Hoeksema. A coronal magnetic field model with horizontal volume and sheet currents. *Solar Physics*, 151(1):91–105, apr 1994. ISSN 0038-0938. doi: 10.1007/BF00654084. URL <http://link.springer.com/10.1007/BF00654084>.
- X. Zhao and J. T. Hoeksema. Prediction of the interplanetary magnetic field strength. *Journal of Geophysical Research*, 100(A1):19, 1995. ISSN 0148-0227. doi: 10.1029/94JA02266. URL <http://doi.wiley.com/10.1029/94JA02266>.

## ACKNOWLEDGMENTS

---

Wilcox Solar Observatory data used in this study was obtained via the web site <http://wso.stanford.edu> at 2020:11:29\_02:45:29 PST courtesy of J.T. Hoeksema.

This work uses data from the Michelson Doppler Imager (MDI) and the Extreme ultraviolet Imaging Telescope (EIT) onboard the Solar and Heliospheric Observatory (SOHO). The SOHO/LASCO data used here are produced by a consortium of the Naval Research Laboratory (USA), Max-Planck-Institut für Aeronomie (Germany), Laboratoire d'Astronomie (France), and the University of Birmingham (UK). SOHO is a project of international cooperation between ESA and NASA to study the Sun, from its deep core to the outer corona, and the solar wind.

Magnetograms from HMI aboard SDO are courtesy of NASA/SDO and the AIA, EVE, and HMI science teams.

Data from NASA's STEREO and ACE missions were used for this work. We thank the STEREO IMPACT and PLASTIC teams and the ACE SWICS, SWEPAM and MAG teams for making the data available to the scientific community.

Prof. Dr. Druckmüller kindly permitted me to use his remarkable photography of the 2008 solar eclipse.

At this point, I would like to thank all those people who have helped me in one capacity or another to finish my dissertation.

First and foremost, I am deeply grateful to my doctoral supervisor Prof. Dr. Robert Wimmer-Schweingruber, who offered me to be part of his research group, guided my scientific interest, always had time to listen to and help solve my various problems, and allowed me to work on a project that is now, literally, out of this world.

Dr. Verena Heidrich-Meisner immensely helped me through rough patches by always inquiring about the state of my work and offering to sift through the program code, even though she did not and could not know I missed a term in line 11027.

I thank my co-authors for their ideas, conversations, help, and patience. Outstandingly, Michael Hauptmann found the last mathematical piece of the puzzle, which would have taken many more months for me to find by myself.

I highly appreciate the help from Dr. Todd Hoeksema and Dr. Steven Cranmer, who devoted their time to explain their instruments, models, and program code.

Incredible gratefulness is due to Dr. Eckart Marsch. Not only did his lifework on heliospheric physics contribute a considerable portion to my current knowledge and understanding, but I am also fortunate to have my office next to his. Whenever I had struggles understanding specific physical processes anywhere in the heliosphere, he patiently and comprehensibly offered his knowledge and wisdom.

Further, my gratitude goes to Dr. Verena Heidrich-Meisner, Sarah Pleuger, Anne Fischer, Dr. Patrick Kühl, and Dr. Robert Elftmann for attentively reading and correcting the various drafts of this thesis. All remaining errors are, of course, my own.

Many thanks go to my colleagues in the Extraterrestrial Physics research group for discussions about and, more importantly, apart from physical topics. In particular, Dr. Lars Berger and Jan Steinhagen helped me improving my analyses and plots.

My wife Sarah, my girlfriend Amira, and my brother Steffen gave me emotional support, valuable distraction, and motivation to keep burning the midnight oil.

## ERKLÄRUNG

---

Ich versichere an Eides Statt, dass ich die vorliegende Dissertation in Form und Inhalt eigentständig angefertigt habe. Abgesehen von der Beratung durch meine Betreuer und der angegebenen Literatur wurde die Arbeit ohne fremde Hilfe erstellt. Ich versichere, dass ich keine andere als die angegebene Literatur verwendet habe. Diese Versicherung bezieht sich auch auf alle in dieser Arbeit enthaltenen Grafiken und bildlichen Darstellungen.

Die Arbeit als Ganzes wurde bisher keiner anderen Prüfungsbehörde vorgelegt. Teile der Arbeit wurden bereits in Fachzeitschriften veröffentlicht und sind als solche gekennzeichnet. Die Quellennachweise der in den einzelnen Veröffentlichungen referenzierten Inhalte finden sich in der jeweiligen Veröffentlichung selbst und werden nicht zusätzlich im Quellennachweis dieser Arbeit aufgeführt. Für das Einbinden der Veröffentlichungen in diese Arbeit wurde die ausdrückliche Genehmigung der publizierenden Fachzeitschrift eingeholt.

Ich erkläre abschließend, dass die Arbeit unter Einhaltung der Regeln guter wissenschaftlicher Praxis der Deutschen Forschungsgemeinschaft entstanden ist und dass mir noch kein akademischer Grad entzogen wurde.

*Kiel, Februar 2021*

---

Martin Alexander Kruse